Understanding the chemical processes leading to in situ ozone production in Delhi, India

Bethany Sian Nelson

Doctor of Philosophy

Chemistry
University of York
October 2021

In loving memory of Mavis Jones, who taught me to sing my times tables.

Abstract

A comprehensive observational data set of 86 volatile organic compounds (VOCs), NO_x ($NO + NO_2$), CO, HONO, and photolysis rates was collected during two intensive fields campaigns in Delhi, India. These observations were used to constrain a detailed chemical box model utilising the Master Chemical Mechanism (MCM) v3.3.1. A radical budget analysis for each campaign revealed high rates of radical initiation, propagation and termination during both the Delhi pre-monsoon and post-monsoon. In the post-monsoon, the largest contributor to radical initiation was HONO photolysis (42%). Carbonyl photolysis (27%) and ozonolysis (23%) were the largest contributors in the pre-monsoon period. The post-monsoon model was used to investigate the sensitivity of in situ O_3 formation to its precursor species. VOCs and NOx were varied in the model to test their impact on local O_3 production rates, $P(O_3)$. Mean morning $P(O_3)$ rates were most sensitive to monoaromatic compounds, followed by monoterpenes and alkenes, where halving their concentrations led to a 15.6%, 13.1% and 12.9% reduction in $P(O_3)$, respectively.

The chemistry of a range of atmospherically important ozone-alkene systems was explored. The product yields of alkene ozonolysis, an important radical source in Delhi, were investigated experimentally using data from an outdoor atmospheric simulation chamber. The yields of stabilised Criegee intermediates (SCIs) and primary carbonyls were determined from the ozonolysis of a range of alkenes. These yields were higher than those used in the MCM, meaning box models using the MCM may be overestimating OH radical yields from ozonolysis. Experimentally calculated yields for *cis*-pent-2-ene (0.38) and *trans*-pent-2-ene (0.32) were particularly high, compared to yields described in the MCM (0.18).

Overall, this study highlights the importance of understanding complicated atmospheric chemistry, used in chemical box models to understand the atmospheric processes underpinning poor air quality in growing urban centres such as Delhi, India.

Declaration

I declare that this thesis is a presentation of original work and I am the sole author. This work has not previously been presented for an award at this, or any other, University. All sources are acknowledged as References. I declare that this thesis is original work, and I am the sole contributor unless otherwise stated. The work presented in Chapter 4 is based on work in the following publication:

B. Nelson et al. "In situ Ozone Production is highly sensitive to Volatile Organic Compounds in the Indian Megacity of Delhi". In: *Atmos. Chem. Phys.* 21 (2021), pp. 1–36

Acknowledgements

Firstly, I'd like to thank my supervisors James Lee, Andrew Rickard and Jim Hopkins for your continued support and guidance throughout my PhD. Thank you for sharing your kindness, encouragement, enthusiasm, and knowledge over the years, which have helped me become the dedicated researcher I am today. I am extremely grateful for your expert guidance, patience and time, as I endeavoured to operate your field Gas Chromatograph (and return it in working order!), struggle through box model development, and pull together a first author paper. I feel very fortunate to have had three incredible supervisors to advise me over the past four years.

I'd also like to thank everyone in WACL who has given me both their support and friendship throughout my PhD. I feel so lucky to have completed my PhD, surrounded by so many knowledgeable and outgoing people, who could as easily pick me up when I'm down, as they could act as a soundboard for my scientific thoughts and ideas. In particular, I would like to thank the wonderfully unique and hilarious Gareth Stewart and Mike Newland. Your support and friendship, through intensive field campaigns, dodgy Uber rides, and endless failed model runs, has been invaluable. I genuinely think Gareth is one of the funniest people I have ever met, and I'd particularly like to thank Mike for being a truely special friend, and for encouraging me to be my unfiltered self.

Special thanks to all my collaborators, both during field campaigns in Delhi, and to everyone at the EUPHORE smog chamber in Valencia. I'd particularly like to thank Will Drysdale, Joe Acton, and Adam Vaughan for their contributions to the success of the Delhi campaigns, and their company. Particular thanks go to Will, for not letting the men who wanted entry to the hotel club "borrow" me! Finally, a massive thank you to Ranu Gadi and Shivani from Indira Gandhi Delhi Technical University for Women, whose resilience and enthusiasm meant the Delhi campaigns could go ahead. You are both incredible role models for aspiring female scientists.

On the topic of role models, I'd like to thank my amazing Zumba instructor, Mariana Lopez. Mariana's livestream classes kept me going through the COVID-19 lockdowns, both physically and mentally. Mariana herself is an amazing role model for women in science and engineering, who is full of compassion and enthusiasm. Her dedication to accessible exercise

for all, equality for all, and her kindness and moral compass have been, and continue to be, inspiring. I'd also like to thank everyone who has stayed on the zoom calls after Zumba for a quick chat, as those brief moments of socialisation were so valuable to me during lockdowns.

Finally, I'd like to thank my undergrad friends, Alex, Anil, Charlotte, Jenny and Stefan, for keeping things light and making me laugh hysterically over the past few years, often to the point of tears. I'd especially like to thank my parents, Beverley and Gary, my brother Michael, my late nan Mavis, and the unwaveringly supportive Jonathan for your love and encouragement.

Contents

List of Figures

List of Tables

Chapter 1

Introduction

In recent years, there has been an increase in the discussion and awareness of the human role in climate change. One of the catalysts for these progressive discussions was a young woman and activist from Sweden, who is now known globally for challenging governments and world leaders on meeting emission reduction targets. Greta Thunberg's activism started when she was just 15 years of age, when she would skip school to protest outside the Swedish parliament. This simple act inspired other children from across the globe to join her in school climate strikes, and in December 2018, more than 20,000 students were thought to be skipping school to protest with her all over the world. Now, three years later, discussions on climate change are a regular feature in the news, and on social media platforms. Greta's key aims are to instill more urgency in global emission reduction strategies, once calling the EU plans to reduce harmful emissions by 2050 as a "surrender". Thunberg said: "We don't just need goals for 2030 or 2050. We, above all, need them for 2020 and every following month and year to come". And she is right. Although the main goals of climate activists like Greta Thunberg are to act now to preserve our future, current levels of global emissions are having severe implications on the human health of millions of people right now in 2021. Reducing emissions of greenhouse gases and other pollutants is very important to reduce the severity of climate change, but is also crucial in improving the poor air quality millions of people are exposed to all over the world, which in many cases leads to respiratory illness, poor cardiovascular health, dementia, and death.

Although we are currently undergoing a new wave of interest in air pollution and environmental issues, the impact of climate change and poor air quality on humankind and the planet is not a new concept. The link between large amounts of carbon dioxide (CO_2) and increases in the Earth's temperature was first observed by Eunice Newton Foote, an experimental scientist and women's rights activist, in 1856 [2]. Her experimental observations, only recently rediscovered, preceded work by John Tyndall in 1859 in which the same conclusions were drawn [3, 4]. Since Tyndall's published lecture on the absorption of heat by gases and vapours, scientific research into the role of greenhouse gases on climate has continued. In the 1950s, climate research intensified. As analytical techniques improved, the significance

of CO_2's role as a greenhouse gas became more apparent. Carbon-14 isotope analysis by Roger Revelle and Hans Suess showed that CO_2 emitted from fossil fuels was not immediately absorbed by the ocean [5]. This finding was later corroborated by Charles Keeling, who demonstrated atmospheric levels of CO_2 were rising [6]. Meanwhile, developing cities across the world were experiencing poor air quality events. Air pollution events in London and Los Angeles were leading to thousands of deaths, propelling the development of air pollution legislation [7, 8]. It was apparent that the sources of air pollutants, harmful to human health, were similar to the sources of greenhouse gases. Despite the improvements in air quality resulting from air quality legislation, air pollution still impacts human health to this day. In 2020, Ella Kissi-Debrah, a 9-year old girl living in south-east London, became the first person in the UK to have air pollution listed as a direct cause of death [9]. Multiple severe asthma attacks leading up to her death were attributed to unlawfully high levels of nitrogen dioxide (NO_2) and particulate matter (PM) in Ella's neighbourhood. In contrast to the "climate emergency", frequently exposed on the news, the coroner cited a "low public awareness" of where to find both national and local air pollution information [9]. The importance of improving air quality in urban areas is evident. However, to further advise both policy makers and the public on national and local air quality, a detailed understanding of the complex chemical processes leading to air pollution, and the production of climate forcing gas and particle phase products, in different urban environments across the globe is required.

1.1 Global Air Quality

1.1.1 Air Quality and Climate Change

Although generally considered as separate, distinct areas of research, air quality and climate change are undoubtedly linked through complex feedback effects. Policy regulations in place to improve either will often lead to consequences in the other. In many cases, legislation to reduce emissions designed to reduce the burden of climate change will improve air quality. However, there are some strategies that have been employed to mitigate climate change, that have ultimately degraded air quality [10]. One example is the increased use of diesel cars, which was successful in the reduction of CO_2 emissions, a greenhouse gas (GHG). However, the consequence of this climate benefit was increased NO_x ($NO + NO_2$) and PM.

One of the main reasons why air pollution and climate change are linked is that air pollutants and GHGs often share the same sources. Thus, legislation to reduce the emissions from these sources to reduce the burden of climate change will also reduce ambient concentrations of pollutants damaging to human health. However, there are additional problems with air quality being exacerbated by global warming. Increased CO_2 leading to higher ambient temperatures may lead to increased emissions of biogenic volatile organic compounds (BVOCs), and impact atmospheric kinetics by increasing the reaction rates of important chemical processes, leading to ozone (O_3) formation. BVOCs are precursors to O_3 formation, which is damaging to crop yields, and reduces air quality [11]. However, the relationship between pollutant emissions and air quality is not always linear, due to the complicated chemical processes that occur in the atmosphere. It is therefore important to consider the consequences of pollution abatement strategies on both climate change and air quality.

1.1.2 Historical motivation for air quality research

Since the industrial revolution, new industrial processes and increasing industrialisation, alongside increased vehicular traffic, have led to increasingly poor air pollution across the globe. In the 1950s, emissions resulting from the increased urbanisation of cities across the world led to smog events, which propelled the funding of research into the understanding of air pollutants, along with the creation of important policy regulations. Smog events were commonplace in London, UK. In 1952, a lethal combination of industrial pollution and high-pressure weather conditions resulted in the "Great Smog of London". For four days, poor visibility brought the city to a standstill, and led to a reported 4,000 deaths during the event, and approximately 12,000 when accounting for the subsequent deaths caused by poor air quality [7]. The stagnant smog layer was mainly composed of the pollutants emitted from cheap sulfurous coal, used for heating homes and in power generation. The toxic mix comprised sulfur dioxide (SO_2), CO_2, and smoke particles. The Clean Air Act of 1956 was enacted in response to the Great Smog, leading to reductions in SO_2 and smoke from ≈ 300 μg m^{-3} to

< 100 μg m^{-3} by 1980 [12].

Meanwhile, in Los Angeles, episodes of smog were also frequent. However, the pollutants responsible for the smog in this city were different to those responsible for The Great Smog of London. In Los Angeles, emissions from automobiles and local industry were identified as the key sources of a different kind of smog, known as photochemical smog [8]. The coastal city of Los Angeles is surrounded by mountains, creating a basin-like topology. The surrounding mountains and the prevailing inland winds mean that pollutants circulate within the basin, creating a stagnant air mass. These pollutants lead to the secondary formation of another pollutant, tropospheric O_3, formed from the photochemical reactions of its precursor species. This pollutant is harmful to human health. Like London, the smog events in Los Angeles motivated the development of a range of pollution abatement strategies which have ultimately led to a decline in ambient O_3 concentrations, from ≈ 400 ppbV in 1970 to ≈ 100 ppbV in 2010.

1.1.3 Air pollution and Global Mortality

Poor air quality is a global public health concern, which is particularly problematic in rapidly growing urban centres. In 2016, an estimated 4.2 million premature deaths were attributed to poor ambient air quality, mainly caused by exposure to PM and O_3 [13]. A recent study by Lelieveld et at al. investigated the number of deaths attributed to outdoor air pollution globally, and found that parts of China and northern India had the largest numbers of pollution related deaths per unit area [14]. Figure 1.1, taken from this study, shows the mortality per unit area attributed to outdoor air pollution in 2010.

The study reported that China and India had the highest death count linked to outdoor air pollution. Globally, there were estimated to be 3,297,000 deaths linked to outdoor air pollution in 2010, 1,357,000 (41%) and 645,000 (20%) of which were from China and India respectively. For both countries, residential and commercial energy use (e.g. from heating and cooking) was attributed to $> 75\%$ of these deaths [14]. Figure 1.2 shows the top sources contributing to air pollution related deaths across the globe.

The largest source of deaths linked to outdoor air pollution varies across the globe. In the southern hemisphere, the majority of deaths were attributed to biomass burning and natural sources. Although deaths per unit area are generally lower in the southern hemisphere (Figure 1.1), some African countries located just above the equator have high moralities with respect to air pollution. For example, Nigeria and Egypt were the 5th and 11th highest ranking countries in premature deaths due to air pollution in 2010. The largest source of pollutants linked to air pollution deaths was natural sources in both cases, making up 52% and 88% of pollution related deaths in Nigeria and Egypt respectively. Natural sources here includes all airborne desert dust, however, there is likely an anthropogenic fraction associated with this category due to the role of humans in agricultural practices and desertification. In the

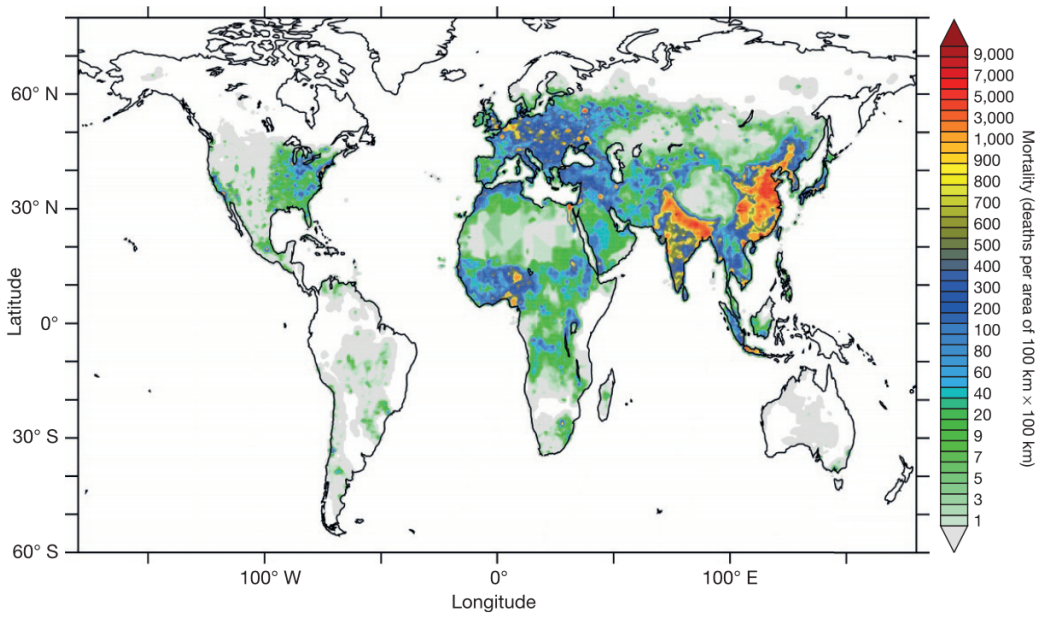

Figure 1.1: Global map of mortality linked to outdoor air pollution in 2010. The map is coloured by deaths per 100 km x 100 km. The white areas correspond to regions where annual mean $PM_{2.5}$ and O_3 are below the concentration response thresholds, where no excess mortality is expected. Taken from Lelieveld et al., 2015 [14].

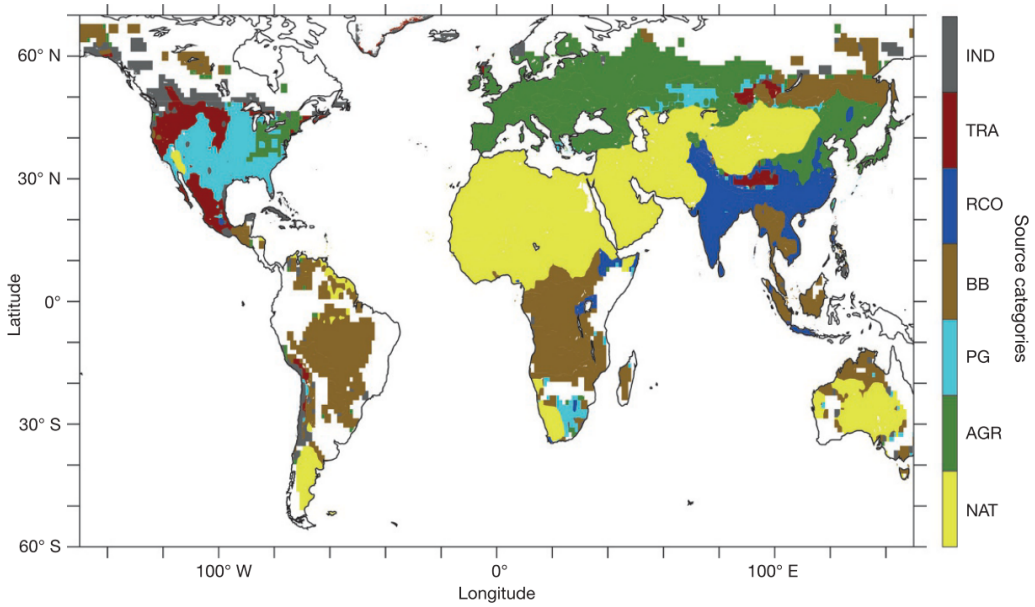

Figure 1.2: Global map coloured by the top contributing sources to deaths linked to outdoor air pollution in 2010. Source categories: IND = industry, TRA = land traffic, RCO = residential and commercial energy use, BB = biomass burning, PG = power generation, AGR = agriculture, and NAT = natural. The white areas correspond to regions where annual mean $PM_{2.5}$ and O_3 are below the concentration response thresholds, where no excess mortality is expected. Taken from Lelieveld et al., 2015 [14].

northern hemisphere, natural sources dominate across the northern parts of Africa, as well as the Middle East. Agricultural sources are the dominant contributor to outdoor air pollution related deaths across Europe, and biomass burning dominates in South East Asia. Deaths in central North America are mostly attributed to power generation sources, with higher contributions from land traffic in the east, and agriculture in the west [14].

1.2 Air pollution and human health

Poor air quality has a variety of health implications, particularly to individuals who already suffer from underlying respiratory or cardiovascular health issues. Short-term exposure to pollutants may lead to coughing, shortness of breath, wheezing and exacerbate asthma and respiratory diseases [15]. The long-term effects of air pollution include chronic asthma, pulmonary insufficiency, cardiovascular diseases and cardiovascular mortality. There are also studies that suggest a link between air pollution and other long term illnesses such as diabetes and dementia [16].

1.2.1 O_3

The main health effect of O_3 on humans is on the respiratory system. From a chemical perspective, O_3 is a strong oxidiser and will react with biomolecules in the body especially those with C=C double bonds, thiols and amines, which are the main components of lipids, proteins and anti-oxidants. The physical effects of O_3 on the respiratory system include damage to the epithelial cells present in airways, airway inflammation, and decreased lung function. For the general population, high O_3 events may led to coughing and throat irritation. For high risk or sensitive populations, high ozone may lead to chest tightness and increased asthma attacks [17]. Epidemiological studies have also reported a link between O_3 and cardiovascular mortality, as well as cognitive development and reproductive health [17–19].

In addition to the direct effects of ozone on health, ozone can indirectly contribute to poor health through its effect on crops. O_3 enters leaves via diffusion through the stomatal pores. This damages crops such as wheat, rice and soybean by reacting with biomolecules in the leaves, forming highly reactive oxygenated compounds. The plant reacts to this by diverting energy to leaf protection mechanisms, rather than seed production. This leads to the degradation of the crop. O_3 crop destruction may lead to large economic losses, and is a particularly important issue in developing countries, where low crop yields can increase food prices, and lead to malnourished populations [20–22].

1.2.2 Particulate Matter (PM)

There is substantial evidence on the health effects of coarse particles, which have a particle diameter of 2.5 - 10 μm. There have been many studies reporting on the link between coarse particles and cardiovascular and respiratory illnesses [17, 23–25]. Generally, the smaller the diameter of the particle, the more likely it is to impact the respiratory system and organs. Particles larger than 10 μm are more likely to collect in the nose and nasopharynx, and can be removed from the body through sneezing, coughing, and nose blowing. Particles smaller than 10 μm can settle in the windpipe. If they are smaller than 2.5 μm, they are more likely to penetrate the lungs. The smaller size of ultrafine particles (< 0.1 μm) means that they can enter the bloodstream. Some studies have reported these particles may migrate to other organs in the body through the bloodstream, including the heart, liver, kidneys and brain [17, 26]. Particles smaller than 2.5 μm may settle in the alveoli of the lungs, which acts as the primary route of gas exchange from the lungs to the bloodstream. An accumulation of particles here can lead to inflammation, scar tissue reducing oxygen supply to the bloodstream, and the transfer of unwanted chemical species to the bloodstream. The physical effects of these processes include reduced respiratory function, thrombosis, the thickening of artery walls, and increased blood pressure. Chemical substances transferred to the bloodstream via small particles may interact with biomolecules in the body, leading to additional health implications. These chemicals may be carcinogenic, mutagenic, teratogenic and reprotoxic, leading to a broad range of health complications. One such chemical substance is the polyaromatic hydrocarbon benzo[a]pyrene, both mutagenic and carcinogenic, which was identified as the cause of skin cancers and tumours in coal tar workers in 1933 [27, 28]. Metals and oxidised compounds may also be transported, leading to the formation of free radicals which may cause oxidative stress, increase the incidence of cell death, and impact DNA copying mechanisms in the body.

1.2.3 NO_2

The predominant health impact of NO_2 is on the respiratory system. In the short-term, NO_2 inhalation can lead to changes in lung function in sensitive population groups, whilst long-term exposure may increase susceptibility to respiratory infections [29]. Although there are many studies that have reported a direct link between NO_2 concentrations and respiratory illnesses, it is often difficult to differentiate between effects caused by NO_2 and other pollutants in epidemiological studies. However, recent studies have made adjustments to account for possible interfering effects from PM, and provide evidence to support that NO_2 has some direct effects on respiratory outcomes [17].

1.3 Reactions of volatile organic compounds with radicals

1.3.1 Atmospheric oxidants

Unlike greenhouse gases, the chemical species responsible for air pollution tend to be short lived due to their reactivity. As a result, atmospheric chemical processes are important in air quality science. Atmospheric chemical processes are driven by the reactivity of radical oxidants. The key radical oxidants present in urban environments are OH, NO_3 and O_3. Understanding the sources and sinks of these radical species is essential in developing a full understanding of the chemical processes leading to surface level O_3, as well as secondary organic aerosol (SOA), formed from the oxidised products of chemically processed organic compounds.

The OH radical is mainly formed through photolysis reactions. As a result, OH radical formation generally occurs in the day, with lower formation rates at night. OH is formed from the photolysis of HONO, and from the reaction of H_2O with O^1D, formed from O_3 photolysis (equations 1.1, 1.2, and 1.3). The main formation route of OH globally is through the photolysis of O_3 and subsequent reaction of $O(^1D)$ with H_2O. The formation of OH radicals from HONO photolysis is often significant in urban environments, where HONO concentrations can be high. HONO is considered to exist in photochemical steady state, whereby it is formed from reactions of OH + NO (equation 1.4), and lost through photolysis, remaking OH, and through reactions with OH to form water and NO_2 (equations 1.3 and 1.5) [30]. If the photochemical steady state holds true, HONO photolysis and recombination from OH and NO are in dynamic equilibrium, with no net production of the OH radical. However, observational HONO concentrations from field campaigns are typically higher than those calculated from photochemical steady state analyses, with daytime concentrations of a few hundred pptV frequently reported [31–33]. This suggests that there are additional sources of HONO, which lead to net OH production. Some of the proposed sources of HONO include, bacterial production of nitrate in soil surfaces, and the conversion of NO_2 and HNO_3 to HONO on ground surfaces in the presence of sunlight [34–37]. Diesel and petrol vehicle exhausts have also been shown to contribute to HONO production [38, 39]. Field studies typically report high concentrations of HONO at night due to the absence of sunlight. This can lead to a night-time build up of HONO, which rapidly photolyses in the morning to form OH radicals.

$$O_3 + h\nu \longrightarrow O(^1D) \tag{1.1}$$

$$O(^1D) + H_2O \longrightarrow 2\,OH \tag{1.2}$$

$$HONO + h\nu \longrightarrow OH + NO \tag{1.3}$$

$$OH + NO\ (+M) \longrightarrow HONO\ (+M) \tag{1.4}$$

$$HONO + OH \longrightarrow H_2O + NO_2 \tag{1.5}$$

OH radicals can also be formed non-photolytically through alkene ozonolysis reactions, described in more detail in Chapters 3 and 5. The OH radical is generally removed via reactions with VOCs, propagating the radical through RO_2 and HO_2 species.

Unlike OH, NO_3 is generally present in higher concentrations at night. The main route of NO_3 formation is through the reaction of NO_2 with O_3 (equation 1.6).

$$NO_2 + O_3 \longrightarrow NO_3 + O_2 \tag{1.6}$$

$$NO_3 + h\nu \longrightarrow NO + O_2 \tag{1.7}$$

$$NO_3 + NO \longrightarrow 2\,NO_2 \tag{1.8}$$

The main removal processes of NO_3 is through photolysis (equation 1.7). NO_3 is also lost through reactions with NO (equation 1.8). At night, this sink is limited by the lack of photolytic regeneration of NO from NO_2.

O_3 is formed in the daytime in urban environments. The photolysis of NO_2 leads to the formation of an $O(^3P)$ atom, which rapidly reacts with molecular oxygen to from O_3. A more detailed description of urban O_3 production is provided in section 1.4. The main removal processes for O_3 include photolysis, and ozonolysis reactions with alkenes.

$$NO_2 + h\nu \longrightarrow NO + O(^3P) \tag{1.9}$$

$$O(^3P) + O_2 \longrightarrow O_3 \tag{1.10}$$

Each atmospheric oxidant reacts at different rates with VOC species. The rate of these reactions, along with the VOC size and structure, lead to a variety of different oxidised products with different atmospheric fates.

1.3.2 VOC reactivity and lifetimes

A summary of the reaction rates and lifetimes of selected VOCs with OH, NO_3 and O_3 is provided in Table 1.1. Generally, VOCs have higher rate coefficients with OH than NO_3, and rate coefficients with O_3 are lower still. However, there are larger concentrations of O_3 present in the atmosphere, meaning the lifetime of some VOCs with respect to O_3 is short. This is particularly true for alkenes, which readily undergo ozonolysis reactions. For example, using preferred rate constants from the IUPAC kinetic database, the lifetime of *trans*-but-2-ene with respect to O_3 is 1.9 h at ambient O_3 levels of 30 ppbV (7.5 x 10^{11} molecule cm^{-3}) [40]. Alkenes also have short lifetimes with respect to OH and NO_3 compared to other classes of VOCs. Because of this, smaller ambient concentrations of alkenes can have a significant effect on the reactivity of the atmosphere.

Table 1.1: Atmospheric rates constants at 298K, and lifetimes with respect to OH, NO_3 and O_3 for a selection of VOCs. Assumed concentrations of OH, NO_3, and O_3 are 1.6 x 10^6, 3.5 x 10^8 and 7.5 x 10^{11} molecule cm^{-3} respectively, typical in urban environments. Preferred rate constants as reported by IUPAC were used [40].

Compound	OH		NO_3		O_3	
	k_{298} x 10^{-12} (cm^3 $molecule^{-1}$ s^{-1})	Lifetime (hours)	k_{298} x 10^{-16} (cm^3 $molecule^{-1}$ s^{-1})	Lifetime (hours)	k_{298} x 10^{-18} (cm^3 $molecule^{-1}$ s^{-1})	Lifetime (hours)
Ethane	0.24	723.4	< 0.10	79365.1	NA	NA
Propane	1.10	157.8	< 0.70	11337.9	NA	NA
Butane	2.35	73.9	0.46	17253.3	NA	NA
Ethene	7.80	22.3	2.10	3779.3	1.55	238.9
Propene	29.00	6.0	95.00	83.5	10.50	35.3
cis-but-2-ene	56.00	3.1	3500.00	2.3	130.00	2.9
trans-but-2-ene	64.00	2.7	3900.00	2.0	200.00	1.9
Isoprene	100.00	1.7	6500.00	1.2	12.80	28.9
Acetylene	0.75	231.5	< 1.00	7936.5	0.01	37037.0
Benzene	1.20	144.7	< 0.30	26455.0	< 0.01	37037.4
Toluene	5.60	31.0	0.78	10175.0	< 0.01	37037.4
α-pinene	53.00	3.3	62000.00	0.1	96.00	3.9

1.3.3 Alkanes

The dominant reaction pathways for alkanes in the atmosphere are with OH radicals. Alkanes may also react with O_3 at much slower rates than with the OH radical, meaning their reactions with O_3 are less atmospherically relevant than the reactions of alkanes with OH. The reaction of alkanes with OH occurs via H-abstraction. OH abstracts a hydrogen atom from the alkane, creating a radical alkyl species. Due to the inductive effect of alkyl groups, H-abstraction preferentially occurs to form secondary or tertiary radicals. This radical rapidly reacts with molecular oxygen in the atmosphere, forming a peroxy radical species (Figure 1.3).

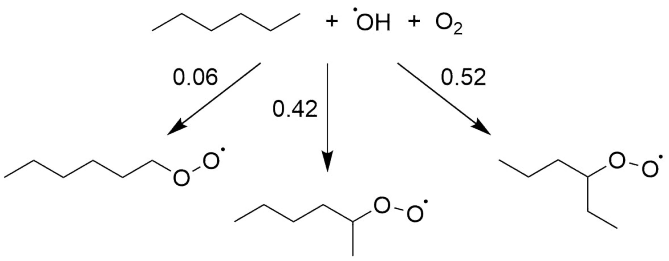

Figure 1.3: Schematic of the possible atmospheric chemical fates of alkanes. The example shown here is for *n*-hexane. From left to right, the branching ratios (the proportion of the reaction following each pathway) of each H-abstraction pathway are 0.06, 0.42, and 0.52.

1.3.4 Alkenes

The double bond character in alkenes makes them more reactive with atmospheric oxidants than alkanes (see Table 1.1). In contrast to alkanes, alkenes rapidly react with O_3, as well as OH and NO_3. The reactions of alkenes with all three oxidants are atmospherically important due to their fast reaction rates (see Table 1.1). Figure 1.4 shows the possible reaction pathways for alkenes. Unlike alkanes, OH addition to the double bond is the dominant pathway rather than H-abstraction. The double bond breaks to form a β-hydroxy radical. This species rapidly reacts with molecular oxygen to form a (β-hydroxy)-peroxy radical (Figure 1.4, pathway (a)). Alkenes also react with O_3 via an addition mechanism, described in more detail in Chapter 5.

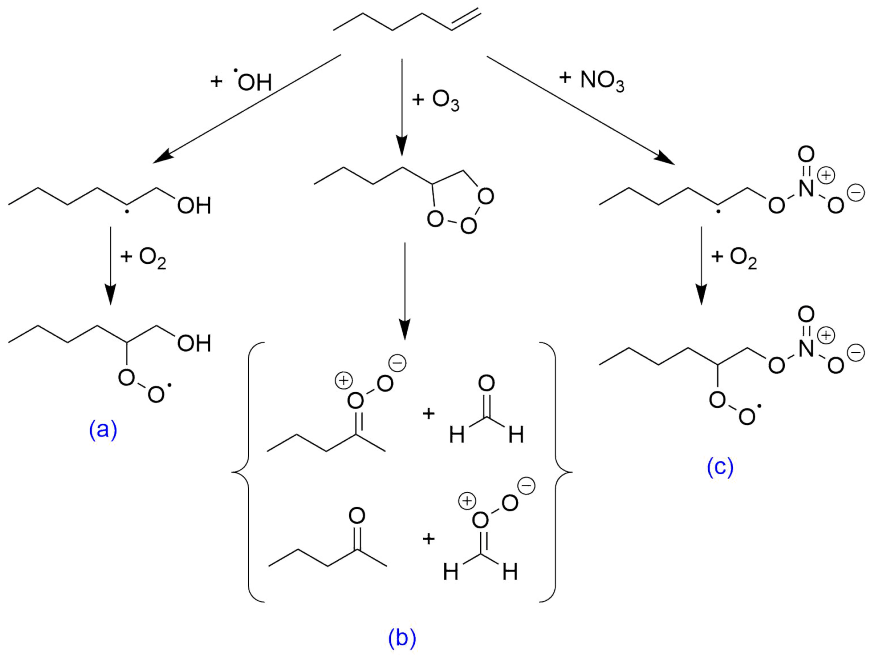

Figure 1.4: Schematic of the possible atmospheric chemical fates of alkenes. The example shown here is for hex-1-ene.

O_3 is added across the double bond, forming a primary ozonide (POZ). This ozonide readily decomposes to form a Criegee intermediate (CI) species and a carbonyl co-product. Depending on the symmetry of the parent alkenes, either one or two pairs of CI and carbonyl co-product can be formed (Figure 1.4, pathway (b)). Finally, alkenes can react with the NO_3 radical, again through an addition mechanism. Similar to OH addition, the nitrate radical adds to the double bond, forming a radical on the β-carbon. In the presence of molecular oxygen, a peroxy nitrate species is rapidly formed (Figure 1.4, pathway (c)).

1.3.5 Aromatics

Like alkenes, the reaction between aromatic species and OH predominantly proceeds via OH addition across the ring, creating a radical β-carbon, known as an OH-adduct species [41]. For some substituted species such as toluene, H-abstraction is also possible (Figure 1.5, pathway (a)). However, this is a minor channel for aromatic species as OH addition occurs at much faster timescales. The resulting hydroxy radical species formed from OH addition can then lose a hydrogen to form a phenol and an HO_2 radical (Figure 1.5, pathway (c)). However, the dominant route is the formation of a peroxy radical species via the addition of molecular oxygen to the radical carbon (Figure 1.5, pathway (a)).

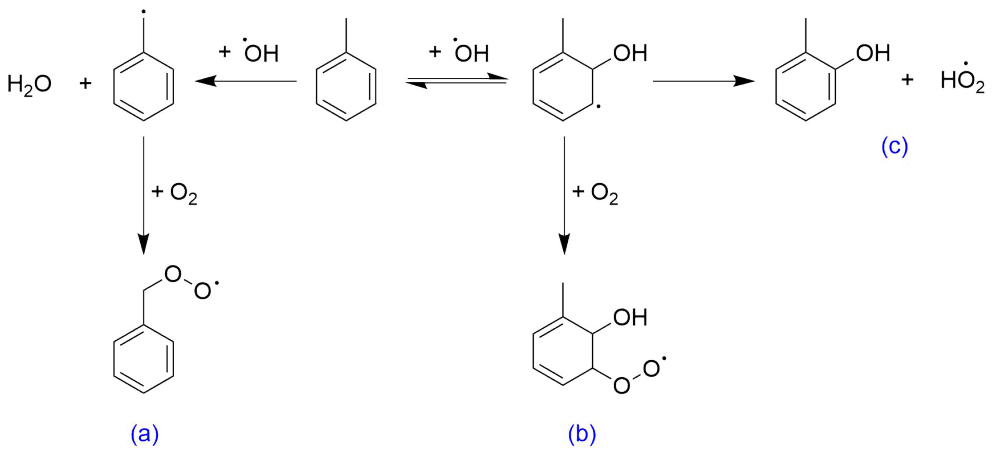

Figure 1.5: Schematic of the possible atmospheric chemical fates of aromatics. The example shown here is for toluene.

The peroxy radical phenol formed via route (b) (Figure 1.5) can then rearrange to form a bicyclic radical compound. Molecular oxygen is readily added to the bicyclic radical and, in the presence of NO, a bicyclic alkoxy radical is formed. The bicyclic alkoxy radical then undergoes ring opening, leading to the formation of a broad range of oxygenated species (Figure 1.6, pathway (e)).

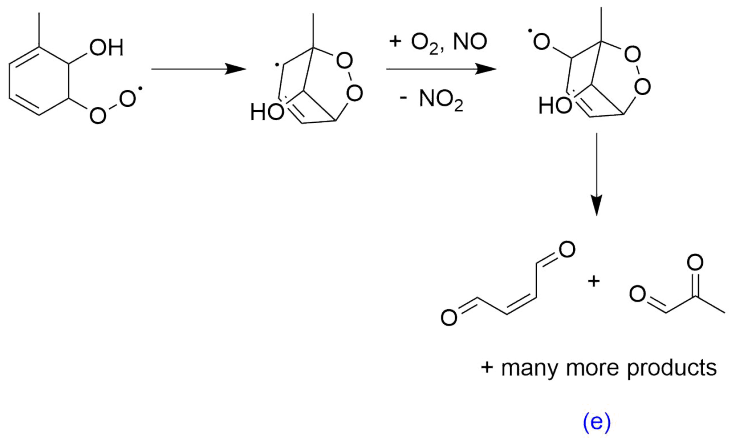

Figure 1.6: Schematic of the ring opening mechanism for the peroxy radical species formed from OH addition to toluene.

1.3.6 Alkoxy and peroxy radicals

Peroxy radicals readily react with other peroxy radicals in the atmosphere, as well as NO. Firstly, a peroxy radical may react with another peroxy radical to form a carbonyl species and an alcohol (Figure 1.7, pathway (a)). Alternatively, the peroxy radical may react with HO_2, to form a hydroperoxide and molecular oxygen (Figure 1.7, pathway (b)). In urban environments where NO is present, peroxy radicals can oxidise NO to NO_2, forming an alkoxy radical (Figure 1.7, pathway (c), see Figure 1.8 for alkoxy radical fates). This route leads to the propagation of radical species, which are described in more detail in section 1.4 and Chapter 3. Through their propagation, the radical species can continue to undergo chemical processes in the atmosphere, important for O_3 formation. Another possible fate for peroxy radicals in urban environments is the formation of a nitrate species (Figure 1.7, pathway (d)). This is a minor route for smaller peroxy radicals, but increases in importance with increasing carbon chain size. In the case of *n*-hexane, this is a significant pathway (22%).

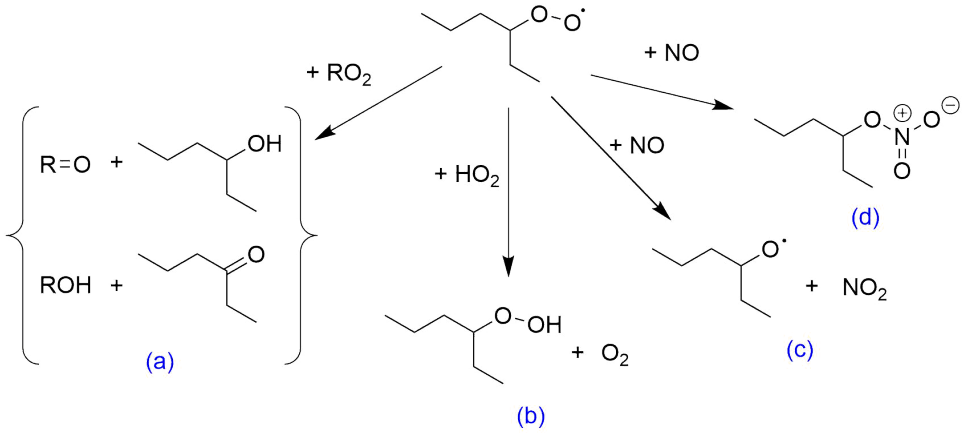

Figure 1.7: Schematic of the atmospheric fate of peroxy radical species. The example given here is for a hexane peroxy radical species.

Alkoxy radicals undergo a range of different atmospheric pathways in the atmosphere. Firstly, alkoxy radicals may undergo unimolecular decomposition, forming an aldehyde and an alkyl radical species. In the atmosphere, molecular oxygen is rapidly added to this radical to form a peroxy radical. The C-C bond breakage can happen either side of the C-O alkoxy radical bond, leading to two possible combinations of aldehyde and radical alkyl compounds from asymmetric alkoxy radicals (Figure 1.8, pathways (e) and (f)).

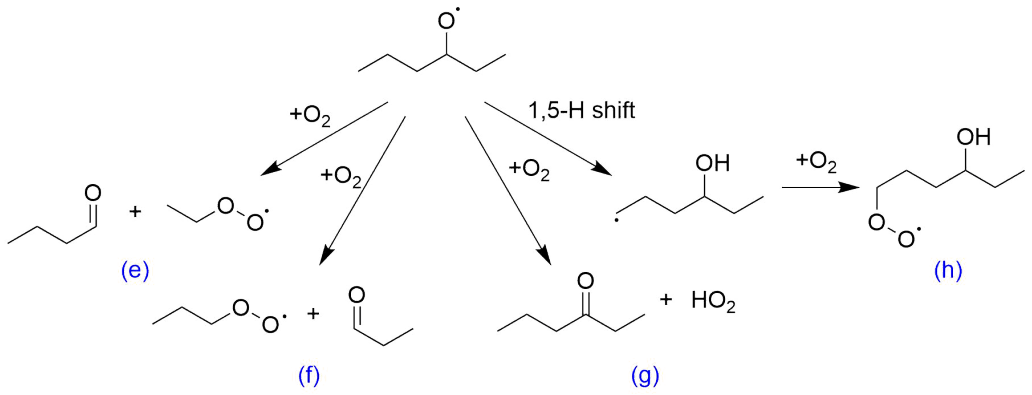

Figure 1.8: Schematic of the atmospheric fate of alkoxy radical species. The example given here is for a hexane oxy radical species.

Another fate for alkoxy radicals is the formation of a ketone (or aldehyde for terminal alkoxy radicals) via the removal of a hydrogen atom in the presence of molecular oxygen, to form an HO_2 radical (Figure 1.8, pathway (g)). Finally, for longer chain alkoxy radicals such as the example provided in Figure 1.8, a 1,5-hydrogen shift can occur, leading to a radical carbon on the alkyl chain, and an alcohol substituent group. In the case shown in Figure 1.8, this leads to the formation of a terminal radical species which is highly unstable due to the limited induction effect from only one neighbouring carbon. The unstable radical readily reacts with molecular oxygen to form an hydroxy peroxy radical (Figure 1.8. pathway (h)).

1.3.7 Secondary Organic Aerosol formation

Generally, the oxidative degradation of VOCs leads to a reduction in volatility in subsequent oxygenated products. Secondary organic aerosol (SOA) is formed when the low volatility oxidation products of VOCs deposit onto existing particles. The breadth of oxidation products present in the atmosphere leads to a complex mixture of SOA species, with a broad range of functional groups, hygroscopicity and chemical compositions [42]. As a result, the role of SOA on climate, and its effect on air quality and human health, is difficult to determine.

1.4 Ozone formation

Ozone is produced in the troposphere via the photolysis of NO_2 (equation 1.11), and the subsequent recombination of $O(^3P)$ with O_2 (equation 1.12). The ozone formed can react with NO, a product of NO_2 photolysis, regenerating NO_2 and O_2 in a null cycle (equation 1.13).

$$NO_2 + h\nu \longrightarrow NO + O(^3P) \quad (\lambda < 420 \text{ nm}) \tag{1.11}$$

$$O(^3P) + O_2 \longrightarrow O_3 \tag{1.12}$$

$$O_3 + NO \longrightarrow NO_2 + O_2 \tag{1.13}$$

The photo-dissociation and regeneration of NO_2 is sufficiently rapid that these species are likely to be in dynamic equilibrium. As a result, NO, NO_2 and O_3 are in a photochemical steady state (see Chapter 3) [43, 44]. This steady state, known as the photostationary steady state, can be described by the Leighton equation (equation 1.14)

$$\phi = \frac{j(NO_2)[NO_2]}{k_{1.13}[NO][O_3]} \tag{1.14}$$

where $k_{1.13}$ is the reaction rate of NO+O_3 (equation 1.13), forming NO_2. When O_3 is the sole oxidant present, $\phi = 1$, equation 1.14 can be rearranged to determine the concentration of O_3 from NO and NO_2 concentrations (equation 1.15).

$$O_3 = \frac{j(NO_2)[NO_2]}{k_{1.13}[NO]} \tag{1.15}$$

When additional oxidants are present, they can react with NO, regenerating NO_2, and breaking the ozone null cycle. Peroxy radicals (RO_2 + HO_2) are atmospheric oxidants which react with NO in this way, leading to net O_3 production (equation 1.16). Consequently, the O_3 production rate is dependent on the rate of RO_2 production. Peroxy radicals are generated in the atmosphere from reactions between VOCs and OH, as described in section 1.3. Peroxy radicals react with NO to form NO_2 and RO which further react, producing oxygenated volatile organic compounds (o-VOCs) and HO_2. OH is regenerated in the O_3 formation cycle, through the reaction of HO_2 with NO (equation 1.17). The O_3 formation cycle is summarised in Figure 1.9.

$$RO_2 + NO \longrightarrow RO + NO_2 \tag{1.16}$$

$$HO_2 + NO \longrightarrow OH + NO_2 \tag{1.17}$$

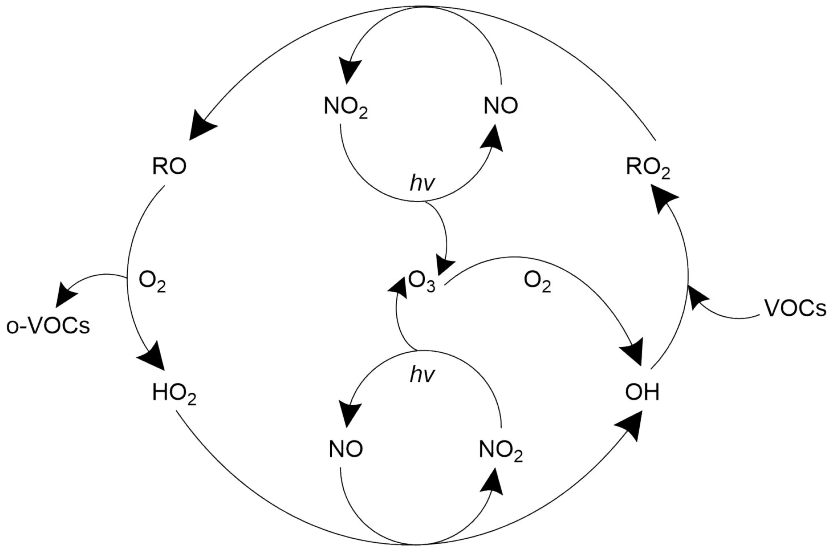

Figure 1.9: O_3 production cycle in urban atmospheres.

Due to its photolytic sources, OH concentrations tend to be higher during the day and negligible at night. In addition, the recycling of NO_2 back to NO is driven by photolysis. This leads to a similar diel profile for O_3, often peaking just after radical concentrations peak. The photolysis of oxygenated VOCs (o-VOCs) produced in the O_3 formation cycle also contributes to the formation of RO_2 species, which re-enter the cycle, leading to further O_3 production.

Environments can be defined as either VOC-limited or NO_x-limited with respect to O_3 production. In a VOC-limited regime, changes in VOC concentrations at fixed NO_x concentrations, lead to a roughly linear response in O_3 formation. At a fixed VOC concentration, reductions in NO_x can lead to increased O_3 production. This is due to a reduction in the NO_2+OH sink pathway, which increases OH in the atmosphere (equation 1.18). This increases RO_2 production through VOC+OH, therefore increasing O_3 production. NO_x-limited regimes describe environments whereby changing NO_x concentrations leads to a roughly linear response in O_3 production. Changes in VOC concentrations in this regime have a minimal effect on O_3 production.

$$NO_2 + OH\ (+M) \longrightarrow HNO_3\ (+M) \tag{1.18}$$

The dependency of O_3 production on NO_x and VOC concentrations can be modelled in an O_3 isopleth (Figure 1.10). The threshold in which the regimes may interchange is shown by the curved head of the isopleth (diagonal line, Figure 1.10). Policymakers may choose to

design their O_3 reduction strategies based on the regime in which cities fall. The majority of urban centres are VOC-limited [45]. Many urban areas focus on NO_x reduction strategies, aiming to bring high levels of NO_2 back into compliance with legal limits. However, a side effect of NO_x reduction in a VOC-limited region, without co-reducing VOCs, is increased O_3 production and/or reduced O_3 titration. Thus, in a VOC-limited case, it is desirable for policymakers to consider reducing both VOC and NO_x concentrations simultaneously, since there are human health consequences from high concentrations of both O_3 and NO_x (see section 1.2).

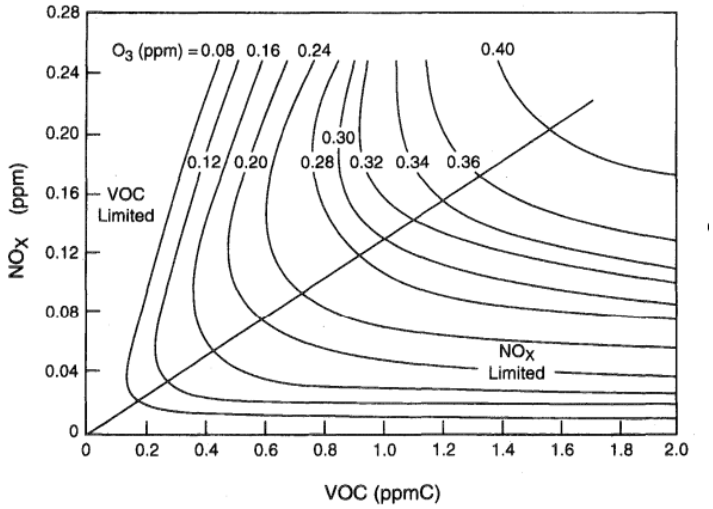

Figure 1.10: An O_3 isopleth generated using the Empirical Kinetic Modelling Approach (EKMA), adapted from Finlayson and Pitts, 1993 [46].

1.5 Air pollution in Delhi, India

India is one of the most highly polluted countries in the world. The 2020 report by IQAir found that 22 of the top 30 most polluted cities in the world were located in India [47]. Some of the major sources of pollutants in India include transportation, biomass burning for cooking, energy generation, and waste burning. Many regions are additionally affected by seasonal agricultural burning. The states of Punjab and Haryana, neighbouring the state of Delhi, undertake open burning practices to prepare crop fields for summer or winter planting. This stubble-burning process provides farmers with a quick and affordable way to transition between crop seasons. Despite government intervention in banning the stubble-burning under Section 188 of the Indian Penal Code and the Air Pollution Control Act of 1981, the practice continues to occur due to a lack of alternative solutions which do not incur excessive additional expenses to farmers.

Emissions from crop residue burning in the neighbouring state of Punjab, coupled with transportation, energy generation and waste burning emissions to name a few, has led to Delhi

being ranked as the most polluted capital city in the World in 2020 (Figure 1.11). Annual average concentrations of $PM_{2.5}$ in the city were 84.1 μg m^{-3}, much higher than the World Health Organisation's target limit of 10 μg m^{-3}. Monthly averages were higher in Delhi during the peak burning season, reaching 157 μg m^{-3} in December 2020.

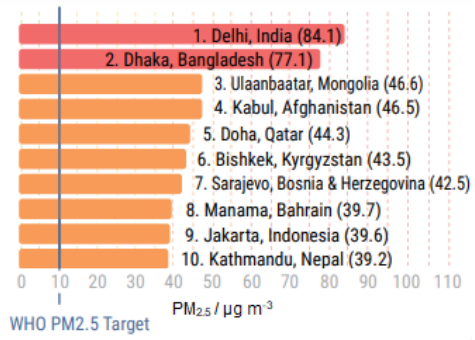

Figure 1.11: Top 10 ranked most polluted capital cities in the world, according to annual average $PM_{2.5}$ concentrations. Taken from IQAir, 2020 [47].

Along with $PM_{2.5}$, O_3 concentration limits are also regularly exceeded in Delhi. A recent report on global O_3 exposure highlighted that India experiences one of the highest average 8-hour maximum O_3 concentrations in the world (66 ppbV, 129 μg m^{-3}). This is more than double average values for the UK (32 ppbV, 63 μg m^{-3}) (Figure 1.12). Average O_3 concentrations in Delhi therefore exceeded the health limits set by the World Health Organisation of 50 ppbV (98 μg m^{-3}).

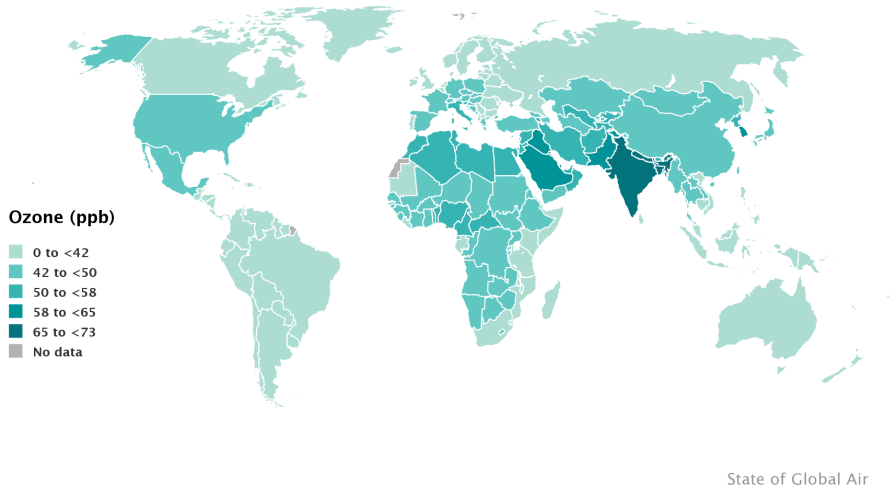

Figure 1.12: Average 8-hour O_3 concentrations by country. Taken from State of Global Air, 2020 [48].

In the world ranking for O_3 exposure in 2019, India was the 3rd highest country. Generally, average O_3 exposure is increasing across the globe, but is increasing more steeply in

India. Between 2010-2019, India experienced the largest increase in population-weighted average 8-hour ozone concentrations [48].

1.5.1 The measurement of pollutants in Delhi, India

Several key atmospheric pollutants are monitored by the Central Pollution Control Board (CPCB), a subgroup of the Ministry of Environment, Forest and Climate Change (MoEFCC), Government of India. The CPCB was created in 1974, initially in line with the Water (Prevention and Control of Pollution) Act, and was subsequently entrusted with managing the Air (Prevention and Control of Pollution) Act of 1981. As part of the Air Act, the CPCB's principal role is to "improve the quality of air and to prevent, control or abate air pollution in the country".

One of the CPCB's main methods of assessing air quality standards is through operating and maintaining a network of ambient air quality monitoring sites, as part of the National Air Quality Monitoring Programme (NAMP). According to the CPCB's webpage, there are 793 operating stations, covering 344 cities/towns in 29 states and 6 Union Territories at the time of writing. Although twelve key air pollutants have prescribed national ambient air quality standard limits, only four of these are regularly monitored at all locations: Sulfur Dioxide (SO_2), Nitrogen Dioxide (NO_2), respirable suspended particulate matter (RSPM / PM_{10}), and fine particulate matter ($PM_{2.5}$). Measurements of other key harmful pollutants such as O_3, benzene and carbon monoxide (CO) aren't included at many of the monitoring sites.

The CPCB co-ordinates and funds multiple agencies in addition to providing technical support and ensuring the "uniformity, consistency of air quality data". Despite the importance of this air quality monitoring to our understanding of pollution levels and subsequent risk to human health, the CPCB's website clearly states that large numbers of people and equipment involved in each step of NAMP, from sampling, to chemical analysis and finally data reporting, "increases the probability of variation and personnel biases reflecting in the data". As a result, the data collected should be "treated as indicative rather than absolute". The current prescribed national ambient air quality standards, as published in The Gazette of India in November 2009, are presented in Table 1.2.

Although O_3 is not listed as one of the key compounds requiring regular monitoring in India, it is measured at several air quality monitoring sites in Delhi, India. However, the data availability is limited, and the CPCB does not report O_3 data above 200 μg m^{-3}, as a maximum value of 200 μg m^{-3} is sufficient for air quality index (AQI) reporting purposes. However, O_3 concentrations were reported to have exceeded the 8-hour standard limits for at least one monitoring station on 290 days in 2020, an increase from 260 days in 2019 [49].

Table 1.2: Indian nationally prescribed air quality standards, and published in The Gazette of India in 2009 [50].

Pollutant	Time weighted average	Concentration in ambient air / μg m^{-3}	
		Industrial, residential, rural, and other areas	Ecologically sensitive areas (notified by Central Government)
Sulfur Dioxide (SO_2)	Annual	50	20
	24 hour	80	80
Nitrogen Dioxide (NO_2)	Annual	40	30
	24 hour	80	80
Particulate Matter < 10 μm (PM_{10})	Annual	60	60
	24 hour	100	100
Particulate Matter < 2.5 μm ($PM_{2.5}$)	Annual	40	40
	24 hour	60	60
Ozone (O_3)	8 hour	100	100
	1 hour	180	180
Lead (Pb)	Annual	0.5	0.5
	24 hour	1.0	1.0
Carbon Monoxide (CO)	8 hour	2000	2000
	1 hour	4000	4000
Ammonia (NH_3)	Annual	100	100
	24 hour	400	400
Benzene (C_6H_6)	Annual	5	5
Benzo[a]pyrene (BaP), particulate phase only	Annual	0.001	0.001
Arsenic (As)	Annual	0.006	0.006
Nickel (Ni)	Annual	0.02	0.02

1.6 The APHH-India project

To fully understand the emissions of air pollutants in Delhi, India, along with their impact on human health, the Atmospheric Pollution and Human Health in an Indian Megacity programme (APHH-India) was developed. The large research programme focused on 5 key ares of research: ASAP-Delhi, DelhiFlux, Promote, DAPHNE, and CADTIME, each with different research themes and goals. The aims for each sub-project are as follows:

- ASAP-Delhi: Identify the sources, formation processes and characteristics of particulate matter (PM) in Delhi and the National Capital Region.
- DelhiFlux: Measure new emission factors for Delhi pollutants, and compare new emission inventories and current inventories to in situ pollutant flux measurements.
- Promote: Investigate the contribution of primary and secondary aerosols to air pollution in Delhi, examine the impacts of meteorology and long range transport, and determine effective emission control measures to reduce air pollution in Delhi.
- DAPHNE: Investigate the impact of air pollution on key health metrics such as (i) birth weight, (ii) acute respiratory infections in children under 2 year of age, and (iii) on asthma in children aged 12 - 18 years.
- CADTIME: Identify the sources and emission trends of air pollutants, and investigate the impact of potential air pollution legislation on future air quality scenarios in Delhi.

To compliment the air pollutant flux data as part of the DelhiFlux sub-project, additional funding was acquired to take ambient air measurements at ground-level. The ground-level concentration data obtained could be used in an atmospheric chemical box model to investigate the chemical processes occurring in Delhi's atmosphere, as well as the types of emissions controlling in situ O_3 formation.

1.7 Atmospheric Chemical Box Modelling and the Master Chemical Mechanism

Atmospheric chemical box models are used to investigate the chemical processes occurring in both urban and remote environments. These models require a chemical mechanism, which is used to generate additional chemical species based on reaction rates, mechanistic pathways, and inputted concentrations of precursor species. An example of a detailed description of atmospheric chemistry is the Master Chemical Mechanism (MCM). The MCM is a near explicit chemical mechanism describing the chemical processes involved in the degradation of atmospherically important VOCs. The MCM describes the detailed atmospheric chemical degradation of 143 VOCs, though 17,500 reactions of 6,900 species (http://mcm.york.ac.uk). The mechanism includes both organic and inorganic atmospheric chemistry. The MCM protocol describes different types of chemical processing, including radical initiation, propagation and termination reactions. The mechanism follows the initial degradation of primary VOC species through reactions with OH, O_3, NO_3 and photolysis, and further reactions of subsequent products. The continued processing of VOCs generates a wide range of oxygenated species, CO, and CO_2 [51].

Reaction rate data used by the MCM is from published laboratory data, atmospheric simulation chamber experimental data, and theoretical data. The rates used are the preferred values described in the IUPAC Kinetic Database [40], which takes into account multiple published rates before a preferred rate is defined. For reactions in which rates and product pathway branching ratios are unavailable, the MCM uses experimental and theoretical data from similar chemical species, and defines a structure activity relationship (SAR) between the species of interest and an analogous set of structurally similar compounds [52].

The MCM is described as *near explicit*, since it does not contain all possible reactions defining the photochemical degradation of a VOC to CO_2 and H_2O. Some strategic simplifications are applied in order to limit the size of the mechanism, but maintaining the necessary reactivity [52]. If the MCM were fully explicit, numerical model run times would be too large. A simplified model is crucial for the computational cost and practicality of atmospheric box models. The simplifications that have been made in the mechanism include: (i) the removal of low probability pathways, (ii) simplified degradation chemistry of minor reaction products, and (iii) the parameterisation of peroxy radical (RO_2) reactions with each other. This means that although peroxy radicals in the MCM are individually defined, their mechanism with

other peroxy radicals proceeds via a grouped RO_2 term. [52].

1.8 Thesis outline

This thesis presents observational data obtained during the APHH-India project, and investigates the chemical processes occurring in Delhi's atmosphere using a tailored chemical box model, based on the MCM. The data used was obtained during two intensive field campaigns in Delhi, as part of the DelhiFlux sub-project, during the pre-monsoon (May-June) and post-monsoon (October) seasons in 2018, and includes speciated VOC observations made using gas chromatography. A more detailed study on the ozonolysis mechanisms of some important alkene species observed in Delhi is discussed in the final results chapter.

Chapter 2 describes the instrumentation used to obtain ambient measurements of a variety of chemical species present in the atmosphere at a measurement site in Delhi, India. This includes a full uncertainty analysis for the gas chromatography measurement of VOCs, and a shorter description of supporting measurements.

Chapter 3 outlines the average concentrations of NO_x, CO, O_3, HONO, and VOCs measured in Delhi as part of the APHH-India project. Diel profiles and time series plots are presented for measured species. Observations are then used to constrain a chemical box model, to investigate the concentrations of radical species, as well as their initiation, propagation, and termination routes. The model is used to produce detailed radical budgets for both the pre- and post-monsoon campaigns. This chapter compares data from the two Delhi campaigns, highlighting the differences in chemical processes.

Chapter 4 investigates the key species important for in situ O_3 production in Delhi, using a campaign tailored chemical box model constrained to observed species. The sensitivity of O_3 production to changes in NO_x, aerosol surface area, photolysis, and VOCs (both by class and individually) is investigated. The sensitivity of O_3 production to pollution sources is investigated by changing precursor concentrations according to their contributions to sources in an emissions inventory.

Chapter 5 utilises data collected from experiments at the EUPHORE outdoor atmospheric simulation chamber to investigate the the products of alkene ozonolysis reactions. The experimental data is used to determine the yields of stabilised Criegee intermediate species, the products of which play an important role in chemical processing in urban atmospheres, including Delhi.

Chapter 6 summarises the key findings of this work, outlines the limitations, and discusses future work.

Chapter 2

Instrumentation and method development

This chapter describes the instrumentation used to obtain ambient measurements of a variety of chemical species present in the atmosphere of a measurement site in Delhi, India. A full uncertainty analysis is provided for the gas chromatography measurement of VOCs in the atmosphere, and shorter descriptions of supporting measurements of NO_x, O_3, CO, SO_2, HONO, aerosol diameter and photolysis rates are also outlined. The O_3 analyser and SO_2 analyser described here are similar (same technique, different instrument models) to those employed during experiments at the EUPHORE smog chamber, Valencia, Spain (see Chapter 5). Experimental details of the chamber, and additional instrumentation employed such as FTIR and PTR-MS, are described in Chapter 5.

2.1 Measurement site location

The APHH-India DelhiFlux post-monsoon measurement campaign took place between 4 October and 5 November 2018. The measurement site was located at Indira Gandhi Technical University for Women (IGDTUW), in Delhi, India. Delhi is situated in the north of India, and lies to the south/southwest of the more rural and agricultural states of Punjab, Uttarakhand, and Uttar Pradesh (pink circle, Figure 2.1).

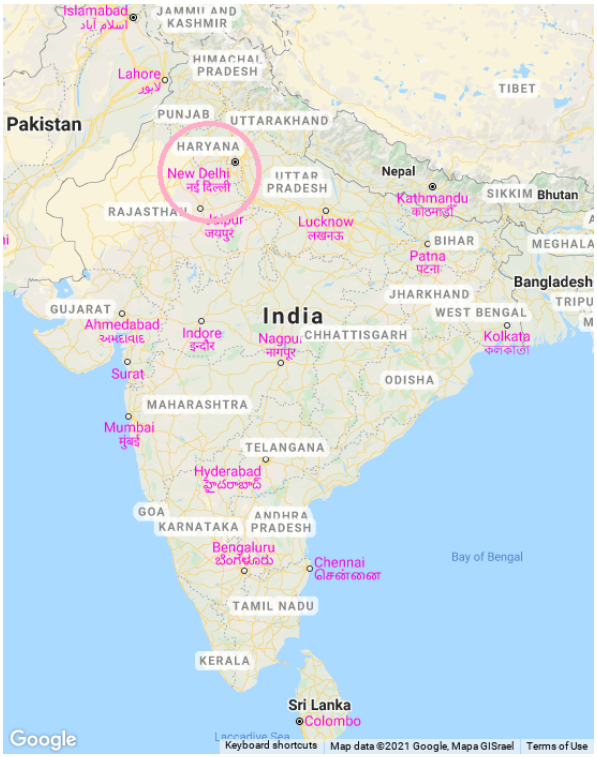

Figure 2.1: Map of India showing the location of individual states (black text on white background), and cities (magenta). New Delhi, Delhi is located to the North of India (pink circle). ©Google Maps 2021.

The measurement site was located on the campus of the IGDTUW, near Kashmere Gate in Old Delhi (28.67 °N, 77.23 °E, Figure 2.2). The instruments were housed in a one story building on campus, with the sample inlets located on the roof (Figure 2.4). The measurement building was situated near a limited access road through the IGDTUW campus, running parallel to a large recreational field. The area immediately outside of the campus was very urbanised, and close to several busy main roads. Measurements were made at the site during two intensive field campaigns in the Delhi pre-monsoon (May-June) and post-monsoon (October) in 2018. IGDTUW campus was an open area, with some green spaces, and was close to major roads and highways: 1.5 km north of the busy Chandni Chowk market, 0.6 km north of Old Delhi (Delhi Junction) Railway Station, and 0.3 km west of National Highway 44 (Figure 2.3). The campus was mostly pedestrianised, with occasional traffic activity from delivery cars, taxis, and auto rickshaws. Inter State Bus Terminal (ISBT) was located < 100

m away from the measurement site. IGDTUW facilitated the sampling of ambient air from a height of ≈ 5 m and measurements were made of a large range of VOCs, o-VOCs, NO_x, CO, SO_2, HONO, photolysis rates, and PM. The site was located just outside of the city centre of New Delhi. The location was thus more representative for the more urban residential areas of the city, where the majority of the population live. The site was less representative of the inner city of New Delhi, and the state of Delhi as a whole, which incorporates more rural areas to the west.

Figure 2.2: Map of the Indian state of Delhi, and the location of the IGDTUW measurement site (red diamond). ©Google Maps 2021.

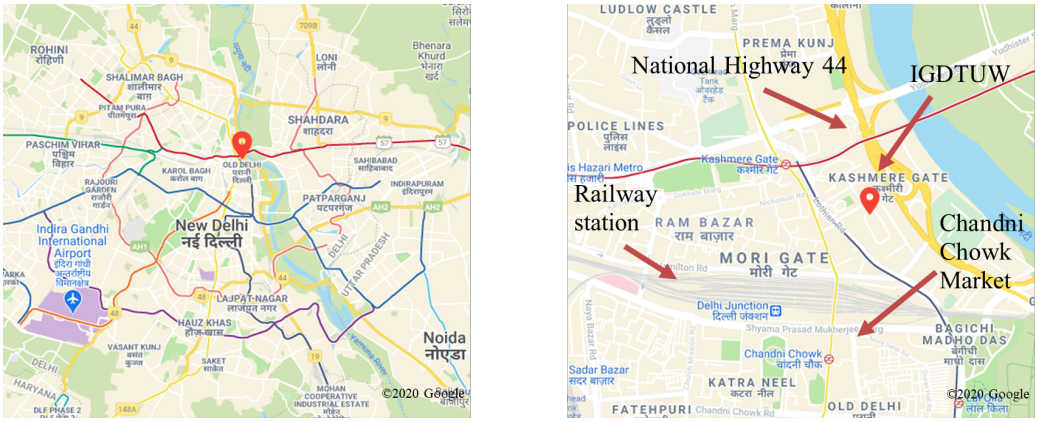

Figure 2.3: The measurement site (IGDTUW) in Old Delhi, north of New Delhi (left). In closer detail (right), the site was just north of the Delhi Junction Railway Station, and west of National Highway 44. Map data ©Google Maps 2020.

The pre-monsoon period is also known and the Delhi summer, beginning in April and continuing through to mid-June. This period is characterised by extreme heat (exceeding 40 °C), and hot, dry winds originating from the west Asian mainland. The post-monsoon period, also known as the Delhi autumn, begins in October and continues to early November. During

(a) (DC)-GC-FID instrumentation

(b) Measurement site

Figure 2.4: (DC)-GC-FID instrumental set-up (a) and outside of measurement site (b) at IGDTUW, Delhi.

this season, the wind direction changes, predominately originating from the north west. Both the pre-monsoon and post-monsoon periods are subject to anti-cyclonic conditions, resulting in warm weather, and generally stagnant conditions [53]. During the fieldwork, I personally recorded my observations of the weather conditions. During both campaigns, there was not any noticeable rainfall, and the pre-monsoon period felt distinctly warmer and brighter than the post-monsoon campaign. I did not recorded any days that were particularly windy.

2.2 The measurement of Volatile Organic Compounds (VOCs)

Two gas chromatography (GC) instruments and a proton transfer reaction time-of-flight mass spectrometer, with quadrupole ion guide (PTR-QiTOF, Ionicon Analytik, Innsbruck) were deployed to measure an extensive range of VOCs and o-VOCs. The GC instrumentation included a dual-channel gas chromatography flame ionisation detector, (DC)-GC-FID, measuring C_2-C_8 hydrocarbons and some o-VOCs, and a two-dimensional GC flame ionisation detector (GC × GC-FID) to measure larger hydrocarbon species (C_6-C_{13}). PTR-QiTOF measurements of a variety of o-VOCs completed the VOC measurement suite of 15 alkanes, 10 alkenes, 2 alkynes, 29 aromatics, 11 carbonyls, 2 alcohols, and 15 monoterpenes (see Chapter 4, Table 4.2.3). All three instruments operated between 11 and 27 October 2018. The two GC instruments shared an inlet, located approximately 5 m above ground level. The sample line from the inlet to the laboratory was made from 1/2 in. O.D. (9.53 mm I.D.) perfluoroalkoxy (PFA) and was heated to limit adsorption of compounds to surfaces. VOCs and o-VOCs were calibrated using 4 ppbV and a 4 ppmV (diluted before calibration) gas standard cylinders (National Physical Laboratory, UK) respectively, containing a variety of VOCs and o-VOCs. The linearity of the detector response to higher mixing ratios was tested on both instruments prior to the campaigns, as described by Stewart et al., 2021 [54].

The (DC)-GC-FID measurement period was 5 October - 27 October 2018. A 500 mL sample pre-purge (flow rate of 100 mL min^{-1} for 15 min) preceded a 500 mL sample collection (flow rate of 25 mL min^{-1} for 20 min) using a Markes International CIA Advantage. The sample was passed through a cold glass finger (-30 °C) to remove water, before being adsorbed onto a Markes International Ozone Precursor dual-bed sorbent cold trap using a Markes International Unity 2 for pre-concentration. After sampling, the trap was heated (250 °C for 3 min) to allow for thermal desorption of the sample and passed to the GC oven in helium carrier gas. The sample was split 50:50 and injected into two columns in the oven, allowing for the detection of both monoxygenated and oxygenated compounds. The oven was held at 40 °C for 5 min, then ramped up to 110 °C at a rate of 13 °C min^{-1}, before a final ramp to 200 °C at 7 °C min^{-1}, where it was held for 30 min [55]. A detailed description of the (DC)-GC-FID instrumentation and methodology is provided in section 2.3.

The GC × GC-FID measurement period was 11 October - 4 November 2018. A 2.1 L sample (flow rate 70 mL min^{-1} for 30 min) was collected and passed through a cold glass finger (-30 °C) to remove water. The sample was absorbed onto a TO-15/TO-17 air toxic cold sorbent trap in a Markes International Unity 2 for pre-concentration. The trap was heated (250 °C for 5 min) to allow for thermal desorption and the sample injected down a transfer line. It was then refocused with liquid CO_2 at the head of a non-polar BPX5 column (SGE Analytical, 15 m × 0.15 μm × 0.25 mm) held at 50 psi for 60 s. This was connected to a polar BPX50 column (SGE Analytical 2 m × 0.25 μm × 0.25 mm) held at 23 psi via a modulator held at 180 °C (5 s modulation, Analytical Flow Products MDVG-HT). The oven was held for 2 min at 35 °C, then ramped up to 130 °C at a rate of 2.5 °C min^{-1} and held for 1 min before a final ramp to 180 °C at 10 °C min^{-1} where it was held for 8 min [54, 56]. More details on the GC × GC-FID instrumentation can be found in section 2.3.5.

2.3 Gas Chromatography

The measurement of a range of trace gases in ambient air can be achieved using gas chromatography instrumentation, coupled with sampling pumps, a pre-concentration unit, and a water removal system. Gas chromatography (GC) is a chemical separation technique, commonly used to determine the concentrations of speciated volatile organic compounds (VOCs), present in trace amounts in the atmosphere. Ambient air in Delhi was sampled using a pre-concentration unit and analysed by a gas chromatograph with flame ionisation detection (GC-FID). This instrument set-up has been deployed in many field campaigns, including two APHH campaigns in Beijing, China, APHH campaigns in Ho Chi Minh and Hanoi, Vietnam, the ClearfLo campaign in London, UK, and the BALI campaign in Boreno, Malaysia [57–60]. This section provides a description of the instrumentation, and outlines the instrument set-up for the measurement of ambient air in Delhi, India.

2.3.1 Instrument set-up

A schematic of the instrumental set-up is given in Figure 2.5. There are five stages involved in sample acquisition and of trace gas separation using the dual channel (DC)-GC-FID: sampling, water removal, pre-concentration of trace gases, column separation and detection. Ambient air is first sampled from the sample inlet. From here, it is sampled from the main sample line, and dried. The sample is then pre-concentrated onto a focusing trap at low temperatures. Once the desired volume of air has been sampled, the trap is heated and a concentrated parcel of trace gases is injected onto the GC columns for speciated separation. The GC is fitted with two columns, which allows for the separation of compounds by boiling point and polarity. The column separated sample is then passed to a flame ionisation detector, where the magnitude of the calibrated resultant signal is proportional to the concentration of a given species. The communications between the CIA ADVANTAGE autosampler, MARKES UNITY2 pre-concentrating unit, and GC oven are controlled using software by MARKES International. Figure 2.6 shows the connecting lines and valves which change throughout a GC sample run. Using this software, the timings of each valve turn, directing the sample to each line, can be controlled and fine-tuned. The software also provides information from pressure gauges, located at various points along the lines. Valves can be manually opened and closed on the lines, and changes in pressure can give some insight into the location of any leaks present. A custom built water removal system is also fitted in-between the CIA advantage and the MARKES UNITY2, not shown in Figure 2.6.

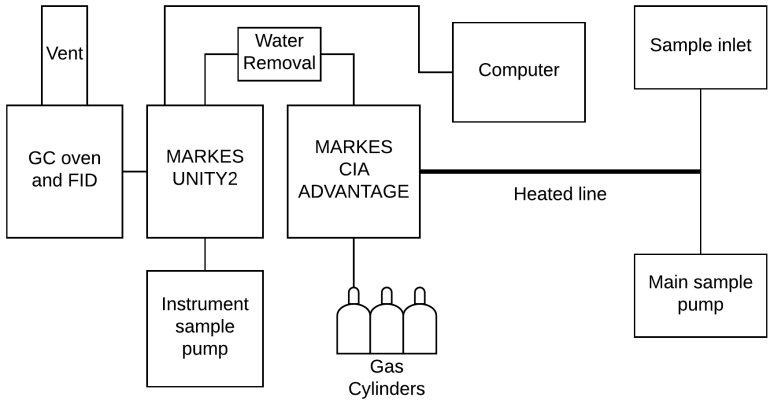

Figure 2.5: Schematic of instrumental set-up on campaign in Delhi, India.

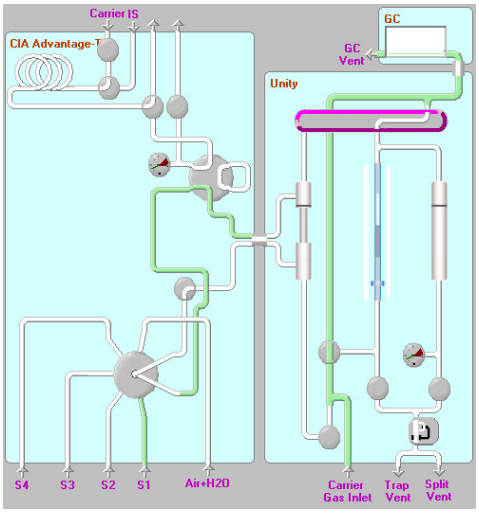

Figure 2.6: Schematic of the valves connecting the MARKES CIA ADVANTAGE, (left blue box), to the MARKES UNITY2 pre-concentration unit (right large blue box). The green lines indicate lines where valves are open to allow the flow of gas. In this scheme, all valves in the autosampler are open and these lines are being purged. The carrier gas is being directed straight to the GC oven. The water removal system is located between the CIA ADVANTAGE and the UNITY2, not shown here.

Sampling

Ambient air was sampled from a sampling inlet $\approx$ 5 m above ground-level, using 1/2“ O.D. (9.53 mm I.D) perfluoroalkoxy (PFA) tubing. The air was pumped through the line at a rate of $>$ 30 L min^{-1}, to minimise the residence time of the sample in the line ($<$ 8 s) before being sub-sampled by the instrumentation. Once inside the building, the line was heated to $\approx$ 40 °C to limit the adsorption of compounds to the inside of the tubing, and to prevent water condensing in the line. A KNF labport sample pump was connected to the MARKES UNITY2 for sub-sampling from the main line. The air in the sample line was sub-sampled using a t-piece, connected to a line of 1/4” tubing, by a MARKES CIA ADVANTAGE autosampler, at a flow rate of 100 mL min^{-1} for 15 min, to purge the sample lines. After this initial purge, the air was again sampled for analysis at a flow rate of 25 mL min^{-1} for 20 min, to achieve a target sample volume of 500 mL.

Water removal

The sample was passed from the CIA ADVANTAGE through a water removal system. The water removal system comprised of six cylindrical glass vessels, known as cold fingers. At any given time, the sample is passed through one cold finger. Two arms at the top of each cold finger allow for the flow of gas in and out of the vessel. The cold fingers are housed in an an aluminium box, and held in place by holes in a polystyrene floor. As water in the cold fingers would freeze, they were replaced every few days to prevent air flow blockages. The presence

of multiple glass fingers allowed for the use of each glass finger in rotation, so that blocked ice fingers could be removed, defrosted, and replaced without impacting sampling time. The block was cooled to ≈ -30 °C by a Stirling cooler.

Sample pre-concentration

The detector is not sensitive enough to detect low concentrations of VOCs at the trace quantities present in the atmosphere. Because of this, it is important to pre-concentrate the VOCs before they are injected onto the GC columns. The samples were pre-concentrated using a MARKES UNITY2 system, fitted with an ozone precursor focusing trap (U-T17O3P-2S), which was prepared and pre-packed by MARKES International, where it was purchased. The trap was packed with trapping materials, allowing for the adsorption of VOCs onto the trap at temperatures of -20 °C, cooled using Peltier plates. Once the sample was passed through the trap, and the GC was ready, the trap was heated to 250 °C, allowing for the thermal desorption of the trapped VOCs, which were then directed onto the GC column.

Column separation and sample detection

The now concentrated VOCs in the sample were separated using a dual column Agilent 7890B GC, fitted with two columns and two flame ionisation detectors. The sample was passed to the two columns in a 50:50 split ratio, using helium carrier gas. The presence of the two columns allowed for the separation of both non-methane hydrocarbons (NMHCs) (50 m × 0.53 mm Al_2O_3 PLOT column), and a small selection of more polar, oxygenated VOCs (10 m × 0.53 mm LOWOX column). The PLOT column separated the sample mainly by boiling point, with a small degree of separation by polarity, whereas the LOWOX column separated species mainly by their polarity. After sample injection, the oven was held at 40 °C for 5 mins, before being increased to 110 °C at 13 °C min^{-1}, before a final ramp to 200 °C at 7 °C min^{-1}, where it was held for 30 min [55]. These oven heating times have been optimised, to maximise separation times and to produce well resolved peaks for each species of interest on the resultant chromatograms for easy analysis. The timings used here were based on the detailed GC methodology work published in Hopkins et al., 2003 [55].

2.3.2 Sampling sequence and peak identification

The signal response for each VOC was calibrated using a standard mixture of gases at known concentrations, provided by the National Physical Laboratory, UK (NPL). At least five calibration samples were run at the beginning and the end of the campaign. After the initial calibrations, fifteen ambient air samples were analysed, followed by two blank samples of compressed air. These blanks enabled the identification of any impurities in the line. The blanks were followed by another fifteen ambient air samples before working standard gas samples.

The working standard cylinder was produced in York, and filled with a range of gases. As cylinder concentrations of the VOCs present in this mix do not change in the cylinder, the working standard was used to check for changes in peak sensitivity, and retention time drift, avoiding excessive use of the expensive NPL standard. This sequence of ambient air samples, blanks and working standard gas samples was repeated throughout the campaign until a final set of NPL standard gas calibrations were performed. Figure 2.7 shows some example chromatograms, processed using ChemStation software, of an NPL standard gas sample, and an ambient air sample.

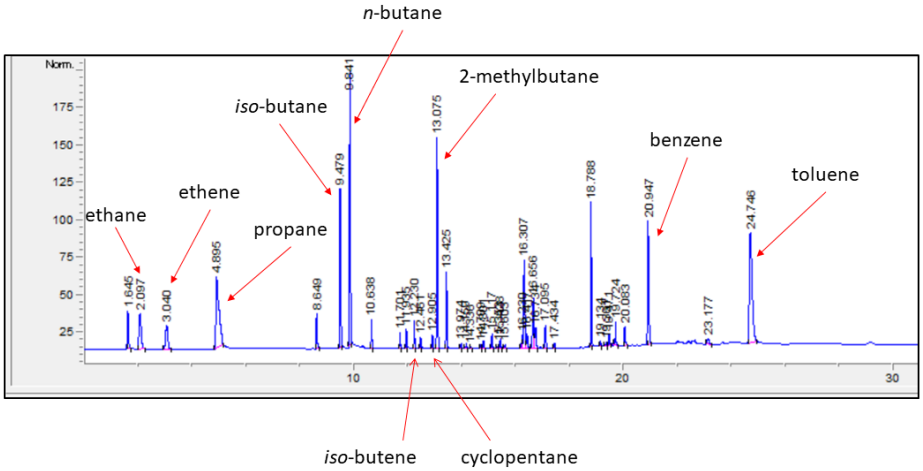

(a) Delhi ambient air

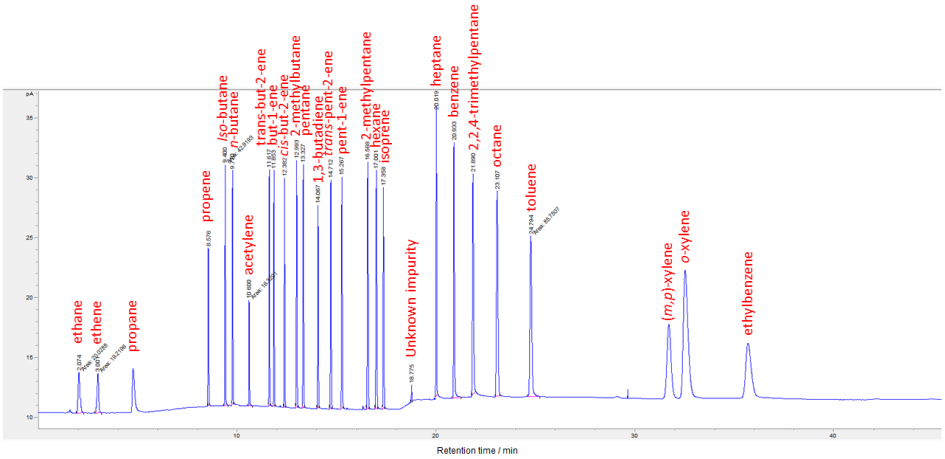

(b) NPL standard gas

Figure 2.7: Example GC chromatograms from a Delhi ambient air (a) and NPL standard gas (b) sample.

The NPL calibration gas samples allowed for the assignment of a variety of VOC by retention time in the ambient air chromatography. The calibration chromatograms were also important for assessing the instrument sensitivity and signal reproducibility of species signals at a fixed volume. In addition, calibrations were crucially used to quantify the signal response

of each species per unit volume, so that species mixing ratios could be calculated from peak area signals. First, the area of each peak must be determined. To simplify this process, an automated integration software, GCWerks MD, was used across all campaign chromatograms. Several parameters were used in this software to identify the correct peaks, such as a retention time range for each species, and a peak threshold to identify peaks from background noise. These parameters were adjusted for each species, and re-adjusted for later chromatograms, in cases where peak drift occured. To ensure the automated software had correctly assigned each peak, chromatograms were manually reviewed and changes to parameters made where appropriate. Once the peak areas of all VOCs of interest were determined from all chromatograms, calibration factors could be determined and applied.

2.3.3 Calibrations

A National Physical Laboratory, UK (NPL) certified 30-component ozone precursor standard gas cylinder was used to perform calibrations. The calibration method described here is based on the NPL calibration scale for VOCs [61], and is routinely performed by the GAW-VOC network [62]. At the beginning and end of the campaign, the peak area per ppb was determined from the VOC signal and its known cylinder concentration, accounting for the GC sample volume ($\approx$ 500 ml). The mean of this value was determined for each chemical species, and this factor was then used to determine mixing ratios from peak areas. If the initial and final calibration factors differed ($> 10\%$), then the working standard could be used to identify the point from which a change in instrument sensitivity occured, and thus which calibration factor to apply to a given chromatogram. During both the pre-monsoon and post monsoon campaigns, no significant changes in sensitivity of drift were observed. Since the signal response is generally proportional to the number of carbons in the compound, the concentration of species not present in the NPL working standard was determined from a proxy species. For example, the concentration of 1,2-butadiene was determined using the calibration factor calculated for 1,3-butadiene. Blank samples were also analysed to ensure no contaminants were interfering with calibration and ambient peak signals. One prominent contaminant was identified at a retention time of $\approx$ 18.7 min. As this species was observed in calibration, working standard and blank samples, it is likely to be an impurity present in the line, and most likely from the focusing trap which was recently replaced. Aside from this, blanks generally looked clean.

2.3.4 Uncertainty analysis

The overall relative uncertainty in the calculated mixing ratio of each VOC $\left(\frac{\sigma(M)}{M}\right)$ was calculated in accordance with the Aerosol Clouds and Trace Gases Research Infrastructure (ACTRIS) measurement guidelines [63]. The relative uncertainty of the NPL standard, blanks and working standard was determined individually, along with the relative instrument precision

uncertainty. The root of the summed squared values of the calculated uncertainties yielded the total combined relative uncertainty for each VOC, which was then multiplied by two to increase the confidence level to 95 %. The total uncertainty was calculated using equation 2.1.

$$\frac{2\sigma(M)}{M} = 2 \cdot \sqrt{\left(\frac{\sigma(M_{cs})}{M_{cs}}\right)^2 + \left(\frac{\sigma(M_{blank})}{M_{blank}}\right)^2 + \left(\frac{\sigma(M_{ws})}{M_{ws}} + \frac{1}{3}LOD\right)^2} \tag{2.1}$$

The relative uncertainty in the NPL calibration standard for each VOC was determined using the uncertainty fraction provided on the cylinder certificate. The uncertainty range was 1.97 - 5.00 % of the compound mixing ratios present in the cylinder. The relative uncertainty of each individual compound present in the NPL standard was calculated by dividing the provided cylinder uncertainty ($\sigma(M_{cs})$) by the cylinder mixing ratio (M_{cs}) for each VOC.

The relative uncertainty from the blanks is calculated from the blank ratio. For species that are present in the blanks, the mixing ratio in the ambient sample is divided by the average mixing ratio determined across all blank samples, to calculate the blank ratio. The blank ratio is then converted to a relative uncertainty as defined in the ACTRIS guidelines. For example, the guidelines define a blank ratio of 2 to be equivalent to an error of 0.1, and a ratio 4 equates to an error of 0.05. The blank relative uncertainty is then defined as this error ($\sigma(M_{blank})$) divided by the average blank mixing ratio (M_{blank}). For species that do not have a blank value, no blank error term is applied to the uncertainty equation. The limit of detection (LOD) was also determined by dividing the mean of the blank mixing ratios by the standard deviation of the blanks. This value was then multiplied by 3 to obtain 3θ, representing a 99.7% confidence interval.

Finally, the instrument precision is determined from the LOD of each compound, and the stability of the working standard throughout the campaigns. For each VOC, the standard deviation of mixing ratios in the working standards ($\sigma(M_{ws})$) was divided by the mixing ratio in the working standard (M_{ws}). The contribution of the LOD to the instrument precision was divided by 3 to obtain a 1θ uncertainty.

The overall uncertainty was determined by summing the squared value of each of the relative uncertainties, before taking the square root of this value. This value was then multiplied by 2, to obtain an uncertainty representing a 95% confidence level. The calculated average percentage uncertainties for each measured compound are presented in Table 2.1. Where mixing ratio measurements fell below the LOD, a value equal to half the LOD was reported, and a 100 % uncertainty applied. A range of uncertainties was determined of 3.98 - 32.94 % in the pre-monsoon, and 4.47 - 44.18 % in the post-monsoon (Table 2.1).

Table 2.1: Uncertainties for the range of species detected in Delhi, India using (DC)-GC-FID instrumentation during pre-monsoon and post-monsoon campaigns.

Compound	Uncertainty / %	
	Pre-Monsoon	Post-Monsoon
ethane	3.98	4.63
ethene	5.19	5.05
propane	4.72	4.82
propene	5.32	4.57
iso-butane	5.37	6.03
n-butane	10.23	12.07
acetylene	10.42	44.18
trans-but-2-ene	4.82	4.59
but-1-ene	7.73	4.64
iso-butene	4.98	4.57
cis-but-2-ene	4.83	4.58
cyclopentane	4.15	4.86
iso-pentane	3.99	5.12
n-pentane	4.11	4.55
1,3-butadiene	5.01	4.91
trans-pent-2-ene	4.37	4.47
pent-1-ene	4.88	4.55
n-octane	5.52	8.34
n-hexane	4.76	9.26
Isoprene	4.08	6.27
n-heptane	4.96	10.70
benzene	6.83	10.60
toluene	10.19	15.20
ethylbenzene	5.09	11.59
(*m*,*p*)-xylene	5.05	11.55
o-xylene	24.79	11.60
methanol	32.94	31.79
acetone	22.65	21.64
ethanol	21.10	20.92
propyne	5.25	4.75
1,2-butadiene	4.29	5.09

Generally, most compounds had an error of $< 12\%$, with some noticeable exceptions. Firstly, high uncertainties were determined for acetylene in the post-monsoon. This was due to variability in the working standard for this compound, leading to a high instrument precision uncertainty. In addition, uncertainties for the oxygenated species methanol, acetone and ethanol are high ($> 20\%$). This is due to the assignment of a large precision uncertainty for these species due to the method by which the calibration was applied. A second NPL certified standard cylinder was sampled during this campaign to determine the mixing ratio of oxygenated species on the second column. Since concentrations in this cylinder were much higher than those in the main NPL standard cylinder (ppm compared to ppb), a dilution unit was used reduce the mixing ratio of VOCs in the standard sample. However, due to the failure of the dilution unit supplying the gas to the auto sampler, the mixing ratios of each compound were diluted by an unknown factor. As benzene is present in both the main

NPL standard and the oxygenated NPL standard, the mixing ratio of benzene present in the oxygenated standard gas was determined using the main NPL calibration. This allowed for the calibration of other oxygenated species present in the cylinder, but the uncertainty for these species has been generously increased as a result.

2.3.5 Two-dimensional Gas Chromatography

The VOC measurements made by the (DC)-GC-FID were supported by additional two dimensional GC measurements (GC × GC-FID), obtained and analysed by Gareth Stewart at the University of York [54]. The GC × GC-FID allowed for the separation of compounds by both boiling point and volatility, enabling for the observation of an extended suite of VOCs from C_7 - C_{12}. This GC operates similarly to the (DC)-GC-FID, requiring a pre-concentration unit, and a water removal system which was shared with the (DC)-GC-FID. Ambient air was sampled from the same line as the (DC)-GC-FID. The GC × GC-FID oven is fitted with an additional feature to allow for a second separation. The sample is passed through a column to separate the sample by boiling point, before being passed to a second column to separate the sample by its volatility via a mechanical valve known as a modulator. The modulator injects the analyte onto the second column at a set time interval, leading to the sub-separation of peaks by this interval [64]. This allows for the separation of larger VOCs which would not be possible using the traditional (DC)-GC-FID. This separation technique has been successfully employed on a previous air quality campaign in London 2012, from which a study has highlighted the missing chemical reactivity when radical chemistry was modelled using just (DC)-GC-FID data, versus using the combined data set from both instruments [57]. An example GC × GC-FID chromatogram from the London 2012 ClearfLo campaign is presented in Figure 2.8 [65].

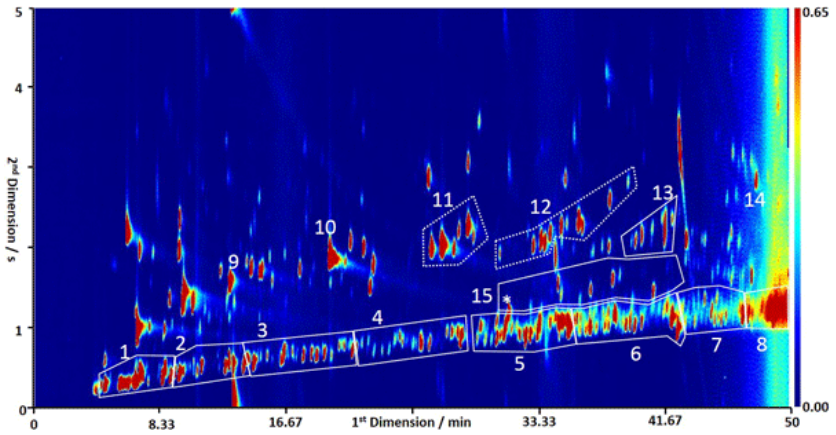

Figure 2.8: Two-dimensional GC chromatogram from the London ClearfLo campaign, 2012 (from Dunmore et al., 2015 [65]). Compounds are separated in two dimensions. Areas 1-8 are C_6 - C_{13} alkanes respectively, 9 = benzene, 10 = toluene, 11 = C_2 substituted aromatics, 12 = C_3 substituted aromatics, 13 = C_4 substituted monoaromatics, 14 = naphthalene, and 15 = C_{10} monoterpenes.

2.4 Supporting measurements

The GC VOC measurements made during the two campaigns in Delhi, India were supported by additional measurements of other atmospheric pollutants. The limits of detection and uncertainties associated with these are presented in Table 2.2. More detailed descriptions of the supporting instrumentation are provided in this section.

Table 2.2: Limits of detection (LOD) and uncertainties of instrumentation deployed during the APHH-India DelhiFlux campaigns.

Instrument	LOD	Uncertainty	Reference
DC-GC-FID	1-40 pptV	≈ 10 - 15 %	Hopkins et al., 2003 [55]
GCxGC-FID	0.01 - 0.2 pptV	≈ 5 - 18 %	Lidster et al., 2014 [66]
TEI 49i	0.05 ppbV	1 ppbV	CEDA DelhiFlux, 2020 [67]
TEI 43i	1 ppbV	1 % or 1 ppb	CEDA DelhiFlux, 2020 [67]
Aerolaser AL5002	3 ppbV	2%	CEDA DelhiFlux, 2020, Squires et al., 2020 [67, 68]
PTR-QiTOF-MS	10 pptV	21%	Huang et al., 2016 [69]
LOPAP	3 pptV	10%	Kleffmann et al., 2002 [70]

2.4.1 NO_x

Nitrogen oxide (NO_x = NO + NO_2) measurements were made at the IGDTUW measurement site by the University of York using a dual-channel chemiluminescence instrument (Air Quality Designs Inc., Colorado). NO was measured by exposing the ambient air sample to O_3, and observing the resultant chemiluminescence. This occurs in a two step process, whereby NO firstly reacts with O_3 to form an excited nitrogen dioxide molecule (NO_2*), and O_2 (equation 2.2). Next, the NO_2* rapidly relaxes to its ground state, releasing a photon in the process (equation 2.3). The photons emitted are detected using a photo-multiplier tube (PMT), where an output voltage is determined. This voltage is linearly proportional to the amount of NO in the air, and its concentration is then calculated.

$$NO + O_3 \longrightarrow {NO_2}^* + O_2 \tag{2.2}$$

$${NO_2}^* \longrightarrow NO_2 + h\nu \tag{2.3}$$

To determine the amount of NO_2 in the air using this technique, NO_2 must first be converted into NO, also producing an O(^{3}P) atom (equation 2.4). Historically, the preferred conversion method has been catalytic conversion using a heated Molybdenum converter due to its high conversion efficiency ($\geq$ 95%). However, one downside to this method is the additional conversion of other reactive nitrogen species to NO, such as peroxyacetyl nitrate (PAN), and other acyl peroxy nitrates [71]. The conversion technique used from this campaign was a photolytic converter with a wavelength range of 385 - 395 nm, which has been shown to have a small spectral overlap with interfering compounds [72, 73]. The ambient air sample is exposed to blue light from two light emitting diodes (LEDs). The narrow wavelength range

ensures that NO_2 conversion is highly specific, to minimise additional conversions to NO from other interfering nitrogen compounds.

$$NO_2 + hv \longrightarrow NO + O(^3P) \quad (310 < \lambda < 420\ nm) \tag{2.4}$$

The NO_x instrumentation was calibrated regularly throughout both campaigns, every 2-3 days. A detailed description of the NO_x measurement methodology can be found in Squires et al., 2020 [74]. This instrument, along with the CO and O_3 instrumentation, was operated by experienced colleagues at the University of York.

2.4.2 O_3

O_3 measurements were made by the University of York, using a Thermo Scientific (Model 49i) UV Photometric Analyser. The mixing ratio of O_3 in ambient air can be quantified by determining the degree to which UV light at a wavelength of 254 nm is absorbed by the sample. As very few atmospheric compounds absorb light at this wavelength, measuring O_3 using this method is highly selective, therefore interferences are limited. The difference between the incident intensity and resultant intensity of the light is proportional to the concentration of O_3, as described by the Beer-Lambert Law (equation 2.5).

$$I = I_0\ e^{-\sigma cl} \tag{2.5}$$

where I is the resultant intensity, I_0 is the incident intensity, σ is the absorption cross section (the probability that a molecule will absorb the incident light), c is the concentration (c) of O_3, and l the path length of radiation. The Beer Lambert law can be rearranged as in equation 2.6, to determine the concentration of O_3.

$$c = \left(\frac{1}{\sigma l}\right) \cdot ln\left(\frac{I}{I_0}\right) \tag{2.6}$$

To determine the incident and resultant light intensity, the sample is split across two cells. In the first cell, O_3 is scrubbed from the sample, and the light intensity measured from this cell is representative of the sample background and referred to as the reference gas. From this, I_0 can be calculated. The incident light intensity from the second, unscrubbed cell is equal to I. Each cell takes turns as the reference and sample cell, controlled by a solenoid valve which switches flow streams every 10 s. The average concentration across both cells is used to determine the final concentration of O_3.

2.4.3 CO

Carbon monoxide (CO) was measured using a resonance fluorescent instrument (Model AL5002, Aerolaser GmbH, Germany). The instrument comprises of a resonance lamp, optical filter,

fluorescence chamber, and a PMT. VUV radiation is generated at ≈ 150 nm, before being collimated with a parabolic mirror and filtered using dielectric mirrors. This filtered light is directed into the fluorescence chamber containing the sample, and the PMT measures the resultant CO fluorescence. As CO fluoresces at wavelengths in the range of 145 - 220 nm, the PMT is configured to detect light within a small window in this range (160 nm $< \lambda <$ 190 nm), maximising the resonance fluorescence of the sample to scattered light. A more detailed description of this instrumentation can be found in Squires, 2020 [68].

2.4.4 SO_2

SO_2 was measured using a Thermo Scientific (Model 43i) SO_2 analyser. The sample is first directed through a hydrocarbon "kicker", which scrubs hydrocarbons from the sample which may otherwise lead to interferences. The sample then flows into a fluorescence chamber where SO_2 molecules are excited by pulsating UV light (equation 2.7).

$$SO_2 + h\nu \longrightarrow {SO_2}^* \longrightarrow h\nu \tag{2.7}$$

The fluorescence chamber is fitted with a focusing lens and highly selective mirror assembly, which only reflects light at wavelengths where SO_2 can be excited. The excited SO_2 molecules decay to lower energy states, emitting UV light at a different wavelength to the incident UV light. The emitted UV light is detected by a PMT, and is proportional to the concentration of SO_2 in the sample.

2.4.5 HONO

HONO was measured with a commercially available long-path absorption photometer (LOPAP) described in Heland et al., 2001 [75], according to the standard procedures outlined in Kleffmann et al., 2008 [76], with baseline measurements taken at regular intervals (8 h). HONO was also observed using the PTR-QiTOF-MS with the protonated HONO ion observed at m/z 48.007. This signal was humidity corrected and calibrated against the LOPAP HONO measurements. HONO measurements using PTR-MS have been reported previously in Koss et al., 2018 [77], and are described in more detail by Crilley et al., 2021 [78] (in preparation).

2.4.6 Additional VOC measurements

The PTR-QiTOF operated at a flow rate of 20 L min^{-1}, sub-sampling from the same inlet line as the GCs. The drift tube pressure and temperature were 3.5 mbar and 60 °C, respectively, giving an E/N (the ratio between electric field strength, E, and buffer gas density, N, in the drift tube) of 120 Td. The PTR-QiTOF was calibrated daily using a calibration gas (Apel-Riemer Environmental Inc., Miami) containing 18 compounds: methanol; acetonitrile; acetaldehyde; acetone; dimethyl sulfide; isoprene; methacrolein; methyl vinyl ketone;

2-butanol; benzene; toluene; 2-hexanone; m-xylene; heptanal; α-pinene; 3-octanone and 3-octanol at 1000 ppbV (±5%); and β-caryophyllene at 500 ppbV (±5%), diluted dynamically into zero air. More details on the PTR-QiTOF can be found in Jordan et al., 2009 [79].

A selection of compounds were measured by the (DC)-GC-FID, GC × GC-FID, and PTR-QiTOF instruments, allowing for an instrument inter-comparison. Between 17/10 and 26/10 good data coverage was available for benzene across all three instruments (Figure 2.9). Across this time period, the diel structure of benzene was consistent between the (DC)-GC-FID, GC × GC-FID and PTR-QiTOF. Observed mixing ratios of benzene from the GC × GC-FID were in good agreement with the (DC)-GC-FID, with an average percentage difference of 12 %. The PTR-QiTOF mixing ratios were marginally higher than measured using the GC instrumentation. On average, PTR-MS benzene mixing ratios were 44 % and 39 % higher than mixing ratios determined from the (DC)-GC-FID and GC × GC-FID respectively.

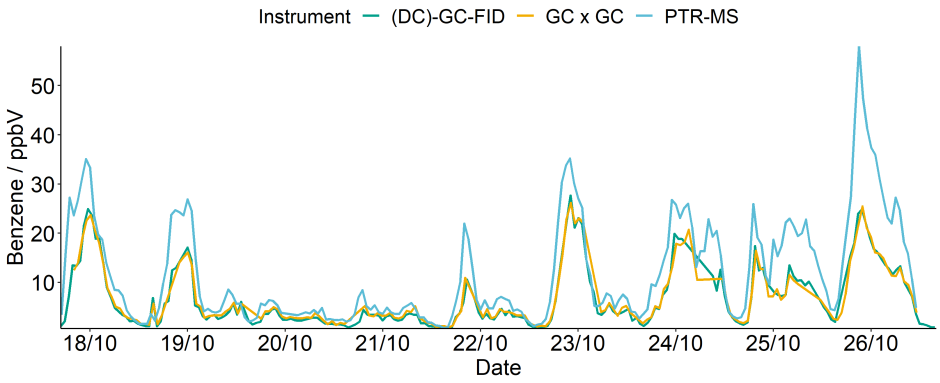

Figure 2.9: Intercomparison of benzene measured by (DC)-GC-FID, GC × GC, and PTR-MS during the Delhi post-monsoon campaign.

2.4.7 Aerosol diameter and aerosol surface area

Aerodynamic diameter NSD, N_a (> 352 nm) was collected using a GRIMM 1.108 (Portable Laser Aerosol Spectrometer and Dust Monitor) and merged into concurrently measured Electric mobility diameters NSD, N_d (14 – 640 nm – measured using a TSI SMPS, consisting of a 3080 Electrostatic Classifier, 3081 DMA and 3775 300 CPC) using the algorithm developed in Beddows et al., 2010 [80]. This analyses was used to determine aerosol surface areas, provided by colleagues at the University of Birmingham.

Aerosol surface area was calculated by multiplying the square of the aerosol diameter of each particle size bin by π, and multiplying this value by the number of particles within the size bin [81]. The total aerosol surface area is the sum of aerosol surface areas across all particle size bins (equation 2.8).

$$Total\ aerosol\ surface\ area\ =\ \sum_i \left(\pi \times D_i^2 \times dN\right) \tag{2.8}$$

2.4.8 Measurement of photolysis rates

Photolysis rates $j(O^1D)$, $j(NO_2)$ and $j(HONO)$ were calculated from their measured wavelength-resolved actinic flux, and published absorption cross sections and photodissociation quantum yields [59]. All other photolysis rates are parameterised as a function of solar zenith angle using a two-stream isotropic scattering model as described by Jenkin et al., 1997 [52] and Saunder et al., 2003 [51]. In each case, clear-sky variation of a specific photolysis rate (j) with solar zenith angle (χ) can be described well by equation 2.9.

$$j = l\ cos(\chi)m\ \times\ e\ -nsec(\chi) \tag{2.9}$$

where the parameters l, m, and n are optimised for each photolysis rate (see Table 2 in Saunders et al., 2003 [51], and http://mcm.york.ac.uk/parameters/photolysis_param.htt).

For species which photolyse at near-UV wavelengths (< 360 nm), such as HCHO and CH_3CHO, the photolysis rates were calculated by scaling the ratio of clear-sky $j(O^1D)$ to observed $j(O^1D)$ to account for attenuation by clouds and aerosol. For species which photolyse further into the visible range, the ratio of clear-sky $j(NO_2)$ to observed $j(NO_2)$ was used.

2.4.9 Discussion of possible instrument interferences

High night-time spikes in O_3 were regularly observed during both the Delhi pre- and post-monsoon campaign, with no instrumental issues reported to yield the data invalid. As O_3 is predominantly formed from photochemical processes, large spikes during the night are highly unusual. This alone has led to the error flagging of large night-time values to be as a result of interferences.

One possible interfering species is SO_2. During the pre-monsoon measurement period, high mixing ratios of SO_2 co-occur with night-time spikes in O_3 on the evenings of 29/05 and 05/06, consistent with a possible SO_2 interference (see Figure 3.10, Chapter 3 for time series plots of O_3 and SO_2). Between the period of 03/06 - 05/06, smaller O_3 spikes are observed at night, along with low levels of SO_2. As a precaution, the night-time O_3 observations used for further analysis were calculated from the average of night-time values during this low SO_2 period. During the post-monsoon campaign, several large night-time spikes in O_3 are observed. The largest of these occurs on 17/10, and coincides with a large spike in SO_2. High concentrations of NO are observed during the post-monsoon (Figure 3.10, Chapter 3). At

such high levels of NO, any residual O_3 from daytime formation is thought to react with NO. For further analysis, post-monsoon night-time mixing ratios for O_3 of 0 ppbV were used.

Although there appears to be a trend in high SO_2 coinciding with high O_3, this interference was not observed during the EUPHORE smog chamber experiments (Chapter 5), despite the presence of very high concentrations of SO_2 (up to 9000 ppbV). This could suggest SO_2 is not interfering with O_3, but another chemical species in the atmosphere could be interfering with both. Another possible interfering species is Hg, with one study suggesting Hg can lead to a positive response in the order of 2 - 3 ppbV in urban areas [82]. However, this is not sufficient to account for the scale of the potential interference in the Delhi post-monsoon campaign. High ambient concentrations of VOCs may also be responsible for interferences, with polar oxygenated aromatics, and nitrogenated derivatives of aromatics the most likely to interfere [82]. However, these species have not been extensively measured in Delhi. A box model study incorporating the Master Chemical Mechanism could be used to investigate the concentrations of the subsequent oxygenated aromatics from measured aromatic species. However, a full study into the possible instrumental interferences is beyond the scope of this work.

Chapter 3

Delhi observations and modelled radical budget

A large range of volatile organic compounds (VOCs), along with NO_x, O_3, SO_2, CO, and HONO were measured during two field campaigns in Delhi, India. Accompanying measurements of photolysis rates, temperature, pressure and relative humidity were made to complete the dataset, allowing for a full photochemical box model study. The campaigns took place at Indira Gandhi Delhi Technical University for Women (IGDTUW) in May/June 2018 (Pre-monsoon) and October 2018 (Post-monsoon). 86 speciated VOCs were measured, allowing for a detailed chemical study. This chapter presents the data obtained during these campaigns, along with modelled radical concentrations and budgets for both campaigns using the respective observational data.

3.1 Seasonal comparisons of campaign medians

Large differences in atmospheric species concentrations and diel profiles were observed between the pre-monsoon and post-monsoon campaigns. This section presents the data from both campaigns, highlighting the seasonal similarities and differences, and suggesting causes behind differences.

3.1.1 Meteorological data

The median temperature, pressure and relatively humidity during the pre- and post-monsoon measurement campaigns is presented in Table 3.1. On average, temperatures were $\approx$ 10 °C higher in the pre-monsoon than the post-monsoon. Median pressure was 6 mbar higher in the post-monsoon, and relatively humidity was $\approx$ 10% higher.

Table 3.1: Median temperature, pressure and relative humidity during the pre- and post-monsoon campaigns

	Pre-monsoon	Post-monsoon
Temperature / °C	33.7	23.8
Pressure / mbar	976	982
Relatively Humidity /%	42	52

3.1.2 Inorganic Compounds

Field measurements of NO and NO_2 are important for a detailed atmospheric chemistry study. As described in Chapter 1, tropospheric ozone (O_3) is formed in a non-linear process from the chemical processing of VOCs in the presence of NO_x.

High median mixing ratios of CO, NO, NO_2 and O_3 were observed during both pre- and post-monsoon campaigns (Figure 3.1). CO, NO and NO_2 mixing ratios were higher during the post-monsoon, with median mixing ratios more than 2.5 times larger for CO and $>$ 40 times larger for NO. The median O_3 mixing ratios reported in Figure 3.1 exclude data that was flagged as having a possible interference (see Chapter 2). Median mixing ratios for O_3 were $\approx$ 20 times larger in the pre-monsoon than the post-monsoon, due to elevated O_3 observed at night-time in the pre-monsoon. The median value is skewed to bottom of the interquartile range due to night-time zeros included in the average. High levels of HONO were observed in both campaigns, but the median HONO mixing ratio was approximately 10 times larger in the post-monsoon than the pre-monsoon. The median HONO mixing ratio during the pre-monsoon and post-monsoon campaigns was 0.58 ppbV and 5.63 ppbV respectively. Pre-monsoon averages are comparable to those observed in London in 2012, where the campaign averaged HONO mixing ratio was 0.44 ppbV [30]. Post-monsoon median HONO was higher than has been observed in Beijing, with a recent study finding average summer and winter

Beijing HONO averages of 1.27 ppbV and 1.13 ppbV respectively [83].

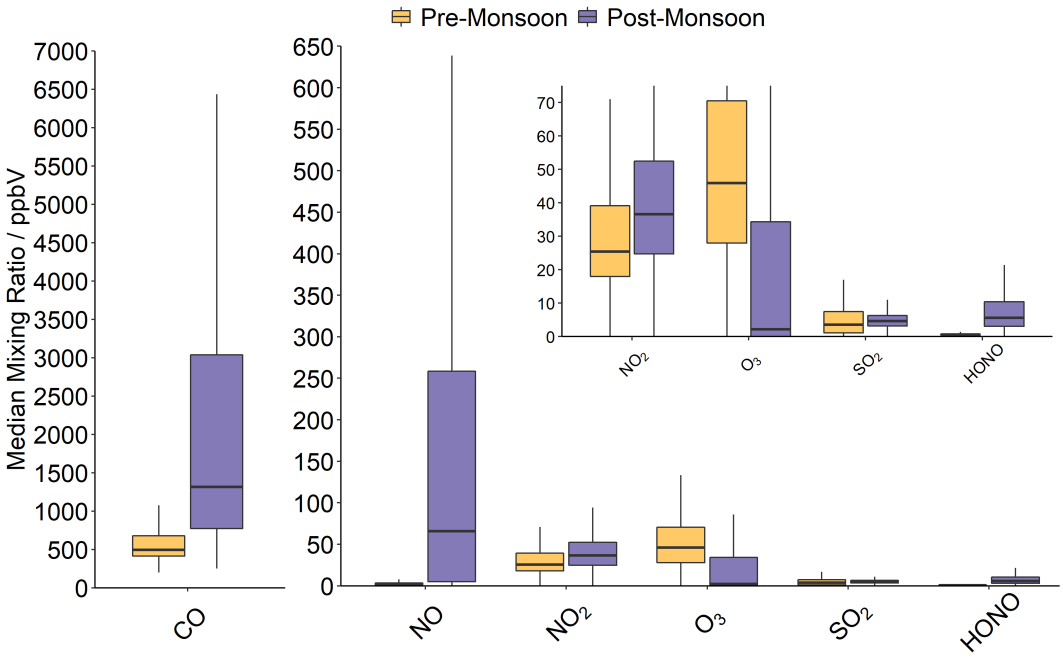

Figure 3.1: Box and whisker plot of of total mixing ratios of inorganic species during pre-monsoon (yellow) and post-monsoon (purple). The central bold black line represents the campaign median mixing ratio of each species/carbon number and the interquartile range (shaded region) represents 50% of the data, with the whiskers representing the upper and lower 25% of the data, excluding outliers.

3.1.3 Volatile Organic Compounds (VOCs)

The measurement of an extended suite of VOCs is important for obtaining a detailed description of the atmospheric chemical processing in urban environments. Due to differences in their structure and reactivities, it is important to obtain a speciated dataset of VOCs. Along with their concentrations in the atmosphere (presented here), their reactivity with OH, and the number of C-C and C-H bonds present in the molecule lead to differences in the VOCs O_3 production potential. As a result, O_3 formation does not scale linearly with bulk VOC concentration, with some species being more important in the formation of secondary species than others, despite being present in lower concentrations. Along with the propensity of VOCs to form O_3, their importance in the formation of secondary organic aerosol (SOA) is dictated by their structure. Larger VOCs, typically with a carbon number greater than 9, are more likely to contribute to SOA formation, as their oxidation products may have sufficiently low volatility to partition to the aerosol phase.

One dimensional gas chromatography (GC) techniques are widely used in measurement campaigns and field work globally, to obtain speciated measurements of VOCs. Of these

studies, only a small proportion are able to extend their measurement suite by using two dimensional gas chromatography (GC × GC) techniques. With GC × GC instrumentation, species of carbon number > 6 can be measured, along with other species which would otherwise co-elute using conventional, one dimensional methods. The breadth of measurement suite expansion on using GC × GC instrumentation was shown by Lewis et al., 2020 [84], where an additional 500 VOCs were separated from urban air, along with approximately 30 speciated compounds measured by a one dimensional GC. A large proportion of the additional VOC measurements gained by using this technique are monoaromatic compounds, many of which are highly reactive and play an important role in photochemical O_3 production and secondary organic aerosol formation urban atmospheres [85].

Using the one and two dimensional gas chromatography techniques described in Chapter 2, 86 individual compounds were speciated. These species have been grouped into 8 VOC classes based on their functionality and by carbon number. As this data is from two instruments with mis-matching, approximately hourly timestamps, the data was linearly interpolated to 1-minute resolution before being merged. The data was then grouped and the mixing ratios summed at each timestamp, before the median value was determined. The median mixing ratio for each grouping during pre-monsoon (yellow) and post-monsoon (purple) is presented in Figure 3.2.

VOCs were grouped by the following functional group classes: alkanes, alcohols, alkenes, aromatics, carbonyls, alkynes, dialkenes and monoterpenes (Figure 3.2a). Across all groups, the median mixing ratio was higher in the post-monsoon than the pre-monsoon, with values in the post-monsoon more than twice that of the pre-monsoon for some groups. During both pre- and post-monsoon campaigns, the highest mixing ratios were observed for alkanes and alcohols, when compared to other VOC classes. During the pre-monsoon, the median alcohol mixing ratio (50 ppbV) was more than double that of the alkane mixing ratio (23 ppbV). In the post-monsoon, the median alkane mixing ratio (97 ppbV) was higher than that of the alcohols (78 ppbV). The median mixing ratio of dialkenes was similar in both campaigns, which is reflected in the diel profile of isoprene (see section 3.3.3). Despite cooler temperatures in the post-monsoon campaign relative to the pre-monsoon, the median mixing ratio of monoterpenes, usually derived from biogenic sources, was higher than in the pre-monsoon. The reason for this may be due to anthropogenic sources of monoterpenes in the post-monsoon, which is discussed in more detail later in this chapter (section 3.3.3).

The median mixing ratio grouped by carbon number is presented in Figure 3.2b. During the pre-monsoon, the sum of the species with only two carbon atoms, C_2 (ethane, ethene, acetylene, ethanol and acetaldehyde) had the highest median mixing ratio, followed by C_3 (propane, propene, propyne and acetone). Pre-monsoon median mixing ratios increased up to C_2, then decreased. In the post-monsoon, C_2 species had the highest median mixing ratio followed by the C_1 (methanol and formaldehyde), C_4 (butanes, butenes, butadienes, ethyl ac-

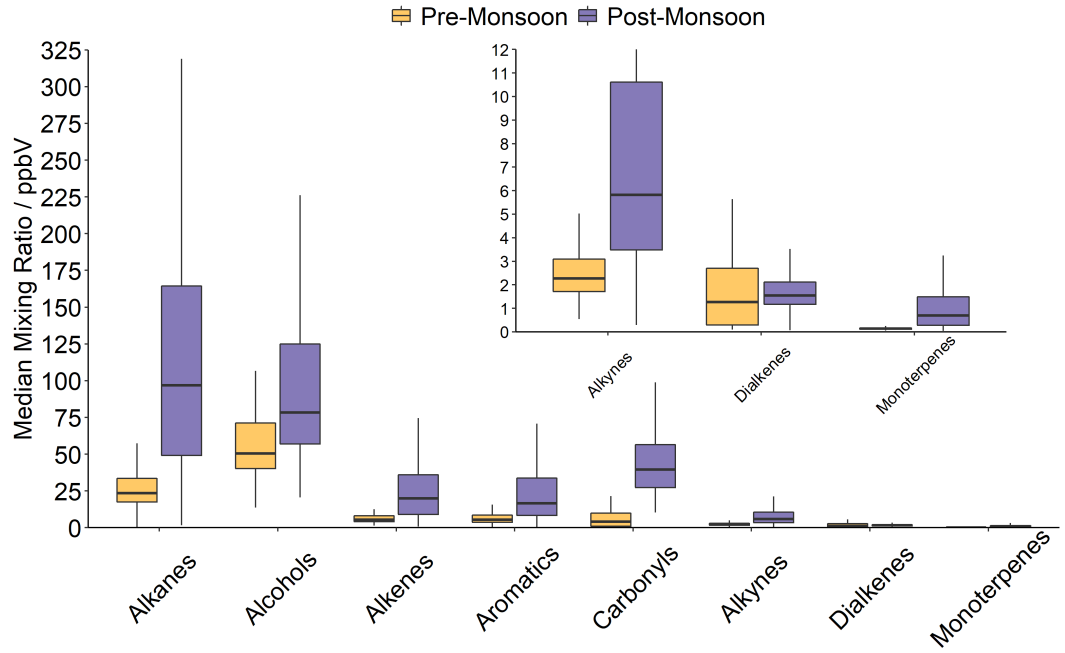

(a)

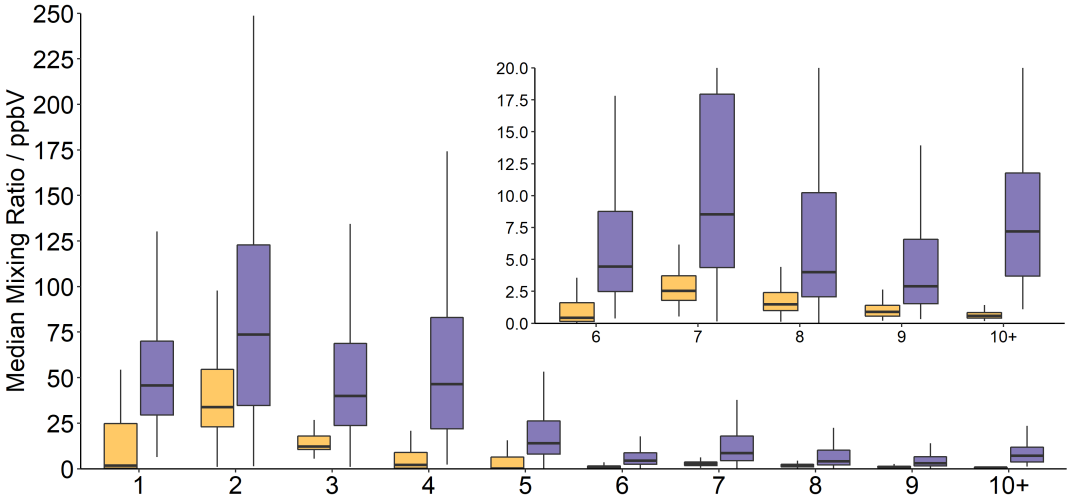

(b)

Figure 3.2: Box and whisker plot of total mixing ratios of VOCs measured by GC-FID and GC × GC-FID by class (a) and carbon number (b) during pre-monsoon (yellow) and post-monsoon (purple). The central bold black line represents the campaign median mixing ratio of each species/carbon number and the interquartile range (shaded region) represents 50% of the data, with the whiskers representing the upper and lower 25% of the data, excluding outliers.

etate, MEK, MVK and metacrolein) and C_3 species respectively. In the pre-monsoon, there was a gradual decrease in median mixing ratio from C_3 to C_5 (pentanes, pentenes, isoprene, methylpropylketone). In the post-monsoon C_1-C_4 median mixing ratios were significantly higher than C_{5+} median mixing ratios. In the post-monsoon, significant proportion of larger

C_{10+} species (7 ppbV) was observed, compared to 0.6 ppbV observed in the pre-monsoon. Two dimensional gas chromatography techniques allowed for the separation of these larger species, the significance of which, in terms of reactivity, is discussed later in Chapter 4.

The GC measurement suite was complimented by a PTR-MS dataset (see Chapter 2 for a more detailed description). This allowed for the measurement of additional carbonyl species, such as acetaldehyde and methylvinylketone, difficult to detect using the traditional GC techniques. A discussion of each VOC species, measured using both GC and PTR techniuques, is given in this section. Each class of VOCs is presented in turn. At the end of the section, the median, maximum and minimum measurements of each observed VOC during the pre- and post-monsoon campaigns are summarised in Table 3.1.3.

Alkanes

In both pre- and post-monsoon campaigns, the alkane VOC class was a large proportion of the total measured mixing ratio of VOCs, representing 25% and 37% of the measured VOCs respectively. In both campaigns, propane had the highest median mixing ratio of all the alkanes measured (Figure 3.3), with median mixing ratios of 5.7 ppbV and 26 ppbV in the pre- and post-monsoon respectively. This is closely followed by *n*-butane in the post-

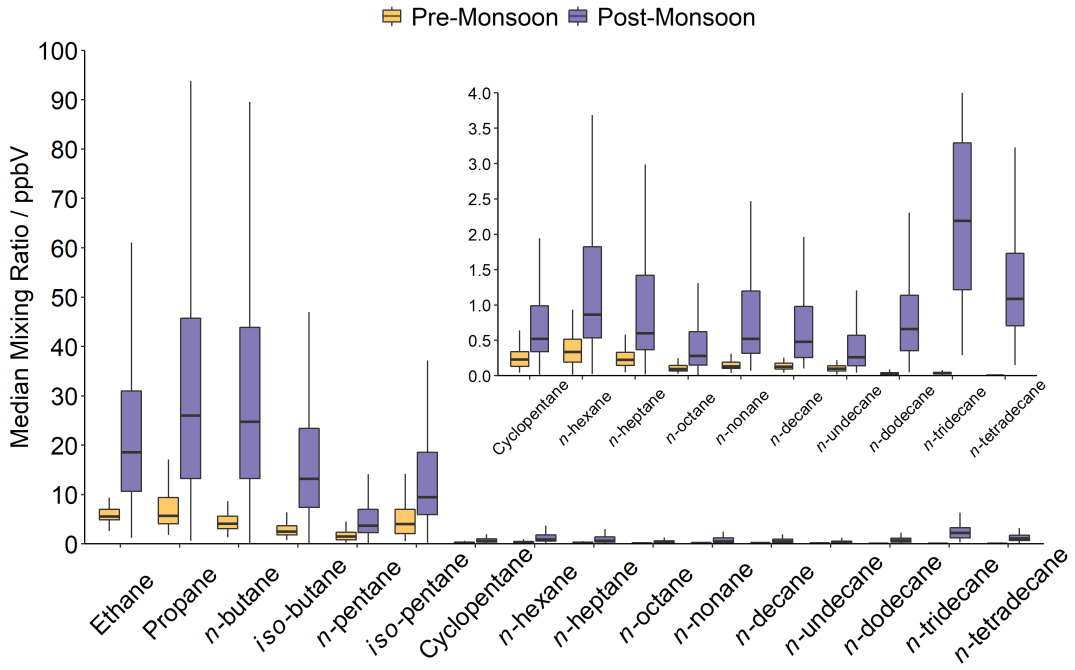

Figure 3.3: Median mixing ratio of alkanes measured by GC-FID and GC × GC-FID during pre-monsoon (yellow) and post-monsoon (purple). The central bold black line represents the campaign median mixing ratio of each species and the interquartile range (shaded region) represents 50% of the data, with the whiskers representing the upper and lower 25% of the data, excluding outliers.

monsoon (25 ppbV) and ethane in the pre-monsoon (5.6 ppbV). The high mixing ratios of the smaller aliphatic compounds dominated this group. The mixing ratios of these species were significantly higher in the post-monsoon relative to the pre-monsoon, with ethane approximately three times greater in the post-monsoon, and propane, *n*-butane and *iso*-butane approximately four, six and five times larger respectively. Likely sources of these species are compressed natural gas (CNG), and liquid petroleum gas (LPG). Generally, the median mixing ratio of alkanes increased from C_2 up to C_4, before decreasing. In the pre-monsoon, mixing ratios of C_6-C_{14} species remained low. In the post-monsoon, median mixing ratios of C_9 species onward deviated from this trend, with median mixing ratios increasing again to C_{13} (2 ppbV). Unfortunately, there were no pre-monsoon measurements of C_{14}. Larger chain *n*-alkanes are likely to be from diesel fuel sources. Despite their low concentrations relative to the C_2-C_4 alkanes, these longer chain alkanes may have an important role in O_3 formation and secondary organic aerosol production [56].

Alkenes, dialkenes and alkynes

Alkenes, dialkenes and alyknes represented 10% of the measured VOC mixing ratios in both the pre- and post-monsoon campaigns. Generally, the median mixing ratio of alkenes decreased from C_2 to C_5 (Figure 3.4). In both the pre- and post-monsoon, ethene had the

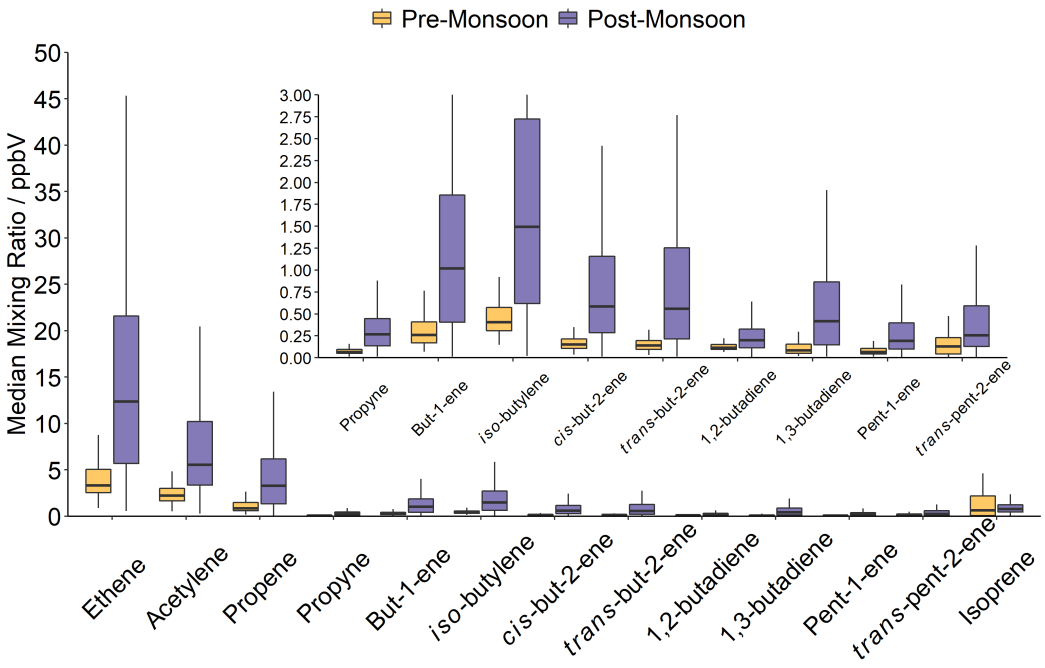

Figure 3.4: Median mixing ratio of alkenes, dialkenes and alkynes measured by GC-FID during pre-monsoon (yellow) and post-monsoon (purple). The central bold black line represents the campaign median mixing ratio of each species and the interquartile range (shaded region) represents 50% of the data, with the whiskers representing the upper and lower 25% of the data, excluding outliers.

highest alkene median mixing ratio, followed by propene. The median mixing ratio of ethene was more than three times higher in the post-monsoon than the pre-monsoon. Along with ethane, an important ethene source is likely to be CNG. Elevated levels of ethene in the post-monsoon are consistent with high mixing ratios of ethane (Figure 3.3). High mixing ratios of acetylene were observed in both campaigns, and the post-monsoon median mixing ratio of acetylene was more than double that of the pre-monsoon. Median isoprene mixing ratios were similar in both the pre- and post-monsoon, 0.64 ppbV and 0.77 ppbV respectively, despite cooler temperatures in the post-monsoon.

Alcohols and carbonyls

Alcohols and carbonyls combined represented 59% and 63% of the measured median VOC mixing ratios in the pre- and post-monsoon respectively. Although the median mixing ratio

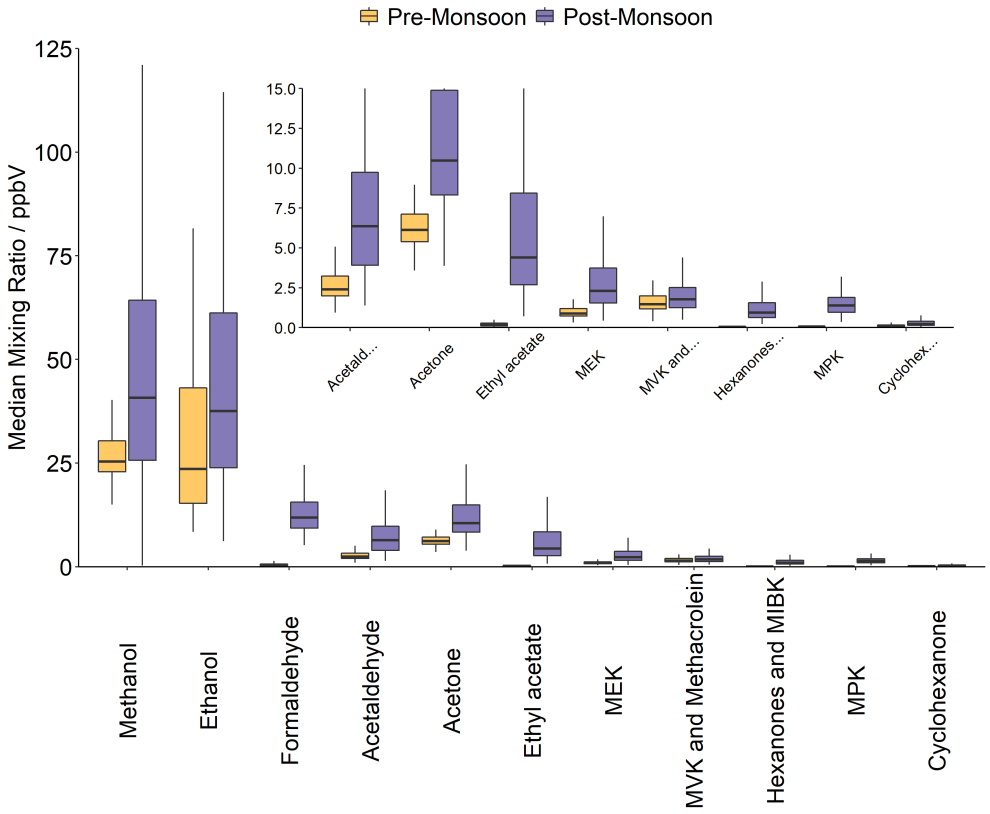

Figure 3.5: Median mixing ratio of alcohols and carbonyls measured by GC-FID and PTR-MS during pre-monsoon (yellow) and post-monsoon (purple). The central bold black line represents the campaign median mixing ratio of each species and the interquartile range (shaded region) represents 50% of the data, with the whiskers representing the upper and lower 25% of the data, excluding outliers.

of alkanes was marginally higher than the alcohol group during the post-monsoon, only two species (methanol and ethanol) were detected, compared to sixteen alkanes (Figure 3.5). Mixing ratios of methanol were marginally higher than ethanol in the pre-monsoon and vice versa

in the post-monsoon. Sources of these species in the urban environment include solvents and process emissions, along with secondary formation from other VOCs. High median mixing ratios of one carbonyl species, acetone, were measured with GC-FID.

Post-monsoon mixing ratios for methanol, ethanol and acetone were approximately 1.5 times higher than in the pre-monsoon period. All other carbonyl species were measured with PTR-MS. Median mixing ratios of the sum of methyl vinyl ketone (MVK) and methacrolein were similar in the pre- and post-monsoon campaigns, and post-monsoon cyclohexanone and methyl ethyl ketone (MEK) were ≈ 2 times greater than in the pre-monsoon campaign. For all other observed carbonyl species, post-monsoon median mixing ratios were significantly higher than pre-monsoon medians. The post-monsoon formaldehyde (HCHO) median mixing ratio was 43 times greater than the pre-monsoon median. The median ethyl acetate mixing ratio was 26 times greater in the post-monsoon, and median methyl propyl ketone (MPK) was 22 times greater.

Monoterpenes

In both and pre- and post-monsoon campaigns, monoterpenes represented $< 1\%$ of the total measured median mixing ratios of VOCs. Monoterpenes are emitted from trees and other

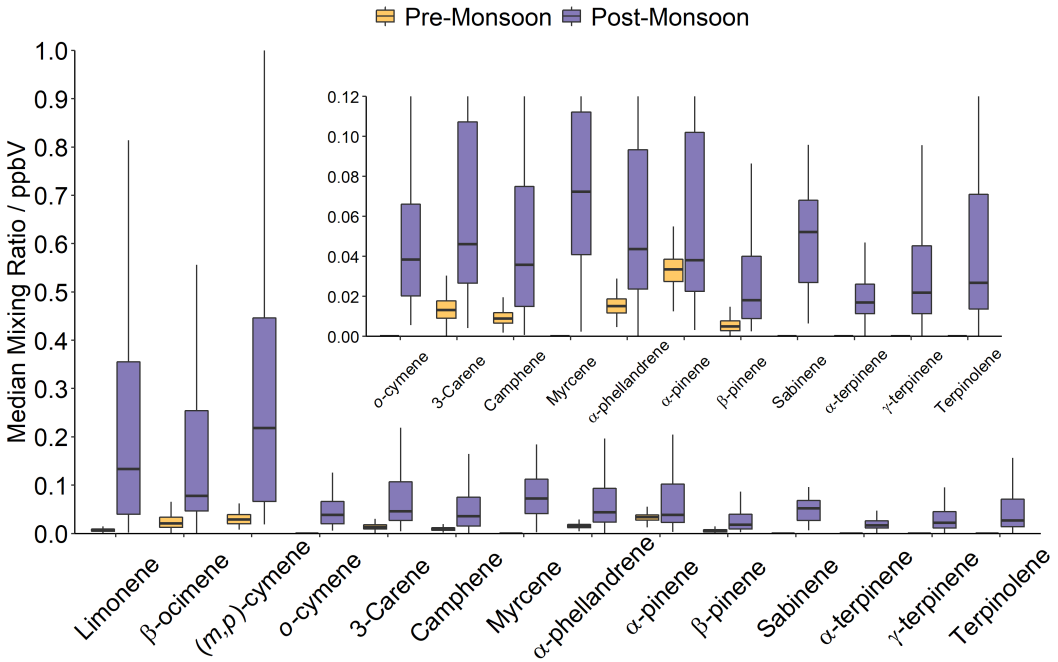

Figure 3.6: Median mixing ratio of monoterpenes measured by GC $\times$ GC-FID during pre-monsoon (yellow) and post-monsoon (purple). The central bold black line represents the campaign median mixing ratio of each species and the interquartile range (shaded region) represents 50% of the data, with the whiskers representing the upper and lower 25% of the data, excluding outliers.

plants, at rates highly dependant on temperature [86]. For all monoterpenes measured (10 in the pre-monsoon, and 14 in the post-monsoon), median mixing ratios were higher in the post-monsoon than the pre-monsoon, despite cooler temperatures in the post-monsoon period. Although the cymenes are C_{10} aromatic species, they have been included in the monoterpene section as their source is commonly biogenic. Measurements of α-terpinene, myrcene, o-cymene and sabinene were only available in the post-monsoon. Median mixing ratios of α-phellandrene and (*m,p*)-cymene were the highest in this group during the pre-monsoon, and (*m,p*)-cymene, limonene and β-ocimene were the highest during the post-monsoon. The very high mixing ratios of monoterpenes observed during the cooler time of year may suggest anthropogenic sources of monoterpenes during the post-monsoon. The diel profile of monoterpenes further supports this, as described later in section 3.3.3.

Aromatics

GC × GC instrumentation allowed for an extensive suite of aromatic compounds to be measured (Figure 3.7). Vehicular emissions are a major source of aromatic species globally, with other key sources including industrial processes and off-gassing from building materials [87]. Across the two measurement campaigns, 31 individual aromatic species were measured. 1,4-diethylbenzene and *n*-butylbenzene have been grouped as they could not be separated by the instrumentation. Only post-monsoon campaign measurements were available for *t*-butylbenzene, indene and tetrahydronapthalene. For some species, including 1,2,4,5-tetramethylbenzene, 1,3-dimethyl-2-ethylbenzene, 2,3-dimethyl-1-ethylbenzene and dimethylinane, median mixing ratios were regularly lower than the instrument limit of detection (LOD). Benzene, toluene, ethylbenzene, (*m,p*)-xylene and *o*-xylene measurements were made by both the (DC)-GC-FID and GC × GC instrumentation (see Chapter 2 for instrument intercomparison). For those species, only the (DC)-GC-FID median mixing ratios are reported here.

Aromatic species represented 6% of the total measured median mixing ratios of VOCs in both the pre- and post-monsoon campaigns. Across all aromatic species measured, median mixing ratios were higher in the post-monsoon than the pre-monsoon. Toluene mixing ratios were the highest of all the aromatic species observed, with a median mixing ratio of 1.6 ppbV in the pre-monsoon and 4 ppbV in the post-monsoon. This was followed by benzene with a median mixing ratio of 1 ppbV and 1.6 ppbV in the pre- and post-monsoon campaigns respectively.

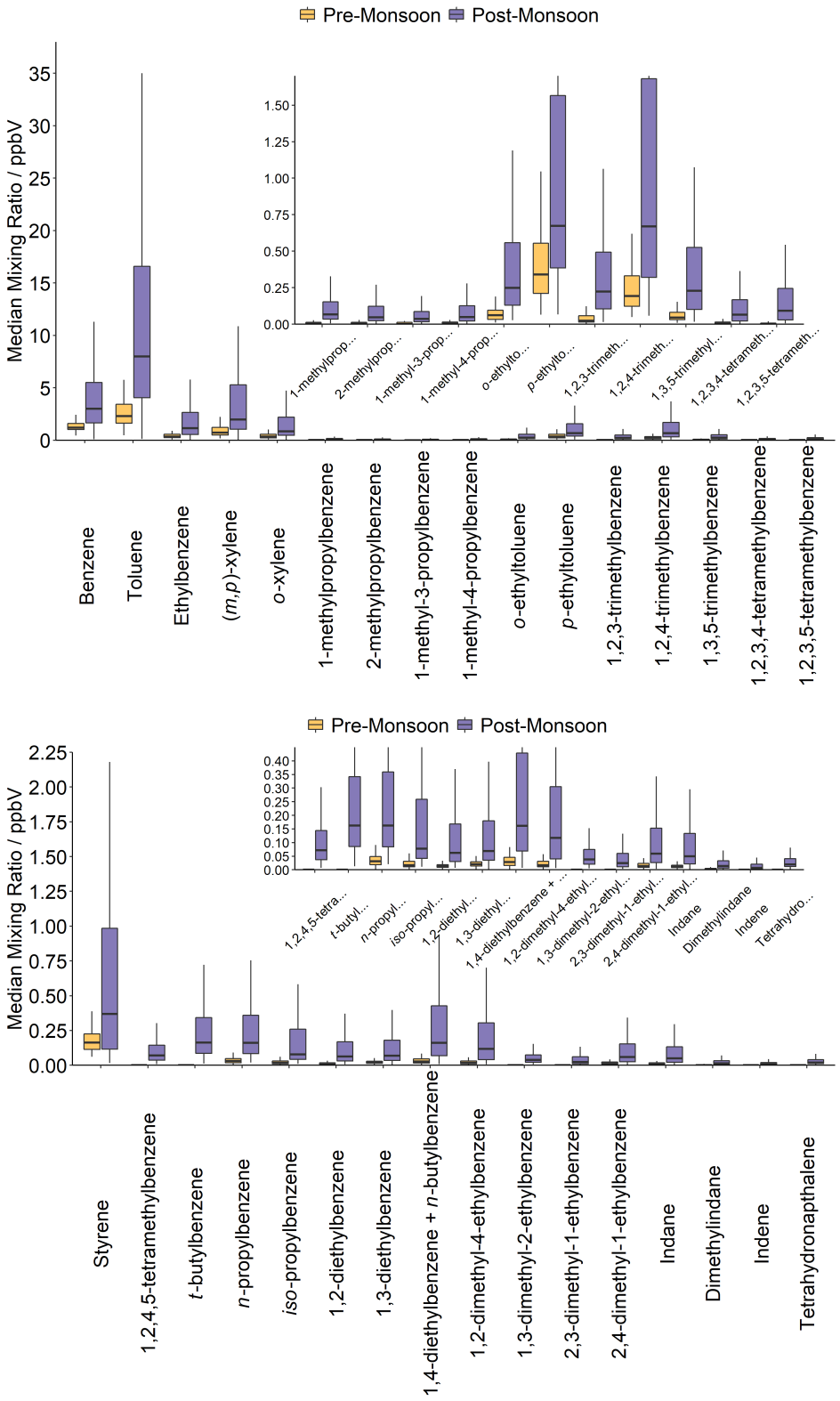

Figure 3.7: Median mixing ratio of alkanes measured by GC-FID and GC × GC-FID during pre-monsoon (yellow) and post-monsoon (purple). The central bold black line represents the campaign median mixing ratio of each species and the interquartile range (shaded region) represents 50% of the data, with the whiskers representing the upper and lower 25% of the data, excluding outliers.

Table 3.2: Median, minimum and maximum mixing ratios of VOCs during the pre- and post-monsoon campaigns.

Species	Class	Pre-monsoon mixing ratio / ppbV			Post-monsoon mixing ratio / ppbV		
		Median	Min	Max	Median	Min	Max
Ethanol	Alcohols	23.5	8.41	240.9	37.5	6.18	211.2
Methanol	Alcohols	25.4	1.83	143.4	40.8	0.30	179.1
Ethane	Alkanes	5.6	2.64	78.8	18.5	1.21	159.1
Propane	Alkanes	5.7	1.81	598.1	26.0	0.62	215.0
n-Butane	Alkanes	4.1	1.37	135.3	24.8	0.00	249.5
iso-Butane	Alkanes	2.5	0.78	115.2	13.2	0.19	120.4
n-Pentane	Alkanes	1.5	0.21	20.1	3.7	0.10	29.8
iso-Pentane	Alkanes	4.0	0.52	58.2	9.5	0.24	79.2
Cyclopentane	Alkanes	0.2	0.04	3.8	0.5	0.02	4.40
n-Hexane	Alkanes	0.3	0.02	5.4	0.9	0.02	10.0
n-Heptane	Alkanes	0.2	0.05	4.2	0.6	0.02	6.7
n-Octane	Alkanes	0.1	0.03	2.0	0.3	0.01	3.1
n-Nonane	Alkanes	0.1	0.04	0.7	0.5	0.07	4.2
n-Decane	Alkanes	0.1	0.04	0.7	0.5	0.1	3.6
n-Undecane	Alkanes	0.1	0.01	0.5	0.3	0.05	2.2
n-Dodecane	Alkanes	0.0	0.00	0.4	0.7	0.05	3.6
n-Tridecane	Alkanes	0.0	0.01	0.1	2.2	0.29	9.0
n-Tetradecane	Alkanes	N/A	N/A	N/A	1.1	0.15	3.4
Ethene	Alkenes	3.3	0.89	50.9	12.4	0.56	96.1
Propene	Alkenes	0.8	0.17	16.7	3.3	0.07	25.5
iso-Butylene	Alkenes	0.4	0.15	7.3	1.5	0.02	10.0
But-1-ene	Alkenes	0.3	0.07	5.2	1.0	0.01	6.6
cis-But-2-ene	Alkenes	0.2	0.04	3.3	0.6	0.01	4.8

Table 3.2 continued from previous page

trans-But-2-ene	Alkenes	0.1	0.03	3.9	0.6	0.01	5.3
Pent-1-ene	Alkenes	0.1	0.01	0.9	0.2	0.01	1.8
trans-Pent-2-ene	Alkenes	0.1	0.01	2.1	0.3	0.01	3.4
Acetylene	Alkynes	2.2	0.53	28.3	5.6	0.28	45.6
Propyne	Alkynes	0.1	0.01	0.9	0.3	0.01	1.9
Benzene	Aromatics	1.2	0.44	30.2	3.0	0.08	27.7
1,2-Diethylbenzene	Aromatics	0.0	0.01	0.1	0.1	0.01	0.7
1,3-Diethylbenzene	Aromatics	0.0	0.01	0.1	0.1	0.00	0.8
1,4-Diethylbenzene and *n*-Butylbenzene	Aromatics	0.0	0.01	0.2	0.2	0.01	2.1
1,2-Dimethyl-4-ethylbenzene	Aromatics	0.0	0.00	0.2	0.1	0.01	1.5
1,3-Dimethyl-2-ethylbenzene	Aromatics	0.0	0.00	0.0	0.0	0.01	0.4
2,3-Dimethyl-1-ethylbenzene	Aromatics	0.0	0.00	0.0	0.0	0.00	0.4
2,4-Dimethyl-1-ethylbenzene	Aromatics	0.0	0.00	0.1	0.1	0.00	0.7
Dimethylindane	Aromatics	0.0	0.00	0.0	0.0	0.00	0.2
Ethylbenzene	Aromatics	0.3	0.06	6.6	1.1	0.03	10.9
Indane	Aromatics	0.0	0.0	0.1	0.0	0.00	0.7
Indene	Aromatics	N/A	N/A	N/A	0.0	0.00	0.0
iso-Propylbenzene	Aromatics	0.0	0.0	0.2	0.1	0.01	1.3
1-Methyl-3-propylbenzene	Aromatics	0.0	0.00	0.0	0.0	0.00	0.4
1-Methyl-4-propylbenzene	Aromatics	0.0	0.00	0.1	0.0	0.00	0.6
1-Methylpropylbenzene	Aromatics	0.0	0.00	0.1	0.1	0.01	0.6
2-Methylpropylbenzene	Aromatics	0.0	0.00	0 .0	0.0	0.00	0.6
(*m*,*p*)-Xylene	Aromatics	0.7	0.18	17.1	2.0	0.02	31.5
o-Ethyltoluene	Aromatics	0.1	0.01	0.5	0.2	0.03	2.7
o-Xylene	Aromatics	0.3	0.07	7.2	0.8	0.02	12.3
n-Propylbenzene	Aromatics	0.0	0.00	0.3	0.2	0.02	1.6

Table 3.2 continued from previous page

p-Ethyltoluene	Aromatics	0.3	0.07	2.8	0.7	0.07	7.5
Styrene	Aromatics	0.2	0.06	0.8	0.4	0.02	5.7
1,2,3,4-Tetramethylbenzene	Aromatics	0.0	0.00	0.1	0.1	0.00	1.0
1,2,3,5-Tetramethylbenzene	Aromatics	0.0	0.00	0.1	0.1	0.01	1.2
1,2,4,5-Tetramethylbenzene	Aromatics	0.0	0.00	0.1	0.1	0.01	0.5
tert-Butylbenzene	Aromatics	N/A	N/A	N/A	0.2	0.01	1.5
Tetrahydronapthalene	Aromatics	0.0	0.00	0.0	0.0	0.00	0.2
1,2,3-Trimethylbenzene	Aromatics	0.0	0.00	0.5	0.2	0.02	2.8
1,2,4-Trimethylbenzene	Aromatics	0.2	0.05	1.7	0.7	0.06	8.1
1,3,5-Trimethylbenzene	Aromatics	0.0	0.01	0.4	0.2	0.02	3.0
Toluene	Aromatics	2.3	0.47	48.4	8.0	0.12	65.4
Acetaldehyde	Carbonyls	2.4	0.95	14.2	6.4	1.39	23.1
Acetone	Carbonyls	6.1	3.58	104.8	10.5	3.87	45.2
Cyclohexanone	Carbonyls	0.1	0.03	0.7	0.2	0.04	1.6
Ethyl acetate	Carbonyls	0.2	0.04	2.3	4.4	0.70	53.9
Formaldehyde	Carbonyls	0.3	0.00	9.9	11.9	5.21	40.1
Hexanones and MIBK	Carbonyls	0.0	0.01	0.3	0.9	0.22	23.4
MEK	Carbonyls	0.9	0.31	5.5	2.3	0.44	18.2
MPK	Carbonyls	0.1	0.02	0.3	1.4	0.35	4.8
MVK and Methacrolein	Carbonyls	1.5	0.40	5.5	1.8	0.49	20.1
1,2-Butadiene	Dialkenes	0.1	0.06	2.2	0.2	0.01	1.5
1,3-Butadiene	Dialkenes	0.1	0.02	2.2	0.4	0.01	4.6
Isoprene	Dialkenes	0.6	0.01	4.6	0.8	0.05	6.7
α-Phellandrene	Monoterpenes	0.0	0.00	0.1	0.0	0.01	0.3
α-Pinene	Monoterpenes	0.0	0.01	0.1	0.0	0.00	0.3
β-Pinene	Monoterpenes	0.0	0.00	0.1	0.0	0.00	0.1

Table 3.2 continued from previous page

α-Terpinene	Monoterpenes	N/A	N/A	N/A	0.0	0.00	0.1
β-Ocimene	Monoterpenes	0.0	0.00	0.2	0.1	0.00	1.2
3-Carene	Monoterpenes	0.0	0.00	0.1	0.0	0.00	0.3
Camphene	Monoterpenes	0.0	0.00	0.1	0.0	0.00	0.3
γ-Terpinene	Monoterpenes	0.0	0.01	0.1	0.0	0.00	0.1
Limonene	Monoterpenes	0.0	0.00	0.2	0.1	0.00	2.0
(m,p)-Cymene	Monoterpenes	0.0	0.01	0.2	0.2	0.02	1.8
Myrcene	Monoterpenes	N/A	N/A	N/A	0.1	0.00	0.2
o-Cymene	Monoterpenes	N/A	N/A	N/A	0.0	0.01	0.3
Sabinene	Monoterpenes	N/A	N/A	N/A	0.1	0.01	0.1
Terpinolene	Monoterpenes	0.0	0.00	0.0	0.0	0.00	0.3

3.1.4 Photolysis Rates

The vast majority of radical species are formed in the atmosphere from the photolysis of stable species. The rates at which compounds in the atmosphere photolyse, along with their ambient concentrations, are crucial for understanding the concentrations of radicals generated during the day. As radicals are essential to tropospheric O_3 formation, the measurement of photolysis rates in the field allows for a more detailed description of the chemical processing in the atmosphere. The median daily photolysis rates measured during the pre- and post-monsoon campaign are summarised in Table 3.3.

Table 3.3: Daily median of 34 measured photolysis rates during the pre- and post-monsoon campaigns.

			Median daily maximum / s^{-1}	
Reactant (MCM name)	J value	Products	Pre-Monsoon	Post-Monsoon
O3	1	$O(^1D) + O_2$	4.52×10^{-5}	1.96×10^{-5}
O3	2	$O(^3P) + O_2$	6.72×10^{-4}	5.56×10^{-4}
H2O2	3	2OH	1.05×10^{-5}	6.57×10^{-6}
NO2	4	$NO + O(^3P)$	9.31×10^{-3}	7.94×10^{-3}
NO3	5	$NO + O_2$	2.74×10^{-2}	2.24×10^{-2}
NO3	6	$NO_2 + O(^3P)$	1.88×10^{-1}	1.45×10^{-1}
HONO	7	NO + OH	1.54×10^{-3}	1.35×10^{-3}
HNO3	8	NO_2 + OH	9.18×10^{-7}	5.70×10^{-7}
HCHO	11	H + HCO	2.94×10^{-5}	2.07×10^{-5}
HCHO	12	H_2 + CO	3.56×10^{-5}	2.60×10^{-5}
CH3CHO	13	CH_3 + HCO	4.71×10^{-6}	4.27×10^{-6}
C2H5CHO	14	C_2H_5 + HCO	1.93×10^{-5}	1.06×10^{-5}
C3H7CHO	15	n-C_3H_7 + HCO	1.40×10^{-5}	8.07×10^{-6}
C3H7CHO	16	C_2H_4 + CH_3CHO	6.54×10^{-6}	3.88×10^{-6}
IPRCHO	17	n-C_4H_9 + HCO	6.91×10^{-5}	3.76×10^{-5}
MACR	18	CH_2=CCH_3 + HCO	8.45×10^{-7}	5.94×10^{-7}
MACR	19	CH_2=$C(CH_3)CO$ + H	8.45×10^{-7}	5.94×10^{-7}
C5HPALD1	20	$CH_3C(CHO)$=$CHCH_2O$ + OH	5.55×10^{-4}	3.81×10^{-4}
CH3COCH3	21	CH_3CO + CH_3	9.83×10^{-7}	5.76×10^{-7}
MEK	22	CH_3CO + C_2H_5	2.59×10^{-6}	1.55×10^{-6}
MVK	23	CH_3CH=CH_2 + CO	2.11×10^{-6}	1.35×10^{-6}
MVK	24	CH_3CO + CH_2=CH	2.11×10^{-6}	1.35×10^{-6}
GLYOX	31	2CO + H_2	7.22×10^{-6}	4.31×10^{-6}
GLYOX	32	HCHO + CO	3.21×10^{-5}	1.87×10^{-5}
GLYOX	33	2HCO	7.69×10^{-5}	4.80×10^{-5}
MGLYOX	34	CH_3CO + HCO	1.26×10^{-4}	9.05×10^{-5}
BIACET	35	CH_3CO + CH_3CO	4.19×10^{-4}	3.23×10^{-4}
CH3OOH	41	CH_3O + OH	6.31×10^{-6}	3.99×10^{-6}
CH3NO3	51	CH_3O + NO_2	1.43×10^{-6}	8.73×10^{-7}
C2H5NO3	52	C_2H_5O + NO_2	2.24×10^{-6}	1.35×10^{-6}
NC3H7NO3	53	n-C_3H_7O + NO_2	3.29×10^{-6}	2.03×10^{-6}
IC3H7NO3	54	$CH_3C(O)CH_3$ + NO_2	3.53×10^{-6}	2.11×10^{-6}
TC4H9NO3	55	t-C_4H_9O + NO_2	1.02×10^{-5}	5.99×10^{-6}
NOA	56	$CH_3C(O)CH_2(O)$ + NO_2 CH_3CO + HCHO + NO_2	3.90×10^{-5}	2.20×10^{-5}

3.2 Time series comparisons of observations

The full observational time series for inorganic species, selected VOCs, and selected photolysis rates are presented here. The pre-monsoon campaign observations are presented alongside the post-monsoon campaign for comparison. Days in which higher concentrations of species are observed are discussed in further detail. Local wind speed and direction data has been used to examine a link between high concentrations of pollutants and possible sources. The NOAA HYSPLIT model has also been used to examine a case study day in the pre-monsoon campaign where concentrations of pollutants are much higher than the rest of the campaign.

3.2.1 Inorganics: NO, NO_2, CO, O_3, SO_2 and HONO

During the pre-monsoon, mixing ratios of CO, NO and O_3 were elevated during the first night (28/05 - 29/05) compared to the rest of the campaign (Figure 3.10). CO mixing ratios peaked at $\approx$ 5 ppmV on the night of 28/05, and two additional peaks occured on the evenings of 29/05 and 31/05 at $\approx$ 2 ppmV (Figure 3.10). From 01/06 onward, CO mixing ratios consistently peaked in the evening at $\approx$ 600 ppbV and were at their lowest in the early hours of the morning. NO mixing ratios peaked at $\approx$ 500 ppbV on the night of 28/05. Another more minor peak was observed just before midnight on the evening of 30/05. From 01/06 onward, NO is $<$ 5 ppbV at night, and peaked between 10 - 20 ppbV during the day. NO_2 peaked on the evening of 29/05 at $\approx$ 120 ppbV, and on the evenings of 28/05 and 31/05 at $\approx$ 90 ppbV. For the remainder of the campaign, NO_2 peaked in the evenings at $\approx$ 60 ppbV. O_3 mixing ratios peaked at the start of the campaign at $\approx$ 190 ppbV. For the remainder of the campaign, O_3 daily peaks were around 100 ppbV. High night time mixing ratios of $\approx$ 60 ppbV were observed on the night of 29/05 into the early hours of the morning on 30/05, and very low night time mixing ratios of $<$ 10 ppbV were observed on the following night. The cause of the high night-time O_3 may be interferences with the O_3 instrument, discussed in further detail in Chapter 2. From 01/06 onward, night-time mixing ratios of O_3 fluctuate around 40 ppbV. SO_2 levels were also higher in the first few days, if you exclude the final few days of the campaign where very large spikes are observed.

Wind direction and wind speed data from Indira Gandhi International Airport (DEL) was used to investigate the direction of emission sources from the measurement site. Only pre-monsoon data from 30/05 onwards was used in this analysis. Figure 3.8 shows the wind direction and speed for each measurement during the pre-monsoon, coloured by the mixing ratio of each species: NO, NO_2, NO_x, CO, O_3 and SO_2. Only daytime measurements of O_3 were used in this analysis, in line with the approximate sunrise and sunset times in Delhi during June and October 2018. Higher CO mixing ratios corresponded with an easterly wind (4 - 6 m s^{-1}). The SO_2 spikes towards the end of the campaign occured with an SE and ESE wind direction, at wind speeds of $\approx$ 4.3 and 5.0 m s^{-1}. Just $\approx$ 100 m east of the measurement site is the National Highway 44, and a crematorium $\approx$ 500 m ESE, which may be the source

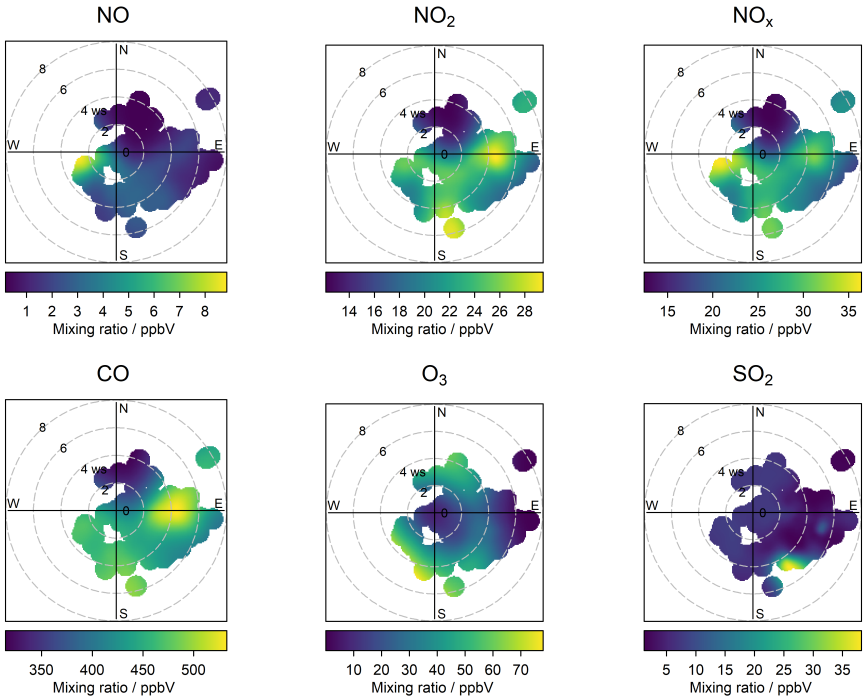

Figure 3.8: Polar plots coloured by the mixing ratios of NO, NO_2, NO_x, CO, O_3 and SO_2 during the pre-monsoon campaign, showing the relationship between mixing ratio and wind speed and direction.

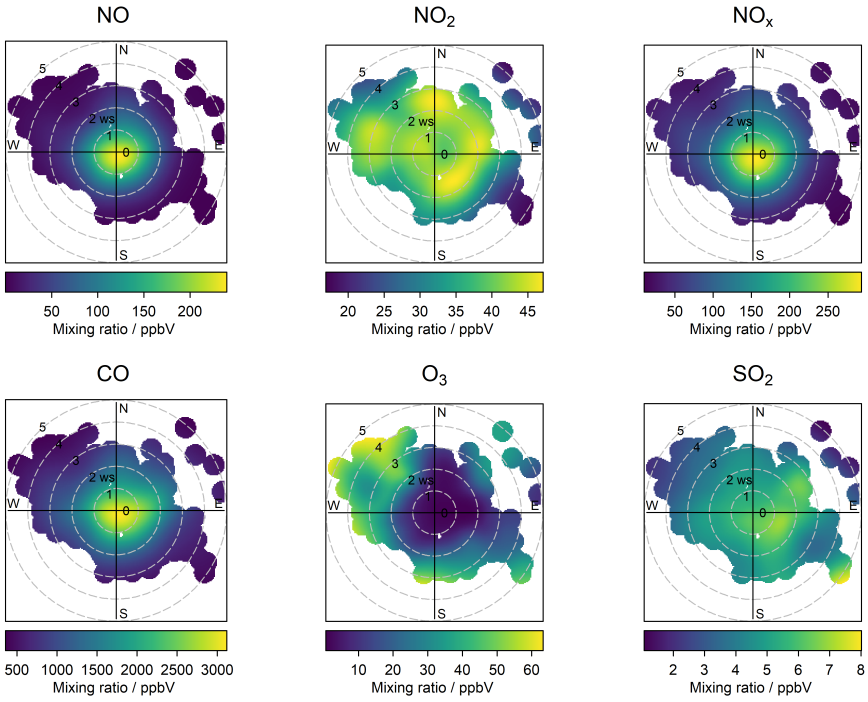

Figure 3.9: Polar plots coloured by the mixing ratios of NO, NO_2, NO_x, CO, O_3 and SO_2 during the post-monsoon campaign, showing the relationship between mixing ratio and wind speed and direction.

of high emissions of these pollutants. High volumes of traffic were observed on the National Highway 44 during the campaigns, which may contribute to the higher CO concentrations coinciding with winds from the east, particularly apparent in the pre-monsoon campaign. CO is emitted from the incomplete combustion of fuels, thus motor vehicles are a key source of CO pollution. Between 1996 and 2012, a drop in the annual emissions of CO from road transport was observed in the Indian state of Delhi [88]. This was a result of policy interventions, particularly the periodic changes in fuel standards, combined with the younger average age of vehicles (≈ 4 years), relative to fleets across the world such as the EU (≈ 8 years) and the USA (≈ 11 years) [88, 89]. In Delhi, there is a higher proportion of diesel four-wheel vehicles (58%) than petrol, due to a government subsidy making diesel cheaper [89]. Although we would expect this to lead to increased fuel efficiency of the fleet, a recent study suggests that a large proportion of the diesel vehicle sales are for four-wheelers with larger engines, which are more inefficient than their smaller engine counterparts. This somewhat mitigates the benefits of switching to a diesel-heavy fleet [89]. Crematoria are also known to be key sources of many harmful pollutants. The majority of crematoria in Delhi are conventional open pyres, where a variety of fuels such as wood, kerosene, and dung cake are burned [90]. The combination of both the incomplete combustion of fuels, as well as the burning of flesh, leads to a toxic mix of emissions, including particulate matter, CO, SO_2, and some heavy metals [90]. With the large SO_2 spikes excluded, high SO_2 levels generally occured during SSE winds. Although there is no obvious source of SO_2 near the measurement site in this direction, it is likely that the SO_2 is being produced from another incomplete combustion process. Higher mixing ratios of NO were observed from the south west at low wind speeds of < 4 m s^{-1}. Old Delhi Railway Station is located ≈ 400 m SSW of the measurement site, so this is a possible source of the higher NO mixing ratios. The Indian rail fleet consists of mostly electric and diesel fueled trains [91]. High NO_x concentrations observed during wind episodes from the SSW may be attributed to NO_x emissions from diesel locomatives, which are known to emit high levels of NO_x [92]. Lower concentrations of NO_x coincided with winds from the north. As the measurement site was located north of the centre of Delhi, any air masses arriving from the north would not have passed through the centre, but instead through the less traffic dense and more suburban outskirts of the state. Although O_3 mixing ratios also peaked with south westerly winds, the highest daytime peaks in O_3 generally occured when wind speeds were low, suggesting higher O_3 concentrations were observed when O_3 was produced locally. In addition, daytime peak O_3 concentrations were anti-correlated with NO concentrations, regardless of wind direction. The lowest daytime peak O_3 concentrations were observed when both wind speed and NO concentrations were higher. This suggests that reductions in the O_3 daytime peak may be due to incoming NO from outside of the local area, titrating O_3. However, although O_3 may be produced locally, its VOC precursor species may originate from the south / south west, leading to higher peak O_3 when the air mass arrives from this direction. One possible source of the precursors to O_3 formation is Chandni Chowk Market, the centre of which is ≈ 1.5 km south of the measurement site. The busy market, covering an area of approximately 5.6 km^2, sells a variety of items including textiles, spices, and hot food. Outdoor cooking, along with

the burning of incense sticks, observed during a brief visit to the area in May 2018, may be contributing to a broad range of VOC emissions such as terpenes and aromatic compounds [93, 94].

During the post-monsoon campaign, CO and NO mixing ratios were generally higher in the last half of the campaign (Figure 3.10). Higher levels of NO, NO_2 and CO occured at lower wind speeds, suggesting high emissions may be local to the measurement site (Figure 3.9). The high mixing ratios were slightly skewed to the east, in the direction of National Highway 44. High SO_2 mixing ratios occured with east and south easterly winds, suggesting National Highway 44, and the crematorium may be possible sources. O_3 mixing ratios were higher at higher wind speeds in all directions, and lower levels of O_3 were observed at low wind speeds. This suggests the observed higher O_3 may have been transported from further afield or, if the high O_3 was being formed in situ, this may mean its production was less determined by the high concentrations of NO_x present locally, and more driven by the transportation of other O_3 precursors to the measurement site from surrounding areas. SO_2 mixing ratios were generally < 20 ppbV throughout the campaign, with a few exceptions. There were two notable spikes around midnight on 09/10 and 17/10 were SO_2 mixing ratios exceed 40 ppbV. SO_2 mixing ratios reached 47 ppbV on 09/10 when there were ESE winds at ≈ 2.3 m s^{-1}, possibly due to emissions from the crematorium. The larger spike at 77 ppbV on 17/10 occured at low wind speeds, suggesting this could be a local SO_2 emission.

On comparing the sources of pollutants in both the pre- and post-monsoon campaigns, it is important to consider that a more limited dataset of only ≈ 1 week was collected in the pre-monsoon campaign, compared to ≈ 3 weeks in the post-monsoon campaign. Although the highest O_3 occured concurrently with wind from the NW in the post-monsoon, and with SW winds in the pre-monsoon, there were limited measurements occurring with NW winds in the pre-monsoon. However, high levels of CO in the pre-monsoon did predominantly occur to the east of the site, rather than occurring more locally to the site at lower wind speeds, as is found in the post-monsoon, and there was sufficient data in the pre-monsoon for both low wind, local data and measurements coinciding with an easterly wind. The most likely source of high CO when the wind arrives from the east is vehicular emissions from the National Highway 44, as a result of the incomplete combustion of fuel.

A shorter dataset of HONO measurements were made during the pre-monsoon and post-monsoon campaigns. In the pre-monsoon campaign, HONO peaked at 2.3 ppbV at midnight on 01/06, and peaked again later in the campaign at 2.2 ppbV at 06:00 on 04/06. In the post-monsoon, HONO mixing ratios were generally higher at the end of the campaign than the start, coinciding with higher NO concentrations observed at the end of October. HONO peaked at 04:00 on 01/11 at 29 ppbV. HONO mixing ratios exceeded 20 ppbV on 7 days during the campaign, all of which were during the later half of the campaign, from 18/10 onward.

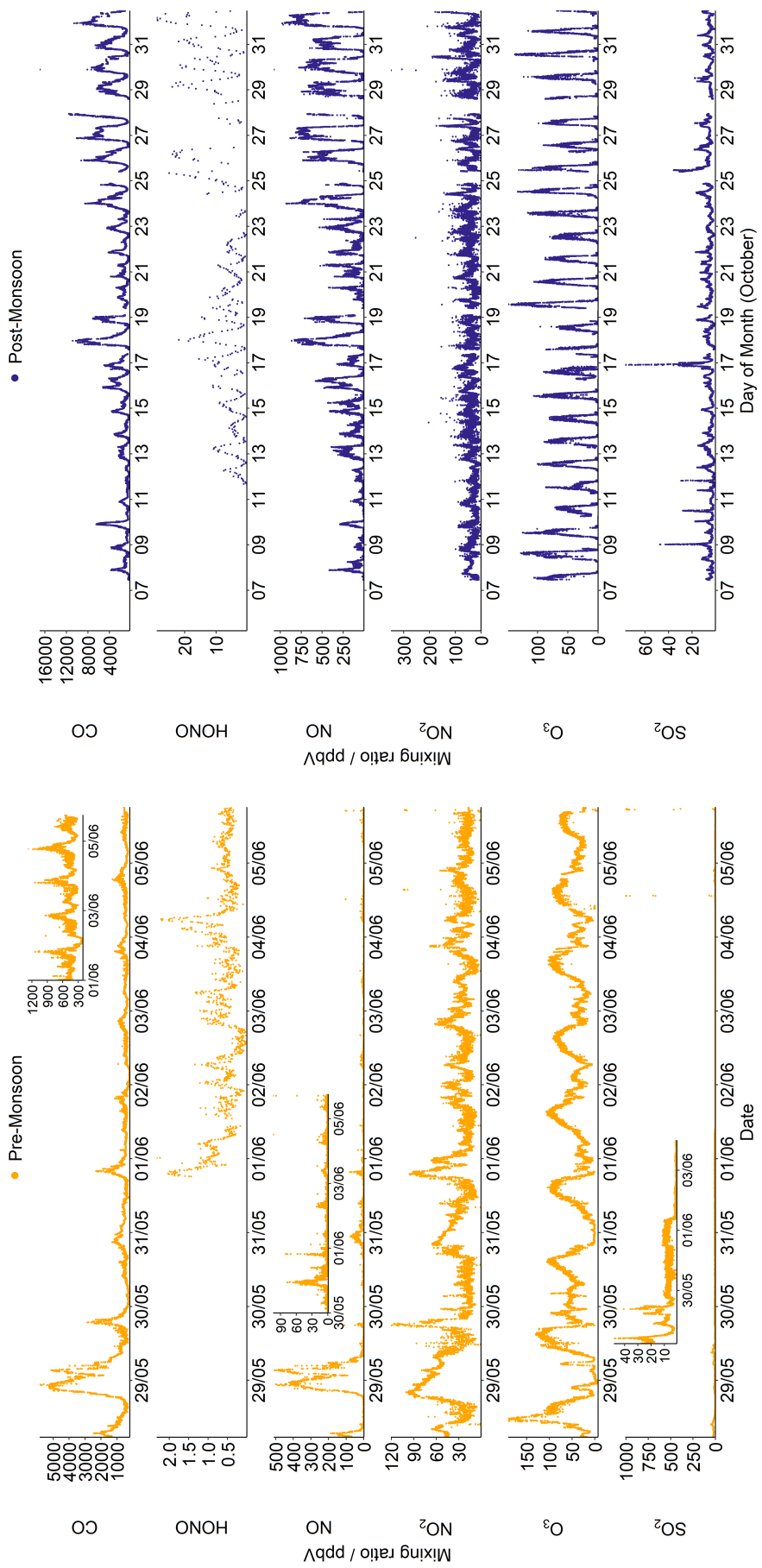

Figure 3.10: Time series mixing ratios of CO, NO, NO_2 and O_3 during pre-monsoon (yellow) and post-monsoon (purple).

3.2.2 Volatile organic compounds (VOCs)

The time series of selected VOCs for both the pre- and post-monsoon campaigns is presented in Figure 3.11. The species presented are: ethane (alkane), ethene (alkene), acetylene (alkyne), benzene (aromatic), ethanol (alcohol) and acetone (carbonyl). The monoterpene and dialkene classes are not presented here, but a more detailed analysis of monoterpenes and isoprene is presented in section 3.3.3.

At the beginning of the pre-monsoon campaign, concentrations of the selected species were much higher than the rest on the campaign. Ethane mixing ratios peaked at 79 ppbV in the early hours of 29/05, compared to a maximum mixing ratio of 18 ppbV between 30/05 and the end of the pre-monsoon campaign. A similar observation was made for ethene, acetylene, benzene and acetone, where maximum concentrations were observed in the late hours of 28/05, or into the early hours of 29/05, of 51 ppbV, 28 ppbV, 30 ppbV and 105 ppbV respectively. This was compared to maximum values from 30/05 until the end of the campaign of 15 ppbV, 7 ppbV, 6 ppbV and 12 ppbV respectively. Higher mixing ratios of ethanol were observed in the early hours of 29/05, peaking at 241 ppbV, but another peak of smaller magnitude was observed on 02/06 at 148 ppbV. This trend is consistent across all measured VOCs, excluding isoprene. Due to instrument issues, there was no data for monoterpene mixing ratios at the start of the campaign, so it is not known whether these species peaked on 28/05 into 29/05.

Post-monsoon mixing ratios of most VOC species peaked in the middle of the campaign, around 18/10, and then again towards the end of the measurement period (27/10). Ethane, ethene and acetylene peaked at 159 ppbV, 96 ppbV and 46 ppbV, respectively on the night of 17/10 into the early hours of the morning on 18/10. Acetone and benzene peaked on 27/10 at 58 ppbV and 34 ppbV respectively, with high mixing ratios of benzene also observed on 17/10 of 25 ppbV.

In both campaigns, higher concentrations of anthropogenic VOCs generally coincided with increased concentrations of inorganic pollutants, such as CO. This suggests that VOCs, CO and NO_x may share the same source. One possible source of these species is from road transport. As the measurement site is located close to the National Highway 44 (see section 2.1), vehicular emissions may be a major source of the pollutants observed at the site. In a 2011 Census survey of Delhi, 21% of households owned at least one 4-wheel vehicle, and 39% of households owned at least one 2-wheel vehicle. The higher proportion of 2-wheel vehicles compared to four-wheel is significant, as the 2-wheel vehicles represent a higher percentage of VOC emissions from road transport (33%), compared to four-wheelers (19%).

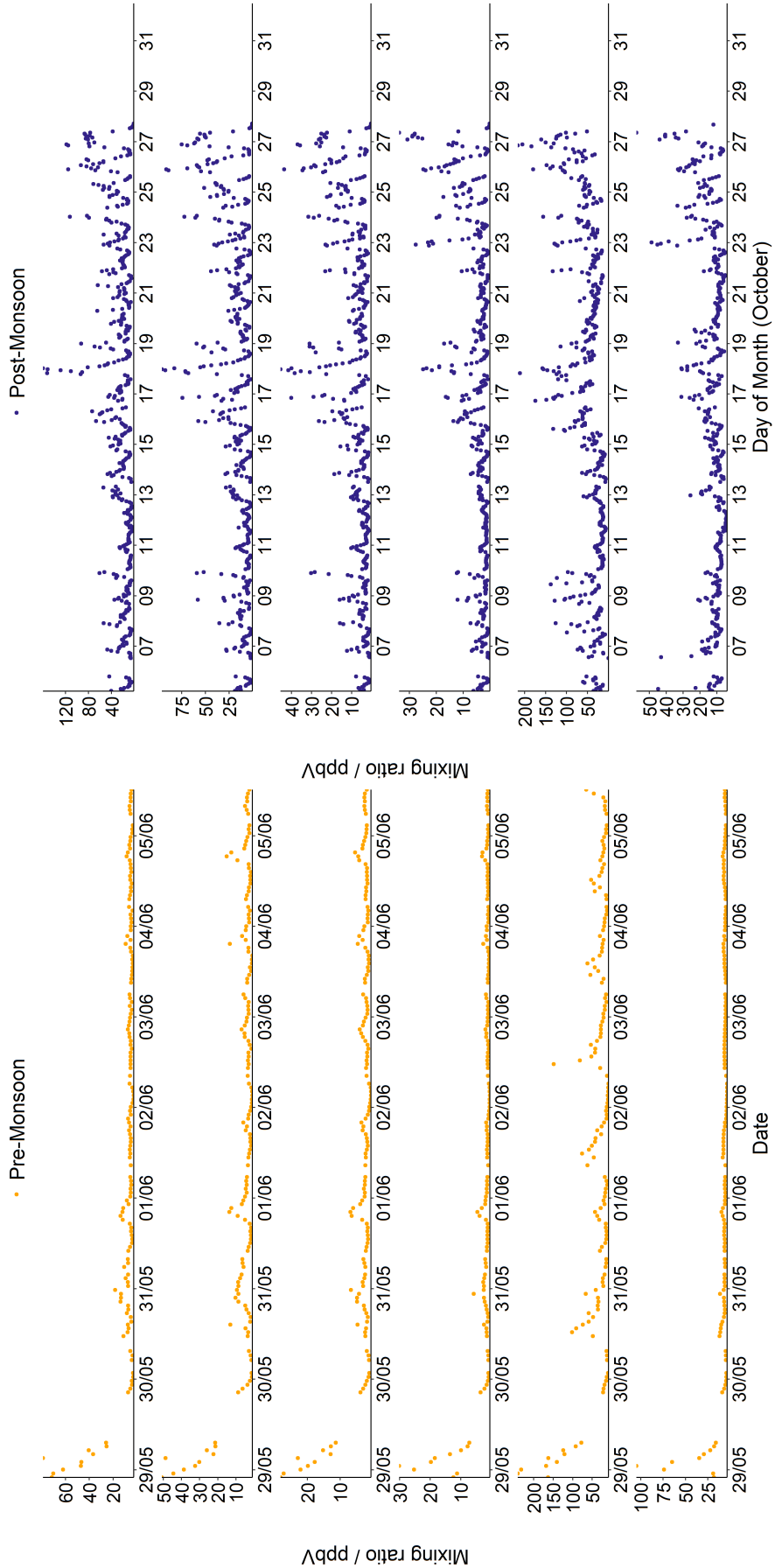

Figure 3.11: Time series of selected VOCs: Ethane, ethene, acetylene, benzene, ethanol and acetone during the pre-monsoon (yellow) and post-monsoon (purple).

3.2.3 Photolysis rates

Time series for three photolysis rates, $j(O^1D)$ (J1), $j(NO_2)$ (J4) and $j(HONO)$ (J7) are presented in Figure 3.12.

$j(O^1D)$ was noticeably higher in the pre-monsoon compared to the post-monsoon, whereas $j(NO_2)$ and $j(HONO)$ rates were comparable in both campaigns. The median value of $j(O^1D)$ was > 2 times higher in the pre-monsoon than the post-monsoon. One reason for this may be differences in aerosol composition and particle concentrations between the two campaigns. Differences in particle composition in the atmosphere may lead to different photolysis attenuation factors. O_3 photolysis occurs at shorter wavelengths, typically where $\lambda < 330$ nm, compared to NO_2 and HONO photolysis which occur at longer wavelengths where $310 < \lambda < 420$ nm and $300 < \lambda < 400$ nm respectively [95–97]. The particles present in the atmosphere may have been better at attenuating shorter wavelength radiation than longer wavelength radiation, leading to greater reductions in $j(O^1D)$ relative to jNO_2 and $j(HONO)$. Towards the end of the post-monsoon campaign, there was a noticeable decrease in $j(NO_2)$ and $j(HONO)$, whereby the photolysis rates were approximately half that of the peak rates observed earlier in the campaign. Also towards the end of October, increased concentrations of $PM_{2.5}$ were reported which may have impacted photolysis frequencies. The $j(NO_2)$ and $j(HONO)$ photolysis rates shown in Figure 3.12 can be split into three distinct periods. Between 13/10 - 18/10, the highest levels of $j(NO_2)$ and $j(HONO)$ photolysis are observed. This is followed by a period of reduced photolysis rates between 19/10 - 23/10. The photolysis rates then reduce again between 24/10 - 27/10. The average photolysis rates during these periods were plotted against the average $PM_{2.5}$ air quality index derived from measurements made at the New Delhi US Embassy monitoring site (Figure 3.13) [98, 99]. For $j(NO_2)$ and $j(HONO)$, a decrease in average photolysis rates is observed with increasing $PM_{2.5}$ air quality index, however this trend is not observed for $j(O^1D)$. Studies suggest photolysis frequencies are dependant on aerosol optical depth, meaning increased aerosol loading may lead to reduced photolysis, and perhaps reduced O_3 formation as a result. However, the effect of aerosol on different photolysis frequencies is complicated, and whether increased aerosol leads to an increase or decrease in photolysis rates may be dependant on aerosol composition, as well as the wavelength ranges of photolysis [100, 101].

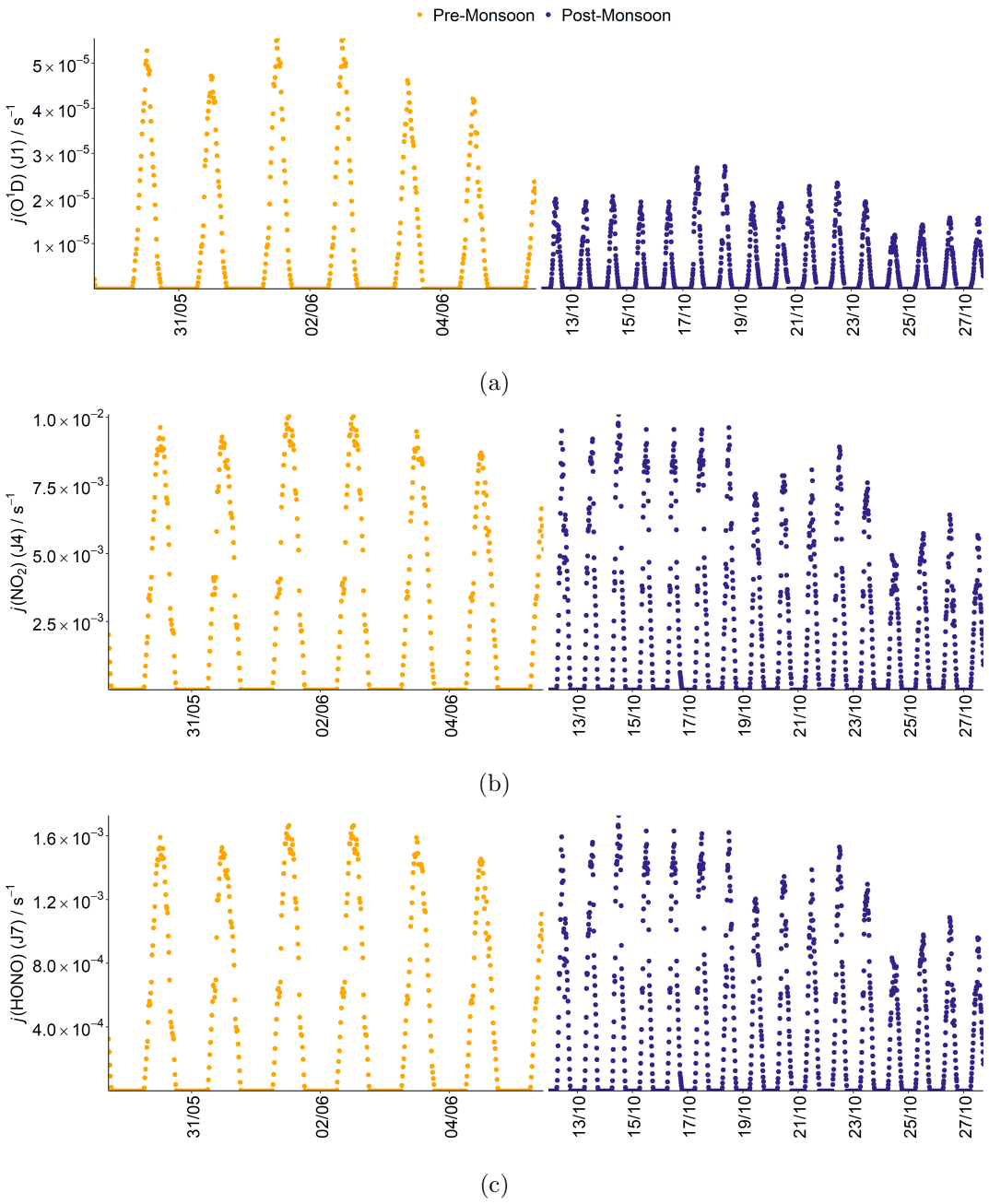

Figure 3.12: Photolysis rate timeseries for $j(O^1D)$ (a), $j(NO_2)$ (b) and $j(HONO)$ (c) during pre-monsoon (yellow) and post-monsoon (purple).

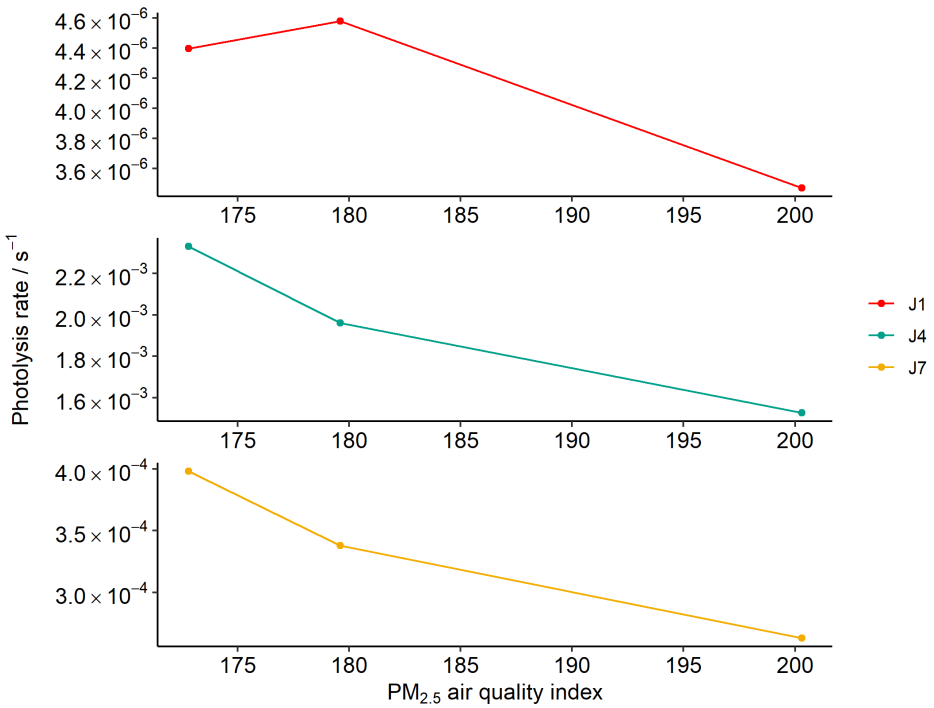

Figure 3.13: Average daily $PM_{2.5}$ air quality index plotted against photolysis rates, both averaged across three distinct periods: 13/10 - 18/10, 19/10 - 23/10, and 24/10 - 27/10. From top to bottom, the plotted photolysis rates are J1 ($j(O^1D)$), J4 ($j(NO_2)$), and J7 ($j(HONO)$) [98, 99].

3.2.4 Examining the possible sources of higher mixing ratios in pre-monsoon Delhi with back trajectories

Elevated levels of NO, CO and many VOC were observed on the night of 28/05 into the early hours of the morning on 29/05 (Figures 3.10 and 3.11). Data from this day was removed from the campaign averaged diel profiles presented in Figures 3.18 and 3.19, as this data skewed the averages to values higher than what was representative of the entire campaign period. Another smaller peak in NO and CO was observed at midnight on 31/05. To investigate the cause of elevated mixing ratios of anthropogenic species at midnight on 29/05 and 31/05, 1-hour NOAA HYSPLIT backward trajectories were calculated at 23:30 IST on the nights of 28th May - 3rd Jun (Figure 3.14). For all nights except for that of 28th and 30th May, the modelled trajectory of the air was of eastern origin, east of the Yamuna River. These trajectories indicate the air mass had travelled from outside the state of Delhi, and did not pass through New Delhi. One trajectory, on the night of 30/05 passed straight through the centre of New Delhi. The HYSPLIT back trajectories calculated here are corroborated by backwards Numerical Atmospheric dispersion Modelling Environment (NAME) modelling.

On the night of 28th May, the 1-hour HYSPLIT backwards trajectory indicated the air mass travelled across the state of Delhi, from the west of the measurement site (yellow trajectory, Figure 3.14). In this hour, the air mass only travelled a distance of 10 km, compared with

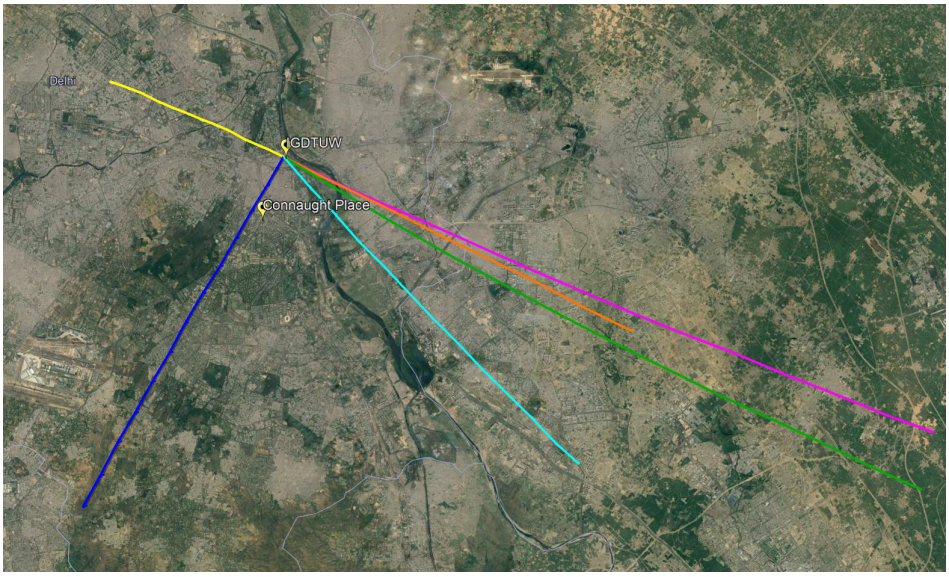

Figure 3.14: 1-hour NOAA HYSPLIT backward trajectories for Delhi from 23:30 IST on 28/05 (yellow), 29/05 (pink), 30/05 (blue), 31/05 (orange), 01/06 (green) and 02/06 (cyan).

other nights in which the trajectories covered a distance of 20-40 km. This analysis suggested the source of high concentrations of NO, CO and many VOCs on the night of 28th May may have been a result of local emissions, or from a source located in North West Delhi. NAME 24-hour backwards trajectories also showed high particle concentrations originating from the North West on midnight on 29th May, compared to the higher concentrations observed east of Delhi on midnight of 2nd June (Figure 3.15).

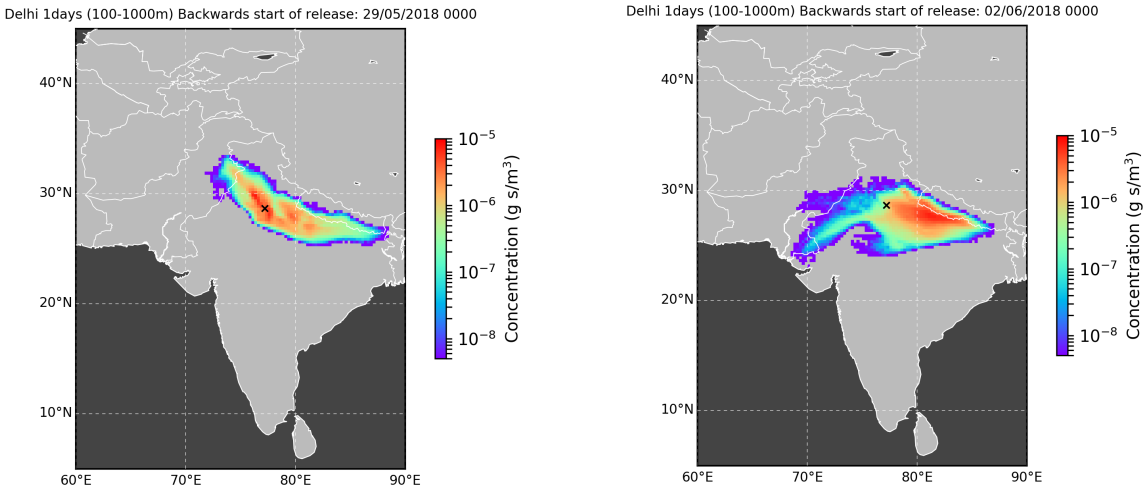

(a) 29/05 00:00 IST

(b) 02/06 00:00 IST

Figure 3.15: NAME 1 day backwards particle dispersion model from IGDTUW, Delhi at midnight on 28/05/18 and 02/06/18.

On the night of 30/05 into 31/05, the modelled air mass trajectory passed right through New Delhi, very close to the high traffic zone of Connaught Place (Figure 3.14). If this 1-hour trajectory is extended, the air mass passed close by the city of Gurgaon, South West of New Delhi, a city of high economic growth. The city is known as a technology hub in the north of India, with a large number of manufacturing sites including Maruti Suzuki, Nestlé, and Hero MotoCorp, who claim to own the world's largest two-wheel vehicle market, with over 50% share in the domestic motorcycle market (https://www.heromotocorp.com/en-in/about-us.php). The cause of the spike on 30th May 2018 may be due to emissions from manufacturing in Gurgoan, combined with emissions from across New Delhi picked up by the air mass before reaching the measurement site.

Due to a variety of issues in the lead up to the Delhi pre-monsoon campaign, there was a delay in instrument set-up, and only 9 days of data were collected. At first glance, the higher concentrations of NO, CO and many VOCs observed on the night of 28th - 29th May may be perceived as an exception during the pre-monsoon campaign, with observations after this night much lower in concentration. 1-hour HYSPLIT backwards trajectories were calculated from 23:30 IST on every night in May in which measurements were not made (1st - 27th May). Of these trajectories, two thirds suggested the air mass originated from a northern or north western direction. If we assume the north western sources were responsible for the high mixing ratios of anthropogenic species observed on the night of 29th May, then high mixing ratios of anthropogenic species throughout the month of May may have been frequent. This suggests the higher mixing ratios observed on 29th May could be representative of the mixing ratios present at the measurement site during the pre-monsoon period.

3.2.5 High concentrations of anthropogenic species, and the crop burning season

A significant proportion of pollutants in Delhi may be attributed to the seasonal burning of crop residues. High concentrations of all inorganic and organic anthropogenic pollutants were observed at the very beginning of the pre-monsoon campaign (27/05 - 30/05), and towards the end of the post-monsoon campaign (from 27/10). The post-monsoon campaign, and to some extent also the pre-monsoon campaign, coincided with the traditional crop residue burning season. In the more rural states surrounding Delhi, the old crop is burned to make space for the new crops to be planted in May and November. As a result, burning is expected in the preceding months. Fire maps for four days, two days in the pre-monsoon and two in the post-monsoon, are presented in Figure 3.16. The plots show the daily average fire spots, reported using data from the VIIRS (S-NPP & NOAA-20) satellite data.

At the very beginning of the pre-monsoon campaign (27/05), some fires are observed in a band across the states north of Delhi. The frequency of fires remains fairly constant, until 30th May when a reduction in the number of fires in the surrounding states is observed. By

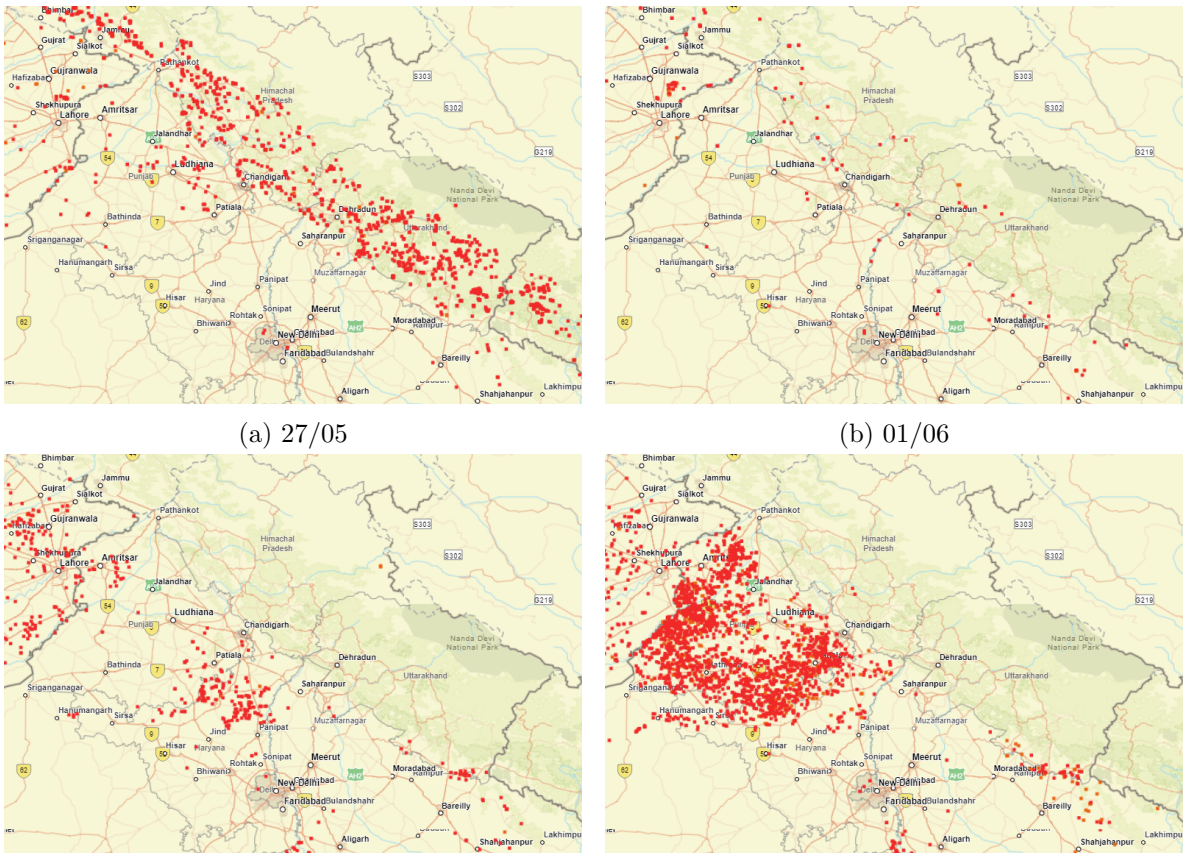

(a) 27/05 (b) 01/06

(c) 13/10 (d) 27/10

Figure 3.16: Fire maps showing fire hotspots, reported by NASA, using VIIRS (S-NPP & NOAA-20) satellite data. The fire hotspots are generated from daily averages on 27/05 (a), 01/06 (b), 13/10 (c), and 27/10 (d). Maps provided by NASA FIRMS, https://firms.modaps.eosdis.nasa.gov/.

June, very few fires are observed north of Delhi. This suggests that burning in the surrounding states may be the cause of the higher levels of pollutants observed at the start of the pre-monsoon campaign. In the post-monsoon, some fires are observed towards the start of the campaign. On 13/10, fires are observed to the north west of the state of Delhi. There are also a smaller proportion of fires to the west and south of the state. However, later in the month, fires become more prevalent. On 27/10 there is a large cluster of fires located to the north west of the measurement site. This coincides with an increase in pollutants.

An analysis of the NOAA HYSPLIT back trajectories during the post-monsoon campaign further supports that fires to the north and north west of the state of Delhi may be contributing to the high pollution levels. Between 8th and 27th October, 35% of daily, mid-day 24 hour back trajectories originated towards the south or east of the state of Delhi, whereas 65% originated from the north or west direction. As a result, potential fire sources in the north or north western direction of Delhi may be transported into the state. Figure 3.17 shows the back trajectories from 25th - 27th October, when elevated levels of pollutants, particularly NO and a broad range of anthropogenic VOCs, were observed.

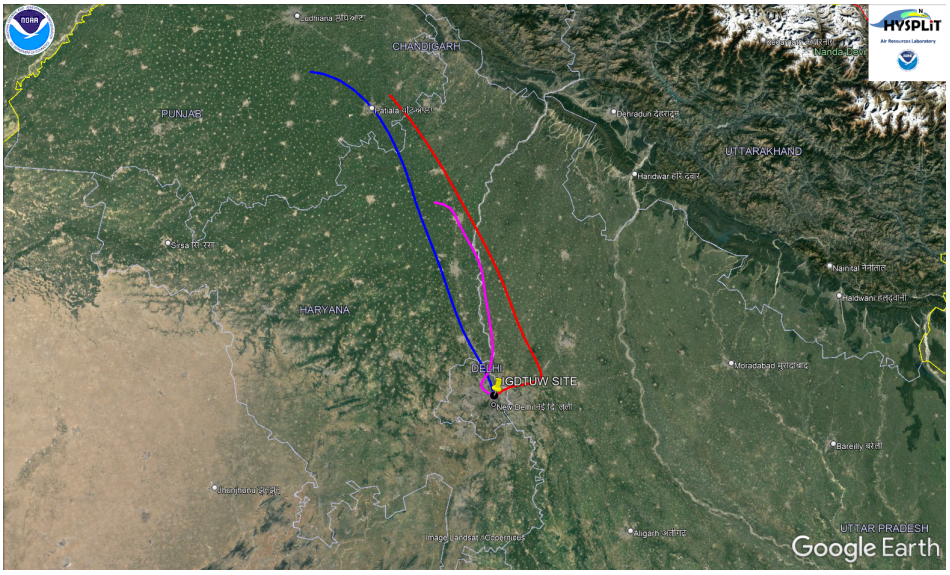

Figure 3.17: 24-hour NOAA HYSPLIT backward trajectories for Delhi from 12:00 IST on 25/10 (red), 27/10 (blue), 28/10 (pink).

3.3 Diel profiles of NO_x, CO, O_3 and selected VOCs

3.3.1 Inorganic diel profiles

The campaign averaged diel profiles for NO, NO_2, CO, O_3, SO_2 and HONO are presented in Figure 3.18. The pre-monsoon diel profiles presented here exclude data before 30/05, as the large concentrations of many VOC species observed on the night of 28/05 - 29/05 skewed the profile. Mean mixing ratios of NO, NO_2 and CO were generally higher in the post-monsoon than the pre-monsoon. The NO and CO post-monsoon profiles were dominated by high night-time mixing ratios peaking at $\approx$ 340 ppbV and 4 ppmV respectively. One possible explanation for these much higher values is emissions into a very shallow boundary layer in October 2018 (see section 1.2.4). Mean mid-day NO mixing ratios were $\approx$ 3 ppbV in both campaigns, and mean mid-day CO mixing ratios were $\approx$ 445 ppbV and $\approx$ 744 ppbV in the pre- and post-monsoon campaigns respectively. Night-time NO_2 mean mixing ratios were comparable in both the pre- and post-monsoon, with both profiles showing an increase in NO_2 from 14:00 into the late afternoon or evening. An additional morning peak was observed in the post-monsoon, where mean NO_2 mixing ratios doubled between 07:00 and 09:00. This can be explained by the rapid photolysis of high mixing ratios of HONO at sunrise, which initiates the O_3 production cycle, leading to the rapid conversion of NO and NO_2.

Mean O_3 mixing ratios peaked at $\approx$ 14:00 and 13:00 in the pre- and post-monsoon campaigns respectively. Mean daytime peak O_3 was 86 ppbV and 79 ppbV in the pre- and post-monsoon campaign periods respectively. Higher night-time O_3 mixing ratios were observed in the pre-monsoon compared to the post-monsoon, with an average O_3 mixing ratio at midnight of $\approx$ 30 ppbV in the pre-monsoon, and 6 ppbV in the post-monsoon. Night-time

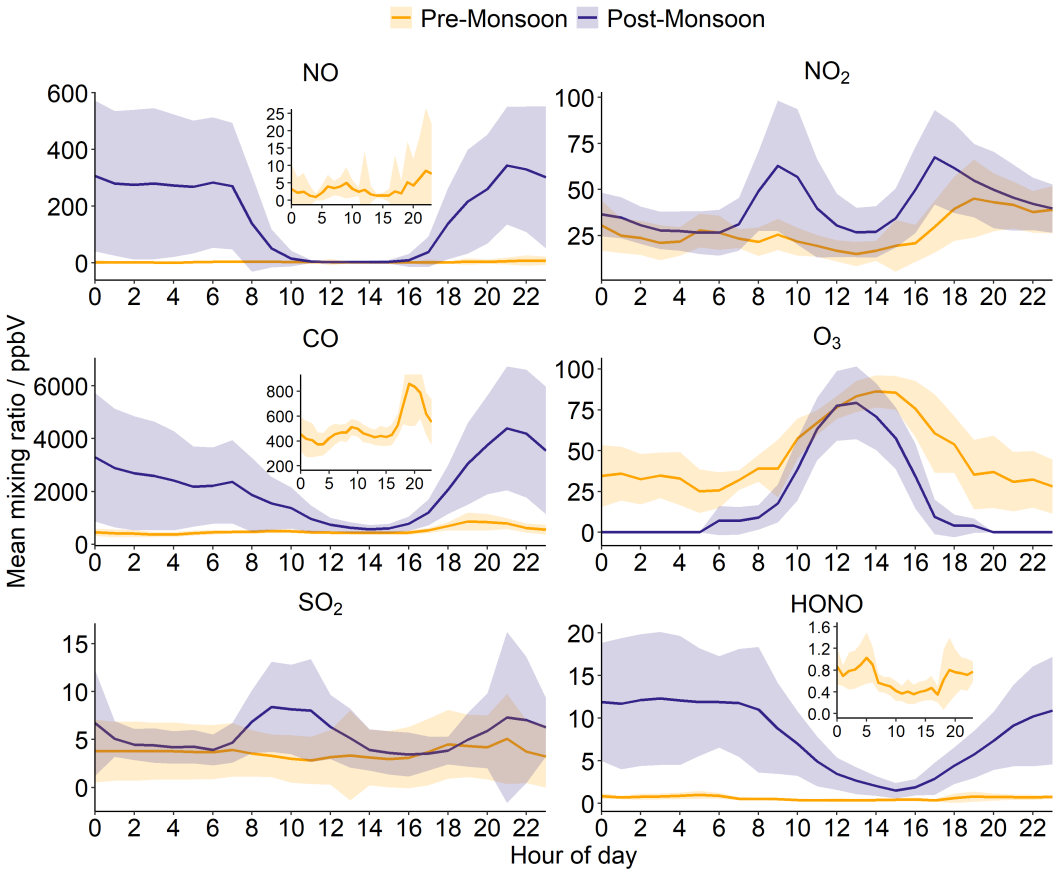

Figure 3.18: Mean mixing ratio diel profile of of NO, NO_2, CO and O_3 during pre-monsoon (yellow) and post-monsoon (purple). The shaded area represents one standard deviation from the mean.

O_3 mixing ratios may have been subject to interferences (see Chapter 2 for further details).

3.3.2 VOC diel profiles

A small selection of the measured VOC species are discussed in this section. Diel profiles of ethane, ethene, acetylene, benzene, ethanol and acetone are presented in Figure 3.19. Generally, mean mixing ratios of VOCs in the post-monsoon were lower during the day, and higher at night. This "U-shaped" profile was also observed in NO and CO mean mixing ratios (section 3.3.1), and may be a consequence of emissions into a shallow boundary layer (section 3.3.4). The diel profiles of alcohols, carbonyls and isoprene were the exception to this pattern. For isoprene, this may be explained by the biogenic nature of its source, discussed in more detail in section 3.3.3. In the post-monsoon, standard deviations from the mean were large at night for most VOCs, due to large variations night-time mixing ratios throughout the campaign. The pre-monsoon diel profiles presented here excluded data before 30/05, as the large concentrations of many VOC species observed on the night of 29/05 skewed the profile.

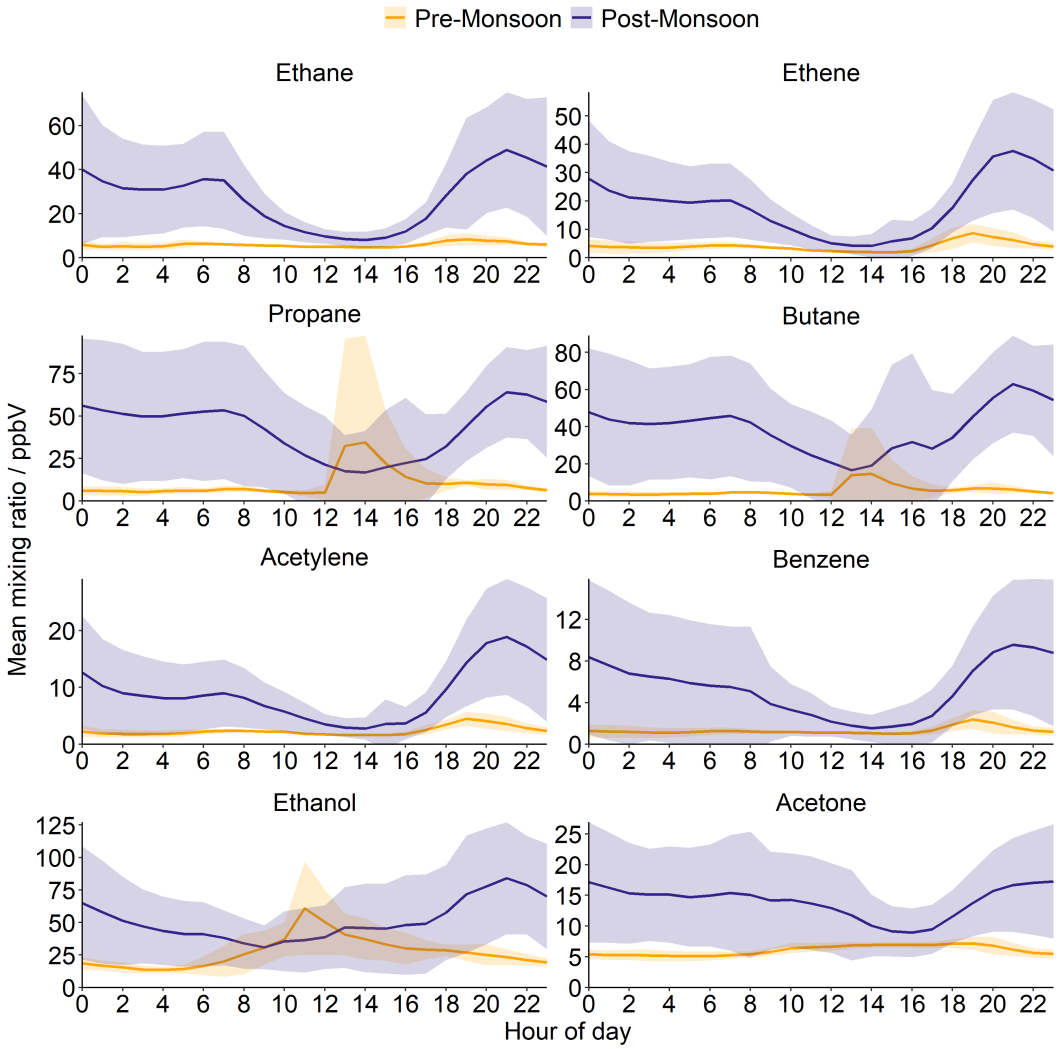

Figure 3.19: Mean mixing ratio diel profile of ethane, ethene, *n*-propane, *n*-butane, acetaldehyde, benzene, ethanol and acetone during pre-monsoon (yellow) and post-monsoon (purple). The shaded area represents one standard deviation from the mean.

Mid-day mean mixing ratios of ethane, ethene, acetylene, benzene were higher in the post-monsoon than the pre-monsoon campaign. In the post-monsoon, ethane, ethene, acetylene and benzene had a campaign averaged daytime minimum at 14:00 of 8.1 ppbV, 4.2 ppbV, 2.7 ppbV and 1.5 ppbV respectively. Acetone had a daily minimum at 16:00 of 8.9 ppbV and ethanol of 09:00 at 30.8 ppbV. Daily maximum values occured for all species in the evening, between 20:00 and 00:00, for these VOC species, with campaign averaged daytime maximum values for ethane, ethene, acetylene, benzene, ethanol and acetone of 48.9 ppbV, 37.6 ppbV, 18.9 ppbV, 9.6 ppbV, 84.1 ppbV and 17.3 ppbV respectively.

Pre-monsoon campaign averaged mixing ratios diel mixing ratios were lower than in the post-monsoon for ethane, ethene, acetylene, benzene and acetone. Daytime minimum mixing ratios of these species were 4.7 ppbV, 1.9 ppbV, 1.6 ppbV, 1.0 ppbV and 5.1 ppbV respectively. For ethane, ethene and acetylene, these minimums occur at 14:00 - 15:00. Minimums

for benzene and acetone occured at 21:00 and 05:00 respectively. The campaign maximum occured at 19:00 for ethane, ethene, acetylene, benzene and acetone at 8.3 ppbV, 8.7 ppbV, 4.5 ppbV, 2.4 ppbV and 7.2 ppbV respectively. Campaign averaged mixing ratios of ethanol were generally lower in the pre-monsoon than in the post-monsoon, except for during the hours of 09:00 - 13:00. Pre-monsoon ethanol mixing ratios peaked at 11:00 at 60.9 ppbV and were almost double that of the post-monsoon campaign averaged mixing ratio at 11:00.

Generally, during both campaigns, concentrations of anthropogenic VOCs were elevated at around 07:00 - 09:00, and again from 17:00. These two periods were mixing ratios were higher may indicate rush hour times in Delhi, when traffic and activity is increased as citizens are travelling to and from work. In the pre-monsoon, an reduction in mixing ratios is observed from around 19:00 onward. However, evening mixing ratios continue to increase well into the night in the post-monsoon, which is likely due to emissions of pollutants into an increasingly shallow boundary layer. The effect of the boundary layer height on pollutant concentrations is discussed in more detail in section 3.3.4.

In the pre-monsoon campaign, large spikes in propane and butane were observed around mid-day (Figure 3.19). In the post-monsoon, the afternoon increase in propane and butane occurs earlier than other anthropogenic VOC species, with mixing ratios beginning to increase after mid-day rather than from 17:00. One common source of propane and butane is LPG fuel. A recent report suggested that more than 70% of Indian households use LPG fuel as their primary cooking fuel [102]. The mid-day spike in these species could be attributed to the use of LPG in lunchtime cooking practices.

In the post-monsoon campaign, there was sufficient data coverage to assess the day to day variation on VOC concentrations (Figure 3.20). Generally, anthropogenic VOC concentrations were found to rise from Monday through to Thursday, before reducing to similar levels on Friday and Saturday. For all anthropogenic VOCs, there was a distinct drop in emissions on Sunday. In India, a six-day working week is standard (Monday - Saturday), with some occupations working a five-day week (Monday - Friday) [103]. The reduction in VOC concentrations on Sundays may be explained by a reduction in industrial processes, and vehicular use due to the day traditionally being taken as a non-working day.

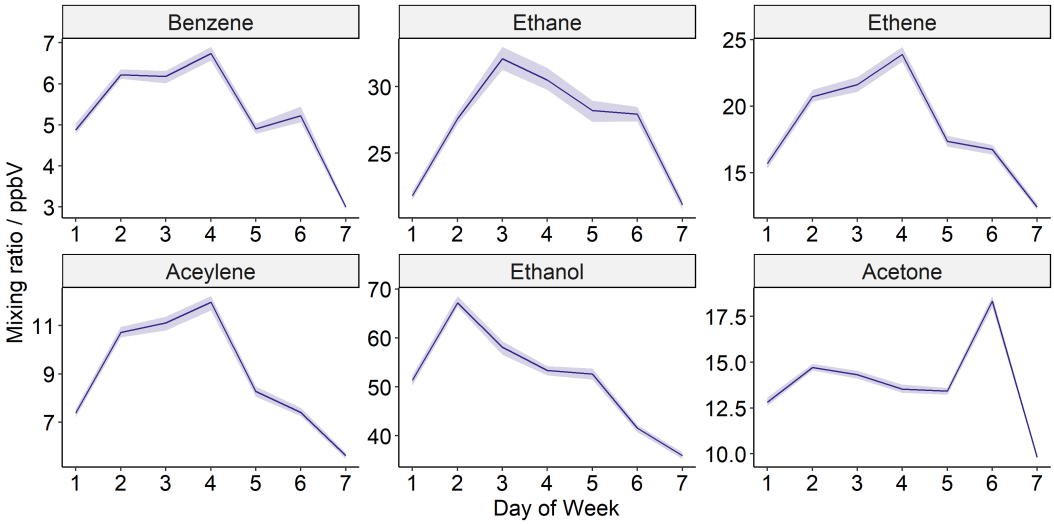

Figure 3.20: Post-monsoon day-to-day variation in the mean mixing ratios of a range of VOCs, where day 1 = Monday and day 7 = Sunday. The shaded region represents a 95% confidence interval in the mean, calculated through bootstrap re-sampling under the hood of the R Openair package.

3.3.3 The anthropogenic nature of traditionally biogenic VOCs

The isoprene diel profile was different from the profile of other observed VOCs during the post-monsoon campaign (Figure 3.21). In both the pre- and post-monsoon campaigns, isoprene was lower at night and higher in the day. In the pre-monsoon campaign, the diel profile of isoprene was consistent with a biogenic source whereby sunlight stimulates foliage to produce isoprene. As photochemical activity peaks at mid-day, isoprene emissions were highest at this time. Biogenic emissions of isoprene were low during the night-time due to a lack of sunlight leading to no photochemical activity. The post-monsoon campaign had a different diel profile. Although it was lower at night, and peaked around mid-day, night-time mean mixing ratios were approximately double those observed in the pre-monsoon. These sustained night-time mixing ratios suggest another, anthropogenic source may have been increasing isoprene levels. In the post-monsoon campaign, particularly towards the end of the measurement period, isoprene lost its strong biogenic diurnal profile (Figure 3.22a). This further suggests anthropogenic sources may have been an important isoprene source during the post-monsoon.

Total monoterpenes mean mixing ratios were much higher in the post-monsoon than the pre-monsoon despite lower temperatures, with mid-day mixing ratios 10 times larger in the post-monsoon than the pre-monsoon (Figure 3.21). Like most other VOCs, monoterpenes were higher at night-time and lower in the day, with a profile similar to that of the anthropogenic VOC 1,3-butadiene. This is surprising, as monoterpenes are commonly considered to come from biogenic sources, and the profile is expected to look more like isoprene, peaking in the day and lower at night. The post-monsoon monoterpene profile was more "U-shaped", like the anthropogenic species presented in Figure 3.19. The high night-time mixing ratios

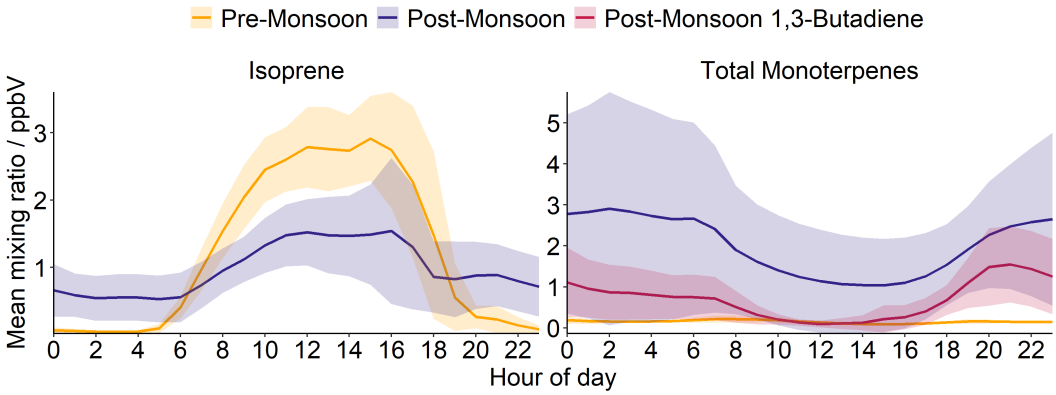

Figure 3.21: Mean mixing ratio diel profile of isoprene and the sum of all monoterpenes during pre-monsoon (yellow) and post-monsoon (purple). The shaded area represents one standard deviation from the mean. Post-monsoon 1,3-butadiene mean mixing ratios are presented along side total monoterpenes as an anthropogenic tracer species (red).

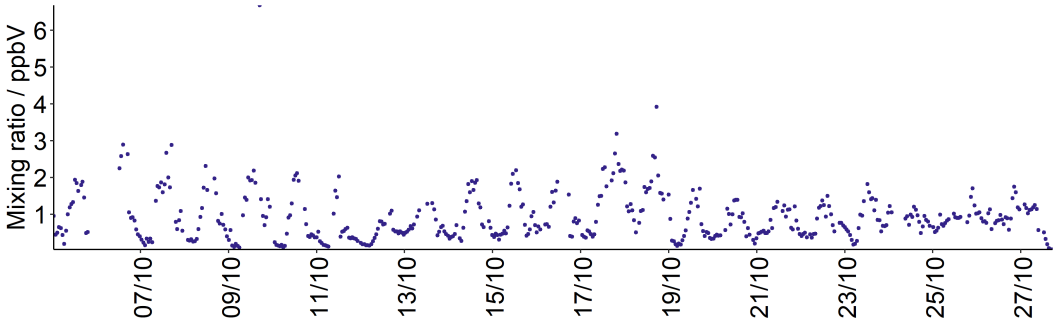

(a) Isoprene

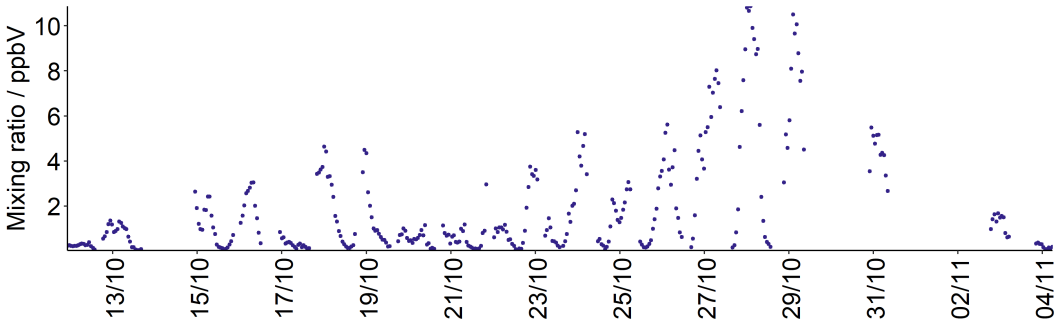

(b) Total monoterpenes

Figure 3.22: Mixing ratio timeseries for isoprene (a) and the sum of all monoterpenes (b) during the post-monsoon campaign.

of monoterpenes in the post-monsoon suggest anthropogenic sources were contributing to the observed mixing ratio. The monoterpene profile is consistent throughout the campaign, peaking in the night and lower during the day (Figure 3.23). The diel profile for monoterpenes in the pre-monsoon was similar to that of alkenes, peaking in the mid-morning and evening (Figure 3.4). This suggests there could also have been an anthropogenic charac-

ter to the monoterpenes in the pre-monsoon campaign. Figure 3.24 presents the correlations between isoprene, total monoterpenes, and two well known anthropogenic species, CO and 1,3-butadiene. In the pre-monsoon, monoterpenes are moderately anti-correlated with isoprene, suggesting the sources of monoterpenes are different to those of the biogenic VOC, isoprene. However, there is a moderately strong correlation between monoterpenes and 1,3-butadiene, which is known to be emitted from vehicle exhausts, and the manufacturing industry [104]. The correlation between total monoterpenes and CO is weak, suggesting that if 1,3-butadiene and total monoterpenes share a source, it is unlikely to be from vehicular emissions. In the post-monsoon, strong correlations between total monoterpenes, and both 1,3-butadiene and CO are observed. In contrast, there is a very week correlation between these three species and isoprene. This further supports that the source of monoterpenes may be of an anthropogenic nature. As vehicular emissions are unlikely to be seasonal, perhaps there is another seasonal source linking the emissions of monoterpenes, 1,3-butadiene and CO in the post-monsoon period, such as crop residue burning.

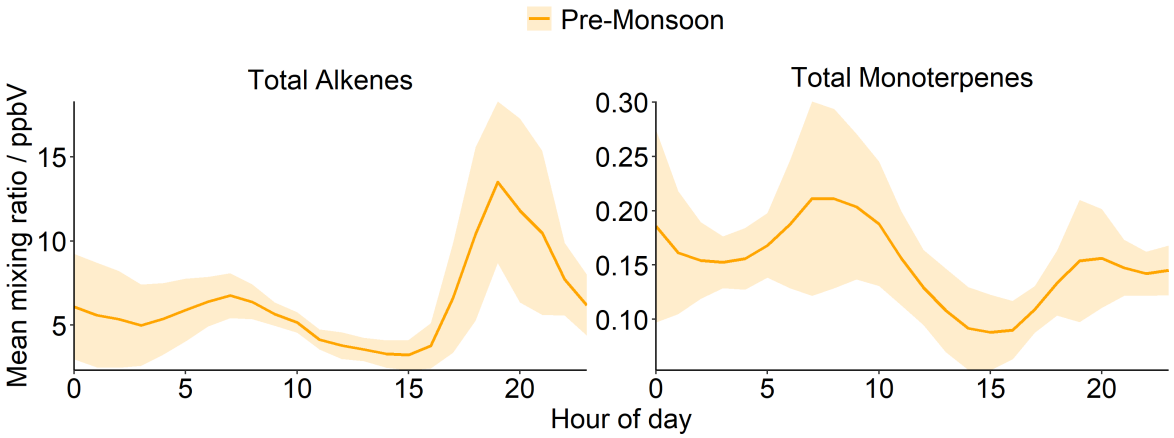

Figure 3.23: Mean mixing ratio diel profile of the sum of alkenes and the sum of all monoterpenes during pre-monsoon (yellow). The shaded area represents one standard deviation from the mean.

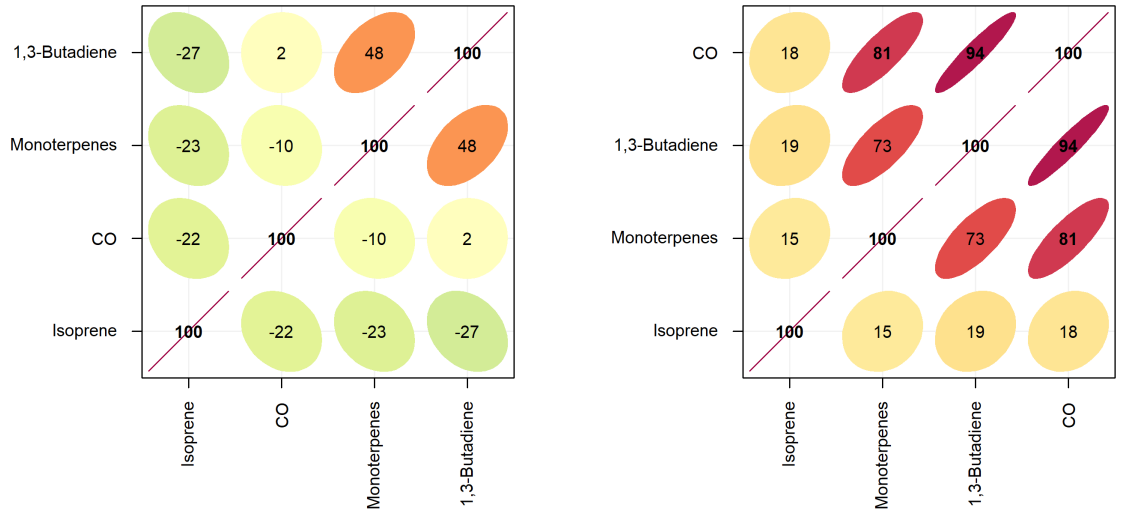

(a) Pre-Monsoon (b) Post-Monsoon

Figure 3.24: Correlation plot comparing the observed mixing ratios of isoprene, CO, total monoterpenes, and 1,3-butadiene during the pre-monsoon (a) and post-monsoon (b) campaigns. A high number is given to species that are well correlated, up to a maximum value of 100. Negative numbers are indicative of anti-correlation.

3.3.4 The effect of Boundary Layer Height on night-time observations

As we have seen in sections 3.2.1 and 3.2.2, the post-monsoon diel profile of NO, CO and the majority of observed VOCs was high during the night, and low during the day. This may have been a consequence of a much lower night-time boundary layer height in the post-monsoon compared to the pre-monsoon (Figure 3.25). Boundary layer height data was downloaded for coordinates Lat. 28.625, Lon. 77.25 from the European Centre for Medium-Range Weather Forecasts at 0.25 degree resolution with, and with a 1 hour temporal resolution (ERA5). Night-time boundary layer heights were $\approx$ 8 times lower in the post-monsoon than the pre-monsoon, with a mean height of 46 m. This may have led to the concentrating of pollutants into a shallow boundary layer. This is further supported by Figure 3.26, in which the variation in NO and CO have been plotted with respect to changing boundary layer height. The very highest mixing ratios of both species were found to occur when the boundary layer height was $<$ 50 m.

As discussed earlier in Chapter 2, 0 ppbV of O_3 was expected at night due to very high NO concentrations. As boundary layer height decreases in the afternoon, NO concentrations began to rise (Figure 3.27a). The boundary layer height reached a stable minimum at around 18:00, and NO continued to rapidly increase due to emissions into a shallow boundary layer. NO mixing ratios remained high with a very minimal decrease in concentrations throughout the night, until the boundary layer height began to rise in the morning (Figure 3.27a). This further suggests a lack of night-time chemistry occurring in the atmosphere, and further sup-

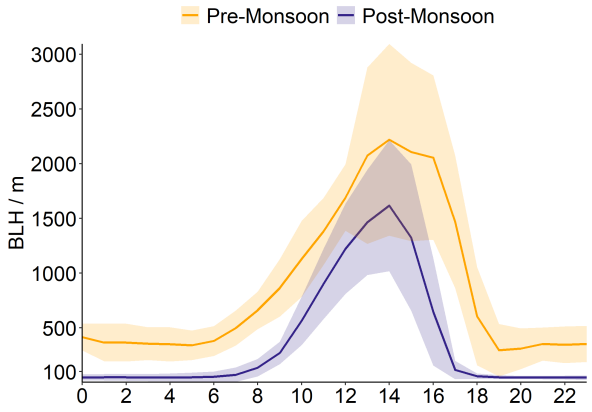

Figure 3.25: Mean boundary layer height (BLH) during the pre- (yellow) and post-monsoon (b) campaigns. The shaded ribbon represents one standard deviation of the mean.

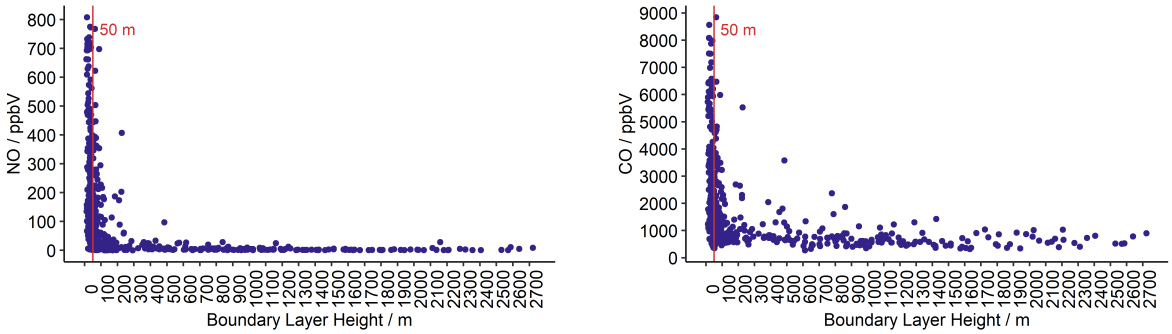

(a) Pre-Monsoon (b) Post-Monsoon

Figure 3.26: The variation of post-monsoon NO (a) and CO (b) mixing ratios at different boundary layer heights. The red line indicates a boundary layer height of 50 m.

ports our assumption that no O_3 was present at night. A small decrease in NO was observed earlier during the night. This may have been a result of NO reacting with the residual O_3 remaining from the daytime. A similar trend was observed with the majority of observed VOC species, where night-time concentrations remained high (Figure 3.27b).

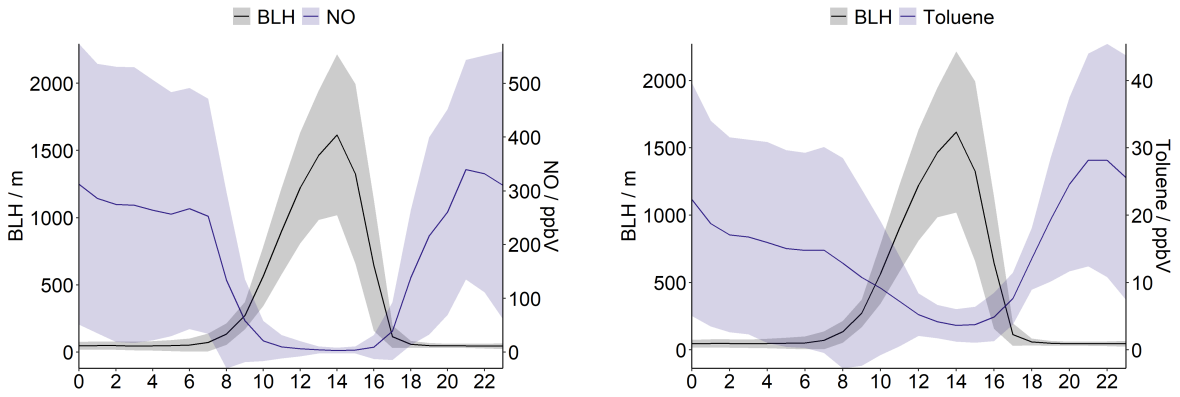

(a) NO (b) Toluene

Figure 3.27: Diel profile of NO (a) and toluene (b), along with BLH during the post-monsoon campaign.

3.3.5 Comparison with Beijing, China

The city of Beijing is an example of an Asian megacity which has undergone many recent policy changes, with the goal of reducing air pollution. However, although ambient NO_x has fallen over the past decade, concentrations of tropospheric O_3 have increased across China [105, 106]. With this in mind, it is interesting to compare the pollutant concentrations of an Asian megacity with a more developed pollution abatement strategy (Beijing), with the observational dataset from Delhi. In particular, a comparison of VOCs and NO_x, the precursor species to tropospheric O_3 formation, may highlight the differences in concentration and sources of highly reactive species between the two cities. This section compares the Delhi pre-monsoon observational dataset to data from the Beijing APHH summer campaign. The relative magnitudes and diel profiles of inorganic species and VOCs, during the same month of the year in Delhi and Beijing, are compared. Measurements made in May-June 2018 as part of the Delhi pre-monsoon campaign are compared and contrasted to a May 2017 measurement campaign in Beijing, China.

Inorganic species

Campaign averaged NO mixing ratios were marginally higher during the Delhi pre-monsoon campaign than the Beijing summer campaign. Mid-day average mixing ratios for Delhi pre-monsoon and Beijing summer were 3.1 ppbV and 0.8 ppbV respectively. The very low NO mixing ratios observed in Beijing reflect a switching of local chemistry due to the transportation of O_3 into urbanised areas. Transported O_3 titrates NO to NO_2 within urban areas, leading to low-NO. This is likely to be observed across a range of highly populated subtropical conurbations of megacities in South East Asia. A detailed analysis of the implications of this low NO is described in Newland et al., 2021 [107]. The study discusses the

significant formation of gas and aerosol phase oxidation products associated with the low-NO "rainforest-like" regime during the afternoon. NO mixing ratios were higher in the Delhi pre-monsoon, suggesting high-NO oxidation pathways dominate. Evening mixing ratios of NO were marginally higher in the Delhi pre-monsoon than the Beijing summer campaign until midnight. Between midnight and 06:00, NO mixing ratios were higher in Beijing than pre-monsoon Delhi, peaking at 15.1 ppbV at 02:00. Campaign averaged Delhi pre-monsoon NO mixing ratios were in the range of 0.9 - 3.9 ppbV between 00:00 - 06:00. The NO diel peaks in the Delhi pre-monsoon campaign at 8.9 ppbV at 22:00.

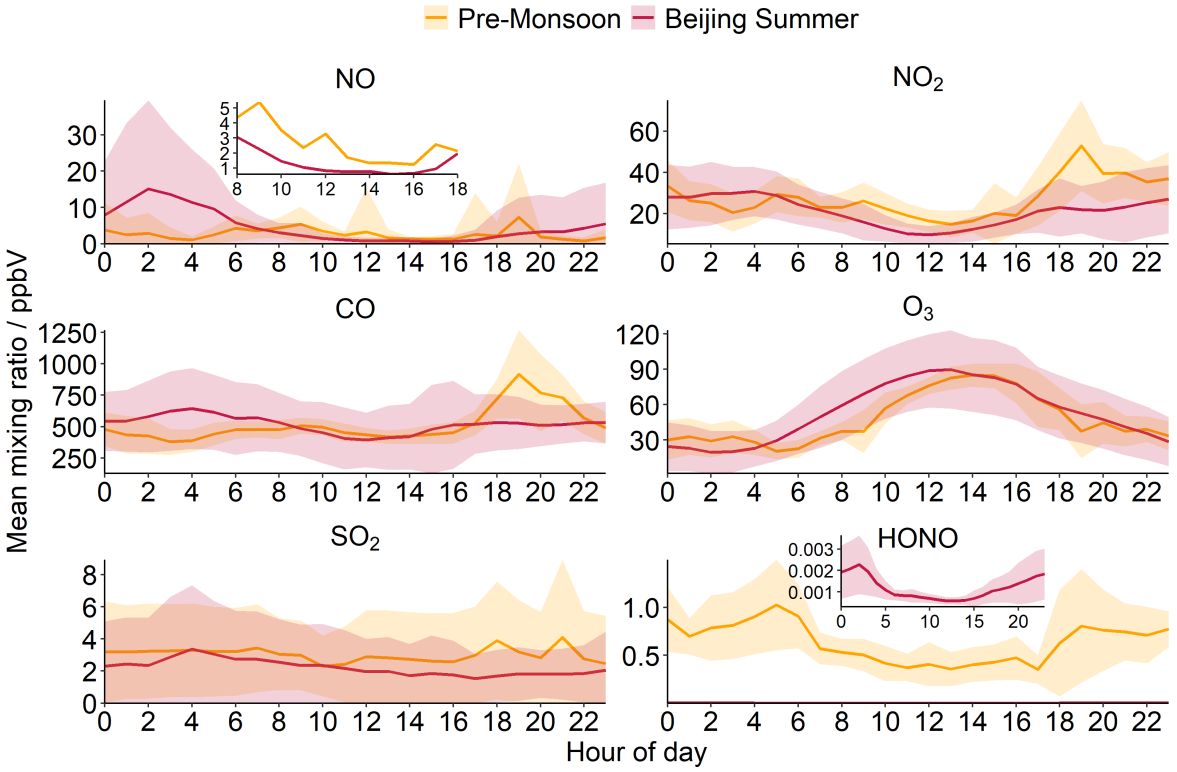

Figure 3.28: Mean mixing ratio diel profile of NO, NO_2, CO, O_3, SO_2 and HONO during pre-monsoon (yellow) and during a summer campaign in Beijing, 2017 (red). The shaded area represents one standard deviation from the mean.

CO mixing ratios were also similar in both Delhi pre-monsoon and Beijing summer, with mid-day average mixing ratios of 445 ppbV and 394 ppbV respectively. Delhi pre-monsoon campaign averaged CO peaked at ≈ 866 ppbV at 19:00, and peaked at ≈ 644 ppbV at 04:00 during the Beijing summer campaign. There were some differences in the diel profile shape, with higher CO observed in the early hours of the morning in Beijing, and during the evening in Delhi. However, it is worth noting the Delhi pre-monsoon diel profiles could be representing an underestimation of the magnitude of species in the pre-monsoon period. Much larger mixing ratios of CO and NO were observed on the first campaign day, which was removed from this diel analysis (see section 3.2.4 for more details). The Delhi pre-monsoon campaign averaged mixing ratios of NO_2 were similar to values observed in the summer

Beijing campaign. Observed values were marginally higher than summer Beijing between 08:00 - 00:00, but were higher in Beijing in the early hours of the morning. NO_2 peaked in pre-monsoon Delhi at 19:00 at 50.7 ppbV, and in the summer Beijing campaign at 04:00 at 30.7 ppbV. O_3 mixing ratios were similar between the two campaigns, with O_3 peaking a few hours earlier in the day in the Beijing summer campaign compared to the Delhi pre-monsoon campaign. Campaign averaged O_3 mixing ratios from the two campaigns were remarkably similar, peaking at 86.4 ppbV at 14:00 in the Delhi pre-monsoon, and 89.9 ppbV at 13:00 in the Beijing summer campaign. SO_2 campaign averaged mixing ratios were higher in the Delhi pre-monsoon than the Beijing summer campaign. There was very little daytime fluctuation in either campaign, with the median of the campaign averaged diels around 3.6 ppbV and 2.1 ppbV during the Delhi pre-monsoon and the Beijing summer campaigns respectively. Campaign averaged HONO mixing ratios were much larger in the Delhi pre-monsoon than the Beijing summer campaign, peaking at ≈ 1 ppbV at 05:00, compared to a Beijing summer peak of ≈ 0.002 ppbV at 02:00. Higher HONO mixing ratios were observed in the Delhi post-monsoon, as was discussed in section 3.3.1.

VOCs

VOC mean mixing ratios were generally higher in pre-monsoon Delhi than the Beijing summer campaign, particularly during the late afternoon and into the evening (Figure 3.29). Isoprene concentrations were higher in the pre-monsoon Delhi campaign than the Beijing summer campaign in the day, but lower at night. In the Delhi pre-monsoon, isoprene concentrations were ≈ 0 ppbV at night, and increased to ≈ 3 ppbV at mid-day before dropping toward the evening. As discussed earlier, this is consistent with a more biogenic profile (section 3.3.3). However, mean isoprene concentrations during the Beijing summer remained high (≈ 0.5 ppbV) at night relative to the mean peak daytime mixing ratio (≈ 1 ppbV). This suggests there could have been an anthropogenic source of isoprene in Beijing, as was observed during the Delhi post-monsoon campaign (section 3.3.3).

Peak mean toluene mixing ratios were more than 3 times larger in the Delhi pre-monsoon campaign than the Beijing summer campaign, and peak *n*-octane concentrations were more than double. Peak *n*-propane levels were approximately 5 times higher. Since VOC concentrations were much higher in Delhi, and urban environments are generally VOC-limited in terms of O_3 production, higher levels of O_3 would be expected in Delhi compared to Beijing. However, mean O_3 in both these cities was similar (Figure 3.28). The reason for this is perhaps due to the time of day VOCs are at their highest in Delhi. VOC concentrations in Delhi generally peaked later in the afternoon and into the evening when photochemical activity is lower, meaning O_3 mixing ratios were not elevated compared to Beijing.

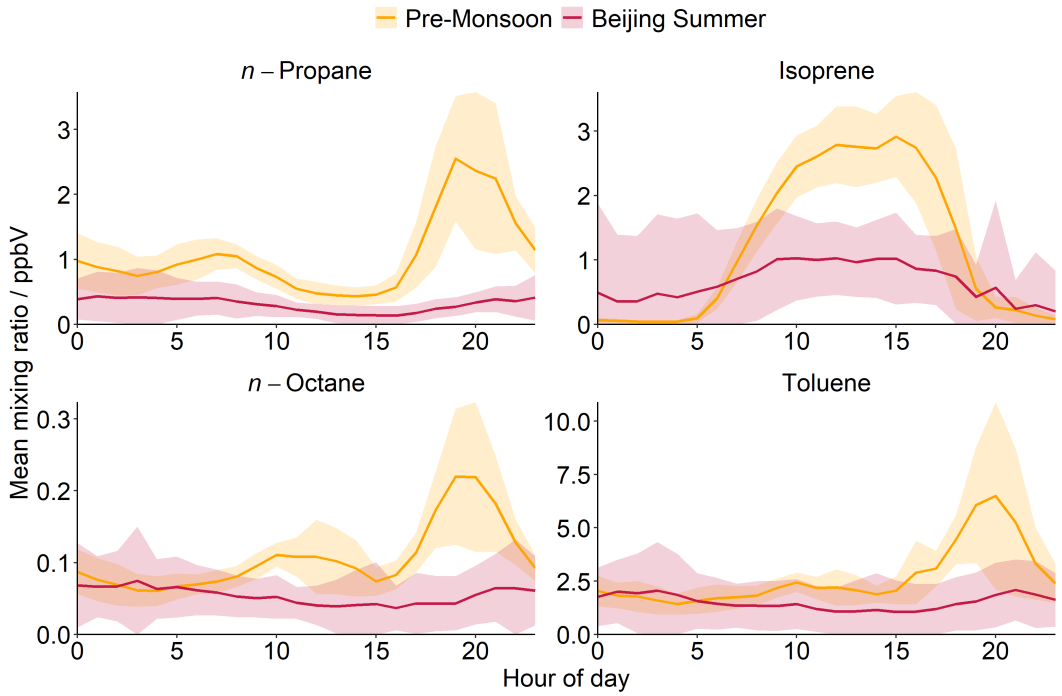

Figure 3.29: Mean mixing ratio diel profile of of n-propane, isoprene, n-octane and toluene during pre-monsoon (yellow) and during a summer campaign in Beijing, 2017 (red). The shaded area represents one standard deviation from the mean.

3.4 Summarised comparison of observations made during Delhi pre-monsoon and post-monsoon campaigns

Much larger concentrations of anthropogenic organic and inorganic species were observed in the post-monsoon compared to the pre-monsoon campaign. In the post-monsoon campaign, concentrations were particularly elevated into the evening, and overnight from around 17:00 onward. This increase coincided with a sharp reduction in boundary layer height (BLH), with BLH decreasing to night-time mean of 46 m in the post-monsoon, 8 times lower than the mean night-time BLH observed in the pre-monsoon campaign. Based on these findings, I suggest that the combination of emissions from evening activities, starting from rush hour, and a very shallow night-time boundary layer, has had the effect of concentrating the pollutants at surface-level.

Although stark differences in pollutant concentrations have been observed between the pre-monsoon and post-monsoon campaigns, the key sources of anthropogenic emissions in and around the city of New Delhi are not seasonal. Large pollutant emissions are expected from traffic on the National Highway 44, with Chandni Chowk market and the crematorium also being potential sources. However, the burning of crop residue is prevalent in the states surrounding Delhi, and this is a particularly common practice during the months of April and October. High concentrations of pollutants were observed at the very beginning of the

pre-monsoon campaign (late May), so it is possible higher mixing ratios observed at the start of the campaign were capturing the back end of this seasonal burning. However, subtle burning was prevalent throughout the month of October, which may have contributed to elevated levels of pollutants in the post-monsoon campaign. This is corroborated by a high frequency of fire hotspots in the states to the north west of Delhi, along with a high frequency of winds originating from the north west, particularly prevalent towards the end of the post-monsoon campaign.

In addition to the higher concentrations of VOCs observed in the post-monsoon, concentrations of o-VOCs were also elevated, especially at night. I hypothesise that this was also due the emission or secondary chemical production of these species, coinciding with a shallow boundary layer at night. During the post-monsoon campaign, sunrise occured an hour later, and sunset and hour earlier, than during the pre-monsoon campaign. This, coupled with reduced peak photolysis rates in October, led to a reduction in carbonyl photolysis. This resulted in the mixing ratios of carbonyls, such as formaldehyde, remaining high overnight until the late morning.

Taking the meteorology into consideration, wind speeds were much lower in the post-monsoon campaign compared to the pre-monsoon campaign. This suggests that the increased concentrations in the post-monsoon campaign may be attributed to local emissions. Every year, the pollution in the city of New Delhi is elevated in line with the crop burning season. However, the low wind speeds observed during the post-monsoon campaign suggest that the contribution to pollution from crop residue burning is likely to be that of longer lived species, such as CO. Whilst I was taking measurements at the field site, I reported on my own observations of the weather conditions. During the pre-monsoon campaign, light levels felt higher, and days felt slightly longer than in the post-monsoon campaign. However, in both campaigns the air felt noticeably polluted, and it was incredibly difficult to distinguish clouds by eye, and thus comment on cloud cover. Based on my analysis, and experience, I conclude that high levels of pollution were observed in Delhi during both campaigns, but particularly during the post-monsoon campaign. There is some evidence to suggest this is linked to the seasonal burning of crop residue, but the stagnant conditions and shallow night-time boundary layer do nothing to help the pollution problem.

3.5 Photostationary Steady State

In a polluted environment devoid of local sources of NO_x, reactions leading to the formation of tropospheric O_3 are thought to be in dynamic equilibrium (reactions 3.1 - 3.3). NO_2 is photolysed, forming NO along with atomic oxygen. This oxygen atom reacts rapidly with molecular oxygen, forming O_3, which then reacts with NO to re-form NO_2.

$$NO_2 + h\nu \longrightarrow NO + O(^3P) \quad (\lambda < 420 \text{ nm}) \tag{3.1}$$

$$O(^3P) + O_2 + M \longrightarrow O_3 + M \tag{3.2}$$

$$O_3 + NO \longrightarrow NO_2 + O_2 \tag{3.3}$$

Through reactions 3.1 to 3.3, there is no net formation of O_3, and ambient NO, NO_2 and O_3 are expected to be in steady state. This photochemical steady state, or photostationary state, can be defined as in equation 3.4, where $k_{3.3}$ = the rate constant of reaction 3.3 (1.8×10^{-14} cm^3 molecule^{-1} s^{-1} at 298 K, [108]).

$$\phi = \frac{j(NO_2)[NO_2]}{k_{3.3}[NO][O_3]} \tag{3.4}$$

The Leighton relationship was used to determine the concentration of tropospheric O_3 in areas polluted by nitrogen oxides [43]. If all NO oxidation occurs via reaction 3.3, with O_3 as the sole oxidant of NO, then $\phi = 1$. Competing oxidants, such as RO_2 and HO_2, are formed from OH-initiated oxidation of hydrocarbons. RO_2 and HO_2 may also form from ozonolysis, hydrocarbon reactions with NO_3, carbonyl photolysis, and peroxyacyl nitrate (PAN) decomposition. The H-abstraction of hydrocarbons can also be initiated by halogen radicals, such as Cl. Additional oxidants compete with O_3 in reaction 3.3, and the only chemical source of O_3 in the troposphere is the perturbation of this photostationary state through the oxidation of NO with non-O_3 oxidants. When NO > 1 ppbV, the OH-initiated oxidation of hydrocarbons and CO is suppressed by a competing reaction of OH with NO_2, forming nitric acid (HNO_3), which terminates the OH radical and NO_2 species crucial for O_3 formation [44]. HNO_3 is readily removed from the atmosphere through deposition processes, making this route a net sink for radicals.

The oxidation of NO by peroxy radicals HO_2 and RO_2 is defined in reactions 3.5 and 3.6 respectively.

$$HO_2 + NO \longrightarrow OH + NO_2 \tag{3.5}$$

$$RO_2 + NO \longrightarrow RO + NO_2 \tag{3.6}$$

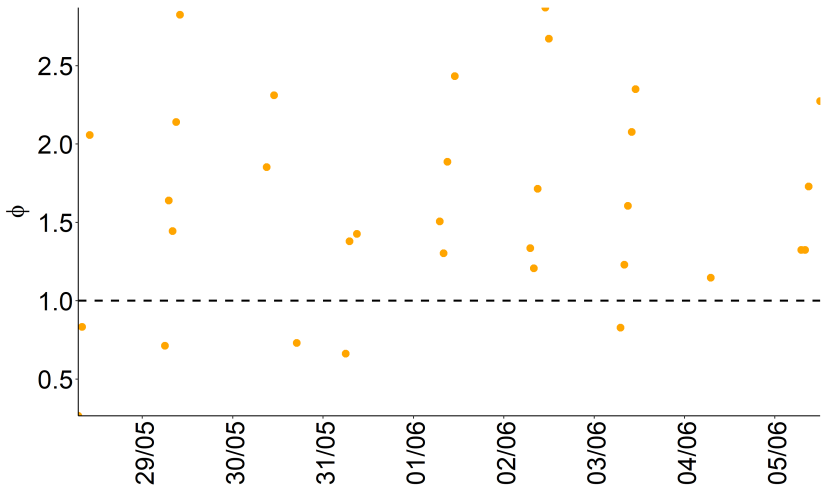

(a) Pre-Monsoon

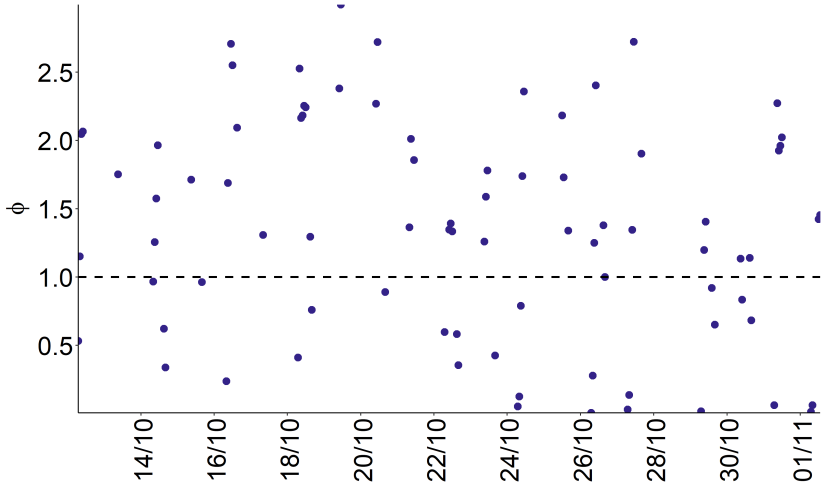

(b) Post-Monsoon

Figure 3.30: Hourly averaged ϕ during the pre-monsoon (yellow) and post-monsoon (purple). The dashed black line represents $\phi = 1$.

If we assume all NO oxidation occurs through O_3, HO_2 and RO_2 reactions (3.3, 3.5, 3.6), equation 3.4 can be re-written to include these oxidative processes (equation 3.7).

$$\frac{[NO_2]}{[NO]} = \frac{k_{3.3}\,[O_3] + k_{3.5}\,[HO_2] + \sum_i k_{3.6_i}\,[RO_{2i}]}{j(NO_2)} \tag{3.7}$$

Since $k_{3.5} \approx k_{3.6}$, equation 3.7 can be simplified to equation 3.8, allowing for the calculation of the peroxy radical concentration required to achieve the calculated value of $\phi = 1$, for photostationary steady state to be achieved.

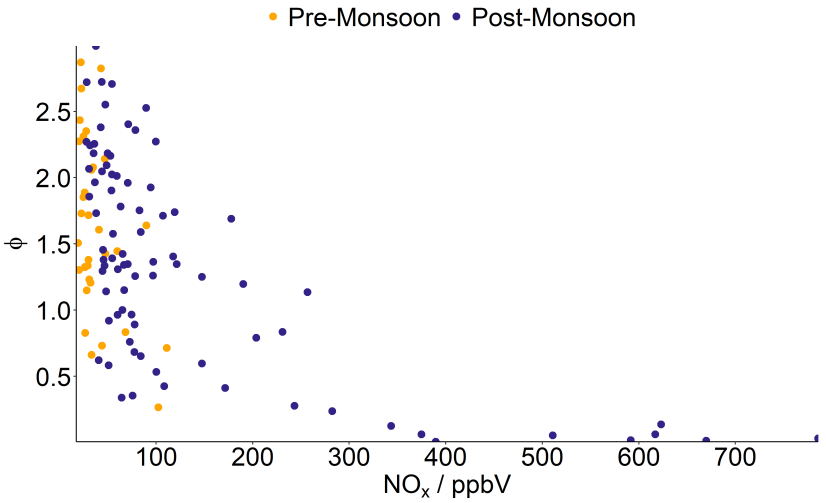

Figure 3.31: ϕ as a function of NO_x mixing ratios during pre-monsoon (yellow) and post-monsoon (purple).

$$[HO_2] + [RO_2] = (\phi - 1)\,\frac{k_{3.3}\,[O_3]}{k_{3.6}} \tag{3.8}$$

As Delhi is a highly polluted megacity with high levels of NO_2, we expect photostationary steady state to be achieved rapidly [44]. During the pre-monsoon campaign, ϕ varied within the range of 0.42 - 2.63. In the post-monsoon, ϕ ranged from 0.005 - 3.76. In both pre- and post- monsoon campaigns, ϕ was generally > 1, suggesting other oxidants aside from O_3 were rapidly converting NO to NO_2. In both campaigns, ϕ was regularly below unity. One possible causes of this is local emissions of NO_x perturbing the photostationary steady state [109]. This is supported by the very low values of ϕ present in the post-monsoon period occurring at times of very high NO_x (Figure 3.31). Possible sources of local NO_x include traffic from the main roads and highways close-by to the measurement site. Negative deviations from ϕ were also observed during a similar campaign in Beijing, which took place in winter 2016 (November - December), and were attributed to high NO_x from traffic sources. In comparison, mainly positive deviations from ϕ were observed during the Beijing summer 2017 campaign (May - June), with the largest deviations occurring when NO_x mixing ratios were low [68].

For periods were $\phi > 1$, the median and mean calculated RO_x ($[HO_2]$ + $[RO_2]$) during the pre-monsoon campaign were 1.7 $\times$ 10^9 molecule cm^{-3} and 2.4 $\times$ 10^9 molecule cm^{-3} respectively. For the post-monsoon, median and mean RO_x were 1.3 $\times$ 10^9 molecule cm^{-3} and 1.9 $\times$ 10^9 molecule cm^{-3} respectively (Figure 3.32). These values were lower than the RO_x concentrations calculated in a study of the photostationary state in summertime Beijing, China [68]. The values calculated here will be compared to modelled concentrations in section 3.6.

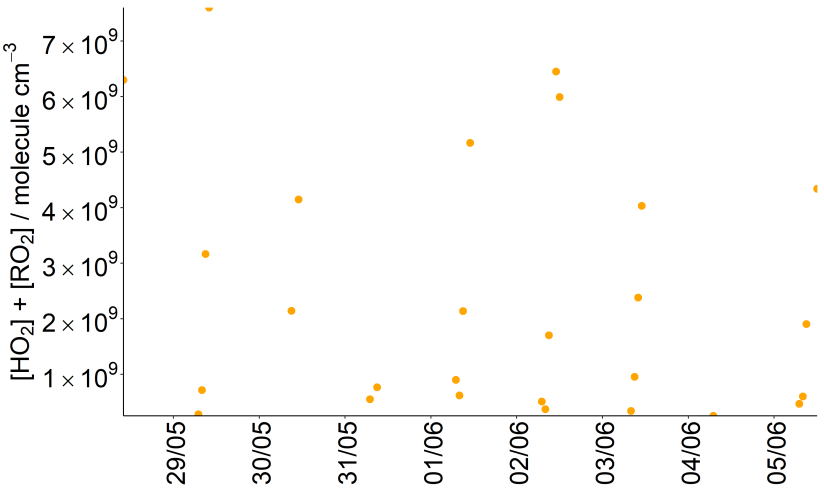

(a) Pre-Monsoon

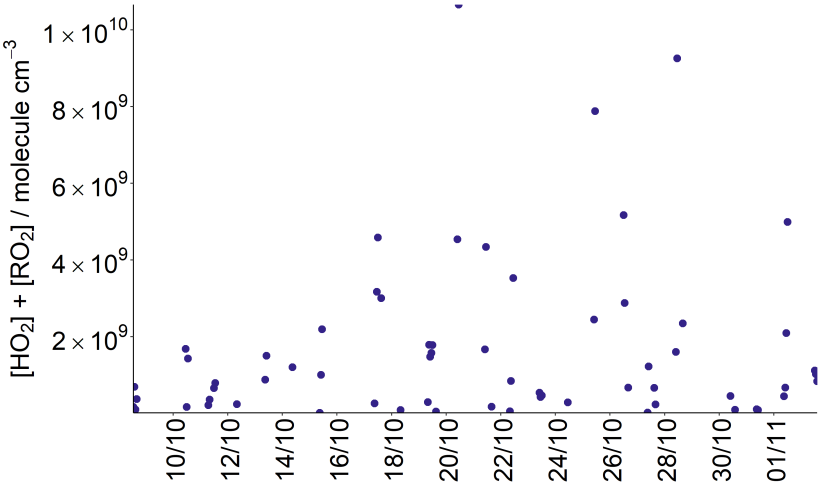

(b) Post-Monsoon

Figure 3.32: Calculated $[HO_2] + [RO_2]$ from photostationary steady state analysis of ambient NO, NO_2, O_3 and $j(NO_2)$ measurements.

3.6 Modelling OH, HO_2 and RO_2

To further understand the chemical processing occurring in Delhi's atmosphere, a campaign tailored chemical box model was developed utilising AtChem2 and the Master Chemical Mechanism (MCM), as described earlier in Chapter 1. OH, HO_2 and RO_2 are the mediating species leading to tropospheric O_3 formation in urban environments. As these species are short lived, having a lifetimes on the order of a few seconds, their concentrations can be calculated using the local concentrations of longer lived species. The low atmospheric lifetimes of radical species means their transport from/to the local environment is negligible.

A zero-dimensional box model was constrained to measurements from both the pre- and post-monsoon campaigns. The models were constrained to observations of NO, NO_2, O_3, CO, VOCs, HONO, photolysis rates, temperature and relative humidity. An extended range of VOCs that are not present in the MCM were added to the mechanism, using proxy species and rate constants from the IUPAC kinetic database, as described in Chapter 4, Table 4.2.3. As CH_4 was not measured during either campaigns, a fixed value of 4.9×10^{13} molecule cm^{-3} was used, in line with global average methane concentrations [110]. A fixed HO_2 uptake coefficient was applied where appropriate ($\gamma_{HO_2} = 0.2$), as defined in Jacob, 2000 [111]. The modelled OH, HO_2 and RO_2 concentration time series are presented in Figure 3.33.

3.6.1 Radical time series

Modelled OH concentrations were comparable in the pre-monsoon and post-monsoon, with campaign averages of $\approx 2.6 \times 10^6$ molecule cm^{-3} and $\approx 2.0 \times 10^6$ molecule cm^{-3} respectively. In the pre-monsoon, OH peaked at similar concentrations each day, at $\approx 9 \times 10^6$ molecule cm^{-3}. In the post-monsoon, there was more variation, with the highest OH peaks occurring at $\approx 1.3 \times 10^7$ molecule cm^{-3} on 16/10 and $\approx 1.6 \times 10^7$ molecule cm^{-3} on 17/10 and 18/10. OH concentrations generally decreased after this date to $\approx 4.0 \times 10^6$ molecule cm^{-3} on 26/10.

HO_2 concentrations were higher in the pre-monsoon than the post-monsoon, with average mixing ratios of $\approx 2.5 \times 10^8$ molecule cm^{-3} and $\approx 1.4 \times 10^8$ molecule cm^{-3} respectively. In the pre-monsoon, HO_2 peaked at 1.5×10^9 molecule cm^{-3} on 31/05, with the lowest daily peak occurring at 5.5×10^8 molecule cm^{-3} on 04/06. There was a larger range of daily peak mixing ratios in the post-monsoon, with a lowest daily peak of 2.3×10^8 molecule cm^{-3} on 21/10 and the highest daily peak of 2.0×10^9 molecule cm^{-3} on 24/10. In the post-monsoon, HO_2 generally increased from $\approx 7.5 \times 10^8$ molecule cm^{-3} up to 1.5×10^9 molecule cm^{-3} on 18/10. HO_2 concentrations on 16/10 were the exception to this trend, as lower peak HO_2 concentrations of 3.1×10^8 molecule cm^{-3} were observed on this day. From 18/10 onward, daily HO_2 peak concentrations began to decrease again to the campaign low on 21/10, before increasing again to the campaign high on 24/10.

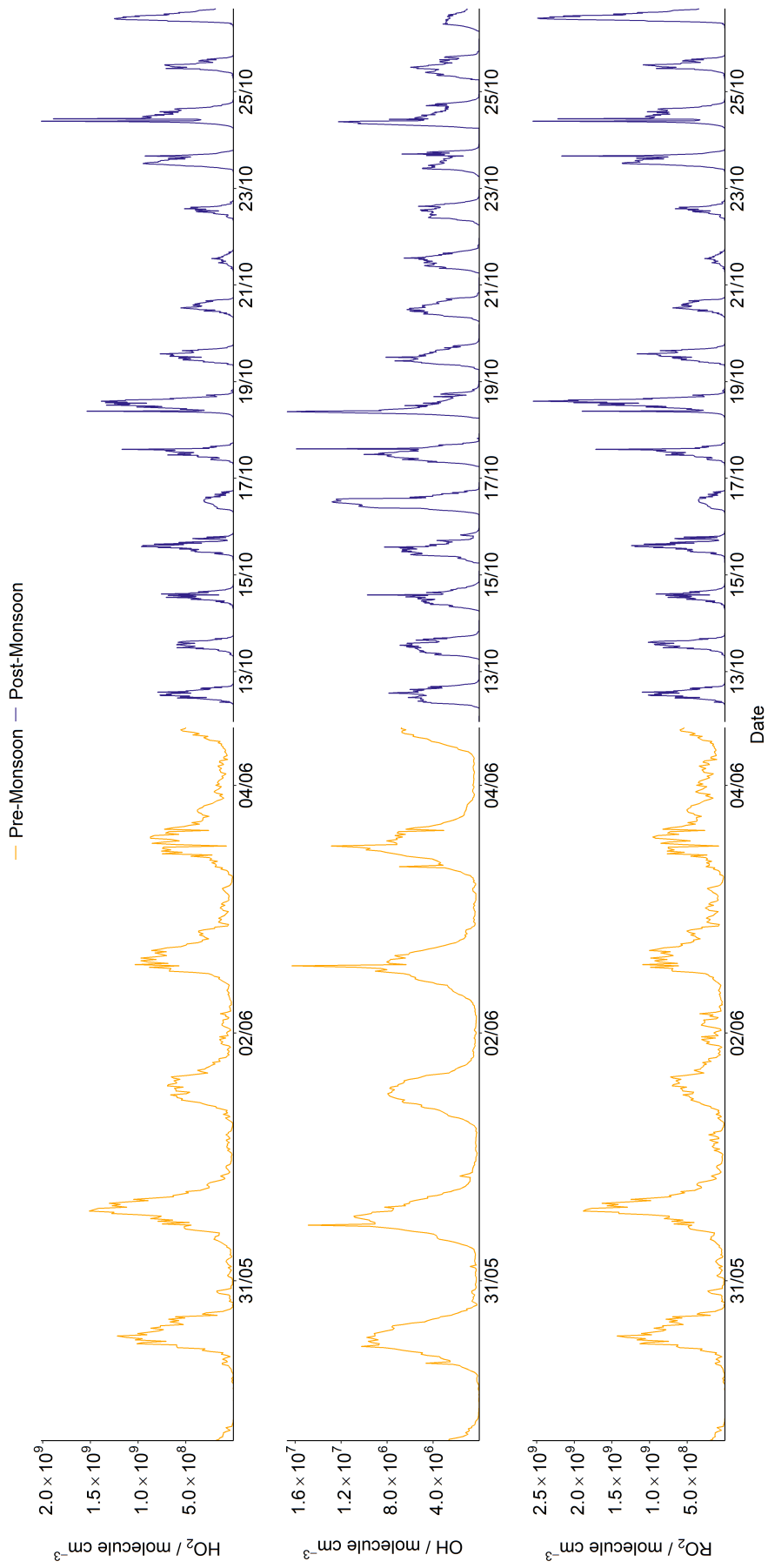

Figure 3.33: Time series of modelled OH, HO_2 and RO_2 concentrations during pre-monsoon (yellow) and post-monsoon (purple)

Modelled RO_2 were higher in the pre-monsoon than the post-monsoon. Campaign mean modelled RO_2 mixing ratios during the pre- and post-monsoon campaigns were 2.96 $\times$ 10^8 molecule cm^{-3} and 1.94 $\times$ 10^8 molecule cm^{-3} respectively. The peak concentrations of RO_2 throughout both campaigns mirror the trend of HO_2 as described above in both the pre- and post-monsoon campaigns. Pre-monsoon RO_2 daily peaks occured between 7.2 $\times$ 10^8 molecule cm^{-3} on 01/06 and 1.9 $\times$ 10^9 molecule cm^{-3} on 31/05. During the post-monsoon, daily peak RO_2 concentrations ranged from 2.7 $\times$ 10^8 molecule cm^{-3} on 21/10 to 2.6 $\times$ 10^9 molecule cm^{-3} on 24/10.

The median modelled RO_2+HO_2 mixing ratios were 5.49 $\times$ 10^8 molecule cm^{-3} and 3.37 $\times$ 10^8 molecule cm^{-3} for the pre- and post-monsoon campaigns respectively. These values were 4.4 and 5.6 times smaller than the RO_x mixing ratios calculated using photostationary steady state in section 3.5. The photostationary RO_x concentrations calculated for summertime Beijing were also much higher than both the measured and modelled concentrations of RO_x [59, 68]. This suggests that the Leighton ratio may be an insufficient method of predicting RO_x concentrations in urban Asian megacities, perhaps as it does not account for deposition processes, and additional chemistry that is depleting radicals, without leading to O_3 formation. This highlights the complexity of the chemical processing in Delhi, as well Beijing, and the importance of using a full chemical box model to assess photochemistry in place of more simplistic calculations such as the Leighton relationship.

3.6.2 Radical rate of production analysis

Rate of production analysis was used to identify the key reactions driving the formation of radical chemistry in Delhi. The main processes involved in the formation and termination of OH, HO_2, RO_2 and RCO_3 have been identified from the $>$ 16,000 reactions in the model. The key propagation routes between radical species have also been isolated. In this section, the production and loss rates of each radical species will be analysed in turn before being summarised in a full radical budget analysis. The radical budget will then be compared to other radical budget analyses from other megacities.

OH

One of the main routes of OH formation is from the reaction of excited oxygen atoms, $O(^1D)$, with water (equation 3.12). $O(^1D)$ is initially formed from the photolysis of O_3 at high energy wavelengths ($<$ 340 nm) (equation 3.9) Although the majority (*ca.* 90%) of this $O(^1D)$ is quenched forming $O(^3P)$ to re-form O_3 via equations 3.10 and 3.11, a smaller proportion (*ca.* 10%) reacts with water to form OH (equation 3.12).

$$O_3 + h\nu \longrightarrow O(^1D) \tag{3.9}$$

$$O(^1D) + M \longrightarrow O(^3P) + M \tag{3.10}$$

$$O(^3P) + O_2 + M \longrightarrow O_3 + M \tag{3.11}$$

$$O(^1D) + H_2O \longrightarrow 2\,OH \tag{3.12}$$

Another major source of OH in urban atmospheres is through HONO photolysis (equation 3.13). A more detailed description of HONO's role in OH formation is provided in Chapter 1.

$$HONO + h\nu \longrightarrow OH + NO \tag{3.13}$$

The final main source of OH radicals is from alkene ozonolysis. Alkenes initially react with O_3 to form a primary ozonide (POZ), which decomposes into a Criegee intermediate (CI) and carbonyl co-product. The fate of the CIs depends on their nascent energy content, as well as its structure and orientation [112, 113]. One of the routes CIs can take involves isomerisation to form a vinylhydroperoxide, which can decompose to yield OH. In addition to this, CIs often have enough internal energy to immediately decompose into many fragments, including OH. The fates of CIs are discussed in more detail in Chapter 5. Unlike the previous two formation routes, this is a non-photolytic OH formation route [114]. As a result, the reaction of alkenes with O_3 presents a source of OH during both day and night.

The campaign averaged diel profile of the key routes of OH initiation during the pre- and post-monsoon campaigns is shown in Figure 3.34. The mean rates of initiation during the day (06:00 - 18:00) and night (19:00 - 05:00) are presented in Table 3.4. In the pre-monsoon, the majority of OH initiation came from HONO and $O(^1D)$ photolysis, forming 40% and 39% of OH during the day (06:00 - 18:00). Ozonolysis contributed to 21% of OH initiation in the day. During the night (19:00 - 05:00), ozonolysis of alkenes was the only source of OH radical formation, at an average rate of 0.4 ppbV h^{-1}. During the post-monsoon campaign, HONO photolysis dominated, despite lower j(HONO) rates compared to the pre-monsoon campaign (Figure 3.3). During the daytime (06:00 - 18:00), j(HONO) represented 73% of OH initiation, and was more significant between 05:00 - 10:00 (89%). There was also a small peak in OH formation from ozonolysis in the early hours of the morning, due to a small increase in O_3 at 06:00, which occured before a more rapid increase in O_3 from 09:00 (see Figure 3.18, section 3.3.1). Between 13:00 - 19:00, j(HONO) and ozonolysis were comparable routes of OH formation, representing 48% and 45% respectively. The relative significance of HONO photolysis to OH production compared to other routes was due to the large concentrations of HONO observed at night during the post-monsoon campaign (Figure 3.1). This explains

Table 3.4: Mean day-time and night-time OH initiation rates during the pre- and post-monsoon campaigns.

	Pre-Monsoon Mean / ppbV h^{-1}		Post-Monsoon Mean / ppbV h^{-1}	
	Day (06:00 - 18:00)	Night (19:00 - 05:00)	Day (06:00 - 18:00)	Night (19:00 - 05:00)
j(HONO)	1.29	0.00	6.53	0.00
$j(O^1D)$	1.28	0.00	0.29	0.00
Ozonolysis	0.67	0.36	2.09	0.04
Total	**3.24**	**0.36**	**8.91**	**0.04**

why HONO photolysis was only dominant between 05:00 and 10:00 in the morning. After 10:00 the high night-time HONO had been photolysed, and lower HONO concentrations were observed during the day. Unlike the pre-monsoon, ozonolysis was not a significant source of OH formation between 19:00 - 05:00, as no O_3 was present during the night in the post-monsoon campaign. $O(^1D)$ was only a minor source of OH production in the post-monsoon, representing only 3% of OH formation during the day. This is consistent with the lower levels of $jO(^1D)$ measured during the post-monsoon campaign compared to the pre-monsoon (Figure 3.12). As discussed in section 3.2.3, this is possibly due to stronger aerosol attenuation of shorter wavelength UV radiation in this campaign. In the pre-monsoon daytime, the largest contributors to OH formation through ozonolysis were from the CH_3CHOO Criegee intermediates, formed from the but-2-enes and *trans*-pent-2-ene (33%), CIs from α-pinene (20%), C_2H_5CHOO from *trans*-pent-2-ene (8%), limonene CIs (5%) and CH_2OO CI from isoprene ozonolysis (5%). In the post-monsoon, α-pinene CI was responsible for 50% of OH formed from ozonolysis in the day, followed by the CH_3CHOO CI (19%) and limonene CIs (14%). A CI derived from β-pinene contributed to 3%, and C_2H_5CHOO 2%. It is worth noting that α-pinene, β-pinene and limonene CIs are used as proxy species for other species with similar structures that are not currently present in the Master Chemical Mechanism. As a result, CIs formed from their mechanisms were also formed from additional species, as detailed in Chapter 4.

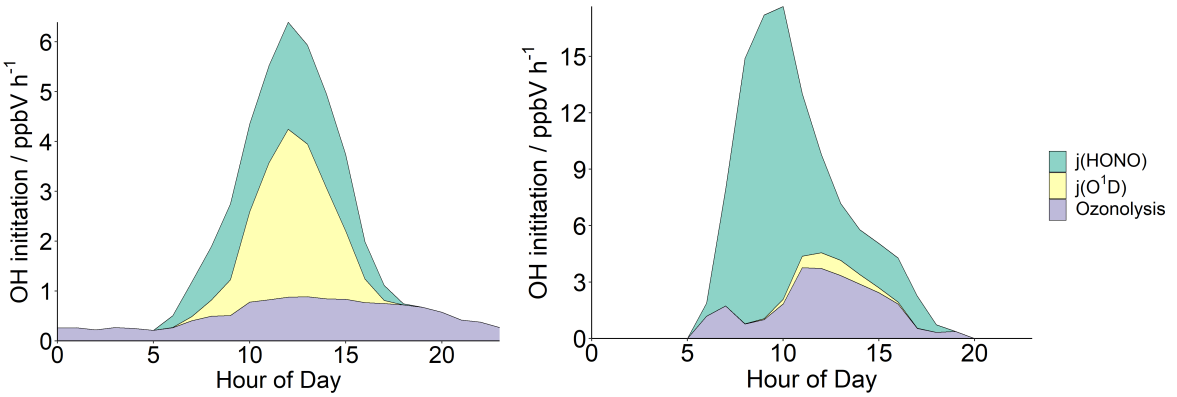

(a) Pre-Monsoon (b) Post-Monsoon

Figure 3.34: Stacked area plots showing the average modelled diel rates of OH radical initiation during the pre-monsoon (a) and post-monsoon (b) campaigns.

It is worth noting, the campaign averaged OH production rates represent a crude picture of OH initiation, and the individual significance of each formation route varied day to day. Figure 3.35 shows the day-time percentage contribution of each OH initiation rate to OH production on each day of the campaigns. In the pre-monsoon, $j(O^1D)$ represented a smaller proportion of OH production on 04/06 relative to other days. Total OH formation was also smaller on this day, compared to the rest of the campaign, but OH formation from ozonolysis and HONO photolysis was comparable (Table 3.5). The lower OH formation rates from O^1D photolysis reflected the lower $j(O^1D)$ rates observed on this day (Figure 3.12). In the post-monsoon campaign, OH formation from O^1D photolysis was less significant towards the end of the campaign, despite higher total OH formation compared to earlier in the campaign. This was due to an increased rate of OH formation from HONO, resulting from increased concentrations of HONO observed towards the end of the month (see Figure 3.10, section 3.2.1).

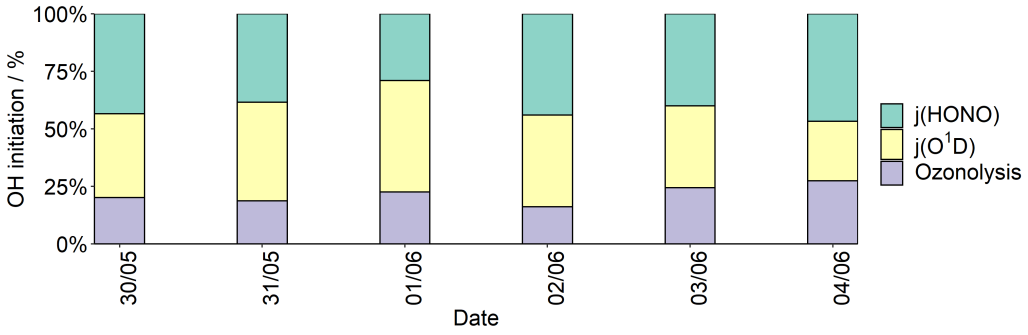

(a) Pre-Monsoon

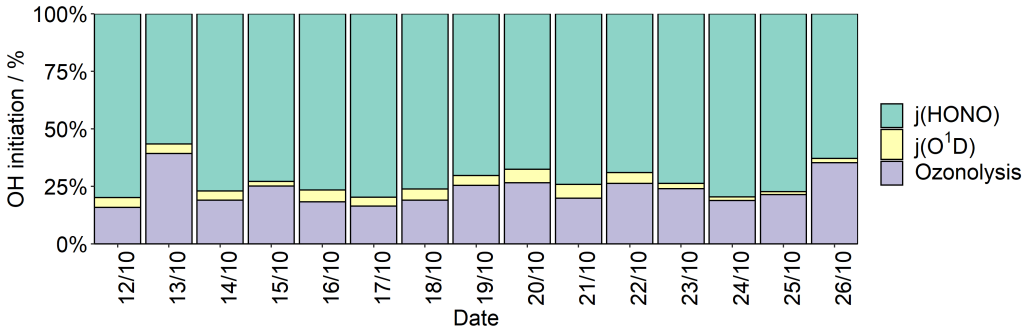

(b) Post-Monsoon

Figure 3.35: Average day-time (06:00 - 18:00) modelled contributions of rates of OH initiation during the pre-monsoon (a) and post-monsoon (b) campaigns.

Table 3.5: Average day-time (06:00 - 18:00) modelled rates of OH initiation for each day during the pre-monsoon and post-monsoon campaigns.

		OH initiation rates / ppbV h^{-1}			
Campaign	Date	j(HONO)	$j(O^1D)$	Ozonolysis	Total
Pre-Monsoon	30/05/18	1.5	1.3	0.7	3.4
	31/05/18	1.6	1.8	0.8	4.1
	01/06/18	0.8	1.4	0.6	2.8
	02/06/18	1.4	1.3	0.5	3.3
	03/06/18	1.3	1.1	0.8	3.1
	04/06/18	1.1	0.6	0.6	2.3
Post-Monsoon	12/10/18	5.5	0.3	1.1	6.8
	13/10/18	3.6	0.3	2.5	6.4
	14/10/18	4.4	0.2	1.1	5.7
	15/10/18	7.5	0.2	2.6	10.3
	16/10/18	5.8	0.4	1.4	7.5
	17/10/18	7.3	0.4	1.5	9.1
	18/10/18	7.9	0.5	2.0	10.4
	19/10/18	4.7	0.3	1.7	6.7
	20/10/18	3.7	0.3	1.5	5.5
	21/10/18	3.4	0.3	0.9	4.6
	22/10/18	4.1	0.3	1.6	5.9
	23/10/18	7.9	0.2	2.6	10.7
	24/10/18	12.5	0.2	3.0	15.7
	25/10/18	10.5	0.2	2.9	13.6
	26/10/18	9.2	0.3	5.2	14.6

There are two main OH termination routes in the urban atmosphere. The majority of OH termination occurs through reactions with either NO_2 or NO (equation 3.14, and the reverse of equation 3.13). The relative importance of these two loss routes is dependant on the partitioning between NO and NO_2, described by the NO:NO_2 ratio. The higher this ratio is, the more important OH+NO termination will be relative to OH+NO_2 termination.

$$OH + NO_2 \quad (+M) \longrightarrow HNO_3 \quad (+M) \tag{3.14}$$

Other loss processes which may be important to OH termination are the reaction with peroxy acetyl nitrates (PANs), and with other organic nitrates (e.g. equation 3.15). Although there are over 200 PAN-type species in the MCM, the analysis presented here suggests both OH loss through PANs and organic nitrates are minor relative to OH+NO_2 and OH+NO.

$$PAN + OH \longrightarrow HCHO + CO + NO_2 \tag{3.15}$$

Mean day-time and night-time rates of termination during the pre- and post-monsoon are summarised in Table 3.6, and the diel profiles of OH termination are presented in Figure 3.36. In the pre-monsoon, OH+NO_2 was the dominant OH termination route between 06:00 - 18:00 (86%), followed by OH+NO (11%) and OH+PAN (3%). OH+organic nitrates only represented a minor proportion of OH termination ($< 0.1\%$). During the post-monsoon,

OH was predominantly terminated by OH+NO_2 between 06:00 - 18:00 (58%), followed by OH+NO (38%) and OH+PAN (4%). Loss to organic nitrates was a minor route of termination for OH with respect to other routes, representing < 1% of OH termination during the day.

Table 3.6: Mean day-time and night-time OH termination rates during the pre- and post-monsoon campaigns.

	Pre-Monsoon Median / ppbV h^{-1}		Post-Monsoon Median / ppbV h^{-1}	
	Day (06:00 - 18:00)	Night (19:00 - 05:00)	Day (06:00 - 18:00)	Night (19:00 - 05:00)
OH+NO_2	3.08	0.43	4.76	0.10
OH+NO	0.39	0.03	3.11	0.24
OH+PAN	0.09	0.01	0.31	0.00
Total	**3.56**	**0.47**	**8.18**	**0.34**

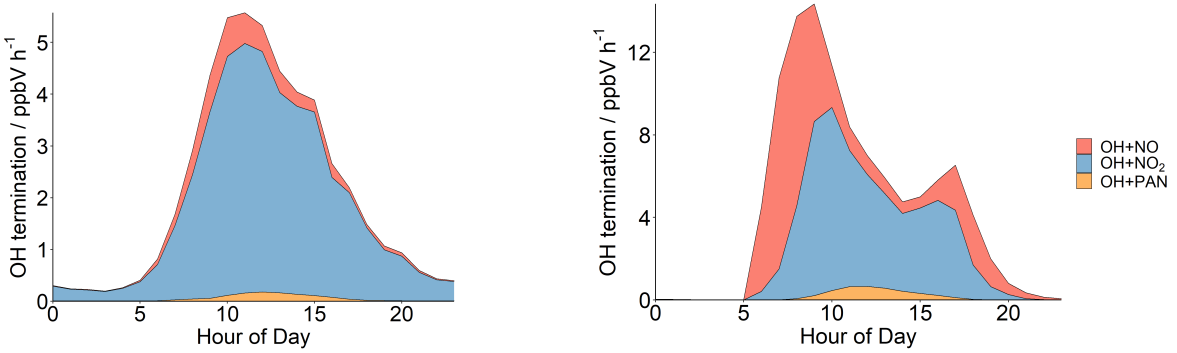

(a) Pre-Monsoon (b) Post-Monsoon

Figure 3.36: Stacked area plots showing the average modelled diel rates of termination of the OH radical during the pre-monsoon (a) and post-monsoon (b) campaigns.

In both campaigns, there was little variability in percentage contributions to OH termination day to day. However, in the post-monsoon campaign, OH+NO termination became more important in the final few days. On the 25/10 and 26/10, OH+NO was the most significant termination route rather than OH+NO_2. This was due to an increase in OH+NO termination in the final days of the campaign, coupled with a small drop in OH+NO_2 termination on 26/10. The increased importance of the OH+NO loss route compared to OH+NO_2 was due to an increased NO:NO_2 ratio towards the end of the campaign. On 25/10 and 26/10, the NO:NO_2 ratios were 6.69 and 4.29 respectively, compared to a campaign average ratio of 2.21. Much smaller NO:NO_2 ratios were observed in the pre-monsoon campaign, with daily ratios ranging between 0.07 - 0.15, explaining the dominance of OH+NO_2 throughout the campaign relative to OH+NO. There was approximately 1.5 times more daytime OH+NO_2 termination in the post-monsoon than the pre-monsoon campaign, compared to approximately 8 times more OH+NO termination (Table 3.7).

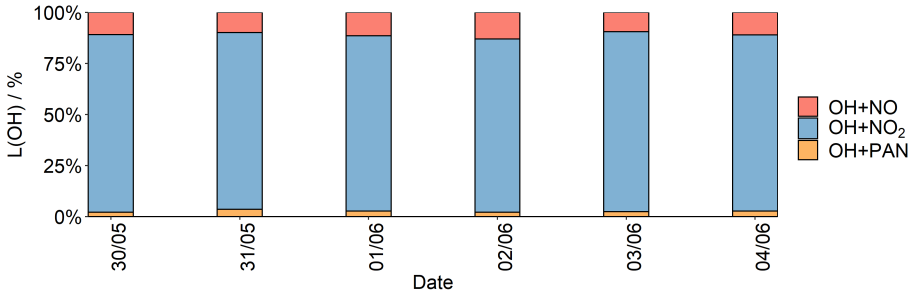

(a) Pre-Monsoon

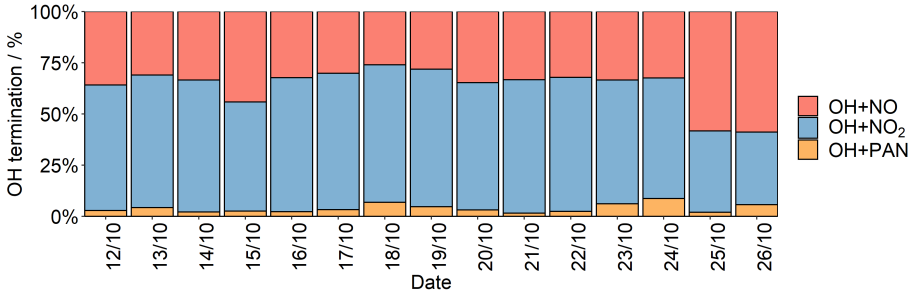

(b) Post-Monsoon

Figure 3.37: Average day-time (06:00 - 18:00) modelled contributions of rates of OH termination during the pre-monsoon (a) and post-monsoon (b) campaigns.

Table 3.7: Average day-time (06:00 - 18:00) modelled rates of OH termination for each day during the pre-monsoon and post-monsoon campaigns.

		OH termination rates / ppbV h^{-1}			
Campaign	Date	$OH+NO_2$	OH+NO	OH+PAN	Total
Pre-Monsoon	30/05/18	3.4	0.4	0.1	3.9
	31/05/18	3.3	0.4	0.1	3.8
	01/06/18	3.1	0.4	0.1	3.6
	20/06/18	2.7	0.4	0.1	3.2
	03/06/18	3.1	0.3	0.1	3.6
	04/06/18	2.8	0.4	0.1	3.2
Post-Monsoon	12/10/18	4.3	2.5	0.2	7.0
	13/10/18	4.5	2.2	0.3	7.0
	14/10/18	4.7	2.4	0.2	7.3
	15/10/18	6.1	5.1	0.3	11.5
	16/10/18	5.8	2.9	0.2	8.9
	17/10/18	5.7	2.6	0.3	8.6
	18/10/18	3.8	1.5	0.4	5.7
	19/10/18	4.2	1.8	0.3	6.2
	20/10/18	3.9	2.2	0.2	6.3
	21/10/18	4.4	2.3	0.1	6.8
	22/10/18	5.3	2.6	0.2	8.1
	23/10/18	5.3	2.9	0.5	8.8
	24/10/18	4.6	2.5	0.7	7.8
	25/10/18	5.0	7.4	0.3	12.7
	26/10/18	3.6	6.0	0.6	10.1

HO_2

HO_2 is predominately formed from the photolysis of carbonyl species. One of the key species in HO_2 initiation is HCHO (equation 3.16). HCHO photolysis can be a significant source of HO_2 as two molecules of HO_2 are formed from one molecule of HCHO.

$$HCHO + h\nu + O_2 \longrightarrow CO + 2\,HO_2 + M \tag{3.16}$$

The contribution of other aldehydes, such as acetaldehyde (equation 3.17), to HO_2 can also be significant. The photolysis of these compounds leads to the formation of one molecule of HO_2, along with an RO_2 radical. The summed HO_2 initiation rates from the photolysis of CH_3CHO, C_2H_5CHO, C_3H_7CHO, *iso*-butyraldehyde and methacrolein are presented as j(Aldehydes).

$$CH_3CHO + h\nu + 2\,O_2 \longrightarrow CO + HO_2 + CH_3O_2 \tag{3.17}$$

Finally, the photolysis of dicarbonyl species formed in the model from constrained precursor VOCs is an important source of HO_2 formation. Glyoxal and methylglyoxal are formed from the degradation of multiple species in the model, and can be major contributors to radical formation. Like HCHO photolysis, glyoxal photolysis leads to the formation of two HO_2 molecules, through the formation of 2HCO which are then oxidised in the presence of O_2 (equation 3.18). Another photolysis route for glyoxal leads to the formation of HCHO (equation 3.19), which then further contributes to HO_2 through HCHO, photolysis described earlier (equation 3.16).

$$CH(O)CHO + h\nu + O_2 \longrightarrow 2\,CO + 2\,HO_2 \tag{3.18}$$

$$CH(O)CHO + h\nu \longrightarrow CO + HCHO \tag{3.19}$$

The photolysis of methylglyoxal yields one molecule of HO_2, along with an RCO_3 radical (equation 3.20).

$$CH(O)C(O)CH_3 + h\nu + 2\,O_2 \longrightarrow CH_3CO_3 + CO + HO_2 \tag{3.20}$$

Campaign averaged diel profiles of the key routes of HO_2 initiation during the pre- and post-monsoon are presented in Figure 3.38, and the mean rates of HO_2 production during the day (06:00 - 18:00) and night (19:00 - 05:00) are presented in Table 3.8. In the pre-monsoon, the main source of HO_2 formation was through photolysis of the model generated dicarbonyl species methylglyoxal and glyoxal, formed mainly from aromatic chemistry. In the day (06:00 - 18:00), these two routes represent 43% and 35% of HO_2 formation respectively. The next largest contributor to HO_2 formation was from ozonolysis reactions (13%), followed

by aldehyde photolysis (6%) and HCHO photolysis (2%). During the post-monsoon, HCHO photolysis was the main source of HO_2, representing 34% of the total daytime HO_2 formation. This was closely followed by methylglyoxal photolysis (30%) and glyoxal photolysis (25%). In the post-monsoon, campaign median mixing ratios of HCHO were 11.9 ppbV compared to only 0.3 ppbV in the pre-monsoon (Table 3.1.3). This led to an increased importance of HCHO photolysis in the post-monsoon compared to the pre-monsoon campaign. Ozonolysis and aldehyde photolysis were also contributing routes to HO_2 formation, representing 6% and 4% respectively. In the pre-monsoon, the top ozonolysis pathways forming HO_2 were from the CH_3CHOO CI from the but-2-enes and *trans*-pent-2-ene (27%); CH_2OO derived from isoprene (17%); CH_2OO from propene, but-1-ene, pent-1-ene, MVK and styrene (13%); CH_2OO derived from isobutylene (8%) and a glyoxal Criegee, from aromatic species (7%). In the post-monsoon, the largest contributors to HO_2 formation via ozonolysis were from the CH_3CHOO CI (38%); CH_2OO from propene, but-1-ene, pent-1-ene, MVK and styrene (16%); CH_2OO from isobutylene (9%), CH_2OO from β-pinene and species for which it was used as proxy (5%); and CH_2OO from isoprene (5%). The daily percentage contributions of each HO_2 initiation route are presented in Figure 3.39, and the mean daily initiation rates are summarised in Table 3.9.

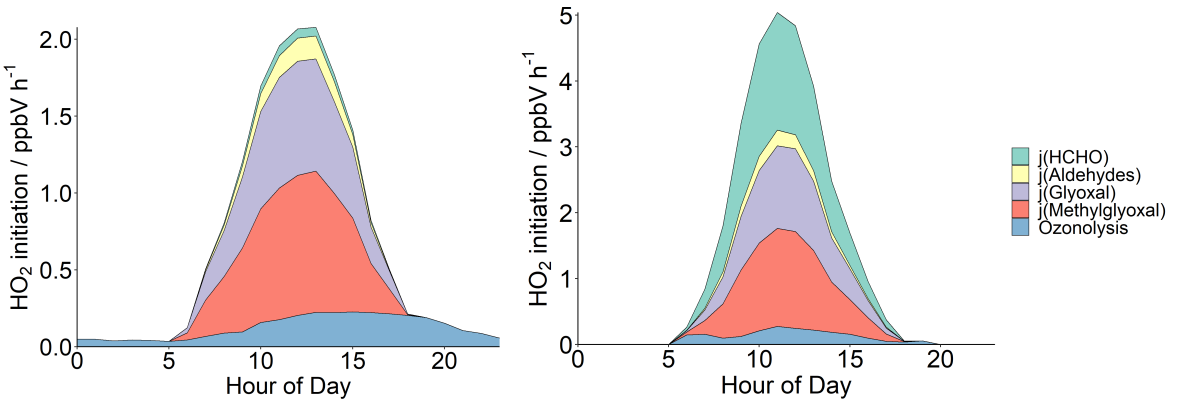

(a) Pre-Monsoon (b) Post-Monsoon

Figure 3.38: Stacked area plots showing the average modelled diel rates of HO_2 initiation during the pre-monsoon (a) and post-monsoon (b) campaigns.

Table 3.8: Mean day-time and night-time HO_2 inititation rates during the pre- and post-monsoon campaigns.

	Pre-Monsoon Mean / ppbV h^{-1}		Post-Monsoon Mean / ppbV h^{-1}	
	Day (06:00 - 18:00)	Night (19:00 - 05:00)	Day (06:00 - 18:00)	Night (19:00 - 05:00)
j(HCHO)	0.03	0.00	0.87	0.00
j(Aldehydes)	0.07	0.00	0.11	0.00
j(Glyoxal)	0.42	0.00	0.63	0.00
j(Methylglyoxal)	0.52	0.00	0.75	0.00
Ozonolysis	0.16	0.08	0.16	0.01
Total	**1.21**	**0.08**	**2.52**	**0.01**

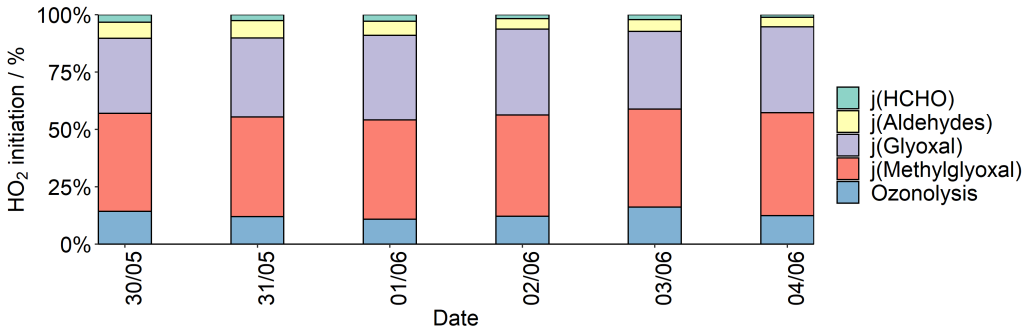

(a) Pre-Monsoon

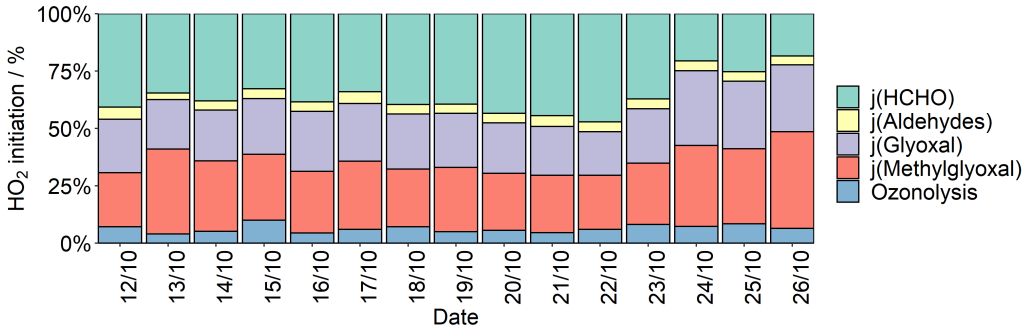

(b) Post-Monsoon

Figure 3.39: Average day-time (06:00 - 18:00) modelled contributions of rates of primary HO_2 formation during the pre-monsoon (a) and post-monsoon (b) campaigns.

In the pre-monsoon campaign, contributions from all HO_2 sources were consistent throughout the campaign, with little variability (Figure 3.39), and little variation in day to day total HO_2 formation rates (Table 3.9). More variation was observed in the post-monsoon campaign, where changes in HCHO concentration impacted on the contribution to HO_2 formation from HCHO photolysis. High concentrations of HCHO were observed on 22/10, peaking at 40 ppbV. This led to HCHO being the largest contributor to HO_2 formation on this day. High mixing ratios of HCHO were also observed on 23/10, peaking at 35 ppbV, but HCHO was a less dominating contributor to HO_2 formation. This was due to increased significance from ozonolysis products on this day, along with higher contributions from glyoxal and methylglyoxal photolysis. There were higher concentrations of aromatic species on this day, which undergo chemical processing to form glyoxal and methylglyoxal. For example, benzene concentrations peaked at maximum mixing ratio of $\approx$ 30 ppbV (Figure 3.11).

Table 3.9: Average day-time (06:00 - 18:00) modelled rates of primary HO_2 initiation for each day during the pre-monsoon and post-monsoon campaigns.

		HO_2 initiation rates / ppbV h^{-1}					
Campaign	Date	j(HCHO)	j(Aldehydes)	j(Glyoxal)	j(Methylglyoxal)	Ozonolysis	Total
Pre-Monsoon	30/05/18	0.04	0.09	0.42	0.54	0.18	1.27
	31/05/18	0.04	0.12	0.56	0.70	0.19	1.62
	01/06/18	0.03	0.07	0.42	0.50	0.12	1.15
	02/06/18	0.02	0.04	0.35	0.41	0.11	0.93
	03/06/18	0.03	0.06	0.41	0.52	0.19	1.21
	04/06/18	0.01	0.04	0.39	0.46	0.13	1.03
Post-Monsoon	12/10/18	0.83	0.11	0.47	0.48	0.14	2.03
	13/10/18	0.85	0.07	0.53	0.90	0.10	2.44
	14/10/18	0.90	0.09	0.52	0.72	0.12	2.36
	15/10/18	1.04	0.13	0.77	0.90	0.31	3.16
	16/10/18	1.14	0.12	0.78	0.80	0.13	2.97
	17/10/18	0.87	0.13	0.64	0.76	0.15	2.56
	18/10/18	1.14	0.12	0.69	0.73	0.21	2.89
	19/10/18	0.80	0.08	0.48	0.56	0.10	2.02
	20/10/18	0.69	0.07	0.35	0.39	0.09	1.59
	21/10/18	0.79	0.08	0.37	0.44	0.08	1.77
	22/10/18	1.00	0.09	0.40	0.50	0.13	2.11
	23/10/18	0.95	0.11	0.61	0.68	0.21	2.55
	24/10/18	0.83	0.17	1.30	1.41	0.29	4.00
	25/10/18	0.63	0.10	0.73	0.82	0.21	2.49
	26/10/18	0.52	0.11	0.82	1.19	0.18	2.83

HO_2 was terminated in both campaigns by HO_2 self reactions and through reactions with RO_2 species. Campaign mean day-time and night-time HO_2 loss rates are presented in Table 3.10, and HO_2 termination diel profiles for both campaigns are shown in Figure 3.40. In the pre-monsoon, HO_2+HO_2 represented the largest proportion of HO_2 termination (64%), whereas HO_2+RO_2 termination dominated in the post-monsoon (57%). This can be seen in elevated modelled RO_2 levels in the post-monsoon relative to the pre-monsoon campaign, as described in section 3.6 (Figure 3.33).

Table 3.10: Mean day-time and night-time HO_2 termination rates during the pre- and post-monsoon campaigns.

	Pre-Monsoon Median / ppbV h^{-1}		Post-Monsoon Median / ppbV h^{-1}	
	Day (06:00 - 18:00)	Night (19:00 - 05:00)	Day (06:00 - 18:00)	Night (19:00 - 05:00)
HO_2+HO_2	0.84	0.04	0.64	0.00
HO_2+RO_2	0.49	0.04	0.83	0.00
Total	**1.32**	**0.08**	**1.47**	**0.00**

In the final two days of the post-monsoon campaign, aerosol surface area data was available, and included as a source of HO_2 uptake in the model. During these days, uptake to aerosol represented 48% and 33% of HO_2 loss during the day respectively (Figure 3.41). It is worth nothing here that HO_2 aerosol uptake is sensitive to an uptake coefficient. The sensitivity of O_3 formation to this coefficient, and the impact of HO_2 aerosol uptake on O_3 production is further discussed in Chapter 4. A breakdown of the daily mean rates of HO_2 termination during both campaigns is presented in Table 3.11.

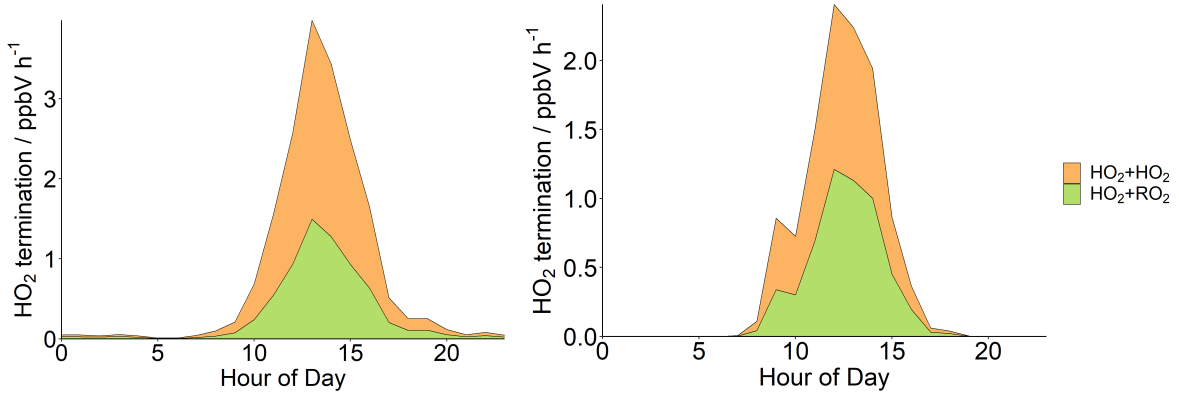

(a) Pre-Monsoon (b) Post-Monsoon

Figure 3.40: Stacked area plots showing the average modelled diel rates of termination of the HO_2 radical during the pre-monsoon (a) and post-monsoon (b) campaigns.

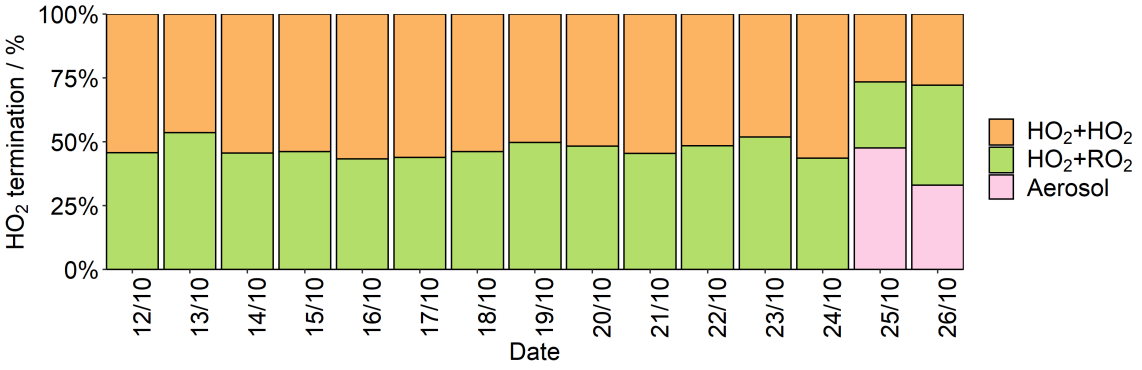

Figure 3.41: Average day-time (06:00 - 18:00) modelled contributions of rates of primary HO_2 termination during the post-monsoon campaigns.

Table 3.11: Average day-time (06:00 - 18:00) modelled rates of HO_2 termination for each day during the pre-monsoon and post-monsoon campaigns.

		HO_2 termination rates / ppbV h^{-1}			
Campaign	Date	HO_2+HO_2	HO_2+RO_2	Aerosol	Total
Pre-Monsoon	30/05/18	0.86	0.57	N/A	1.43
	31/05/18	1.59	0.93	N/A	2.52
	01/06/18	0.55	0.30	N/A	0.85
	02/06/18	0.79	0.44	N/A	1.23
	03/06/18	0.71	0.40	N/A	1.11
	04/06/18	0.28	0.16	N/A	0.44
Post-Monsoon	12/10/18	0.35	0.30	N/A	0.35
	13/10/18	0.23	0.27	N/A	0.23
	14/10/18	0.20	0.17	N/A	0.20
	15/10/18	0.43	0.37	N/A	0.43
	16/10/18	0.09	0.07	N/A	0.09
	17/10/18	0.41	0.32	N/A	0.41
	18/10/18	1.54	1.31	N/A	1.54
	19/10/18	0.36	0.35	N/A	0.36
	20/10/18	0.17	0.16	N/A	0.17
	21/10/18	0.02	0.01	N/A	0.02
	22/10/18	0.09	0.09	N/A	0.09
	23/10/18	0.67	0.72	N/A	0.67
	24/10/18	1.30	1.00	N/A	1.30
	25/10/18	0.28	0.27	0.50	1.05
	26/10/18	1.01	1.41	1.19	3.61

RO_2

Initiation routes for RO_2 in the atmosphere include carbonyl photolysis, and the product of ozonolysis and VOC+NO_3 reactions. RO_2 loss diel profiles are presented in Figure 3.42 and mean RO_2 production rates from each route are presented in Table 3.12. In the pre-monsoon campaign, ozonolysis was the largest source of RO_2 radical initiation in the day-time (36%), followed by methylglyoxal photolysis (30%) and VOC+NO_3 reactions (26%). At night, VOC+NO_3 was the dominant initiation source of RO_2 radicals (58%), followed by ozonolysis (42%). Photolytic sources were more important around mid-day, when photolysis rates peaked, with the VOC+NO_3 formation route increasing in importance later in the afternoon. Ozonolysis rates peaked at around mid-day, but remained an important source later into the afternoon. The importance of ozonolysis to RO_2 initiation in the afternoon was due to O_3 campaign average concentrations peaking at 14:00, and remaining above 50 ppbV until 19:00 (Figure 3.18). This trend was also seen in the VOC+NO_3 formation route, as O_3 is a precursor to NO_3 formation. Campaign averaged O_3 mixing ratios were $\approx$ 30 ppbV throughout the night, leading to a night-time RO_2 formation from ozonolysis and VOC+NO_3 routes. The formation of PAN from RO_2+NO_2 generally led to RO_2 loss, but occasionally the rate of the backward reaction was larger, leading to net RO_2 formation. Although some RO_2 formation from PAN happened in the pre-monsoon, it was very small and only occured in the early hours of the morning and late afternoon.

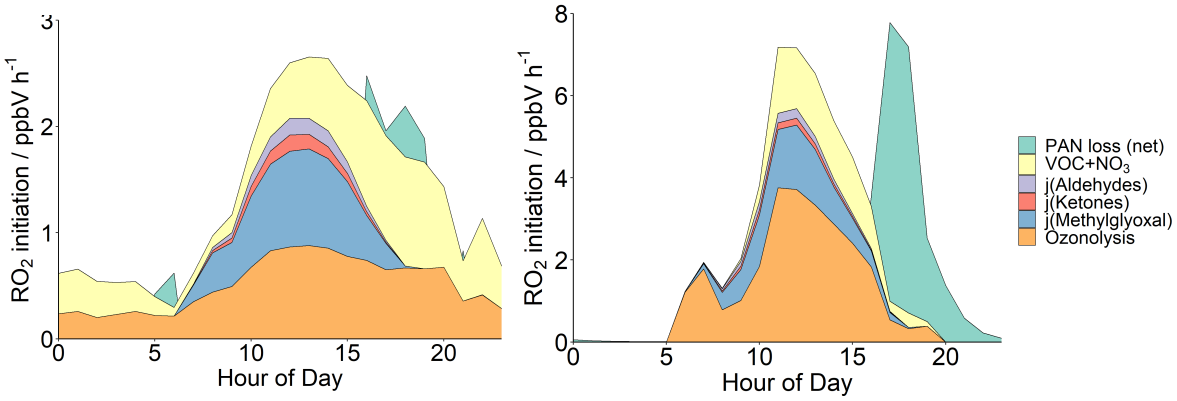

(a) Pre-Monsoon (b) Post-Monsoon

Figure 3.42: Stacked area plots showing the average modelled diel rates of RO_2 initiation during the pre-monsoon (a) and post-monsoon (b) campaigns.

Table 3.12: Mean day-time and night-time RO_2 initiation rates during the pre- and post-monsoon campaigns.

	Pre-Monsoon Median / ppbV h^{-1}		Post-Monsoon Median / ppbV h^{-1}	
	Day (06:00 - 18:00)	Night (19:00 - 05:00)	Day (06:00 - 18:00)	Night (19:00 - 05:00)
$VOC+NO_3$	0.47	0.50	0.76	0.00
j(Aldehydes)	0.08	0.00	0.11	0.00
j(Ketones)	0.07	0.00	0.07	0.00
j(Methylglyoxal)	0.54	0.00	0.75	0.00
Ozonolysis	0.65	0.06	2.09	0.00
PAN	0.00	0.00	0.00	0.44
Total	**1.81**	**0.56**	**3.78**	**0.44**

In the post-monsoon, ozonolysis was also the biggest contributor to primary RO_2 formation in the day-time (55%), followed by $VOC+NO_3$ (20%) and methylglyoxal photolysis (20%). In this campaign, photolysis, ozonolysis and $VOC+NO_3$ initiation routes all peaked around mid-day, with production rates decreasing into the afternoon. As in the pre-monsoon campaign, the peak in RO_2 formation from ozonolysis and $VOC+NO_3$ was due to O_3 concentrations. In the post-monsoon campaign, O_3 peaked earlier (13:00), and O_3 levels droped off faster into the afternoon. At 19:00, campaign averaged O_3 concentrations were $\approx$ 10 ppbV in the post-monsoon, compared to $\approx$ 60 ppbV in the pre-monsoon at this time. In the evening, PAN became an important source of RO_2 in this campaign, with PAN decomposition out-competing PAN formation from RO_2+NO_2, leading to net RO_2 formation. In the post-monsoon campaign, large concentrations of PAN were produced in the day, with the campaign average diel peaking at $\approx$ 12 ppbV at 13:00. The production of PAN from RO_2 and NO_2 was a large RO_2 sink route, as described later in this section. However, towards the late afternoon, RO_2 production declined due to decreasing photolysis rates (see section 3.2.3). In addition to this, $NO:NO_2$ ratios were low before 15:00, as NO_2 dominated, but increased rapidly from 0.1 at 15:00 to 7.6 at 22:00. As a result of this, the formation of PAN from RO_2 and NO_2 was slowed [115]. As temperatures in Delhi were still high in the late afternoon,

with campaign average temperatures of 31°C at 15:00, PAN thermal decomposition was rapid and this led to PAN loss dominating in the late afternoon, resulting in RO_2 initiation from around 15:00, shifted from the mid-day RO_2 initiation peak.

The day-time percentage contributions of all initiation routes for RO_2 on a day by day basis for both campaign are presented in Figure 3.43, and day-time averaged RO_2 initiation rates from each source are presented in Table 3.13. During the pre-monsoon campaign, there was little variation between percentage contributions each day, with more variation observed in the post-monsoon campaign mainly due variations in RO_2 initiation from ozonlysis and NO_3, due to O_3 variations (see section 3.2.1, Figure 3.10). On the final day of the post-monsoon campaign, total RO_2 production was higher than previous days, with a production rate of 5.32 ppbV h^{-1}, due to elevated RO_2 production from ozonolysis and VOC+NO_3 routes. This coincided with elevated night-time concentrations of VOCs and NO, leading to large concentrations of these species on the morning of 26/10. For example, average concentrations of toluene and NO at 9:00 were 69 ppbV and 357 ppbV respectively. A campaign peak in NO_2 was also observed at 09:45 of 147 ppbV. As O_3 concentrations were low at this time (≈ 6

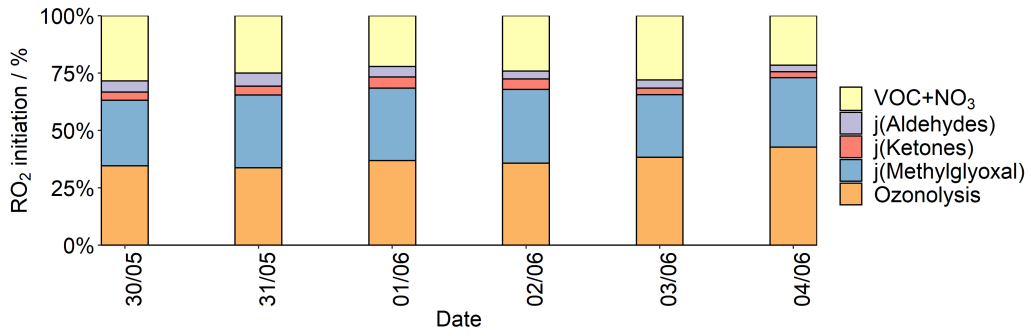

(a) Pre-Monsoon

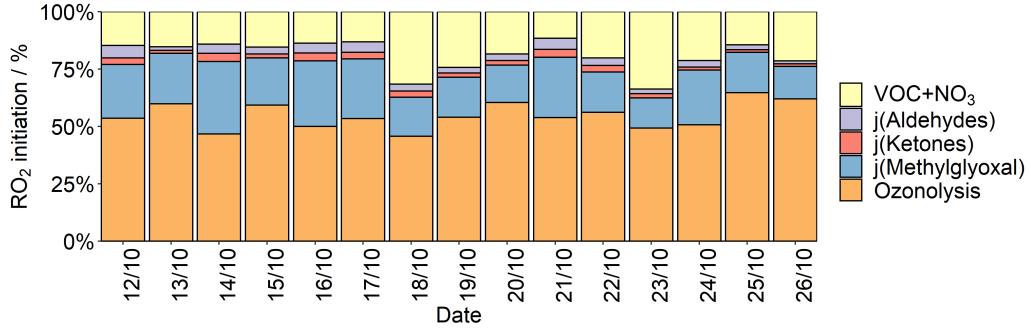

(b) Post-Monsoon

Figure 3.43: Average day-time (06:00 - 18:00) modelled contributions of rates of primary RO_2 formation during the pre-monsoon (a) and post-monsoon (b) campaigns.

ppbV), this may have been due to a primary emission, perhaps from nearby road transport. Alternatively, this may be due to a delay between radical formation and O_3 formation, which then consumed NO_2, forming NO_3. Towards mid-day, NO_2 decreased as O_3 increased, peak-

Table 3.13: Average day-time (06:00 - 18:00) modelled rates of RO_2 initiation for each day during the pre-monsoon and post-monsoon campaigns.

		RO_2 initiation rates / ppbV h^{-1}					
Campaign	Date	NO_3	j(Aldehydes)	j(Ketones)	j(Methylglyoxal)	Ozonolysis	Total
Pre-Monsoon	30/05/18	0.54	0.09	0.07	0.54	0.65	1.89
	31/05/18	0.55	0.13	0.09	0.70	0.75	2.22
	01/06/18	0.36	0.08	0.08	0.51	0.59	1.61
	02/06/18	0.31	0.05	0.06	0.42	0.47	1.30
	03/06/18	0.53	0.07	0.05	0.51	0.72	1.88
	04/06/18	0.31	0.04	0.04	0.44	0.61	1.44
Post-Monsoon	12/10/18	0.30	0.11	0.06	0.48	1.10	1.26
	13/10/18	0.64	0.07	0.05	0.91	2.49	2.61
	14/10/18	0.33	0.09	0.08	0.73	1.09	1.26
	15/10/18	0.69	0.13	0.08	0.91	2.64	2.85
	16/10/18	0.38	0.12	0.09	0.79	1.38	1.59
	17/10/18	0.38	0.13	0.08	0.74	1.52	1.74
	18/10/18	1.35	0.12	0.11	0.73	1.94	2.18
	19/10/18	0.76	0.08	0.06	0.55	1.69	1.82
	20/10/18	0.45	0.07	0.05	0.40	1.46	1.58
	21/10/18	0.19	0.08	0.06	0.44	0.90	1.04
	22/10/18	0.56	0.09	0.08	0.49	1.56	1.73
	23/10/18	1.74	0.11	0.09	0.68	2.54	2.74
	24/10/18	1.26	0.17	0.08	1.41	2.99	3.24
	25/10/18	0.66	0.10	0.05	0.80	2.94	3.09
	26/10/18	1.78	0.10	0.09	1.17	5.13	5.32

ing at 82 ppbV. As NO_3 is formed from a reaction between O_3 and NO_2, this, coupled with large concentrations of VOCs, could explain the increased RO_2 formation from VOCs+NO_3.

The large concentrations of VOCs also explain the increased contribution from ozonolysis routes. Photolysis routes were less significant on this day due to lower photolysis rates towards the end of the campaign. The largest daytime contributors to ozonolysis forming RO_2 in the pre-monsoon were α-pinene and the species for which it was used as proxy (32%); CH_3CHOO from the but-2-enes and *trans*-pent-2-ene (31%); limonene and the species for which it was a proxy (12%); C_2H_5CHOO CI from *trans*-pent-2-ene (8%); and a CI derived from methacrolein (3%). In the post-monsoon, the largest contributors to RO_2 forming ozonolysis were also the α-pinene derived CIs (58%), followed by limonene derived CIs (18%), CH_3CHOO (14%), a β-pinene derived Criegee (3%), and C_2H_5CHOO (1%).

RO_2 termination in both campaigns was dominated by PAN formation, RO_2+HO_2, and RO_2+NO reactions forming carbonyls. RO_2+RO_2 was an unimportant RO_2 termination route, with negligible contributions to RO_2 termination in both campaigns. A diel profile of RO_2 termination for both campaigns is presented in Figure 3.44, and day-time and night-time mean termination rates from each route for both campaigns are presented in Table 3.14.

In the pre-monsoon campaign, RO_2+NO forming carbonyls contributed to 42% of the total RO_2 loss, followed by PAN formation (32%), RO_2+HO_2 (25%) and RO_2+RO_2 (1%).

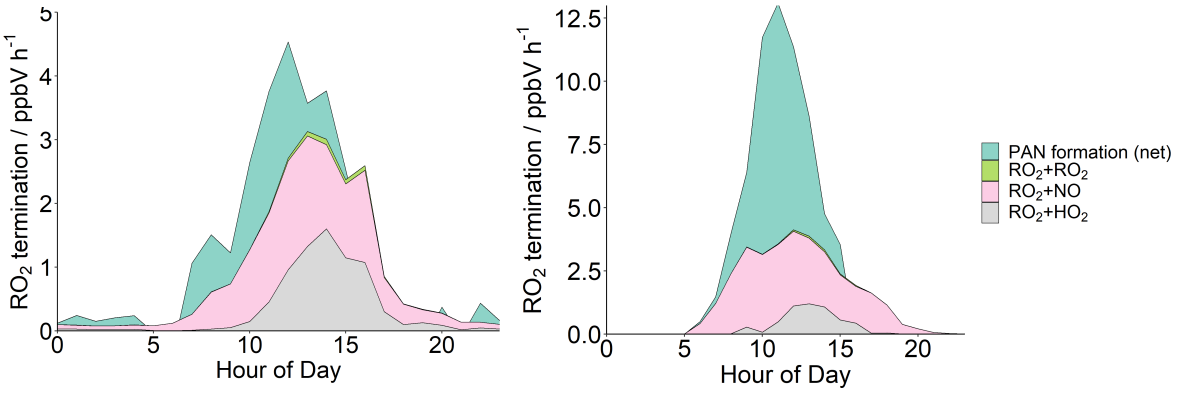

(a) Pre-Monsoon (b) Post-Monsoon

Figure 3.44: Stacked area plots showing the average modelled diel rates of RO_2 initiation during the pre-monsoon (a) and post-monsoon (b) campaigns.

Table 3.14: Mean day-time and night-time RO_2 termination rates during the pre- and post-monsoon campaigns.

	Pre-Monsoon Median / ppbV h^{-1}		Post-Monsoon Median / ppbV h^{-1}	
	Day (06:00 - 18:00)	Night (19:00 - 05:00)	Day (06:00 - 18:00)	Night (19:00 - 05:00)
PAN formation	0.75	0.06	2.54	0.00
RO_2+RO_2	0.03	0.00	0.03	0.00
RO_2+NO	1.00	0.10	2.16	0.08
RO_2+HO_2	0.59	0.04	0.44	0.00
Total	**2.37**	**0.20**	**5.17**	**0.08**

In the post-monsoon campaign, PAN formation (49%) and RO_2+NO (42%) dominated RO_2 radical loss in the daytime, followed by RO_2+HO_2 (8%). RO_2+RO_2 representing 1% of RO_2 termination routes.

The daily variation in day-time percentage contributions to RO_2 loss are presented in Figure 3.45, and the average RO_2 routes on a day to day basis are summarised in Table 3.15. In the pre-monsoon campaign, there were some variations between contributions of different RO_2 termination sources to total RO_2 termination. Although there were only small variations in the total RO_2 termination rates, the highest rates occur on 31/05 due to elevated RO_2+HO_2 and PAN termination. In the post-monsoon, some variation in RO_2 termination contributions was observed, particularly on 14/10 when PAN formation did not contribute to RO_2 loss. This is due to the backward reaction of PAN destruction to re-form RO_2 radicals occurring at the same rate as PAN formation, leading to a net zero day-time RO_2 initiation/termination from this route.

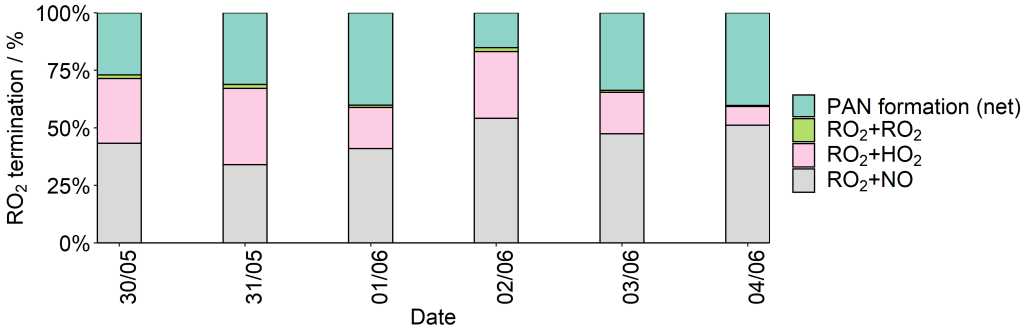

(a) Pre-Monsoon

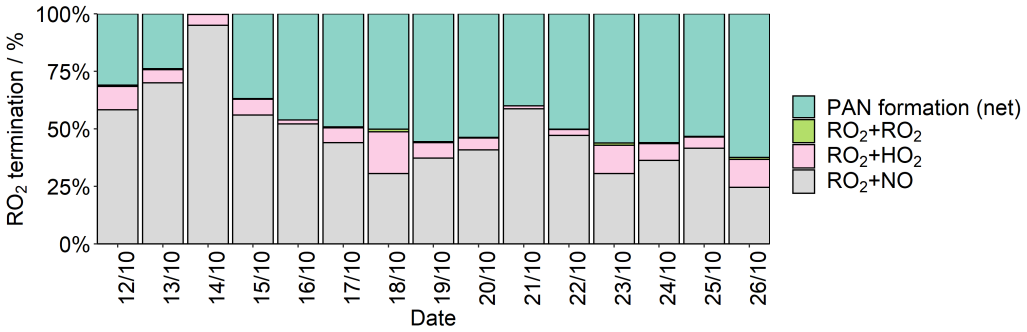

(b) Post-Monsoon

Figure 3.45: Average day-time (06:00 - 18:00) modelled contributions of rates of RO_2 termination during the pre-monsoon (a) and post-monsoon (b) campaigns.

Table 3.15: Average day-time (06:00 - 18:00) modelled rates of RO_2 termination for each day during the pre-monsoon and post-monsoon campaigns.

		RO_2 termination rates / ppbV h^{-1}				
Campaign	Date	PAN	RO_2+RO_2	RO_2+HO_2	RO_2+NO	Total
Pre-Monsoon	30/05/18	0.61	0.04	0.63	0.97	2.25
	31/05/18	1.02	0.06	1.08	1.11	3.27
	01/06/18	0.92	0.02	0.41	0.94	2.29
	02/06/18	0.22	0.02	0.42	0.79	1.46
	03/06/18	0.78	0.02	0.41	1.10	2.32
	04/06/18	0.72	0.01	0.15	0.91	1.79
Post-Monsoon	12/10/18	0.83	0.01	0.27	1.56	2.69
	13/10/18	0.95	0.02	0.23	2.78	3.98
	14/10/18	0.00	0.01	0.09	1.89	1.99
	15/10/18	1.87	0.02	0.35	2.83	5.06
	16/10/18	2.10	0.00	0.07	2.37	4.54
	17/10/18	2.40	0.02	0.31	2.15	4.88
	18/10/18	3.67	0.08	1.32	2.22	7.29
	19/10/18	2.47	0.02	0.30	1.65	4.43
	20/10/18	1.69	0.01	0.16	1.28	3.14
	21/10/18	0.72	0.00	0.02	1.06	1.80
	22/10/18	1.49	0.00	0.08	1.40	2.97
	23/10/18	3.86	0.06	0.85	2.09	6.86
	24/10/18	6.44	0.04	0.83	4.17	11.49
	25/10/18	2.74	0.02	0.25	2.13	5.15
	26/10/18	7.14	0.09	1.39	2.80	11.42

Full radical budget analysis

The total RO_x initiation and termination routes for each campaign are presented in Figure 3.46. During the pre-monsoon, the summed total of OH, HO_2 and RO_2 (RO_x) initiation and termination rates peaked around mid-day, In the post-monsoon, the total rate also peaked around mid-day, but some individual initiation and termination routes peaked earlier or later in the day. Unlike the pre-monsoon campaign, j(HONO) and RO_x+NO peaked around 09:00, as NO concentrations were high, and high levels of night-time HONO were photolysed in the morning, and reformed, terminating OH. Despite smaller photolysis rates in the post-monsoon, particularly towards the end of October, total RO_x initiation and termination rates were $\approx$ 2.5 times higher than the pre-monsoon. Carbonyl photolysis represented the largest source of day-time radical initiation in the pre-monsoon (27%), followed by ozonolysis (23%), $j(O^1D)$ (21%), j(HONO) (21%), VOC+NO_3 (7%) and PAN loss (1%). In the post-monsoon, j(HONO) was the largest contributor to radical initiation (42%), followed by ozonolysis (27%), j(Carbonyls) (21%), VOC+NO_3 (5%), PAN (4%) and $j(O^1D)$ (2%).

Termination rates in the pre-monsoon were dominated by OH+NO_2 (42%), followed by RO_x+NO (19%), HO_2+RO_2 (15%), HO_2+HO_2 (12%) and PAN formation (10%), with smaller contributions from OH+PAN (1%) and RO_2+RO_2 (<1%). In the post-monsoon, radical terminations were dominated by RO_x+NO (37%), closely followed by OH+NO_2 (33%).

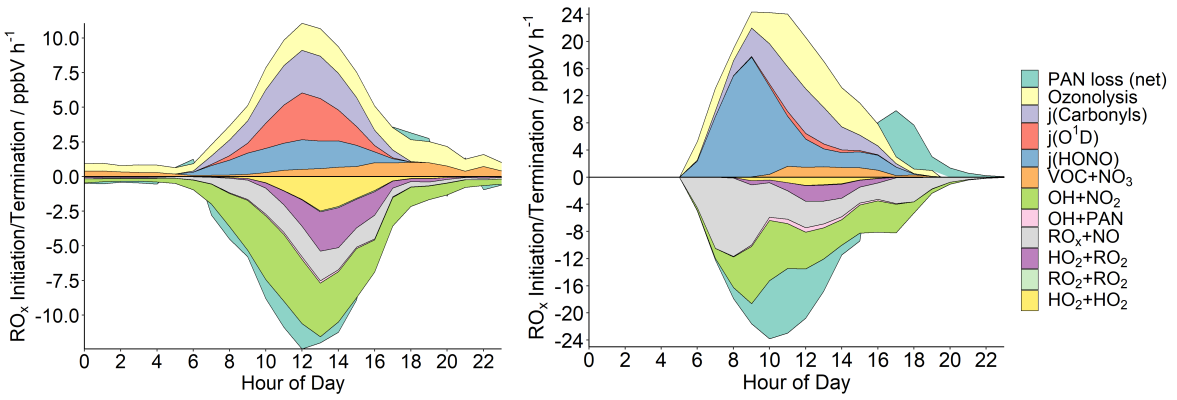

(a) Pre-Monsoon (b) Post-Monsoon

Figure 3.46: Stacked area plots showing the average modelled diel rates of initiation (positive) and termination (negative) of OH, HO_2 and RO_2 (RO_x) radicals during the pre-monsoon (a) and post-monsoon (b) campaigns.

Other important contributors were PAN formation (18%) and HO_2+RO_2 (6%). HO_2+HO_2, OH+PAN and RO_2+RO_2 had smaller contributions to radical termination (3%, 2% and <1% respectively). The higher radical initiation and termination rates in the post-monsoon can be attributed to much higher concentrations of VOCs, NO_x and HONO observed, as described in sections 3.1, 3.2, and 3.3.

A full radical budget for both campaigns, including propagation steps, is presented in Figure 3.47. Mean radical flux rates between 11:00 - 15:00 are presented, for easy comparison with other studies, and as radical fluxes are high during this time of day. In this analysis, RO_2 and RCO_3 have been differentiated. In both campaigns, rates of propagation from RO_2 to RO, RO to HO_2 and HO_2 to OH were high relative to RO_2 and HO_2 termination rates, suggesting propagation of this reaction sequence is efficient. This is important as this propagation sequence can lead to the formation of tropospheric O_3, when RO_2 propagates to RO through a reaction with NO. During the afternoon (11:00 - 15:00), 90% of RO_2 propagated to RO in the pre-monsoon and 93% in the post-monsoon. Of this RO_2 to RO term, 99% of propagation occured through the conversion of NO to NO_2 in the pre-monsoon, and >99% in the post-monsoon.

Radical initiation, propagation and termination rates from the pre- and post-monsoon Delhi campaigns were compared to those calculated from other campaigns in the literature. Table 3.16 summarises the mean daytime (11:00 - 15:00) radical initiation, propagation and termination fluxes from the PUMA campaign (Birmingham, UK), TORCH campaign (Chelmsford, 2003), and ClearfLo (London, 2012) campaigns.

Radical fluxes were much larger in the Delhi pre- and post-monsoon campaigns, compared to the other UK campaigns referenced in Table 3.16. The total initiation and termination rates during the pre-monsoon were closest to those observed during the TORCH 2003 campaign,

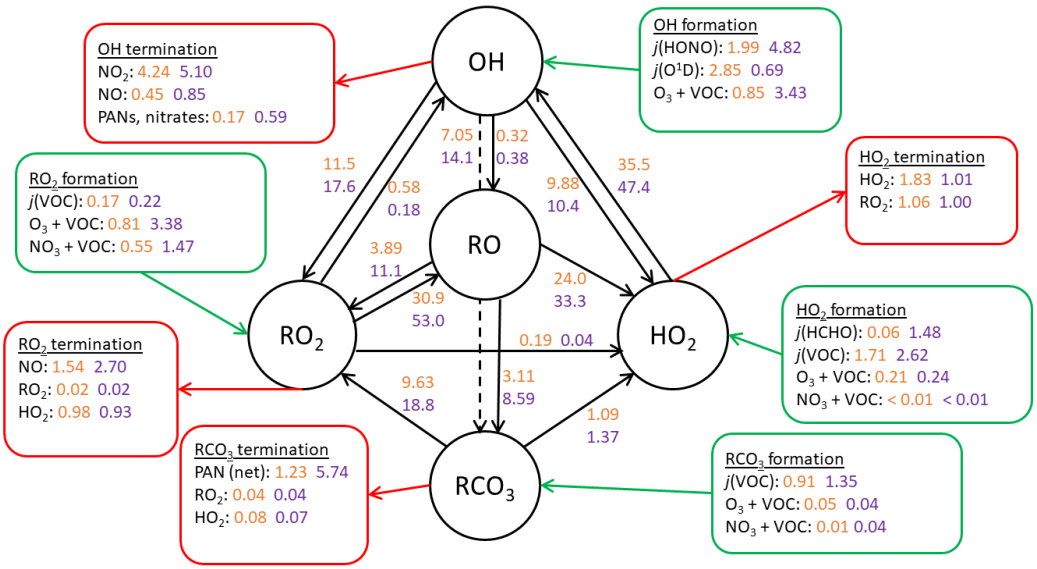

Figure 3.47: Model reaction flux analysis of the daytime mean rate of reaction for the formation, propagation and termination of radicals between 11:00 - 15:00 during the pre-monsoon (orange) and post-monsoon (purple) campaigns in ppbV h^{-1}. Radical initiation and termination routes are shown in green and red boxes respectively.

with radical initiation rates in the pre-monsoon campaign were 33% larger. However, propagation rates were much higher during both DelhiFlux campaigns, with Delhi post-monsoon daytime mean HO_2-OH propagation rates approximately 10 times greater than those calculated for PUMA 2000 and TORCH 2003. Higher initiation rates in the Delhi campaigns may be due to the very high VOC concentrations observed during the campaigns, leading to the formation of radicals through carbonyl photolysis, as well as HONO photolysis. The availability of VOCs for ozonolysis will have also contributed to the high initiation rates, as described earlier.

Table 3.16: Mean daytime (11:00 - 15:00) radical initiation, propagation and termination rates from four field campaigns, along with the Delhi pre-monsoon and post-monsoon rates described in this work.

		Campaign averaged daytime (11:00 - 15:00) radical fluxes / ppbV h^{-1}					
Campaign		PUMA (1999)	PUMA (2000)	TORCH (2003)	ClearfLo (2012)	DelhiFlux (2018)	DelhiFlux (2018)
Location		Birmingham, UK	Birmingham, UK	Chelmsford, UK	London, UK	Delhi, India	Delhi, India
Month		June - July	January - February	July - August	July - August	May-June	October
Reference		Emmerson et al., 2005 [116]	Emmerson et al., 2005 [116]	Emmerson et al., 2007 [117]	Whalley et al., 2018 [58]	this work	this work
OH	initiation	1.16	1.25	0.93	2.54	5.69	8.94
OH	termination	2.00	1.18	1.64	2.31	4.86	6.54
HO_2	initiation	1.70	0.51	3.35	1.20	1.98	4.34
HO_2	termination	0.12	0.03	2.95	0.20	2.89	2.01
RO_2	initiation	1.73	1.12	3.34	0.82	2.50	6.50
RO_2	termination	2.59	1.74	3.16	2.45	3.89	9.50
OH-HO_2	propagation	1.06	0.69	0.95	2.00	9.88	10.38
HO_2-OH	propagation	8.31	5.21	5.03	5.53	35.50	47.44
OH-RO_2	propagation	7.27	5.05	3.51	3.77	18.55	31.70
RO_2-HO_2	propagation	6.70	4.87	3.60	0.06	1.13	1.41
Total	initiation	4.59	2.88	7.66	4.57	10.17	19.78
Total	termination	4.71	2.94	7.76	4.96	11.64	18.05

In the Delhi post-monsoon campaign, photolysis rates were comparable to those observed during a campaign in Beijing in May 2017 (Figure 3.48). This allowed for an interesting comparison of the radical budgets between the two campaigns (Figure 3.49).

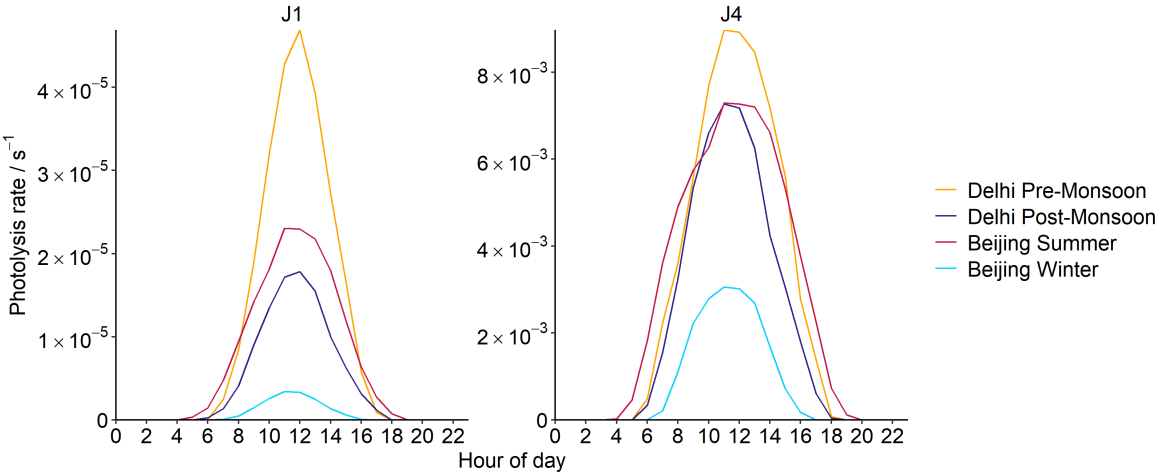

Figure 3.48: Mean diel profiles of $j(O^1D)$ (J1) and $j(NO_2)$ (J4) photolysis rates during four campaigns in pre-monsoon Delhi (orange), post-monsoon Delhi (purple), summer Beijing (red) and winter Beijing (blue). The hour of day is given as the local time of Delhi and Beijing respectively.

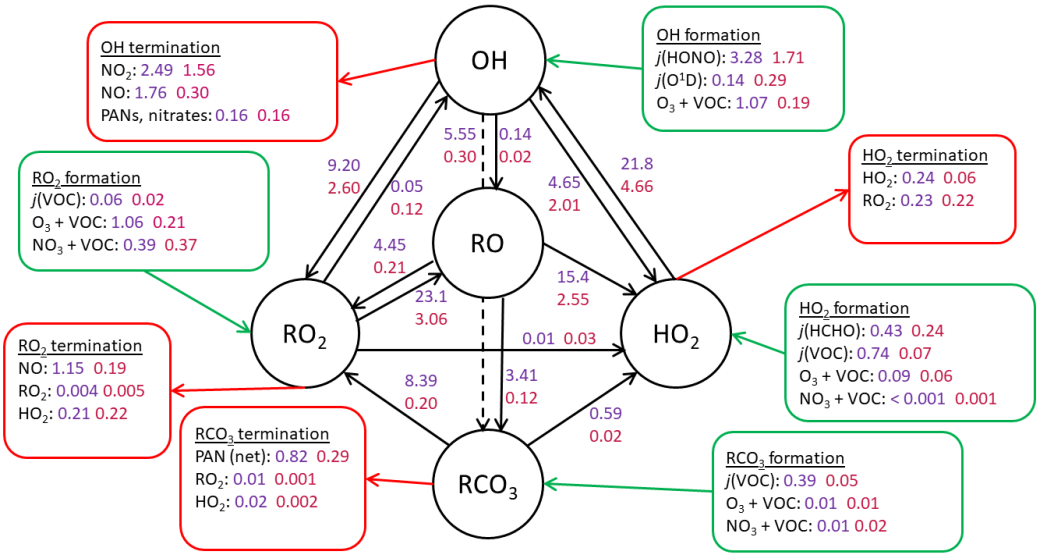

Figure 3.49: Model reaction flux analysis of the diel mean rate of reaction for the formation, propagation and termination of radicals during the post-monsoon Delhi campaign (purple) and the Beijing summer campaign (red) in ppbV h^{-1}. Radical initiation and termination routes are shown in green and red boxes respectively.

In both campaigns, $j(HONO)$ was the dominant source of OH formation. Although the reaction fluxes propagating RO_2 to RO, followed by RO to HO_2 and HO_2 to OH were larger in the Delhi post-monsoon campaign, RO_2 and HO_2 termination rates were also larger in Delhi

than the Beijing summer campaign. This explains why larger radical fluxes in Delhi did not lead to very high O_3 concentrations relative to those observed in Beijing.

3.6.3 Model uncertainties

Although this study presents a detailed analysis of the radical budgets in the Delhi pre-monsoon and post-monsoon, it is important to consider that it was not possible to compare the model generated radical concentrations to measured data. The radical concentrations presented here are therefore a modelled estimation of the radical concentrations, derived from the concentrations and reactivity of an extensive range of model constrained species and parameters. There have been many studies in the field were radical concentrations have been measured, allowing for discrepancies between measured and modelled radical concentrations to be addressed.

One example is the ClearfLo campaign in London, in the summer of 2012 [58]. In this study, the model generally performed well at estimating OH concentrations, and the OH reactivity budget was mostly closed. Although modelled-measured OH concentrations were in agreement during easterly winds, the model overestimated RO_2 concentrations by almost a factor of 2. Due to the good agreement in modelled-measured OH concentrations, particularly when the VOC suite was extended to include the larger species measured using GC $\times$ GC instrumentation, this was unlikely due to an overestimation in RO_2 sources. Instead, it is possible that a RO_2 sink route had not been accounted for [58]. However, more generally across the campaign period, RO_2 concentrations were found to be under-predicted by the model when NO was high. This was also observed in the APHH Beijing summer campaign in 2016. [59]. The cause of this was attributed to missing photolytic RO_2 sources, that are co-emitted with NO and may thus build up over-night. One example is $ClNO_2$, which photolyses to form Cl radicals which behave as atmospheric oxidants, leading to the formation of RO_2. On the addition of $ClNO_2$ to the Beijing box model study, large increases in modelled RO_2 were observed, and this brought the measured and modelled RO_2 into good agreement on several occasions during the campaign [58]. As there are not any radical concentrations available from either the pre-monsoon or post-monsoon Delhi campaigns, it is not possible to examine the discrepancies between the modelled and observed radical concentrations. This represents the largest uncertainty in the use of the box model to assess both radical concentrations, and the radical budget.

3.7 Conclusions from the modelled radical budget analysis of Delhi

Modelled concentrations of HO_2 and RO_2 in both the Delhi pre-monsoon and post-monsoon campaigns were much smaller than those calculated using the photostationary steady state analysis, incorporating the Leighton ratio. This is consistent with Beijing, another Asian megacity, and highlights the importance of using a detailed chemical box model to assess radical concentrations, rather than the more idealised photostationary steady state calculations. The radical budget analysis of both pre-monsoon and post-monsoon Delhi revealed rapid radical processing, when compared to previous studies across the globe. In the post-monsoon campaign, HONO photolysis was the most significant route to OH initiation by far (73%). In this campaign, HONO photolysis alone contributed to 42% of total radical initiation. In both the pre-monsoon and post-monsoon campaigns, ozonolysis was found to be a significant contributor to total radical initiation, contributing to 23% and 27% of radical initiation respectively. The but-2-enes and pent-2-enes were found to be the largest contributors to this ozonolysis. In the pre-monsoon, these compounds were responsible for 27% of HO_2 initiation through ozonolysis, and 39% of RO_2 initiation through ozonolysis respectively. In the post-monsoon, the but-2-enes and pent-2-enes were responsible for 38% of HO_2 initiation through ozonolysis, and 14% of RO_2 initiation through ozonolysis respectively. It is therefore essential that the mechanisms for radical production from these species are well described in the Master Chemical Mechanism (MCM). A more detailed analysis of the formation pathways of these alkenes, along with a description of the possible discrepancies between experimentally determined pathways and those described in the MCM, is provided in Chapter 5. This chapter goes on to suggest that the propensity for these species to produce the OH radical may be overestimated in the MCM, which leads to additional uncertainties in modelled concentration of radicals and well as the radical budget analysis. As radicals concentrations were not measured during the Delhi field campaigns, it is not possible to assess the possible discrepancies of modelled radicals with observations. This represents the largest uncertainty with this study, and so any conclusions drawn from this analysis should be with this in mind. As there is more data available for the Delhi post-monsoon than the Delhi pre-monsoon campaign, the next chapter of this thesis will focus on the atmospheric chemistry of the post-monsoon campaign only. The rapid radical processing described in Chapter 3 suggests that ozone formation may be very efficient in Delhi, particularly during the post-monsoon. Chapter 4 builds on the detailed chemistry described in Chapter 3, by using the chemical box model to investigate the sensitivity of in situ ozone production to NO_x and VOCs, both grouped and individually.

Chapter 4

Ozone production sensitivity to VOCs and NO_x

During October 2018, concentrations of speciated non-methane hydrocarbons volatile organic compounds (C_2 – C_{13}), oxygenated volatile organic compounds (o-VOCs), NO, NO_2, HONO, CO, SO_2, O_3, and photolysis rates, were continuously measured at an urban site in Old Delhi (see Chapters 2 and 3). These observations were used to constrain a campaign tailored chemical box model, incorporating the Master Chemical Mechanism (MCM). The sensitivity of in situ O_3 production to changes in NO_x, VOCs, aerosol surface area, and photolysis rates was explored. A discussion of the the sensitivity of O_3 production to the observational data grouped by sources described by the EDGAR emissions inventory follows. This chapter is based on work published in Nelson et al., 2021, in which I took the lead role in data analysis, paper composition, and authorship [1].

4.1 The importance of investigating ozone production sensitivities in India

The majority of the world's population now live in urban areas. This is projected to increase from 55% in 2018 to 68% of the global population by 2030, with 90% of this growth occurring in Asia and Africa [118–120]. Rapidly increasing industrialisation and urbanisation, coinciding with fast population growth has led to worsening air quality in many of these densely populated regions. This is driven by the increasing emissions of nitrogen oxides (NO_x = NO + NO_2), largely associated with transport, and volatile organic compounds (VOCs), released from a diverse range of sources. Photochemical reactions in the atmosphere then lead to the formation of a wide range of important secondary pollutants, including ozone (O_3) and secondary inorganic and organic aerosol.

Tropospheric O_3 is both an air pollutant and an important greenhouse gas throughout the troposphere [121]. High levels of O_3 can adversely affect vegetation, global crop yields [122], and human health, with long-term exposure increasing the risk of death from cardiovascular and respiratory illnesses [123], and short-term exposure leading to the exacerbation of asthma in children [124]. O_3 exposure has been linked to both acute and chronic pulmonary and cardiovascular health outcomes through both animal toxicological and human clinical studies, with one study showing statistically significant decreases in the lung function of adults on an average exposure of 70 ppbV of O_3 across five 6.6-hour windows [17, 125–127]. As a result of increased anthropogenic emissions, tropospheric O_3 increased globally during the 20th century, and has continued to rise regionally in Asia during the 21st century [127–129]. Background tropospheric O_3 has also continued to increase [130, 131]. Since the 1990s, surface O_3 trends have varied by region [129, 132, 133], but trends in the free troposphere have been overwhelmingly positive [134, 135]. Both satellite data and global chemical transport models have identified India and East Asia as the region with the greatest O_3 increases between 1980-2016 [136], with the rate of change per decade between 2005-2016 more than double that of the rate between 1979-2005 [136].

Unlike other pollutants such as NO_x and SO_2, ground-level O_3 is not directly emitted but is formed in the atmosphere from the photochemical processing of a range of reactive precursor species [137]. O_3 reduction strategies are complicated by its non-linear relationship with its precursor species NO_x, CO and VOCs; their reduction does not necessarily lead to a reduction in O_3, and O_3 production is also influenced by longer lived gases such as CH_4 and CO. The urban atmosphere can be classified as being either VOC-limited or NO_x-limited. In a VOC-limited environment, O_3 can be effectively reduced by reducing VOCs, whereas decreasing NO_x may have a limited effect or even increase the local O_3 production rate, $P(O_3)$ [138]. In a NO_x-limited regime, reducing NO_x emissions is the most efficient approach for reducing O_3 production. Before implementing emission abatement strategies, it is therefore important to consider which regime prevails. Highly populated urban areas are commonly

VOC-limited, meaning reducing NO_x without also reducing VOC sources may potentially lead to an increase in local $P(O_3)$ [139, 140], and hence lead to an increase in ground-level O_3 concentrations.

As discussed in Chapter 1, O_3 formation is mediated by the reactions of peroxy radicals, RO_2 and HO_2, formed in the OH-initiated oxidation of VOCs (equation 4.1), with NO to produce NO_2 (equations 4.2 and 4.4). NO_2 is then rapidly photolyzed back to NO, forming $O(^3P)$ (equation 4.5), which can rapidly react with O_2, leading to O_3 (equation 4.6). This recycling of NO to NO_2 leads to net production of O_3 [137]. A description of how net O_3 production, $P(O_3)$, is calculated from observed and modelled concentrations can be found in section 4.3.4.

$$RH + OH + O_2 \longrightarrow RO_2 + H_2O \tag{4.1}$$

$$RO_2 + NO \longrightarrow RO + NO_2 \tag{4.2}$$

$$RO_2 + O_2 \longrightarrow R'{=}O + HO_2 \tag{4.3}$$

$$HO_2 + NO \longrightarrow OH + NO_2 \tag{4.4}$$

$$NO_2 + h\nu \longrightarrow NO + O(^3P) \quad (\lambda < 420 \text{ nm}) \tag{4.5}$$

$$O(^3P) + O_2\ (+M) \longrightarrow O_3\ (+M) \tag{4.6}$$

The propensity of a particular VOC species to enhance O_3 production is determined by its reactivity, structure and ambient concentration [141]. The sources of emissions, and their relative magnitudes, differ between cities, leading to differences in the role played by individual VOCs with respect to O_3 production. Previous studies in megacities have found that a range of different VOC classes lead to ground-level O_3 production. A comprehensive study of chemical processing in London, during the 2012 summer ClearfLo campaign, found biogenic and longer-chain VOCs from diesel sources to be of greatest importance to VOC-hydroxyl radical reactivity, and thus in situ O_3 formation [57, 65]. Studies investigating the sensitivity of O_3 production to different VOC classes in Shanghai (2006 – 2007) found that monoaromatic species dominated, accounting for 45% of the total O_3 production [142]. Another study in Shanghai (summer 2009) identified significant contributions to O_3 production from but-2-enes

[143]. Biogenic species, such as isoprene, were found to have the greatest impact on OH reactivity, $k(OH)$, an indicator for O_3 production, in Seoul in 2015 [144] and the Pearl River Delta in 2006 [145], whereas another study pointed to the importance of monoaromatics, followed by isoprene and anthropogenic alkenes to O_3 production in Seoul in spring 2016 [146]. These studies incorporated a variety of chemical detail into their models, dependent on the breadth of their VOC measurement suite, with many studies not accounting for oxygenated, or biogenic species other than isoprene [145]. Zavala et al., 2020 show that the key contributors to VOC-OH reactivity in the Mexico City Metropolitan Area (MCMA) between the 1990s and 2019 have changed, with aromatic and alkene contributions decreasing with reduced VOC emissions from vehicular sources [147]. Oxygenated VOCs from solvent consumption and personal care products dominate the VOC-OH reactivity in recent years, leading to sustained high O_3 concentrations in the MCMA [147, 148]. Understanding which precursor species are key to O_3 production in any given city allows governments to introduce measures to combat air quality problems [118].

Over the past two decades, advances in vehicle emission technology, along with improvements in residential heating, have led to decreased NO_x emissions in industrialised and highly populated regions of the western world [149]. In many European cities, additional measures banning vehicle types in busy areas during weekdays, and upgrading the Heavy Goods Vehicle (HGV) vehicle fleet, has led to further reductions in ambient NO_2 [150]. In 2013, China introduced the Air Pollution Prevention and Control Action Plan [151]. New measures included the improvement of industrial emissions standards, the promotion of cleaner fuels to replace coal in the residential sector, and the removal of older vehicles from the roads. As a result of these new controls, NO_2 emissions in Beijing have decreased by 32% since 2012 [152–154]. Despite these successes, surface O_3 pollution across China has continued to increase [105, 106]. The overall O_3 formation potential (OFP) of VOCs has increased alongside this, despite reduction strategies leading to reduced emissions of alkanes and alkenes. This is explained by an increasing emission of VOC species with higher OFPs, such as toluene and xylenes, driven by solvent use and industrial processes [105].

The megacity of Delhi, with an estimated population of over 28 million in 2018 [120], suffers from some of the world's poorest air quality [155]. Significant efforts have been made over the past two decades to reduce the air pollution burden in Delhi, including the introduction of fuel quality standards, a new metro system to improve public transport, and an odd-even traffic number plate system [156, 157]. Since the late 1980s, steps to mitigate the impacts of vehicle and fuel emissions in India have been implemented. Initial interventions included switching to compressed natural gas (CNGs) for autorickshaws and buses in Delhi and other major cities. Since 2010, Bharat IV fuel quality standards have been implemented across cities in India, based on the 2003 Auto Fuel Policy. These changes have resulted in reduced annual NO_x emissions nationally, compared with the projected emissions without policy implementation [156].

A recent study of the implications of the SARS-CoV-2 pandemic on air quality compared pollutant levels of $PM_{2.5}$, PM_{10}, NO_2, CO and O_3 in Delhi, and across other Indian cities, before and after a national lockdown [158–160]. The results showed significant improvements in post lockdown air quality, with reductions in ambient NO_2, $PM_{2.5}$ and PM_{10} exceeding 50% compared to business as usual. However, increased concentrations of ground-level O_3 (>10%) were also observed and were attributed to reductions of NO leading to reduced consumption of O_3. Another study found that, after removing meteorological biases, concentrations of NO_2 and $PM_{2.5}$ at urban background sites in Delhi to have reduced by $\approx$ 51% and $\approx$ 5% respectively, with O_3 concentrations increasing by $\approx$ 8% [161]. Prior to the SARS-CoV-2 pandemic, studies have observed high concentrations of ambient O_3 in New Delhi, with high levels associated with anti-cyclonic conditions (sunny and warm, stagnant winds and lower humidity) typical during October, the month in which the observational dataset used in this study was obtained [53, 162]. Poor air quality is exacerbated in late October - November, when additional O_3 precursor pollutants are emitted from regional agricultural biomass burning of crop residues within the wider area, and from firecrackers and the burning of effigies as part of seasonal festivities [163, 164].

Several recent studies have examined the sources of VOCs in Delhi. Top down and bottom-up approaches have shown gas-phase organic air pollution to be predominantly from petrol (gasoline) and diesel fuel sources. In two 2018 studies at two different urban sites in Delhi, Stewart et al., 2021 [54] and Wang et al., 2020 [165] showed that 52% and 57% of the measured mixing ratio were from combined petrol and diesel sources. Smaller contributions to the overall VOC burden were found from solid fuel combustion, 16% [54] and 27% [165]. These data were in line with Guttikunda and Calori, 2013 [166], who produced an inventory which showed that petrol and diesel sources were responsible for 65% by mass of hydrocarbons in Delhi. VOC emissions have also been shown to be dominated by petrol and diesel sources ($\approx$ 50%) in a study which conducted positive matrix factorisation (PMF) analysis on proton transfer reaction mass spectrometer flux measurements taken in a follow-on campaign in early November 2018 at IGDTUW [167].

There have been several recent studies focused on understanding VOC emissions from sources specific to Delhi. Stewart et al., 2021 [168] studied the types of intermediate-volatility and semi-volatile gases released from solid fuels in Delhi to better understand their potential impact on air quality, and Stewart et al., 2021 [169] produced highly speciated non-methane VOC emission factors from a range of solid fuel combustion sources characteristic to Delhi, which were used by Stewart et al., 2021 [170] for use in regional policy models and global chemical transport models. Stewart et al., 2021 [171] found that fuel wood, crop residue, cow dung cake and municipal solid waste burning were shown to be 30, 90, 120 and 230 times more reactive with the OH radical, which can lead to O_3 formation, than liquified petroleum gas (LPG), and may be one the factors for the high O_3 levels, and overall poor air quality, observed.

To implement successful ground-level O_3 reduction strategies, a good understanding of the non-linear, chemically complex processing of its precursor species is imperative. This work presents a comprehensive in situ O_3 production sensitivity study, using an extensive speciated VOC and o-VOC measurement suite obtained in Delhi during the Atmospheric Pollution and Human Health program in an Indian Megacity (APHH-India) DelhiFlux project post-monsoon field campaign in October 2018. Measurements of NO_x, CO, SO_2, O_3, HONO, 34 photolysis rates, pressure, temperature and relative humidity complete the data set. The observations were used to constrain a detailed zero-dimensional chemical box model, incorporating the Master Chemical Mechanism v3.1.1 (MCM: mcm.york.ac.uk). Significant VOC classes and sources contributing to the OH reactivity, k(OH), are identified by constraining the model to the full VOC suite. By modifying the constraints of these species, their contribution to in situ O_3 production was investigated by comparing relative changes in the modelled rate of O_3 production. The sensitivity of in situ O_3 production to changes in NO, photolysis and PM was also investigated.

4.2 Experimental

4.2.1 Site description

The APHH-India DelhiFlux post-monsoon measurement campaign took place between 4 October and 5 November 2018. The primary measurement site was located on the campus of the IGDTUW, near Kashmere Gate in Old Delhi (28.67 °N, 77.23 °E). A more detailed description of the measurement site is provided in Chapter 2.

4.2.2 VOC and o-VOC measurements

Two gas chromatography (GC) instruments and a proton transfer reaction time-of-flight mass spectrometer, with quadrupole ion guide (PTR-QiTOF, Ionicon Analytik, Innsbruck) were deployed to measure an extensive range of VOCs and o-VOCs. A more detailed description of the instrumentation can be found in Chapter 2. A comprehensive list of the VOC species measured, and used in this box model study, is detailed in Table 4.2.3.

4.2.3 Supporting measurements

Measurements of nitrogen oxides (NO_x) were made using a dual-channel chemiluminescence instrument (Air Quality Designs Inc., Colorado, USA), and carbon monoxide (CO) was measured with a resonance fluorescent instrument (Model Al5002, Aerolaser GmbH, Germany). O_3 was measured using an ozone analyser (49i, Thermo Scientific), and SO_2 was measured using an SO_2 analyser (43i, Thermo Scientific). A more detailed description of these instruments is provided in Chapter 2. Supporting measurements of additional VOCs (PTR-QiTOF-MS), HONO (LOPAP), aerosol diameter (SMPS and GRIMM) and photolysis rates (spectral radiometer) are also detailed in Chapter 2.

Table 4.1: List of observed VOCs, along with campaign averaged mixing ratios and proxy mechanisms for species not found in the master chemical mechanism (MCM). Rate constants for additional species to those in the MCM can be found on the IUPAC Task Group on Atmospheric Chemical Kinetic Data Evaluation database (http://iupac.pole-ether.fr/, last access: August 2018), originally published in [172, 173].

Species	Class	Campaign Average Mixing Ratios / ppbv			Proxy Mechanism used for species not in the MCM	Instrument
		Mean	Min.	Max.		
Ethanol	Alcohol	50.98	29.69	92.00	-	(DC)-GC-FID
Methanol		49.87	21.10	81.71	-	(DC)-GC-FID
Ethane	Alkane	27.09	7.09	51.63	-	(DC)-GC-FID
Isobutane		19.89	5.96	34.95	-	(DC)-GC-FID
Isopentane		15.86	3.97	36.00	-	(DC)-GC-FID
n-Butane		37.21	6.70	69.21	-	(DC)-GC-FID
n-Decane		1.07	0.20	1.99	-	GC × GC-FID
n-Dodecane		1.09	0.16	1.87	-	GC × GC-FID
n-Heptane		1.18	0.20	2.93	-	(DC)-GC-FID
n-Hexane		1.63	0.30	3.69	-	(DC)-GC-FID
n-Nonane		1.35	0.24	2.67	-	GC × GC-FID
n-Octane		0.54	0.09	1.33	-	(DC)-GC-FID
n-Pentane		6.05	1.40	13.48	-	(DC)-GC-FID
n-Tetradecane		1.42	0.41	2.28	*n*-Dodecane	GC × GC-FID
n-Tridecane		2.93	0.52	4.67	*n*-Dodecane	GC × GC-FID
n-Undecane		0.54	0.09	0.95	-	GC × GC-FID
n-Propane		39.12	9.84	68.95	-	(DC)-GC-FID
1,2-Butadiene	Alkene	0.28	0.07	0.45	1,3-Butadiene	(DC)-GC-FID
1,3-Butadiene		0.70	0.07	1.65	-	(DC)-GC-FID
But-1-ene		1.47	0.21	3.02	-	(DC)-GC-FID

cis-But-2-ene		1.03	0.20	2.19	-	(DC)-GC-FID
Ethene		18.34	3.14	39.82	-	(DC)-GC-FID
Isopropene		2.22	0.32	4.65	-	(DC)-GC-FID
Pent-1-ene		0.34	0.06	0.77	-	(DC)-GC-FID
Propene		5.26	0.64	11.30	-	(DC)-GC-FID
cis-But-2-ene		1.07	0.16	2.36	-	(DC)-GC-FID
cis-Pent-2-ene		0.53	0.09	1.40	-	(DC)-GC-FID
Acetylene	Alkyne	8.91	2.16	20.20	-	(DC)-GC-FID
Propyne		0.38	0.09	0.82	Acetylene	(DC)-GC-FID
1,2,3,4-Tetramethylbenzene	Aromatic	0.21	0.01	0.50	1,2,3-Trimethylbenzene	GC × GC-FID
1,2,3,5-Tetramethylbenzene		0.28	0.02	0.64	1,2,3-Trimethylbenzene	GC × GC-FID
1,2,3-Trimethylbenzene		0.64	0.06	1.48	-	GC × GC-FID
1,2,4,5-Tetramethylbenzene		0.16	0.02	0.32	1,2,4-Trimethylbenzene	GC × GC-FID
1,2,4-Trimethylbenzene		1.86	0.20	4.30	-	GC × GC-FID
1,2-Diethylbenzene		0.18	0.02	0.39	*o*-Ethyltoluene	GC × GC-FID
1,2-Dimethyl-4-ethylbenzene		0.35	0.02	0.84	3,5-Dimethyl-1-ethylbenzene	GC × GC-FID
1,3,5-Trimethylbenzene		0.61	0.05	1.41	-	GC × GC-FID
1,3-Diethyl-2-ethylbenzene		0.1	0.02	0.21	3,5-Dimethyl-1-ethylbenzene	GC × GC-FID
1,3-Diethylbenzene		0.2	0.02	0.44	*m*-Ethyltoluene	GC × GC-FID
1,4-Diethylbenzene		0.51	0.04	1.20	*p*-Ethyltoluene	GC × GC-FID
1-Methyl-3-propylbenzene		0.1	0.01	0.21	Propylbenzene	GC × GC-FID
1-Methyl-4-propylbenzene		0.14	0.01	0.33	Propylbenzene	GC × GC-FID
1-Methylpropylbenzene		0.17	0.02	0.36	Propylbenzene	GC × GC-FID
2,3-Dimethyl-1-ethylbenzene		0.09	0.01	0.22	3,5-Dimethyl-1-ethylbenzene	GC × GC-FID
2,4-Dimethyl-1-ethylbenzene		0.17	0.02	0.40	3,5-Dimethyl-1-ethylbenzene	GC × GC-FID
2-Methylpropylbenzene		0.16	0.02	0.36	Propylbenzene	GC × GC-FID
Benzene		5.26	1.15	10.05	-	(DC)-GC-FID

Ethylbenzene		2.09	0.36	4.88	-	(DC)-GC-FID
Isoproylbenzene		0.29	0.03	0.72	-	GC × GC-FID
m-Xylene		2.19	0.32	6.02	-	(DC)-GC-FID
n-Butylbenzene		0.51	0.04	1.20	Propylbenzene	GC × GC-FID
o-Ethyltoluene		0.65	0.08	1.47	-	GC × GC-FID
o-Xylene		1.85	0.30	4.86	-	(DC)-GC-FID
p-Ethyltoluene		1.78	0.27	4.13	-	GC × GC-FID
Propylbenzene		0.39	0.06	0.87	-	GC × GC-FID
p-Xylene		2.19	0.32	6.02	-	(DC)-GC-FID
Styrene		0.90	0.06	1.69	-	GC × GC-FID
Toluene		14.09	2.62	30.09	-	(DC)-GC-FID
Acetaldehyde	Carbonyl	8.30	2.93	11.89	-	PTR-QiTOF-MS
Acetone		13.24	7.44	18.64	-	(DC)-GC-FID
Cyclohexane		0.35	0.12	0.55	-	PTR-QiTOF-MS
Ethyl acetate		8.48	2.04	14.14	-	GC × GC-FID
Formaldehyde		14.29	8.69	18.25	-	PTR-QiTOF-MS
Hexa*n*-2-one		0.48	0.15	0.67	-	PTR-QiTOF-MS
Hexa*n*-3-one		0.48	0.15	0.67	-	PTR-QiTOF-MS
Methacrolein		1.01	0.49	1.46	-	PTR-QiTOF-MS
Methyl isobutyl ketone		0.48	0.15	0.67	-	PTR-QiTOF-MS
Methyl propyl ketone		1.64	0.73	2.28	-	PTR-QiTOF-MS
Methyl vinyl ketone		3.59	1.20	5.29	-	PTR-QiTOF-MS
Isoprene	Isoprene	0.94	0.44	1.57	-	(DC)-GC-FID
α-Phellandrene	Monoterpene	0.09	0.02	0.15	α-Pinene	GC × GC-FID
3-Carene		0.08	0.02	0.15	α-Pinene	GC × GC-FID
Camphene		0.09	0.01	0.16	β-Pinene	GC × GC-FID
Limonene		0.38	0.02	0.79	-	GC × GC-FID

m-Cymene	0.53	0.04	1.03	*m*-Ethyltoluene	GC × GC-FID
Myrcene	0.08	0.01	0.14	Limonene	GC × GC-FID
o-Cymene	0.06	0.01	0.11	*o*-Ethyltoluene	GC × GC-FID
p-Cymene	0.53	0.04	1.03	*p*-Ethyltoluene	GC × GC-FID
Sabinene	0.06	0.02	0.13	*β*-Pinene	GC × GC-FID
Terpinolene	0.07	0.00	0.15	*β*-Pinene	GC × GC-FID
α-Pinene	0.09	0.01	0.18	-	GC × GC-FID
α-Terpinene	0.03	0.01	0.06	*α*-Pinene	GC × GC-FID
β-Ocimene	0.31	0.02	0.67	Limonene	GC × GC-FID
β-Pinene	0.05	0.01	0.09	-	GC × GC-FID
γ-Terpinene	0.05	0.01	0.10	*α*-Pinene	GC × GC-FID

4.2.4 Model description

A tailored zero-dimensional chemical box model of the lower atmosphere, incorporating a subset of the Master Chemical Mechanism [174] into the AtChem2 modelling toolkit [175], was used to identify the main drivers of in situ O_3 production, $P(O_3)$, in Delhi. The MCM describes the detailed atmospheric chemical degradation of 143 VOCs, though 17 500 reactions of 6900 species. More details can be found on the MCM website (http://mcm.york.ac.uk, last access: March 2020). Observations of 86 unique VOCs, NO_x , CO, SO_2, and total aerosol surface area (ASA), along with 34 observationally derived photolysis rates, temperature, pressure, and relatively humidity, were averaged or interpolated to 15 min data and used to constrain the model. Some measured VOCs are not described in the MCM. For these species, an existing mechanism in the MCM was used as a surrogate mechanism. Surrogate species were selected based on their structural similarly to the species of interest, and reaction rates with OH, HO_2 and NO_3 were amended to values found in the IUPAC atmospheric chemical kinetics database [172, 173] (see Table 4.2.3). A fixed deposition rate of 1.2×10^{-5} s^{-1} was used, giving model-generated species a lifetime of approximately 24 h.

The model was constrained to an adjusted value of the observed HONO to account for high surface concentrations and an expected decline in concentration with height. This adjustment is particularly important for HONO, as it is very short lived relative to VOCs, and the atmospheric mixing time. As a result, the high concentrations of HONO measured at ground level are not representative of HONO concentrations throughout the boundary layer [176]. The rate of vertical transport of chemical species through turbulence, or Deardorff velocity (w^*), was calculated during a 2-week follow-on chemical flux campaign in early November 2018 at IGDTUW, after the ground-level measurement period ended. Measurements made from a 30 m tower allowed for the calculation of w^*, from which an hourly averaged diel has been used to determine an approximate rate of vertical HONO transport. Observed HONO concentrations ($[HONO]_{meas}$) were converted to an adjusted HONO concentration ($[HONO]_{input}$) with equation 4.7

$$[HONO]_{input} = [HONO]_{meas}\ e^{\,j(HONO)_t} \tag{4.7}$$

where t is calculated as the time for $[HONO]_{meas}$ to travel to half the boundary layer height at the measured Deardorff velocity, w^*.

The first-order loss of HO_2 to aerosol surface area (k) was calculated with equation 4.8.

$$k = \frac{\omega A \gamma}{4} \tag{4.8}$$

where ω is the mean molecular speed of HO_2 (equal to 43 725 cm s^{-1} at 298 K), γ is the aerosol uptake coefficient (0.2 is used here as recommended by Jacob, 2000), and A is the measured aerosol surface area in cm^2 cm^{-3} calculated (as NSD $\cdot \pi \cdot d^2$) from hourly number size distributions (NSDs).

The base reference model was run for 5 d, with each day being constrained to the diel campaign-averaged observations, to allow for the spin-up of model-generated species. Only the fifth day was taken for analysis to ensure steady state was reached. A range of additional modelling scenarios, based on this base model, were used to investigate the sensitivity of O_3 production, $P(O_3)$, to changes in VOCs, NO_x, aerosol surface area, and/or photolysis rates:

- Scenario 1: vary both total VOC and NO_x by a factor. VOC and NO_x observations were multiplied by a factor of 0.01, 0.1, 0.25, 0.5, 0.75, 0.9, 1.1, 1.25, 1.5, 1.75, and 2.
- Scenario 2: vary individual primary VOCs and NO_x by a factor. A VOC of interest and NO_x observations were multiplied by a factor of 0.01, 0.1, 0.25, 0.5, 0.75, 0.9, 1.1, 1.25, 1.5, 1.75, and 2. Observed carbonyls (all oxygenated compounds excluding alcohols) were not constrained in this scenario to allow for secondary compounds to be varied with changes in concentrations of their precursor VOC.
- Scenario 3: vary by VOC class and vary NO_x. Individual VOC classes were multiplied by a factor of 0.2, 0.4, 0.6, 0.8, 1.2, 1.4, 1.6, 1.8, and 2. NO_x was multiplied by a factor of 0.25, 0.5, and 0.75. All possible combinations of altered VOC class and NO_x observations were constrained in the model. The remaining VOCs not grouped into the class of interest are constrained at their observed values. Observed carbonyls were not constrained in this scenario to allow for secondary compounds to be varied with changes in concentrations of their precursor VOC.
- Scenario 4: increase individual VOC of interest by 5%. The constrained concentration of a VOC species of interest was increased by 5% by molar mass following the procedure carried out in Elshorbany et al., 2009 [177]. Comparison of the change in $P(O_3)$ against the base model allowed for the determination of $\Delta P(O_3)_{increm}$ (section 4.3.4). Observed carbonyls were not constrained in this scenario to allow for secondary compounds to be varied with changes in concentrations of their precursor VOC.
- Scenario 5: vary ASA. ASA was multiplied by a factor of 0.1, 0.3, 0.5, 0.7, 0.9, 1.1, 1.3, 1.5, 1.7, 1.9, and 2. The difference in $P(O_3)$ between each model and the base model was examined.
- Scenario 6: vary photolysis rates. All 34 photolysis rates were multiplied by a factor of 0.1, 0.3, 0.5, 0.7, 0.9, 1.1, 1.3, 1.5, 1.7, 1.9, and 2. The difference in $P(O_3)$ between each model and the base model was examined.
- Scenario 7: vary both individual primary VOCs and NO_x by Emissions Database for Global Atmospheric Research (EDGAR) source sector. VOCs were grouped and observed concentrations were divided into each source sector as described by the EDGAR v5.0 Global Air Pollutant Emissions and EDGAR v4.3.2_VOC_spec inventories. The proportions of VOC and NO_x concentrations attributed to each individual source were multiplied by a factor of 0.01, 0.1, 0.25, 0.5, 0.75, and 0.9. Observed carbonyls were not constrained in this scenario to allow for secondary production of these compounds to be

varied with changes in concentrations of their precursor VOC. For each of these model runs, there were six variations were monoterpenes were assumed to be 0%, 10%, 25%, 50%, 75%, and 100% anthropogenic.

4.3 Results

4.3.1 Observed NO_x, CO, and O_3

The observed mixing ratio (ppbV) time series of NO, NO_2, CO, and O_3 during the campaign are presented in Figure 4.1. High concentrations of NO and CO were observed towards the latter half of the month, with high daytime O_3 concentrations observed throughout the entire measurement period.

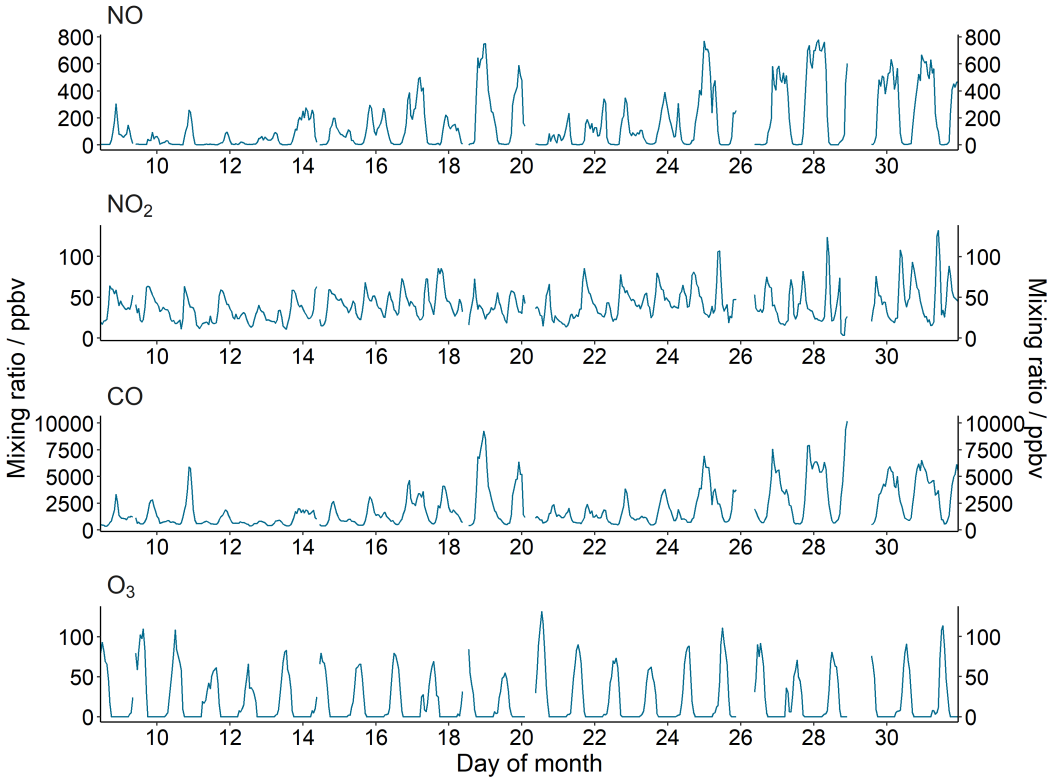

Figure 4.1: Observed mixing ratio time series of (from top to bottom): NO, NO_2, CO, and O_3 during October 2018.

The diel profile of NO, and to a lesser extent CO, has a U-shaped profile, with much higher concentrations observed at night compared to the day Figure 4.2. This profile results from a shallow and stagnant nocturnal boundary layer, described in more detail in Stewart et al. [54]. Average daytime concentrations (06:00–18:00 IST, Indian standard time, roughly in line with sunrise and sunset times) of NO and CO were 58.8 ppbV and 1.2 ppmV, respectively. These campaign-averaged diel profiles have large standard deviations, representing the day-to-day variation in concentration throughout October (Figure 4.1). Average night-time concentra-

tions (18:00–06:00) of NO and CO were 247.0 ppbV and 2.9 ppmV, respectively, with NO and CO concentrations occasionally exceeding 800 ppbV and 10 ppmV, respectively, in the latter half of the month (Figure 4.1). The NO_2 profile shows two peaks, at approximately 09:00 and 18:00, perhaps due to increased commuting traffic during these times. The O_3 diel profile peaks at approximately 13:00, with a mean peak concentration of 78.3 ppbV. A rapid increase in O_3 concentration is observed first thing in the morning from around 05:00, which levels off at around 06:00 before again rapidly increasing from 08:00 to a peak concentration $\approx$ 13:00. As the precursor species of O_3 depend on light to undergo the chemical processing that leads to O_3 production, this profile suggests that as the Sun rises rapid photochemical formation of O_3 is initiated by the photolysis of precursors that have accumulated in the lower atmosphere during the night-time. The early morning increase in O_3 concentrations may also be influenced by the reduced NO titration as the boundary layer height increases (Figure 4.2).

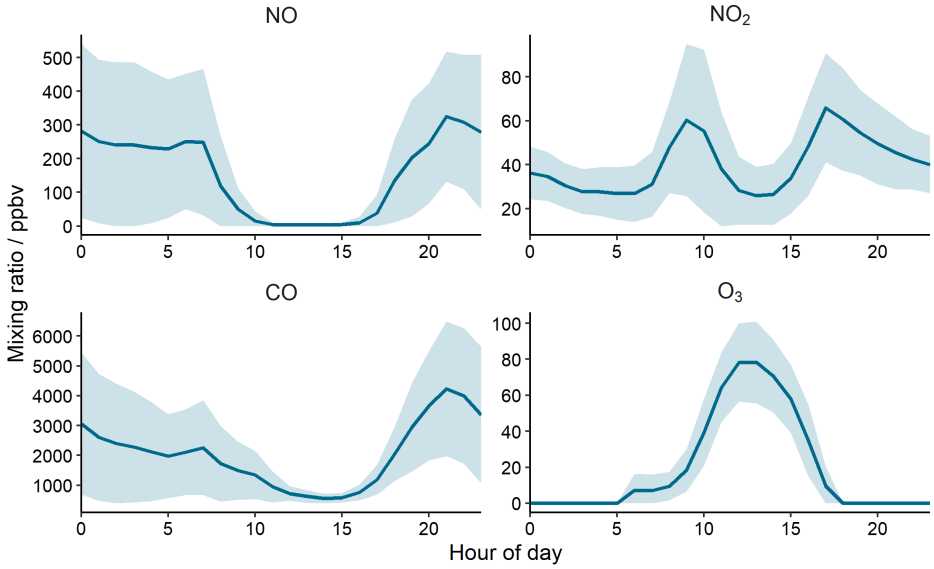

Figure 4.2: October campaign-averaged diel profiles. The shaded ribbon represents the standard deviation of this average.

Average mixing ratios of NO_x and VOCs observed during the post-monsoon Delhi campaign are comparable to those observed in 1970s Los Angeles. High concentrations of NO_x ($\approx$ 200 ppbV) and VOCs (e.g. benzene $\approx$ 10 ppbV; toluene $\approx$ 30 ppbV) led to large concentrations of O_3 in the US city, averaging at around 400 ppbV [178]. Despite the high O_3 concentrations observed in Delhi, O_3 concentrations in post-monsoon Delhi did not exceed 150 ppbV and are of similar magnitude to observed O_3 in Beijing, Shanghai, and Guangzhou despite much higher observed VOC and NO_x concentrations [179]. The lower O_3 observed in Delhi compared to 1970s Los Angeles can be attributed to differences in both topography and meteorology. The isolated coastal city of Los Angeles is surrounded by mountains to the north and east, with the prevailing wind dominating from the coast. Due to its basin-like topography, and with a cool onshore sea breeze often creating a temperature inversion, the

air mass circulates within the city and the transport of emissions out of the basin is impeded. Although landlocked Delhi lies to the southwest of the Himalaya, the city is very flat and resides far enough away from the mountain range to allow for the efficient transportation of air masses from the city. It is also important to consider that the very high concentrations of NO_x and VOCs observed peak to comparable concentrations to Los Angeles during the evening and at night, where they are trapped due to a shallow, stagnant boundary layer, and there is little to no photochemical activity. O_3 production rates in Delhi peak in the morning, when concentrations of pollutants, though still high, are much lower than at night due to rapid boundary layer expansion (see section 4.3.4).

Although 12 key air pollutants, including O_3, have prescribed national ambient air quality standards [50], only four have been identified for regular and continuous monitoring: sulfur dioxide (SO_2), nitrogen dioxide (NO_2), respirable suspended particulate matter (RSPM, or PM_{10}), and fine particulate matter ($PM_{2.5}$). The prescribed national standards for O_3 are an 8-hourly limit of 100 μg m^{-3} ($\approx$ 50 ppbV) and 1-hourly limit of 180 μg m^{-3} ($\approx$ 90 ppbV). The observed O_3 8 h averages between 09:00 and 17:00 throughout the measurement period are shown in Figure 4.3, along with the hourly averaged maximum O_3 concentrations. Our

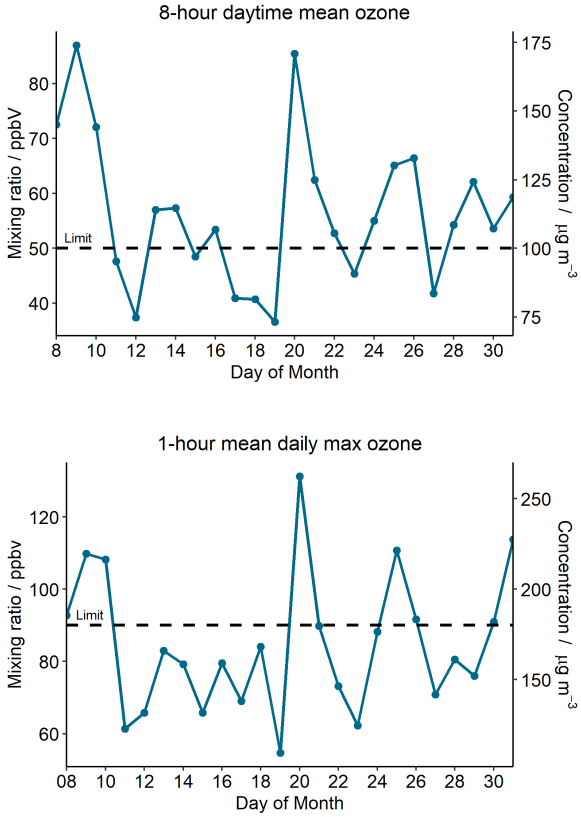

Figure 4.3: The 8 h mean O_3 concentration between 09:00 and 17:00 IST (top) and hourly averaged maximum daily O_3 concentration (bottom) during October 2018. The dashed black line shows the prescribed national standards for O_3.

observations show that the 8 h O_3 prescribed national standard is exceeded on 16 d during our 24 d measurement period (67% of days), and the 1 h max is exceeded on 8 d (33% of days). The published national standards state that any pollutant which exceeds the prescribed values for two consecutive days qualifies for regular and continuous monitoring. As there are up to four consecutive days in which the 8 h daytime mean O_3 limit was breached during our campaign, this implies that O_3 should be continuously and regularly monitored in this part of Old Delhi.

4.3.2 Observed VOCs

Alkanes were the predominant VOC class contributing to the total measured VOC mass concentration (42%), consistent with previous observations at the site [180], followed by alcohols (18%), aromatics (17.8%), and carbonyls (13.9%). The percentage contributions of each VOC class to total measured VOCs, along with mean mass concentrations of the top 10 contributors, are presented in Figure 4.4. The top individual species contributing to the VOC mass concentrations were ethanol (10.7%), *n*-butane (9.9%) and *n*-propane (7.9%).

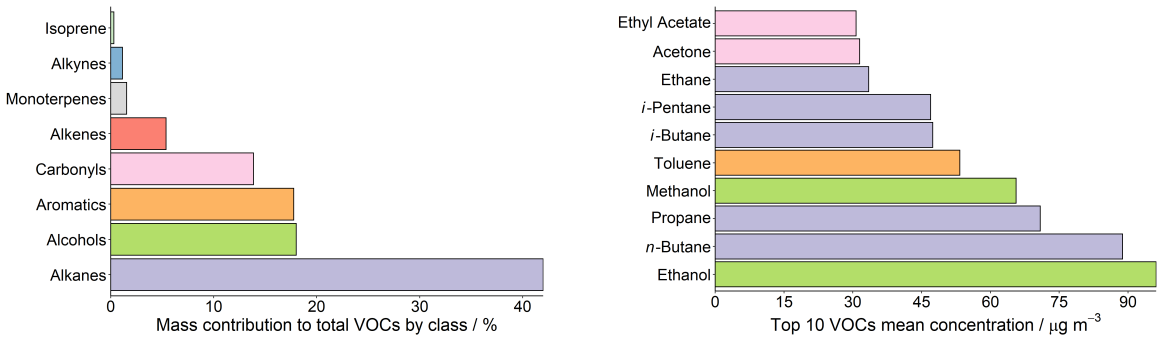

Figure 4.4: Percentage contribution of different VOC classes to the total mean measured NMVOCs (left) and the mean concentrations of the top 10 contributors to total measured VOC concentrations (right) during the campaign in µg m^{-3}. Colours correspond to the different VOC classes.

The general diel profile for all VOCs, excluding isoprene and some oxygenated species, is U-shaped (Figure 4.5). This U shaped profile is also observed for NO and CO. Concentrations are much higher during the night, and lower in the day, as they are concentrated in a stagnant, shallow boundary layer that forms over the city at night [54], and are subject to photochemical losses during the day. The U shape is less apparent for acetone, methanol, and ethanol. This may be a result of very high emissions of these compounds during the day and/or formation through secondary chemistry [54]. Isoprene has a typical biogenic diurnal profile, in contrast to monoterpenes which have a similar trend to other anthropogenic species (see α-terpinene, Figure 4.5). A separate study which conducted PMF analysis on the co-located PTR-QiTOF flux measurements, resolved two traffic-related factors [167]. A large

proportion of the total measured monoterpenes were resolved within traffic factors (≈ 60%) and traffic emissions dominated throughout the campaign (≈ 50% of total VOC emissions). Gkatzelis et al., 2021 [181] have recently shown that monoterpene measurements in New York City can be predominantly apportioned to fragranced volatile consumer products (VCPs) and other anthropogenic sources (e.g. cooking and building materials), and that although biogenic sources are the dominant source of monoterpenes globally, in urban environments monoterpene fluxes from fragranced VCPs can compete with the emissions from local vegetation (see section 4.4 for further discussion of anthropogenic sources of monoterpenes).

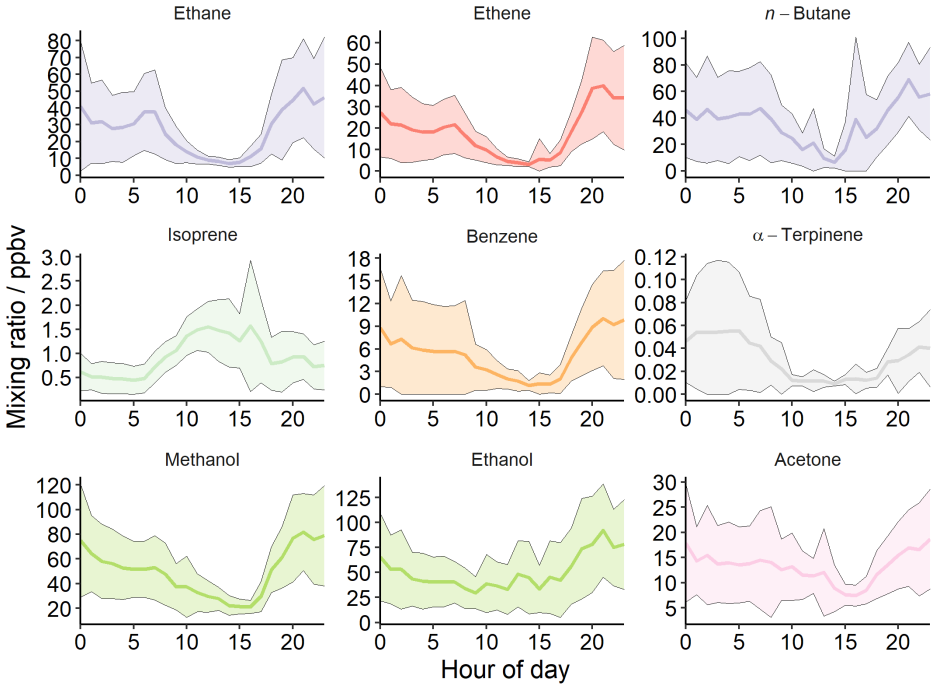

Figure 4.5: Mean campaign-averaged diel mixing ratio profiles of selected VOCs during the campaign: ethane, ethene, *n*-butane, isoprene, benzene, α-terpinene, methanol, ethanol, acetone. The shaded ribbon represents 1 standard deviation from the mean. Colours correspond to the different VOC classes.

The standard deviation of all the aggregate VOC diel profiles is large due to large variations in concentrations from day to day throughout the month. Generally, high concentrations of all species are observed at the end of October and lower concentrations at the start (see Figures 4.6 and 4.7).

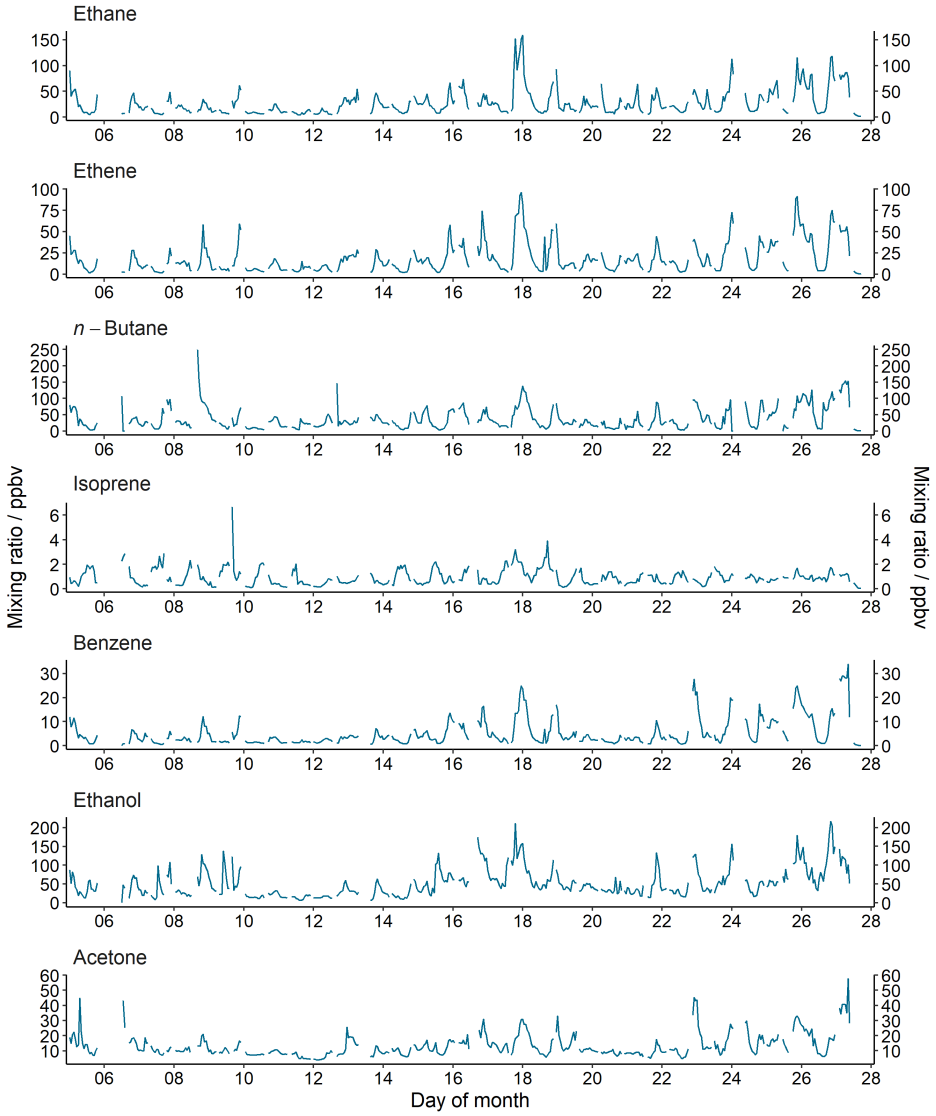

Figure 4.6: Selected timeseries for VOCs measured during October, 2018 at Indira Gandhi Delhi Technical University for Women. Top to bottom: ethane, ethene, *n*-butane, isoprene, benzene, ethanol, acetone.

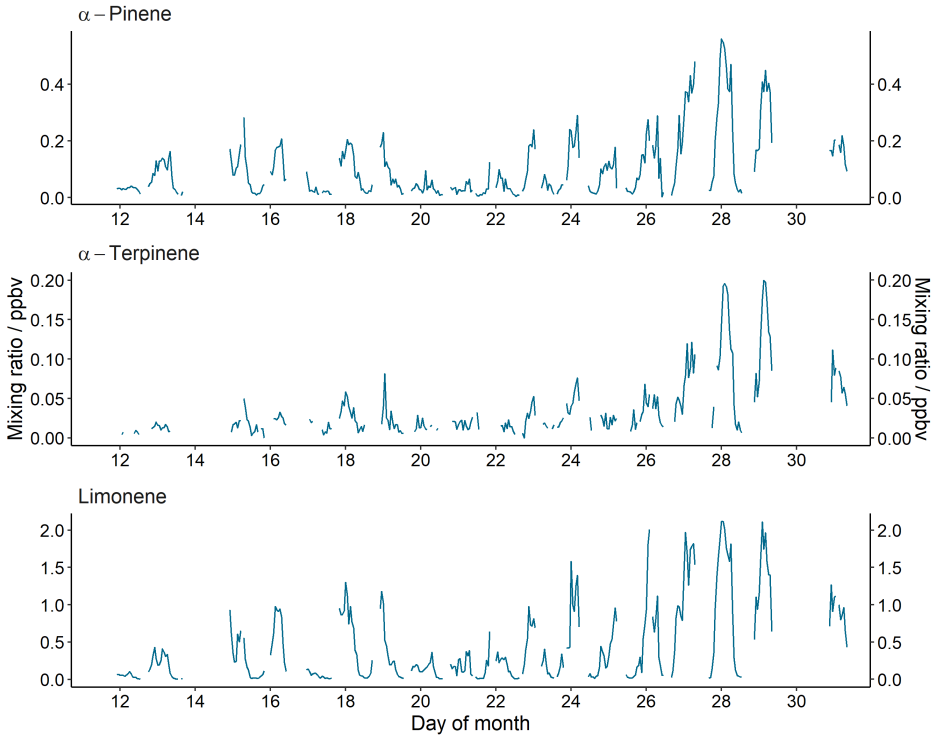

Figure 4.7: Selected timeseries for monoterpenes measured during October, 2018 at Indira Gandhi Delhi Technical University for Women. Top to bottom: α-pinene, α-terpinene, limonene.

4.3.3 OH reactivity, k(OH)

Speciated VOC concentrations alone do not indicate which individual compounds are important for O_3 formation. It is crucial to account for their reactivities with atmospheric oxidants, and their structure, to gain insight into each individual species and compound class contribution to in situ $P(O_3)$. All VOCs react with OH, leading to peroxy radical formation. These peroxy radical species (HO_2 and RO_2) mediate the conversion of NO to NO_2, leading to $P(O_3)$ (equations 4.1 - 4.4). The rate at which VOCs react with OH is thus the rate-determining step in the amount of O_3 formed.

The chemical box model described in section 4.2.4 was used to investigate the total OH reactivity, expressed as k(OH) – a first-order loss rate in units of s^{-1}, of observed precursors to O_3 (base reference model). NO_x, CO, and individual VOC class contributions to k(OH) are presented in Figure 4.8, along with the k(OH) of unmeasured species generated by the model (referred to as "model-generated species" from now on). VOCs and model-generated species represented 67.4% of the total k(OH), with alkenes (9.6%) and aromatics (8.8%) being the largest VOC class contributors. The k(OH) value was higher during the night, showing an inverse relationship with boundary layer height. This is typical for urban environments where nighttime emissions are typically released into a shallow boundary layer (discussed further in Stewart et al., 2021 [54]).

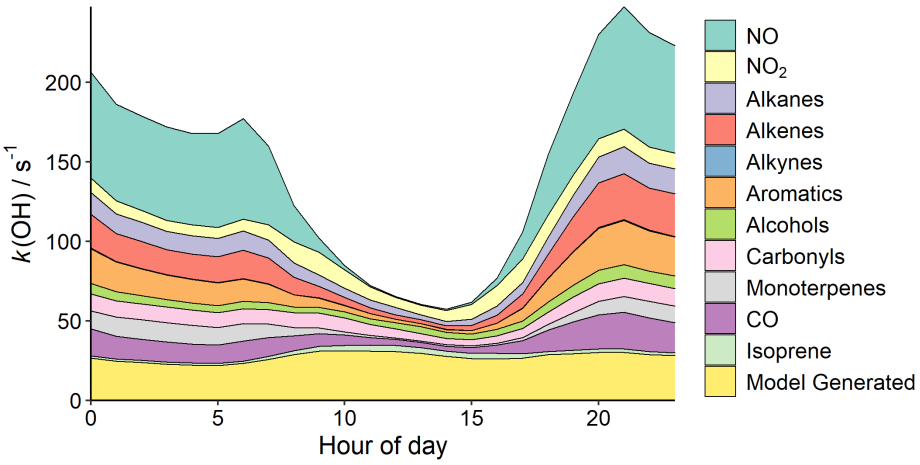

Figure 4.8: Diel profile of campaign-averaged VOCs, CO, and NO_x contributions to OH reactivity, k(OH).

Nighttime boundary layer heights in Delhi were very low, leading to a clearly defined k(OH) profile with a maximum of ≈ 250 s^{-1} at around 21:00 and a minimum of ≈ 57 s^{-1}at 14:00. The campaign average boundary layer height range was approximately 39 – 1550 m. Generally, k(OH) in megacities is found to peak at around 06:00, consistent with morning emissions into a shallow boundary layer. A small peak is also observed around this time in Delhi, but the largest peak is calculated at around 21:00. NO_x represents $\approx 35\%$ – 40% of the total k(OH) at these times, perhaps due to high volumes of traffic. This is supported by VOC traffic PMF factors described in Cash et al. (2021) [167], which peaks during the evening ($\approx$ 19:00–21:00), and account for $\approx 87\%$ of the total emissions at this time.

The values of k(OH) determined in this work are significantly higher than those observed in other megacities, with a daytime minimum k(OH) more than double that observed in Beijing during the summer of 2017 [59]. Previous studies in New York City, Mexico City, and Tokyo have observed k(OH) > 100 s^{-1} [182–184]. A maximum summertime k(OH) of 116 s^{-1} was observed in London during rush hour, but lower OH reactivities of 22–37 s^{-1}were more typical during the campaign [57]. In a study during summertime in Seoul, average k(OH) was approximately 15 s^{-1} in the afternoon, increasing to 20 s^{-1} at night [144]. High OH reactivities were observed in the Pearl River Delta (PRD), with mean maximum reactivities of 50 s^{-1} at daybreak, and mean minimums of 20 s^{-1} observed at noon [145]. The measurement site in the PRD was situated just 60 km north of the industrialised and growing city of Guangzhou. The large reactivities observed here are indicative of large emissions of pollutants from industrial and residential processes, along with the dense traffic network. The inland location is also subject to low wind speeds during the summer months, exacerbating the accumulation of air pollutants. Average summertime k(OH) observations from Beijing, China, observed a k(OH) maximum of ≈ 37 s^{-1} at around 06:00 and daily minimum of k(OH) ≈ 22 s^{-1} at 15:00 [59], within a boundary layer range of approximately 150–1500 m.

In Delhi, O_3 concentrations rapidly increase from ≈ 08:00, peaking around ≈ 13:00 before declining in the afternoon (Figure 4.2). A breakdown of the percentage contribution of each species class to morning k(OH) (08:00–12:00) is presented in Figure 4.9. The average morning k(OH) was dominated by model generated species (31.9%), followed by NO_x (21.5%) and carbonyls (9.2%).

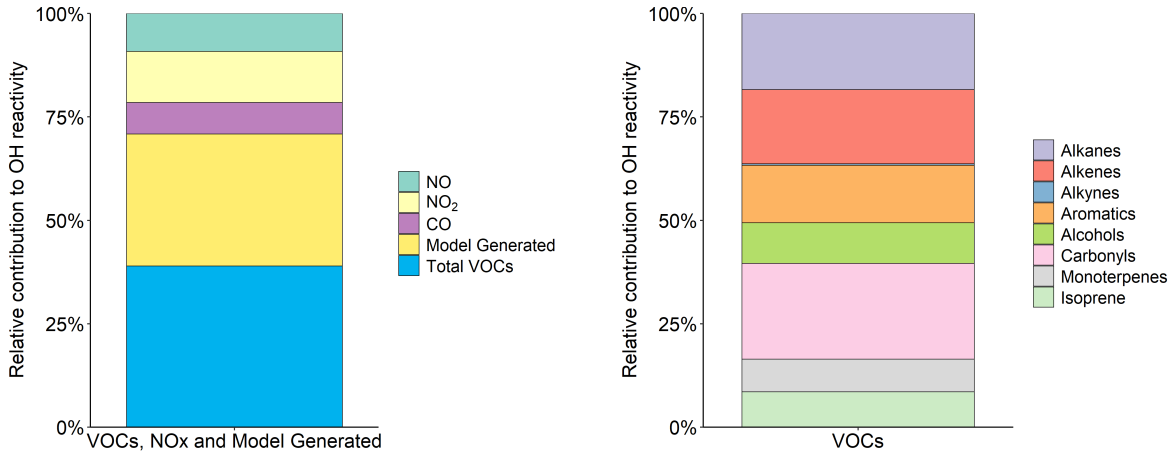

Figure 4.9: Relative contribution of species classes to average morning OH reactivity, k(OH), (08:00–12:00). The contribution of each group to the total k(OH) including NO_x and model-generated species (left) and the contribution of each class to just the VOC proportion of k(OH) (right).

4.3.4 O_3 production potentials

Model-generated species are the products of reactions of VOCs of all classes, meaning the overall contribution of individual classes of VOCs to k(OH) is underestimated in Figures 4.8 and 4.9 (section. 4.3.3). To assess the true contribution of VOCs to k(OH) and production, several model runs where each constrained VOC class was increased by 5% were compared to the base reference model (scenario 4, section 4.2.4).

One way to assess the contributions of different VOCs to O_3 production is to determine the change in O_3 production, $\Delta P(O_3)$, when the base reference model is compared to an adapted model where the VOC of interest is increased by 5% [177]. For both the base and 5% scenarios, the net rate of O_3 production, $P(O_3)$, was calculated by subtracting the instantaneous rate of O_3 loss, $L(O_3)_{inst}$, by the instantaneous rate of O_3 production, $P(O_3)_{inst}$, via Equations 4.9 - 4.11. $P(O_3)_{inst}$ was calculated by determining the NO_2 production rate through reactions of NO with HO_2 and RO_2, assuming the production of a molecule of NO_2 equates to the production of a molecule of O_3. NO_2 loss processes which do not yield O_3, such as removal by reaction with OH and reaction with acyl peroxy radicals to form peroxy acetyl nitrates (PANs), must also be accounted for. In these calculations, OH, HO_2, and RO_2

concentrations are generated from the observationally constrained model.

$P(O_3)_{inst}$ is the rate of NO oxidation by HO_2 and RO_2 radicals:

$$P(O_3)_{inst} = (k_{\mathrm{HO_2 + NO}}[\mathrm{HO_2}][\mathrm{NO}] + \sum_i k_{\mathrm{RO_{2_i} + NO}}[\mathrm{RO_2}][\mathrm{NO}]) \tag{4.9}$$

$L(O_3)_{inst}$ is the rate of loss of O_3 though reactions with OH, HO_2, and photolysis followed by a reaction with H_2O vapour, along with the loss of NO_2 through reactions with OH:

$$\begin{aligned} L(O_3)_{inst} = {} & j(\mathrm{O^1D})[\mathrm{O_3}]{\cdot}f + k_{\mathrm{OH + O_3}}[\mathrm{OH}][\mathrm{O_3}] \\ & + k_{\mathrm{HO_2 + O_3}}[\mathrm{O_3}][\mathrm{HO_2}] \\ & + k_{\mathrm{OH + NO_2 + M}}[\mathrm{NO_2}][\mathrm{OH}][M] \\ & + \sum_i k_{\mathrm{RO_{2_i} + NO_2 + M}}[\mathrm{RO_2}][\mathrm{NO_2}][M] \end{aligned} \tag{4.10}$$

where f is the fraction of $O(^1D)$ atoms (formed in the photolysis of O_3) that react with H_2O vapour to form OH, rather than undergo collisional stabilisation. Net O_3 production, $P(O_3)$, can then be calculated as:

$$P(O_3) = P(O_3)_{inst} - L(O_3)_{inst} \tag{4.11}$$

The O_3 production resulting from an incremental increase of each VOC between 08:00 and 12:00, $P(O_3)_{increm}$, was then calculated with equation 4.12:

$$\Delta P(O_3)_{increm} = \mathrm{Mean}(P(O_3)_i - P(O_3)_{base}) \tag{4.12}$$

where $P(O_3)_i$ is the mean O_3 production between 08:00 and 12:00, calculated from the model run where the VOC of interest is increased by 5%. Using this approach, the 10 VOCs contributing to the greatest change in $P(O_3)$ on an incremental increase, $P(O_3)_{increm}$, are isoprene, α-terpinene, ethene, toluene, propene, α-phellandrene, ethanol, 1,2,4-trimethylbenzene, CO, and β-ocimene (Table 4.2) The full list of $P(O_3)_{increm}$ for 77 VOCs is provided in Appendix B (Table B.1).

Table 4.2: The top 10 highest $\Delta P(O_3)_{increm}$ VOCs, and their respective classes, averaged between 08:00 and 12:00.

Species	Class	$\Delta P(O_3)_{increm}$ (ppb h^{-1})	$P(O_3)$ increase (%)
Isoprene	Isoprene	0.94	0.74
α-Terpinene	Monoterpene	0.66	0.53
Ethene	Alkene	0.40	0.32
Toluene	Aromatic	0.37	0.30
Propene	Alkene	0.35	0.27
α-Phellandrene	Monoterpene	0.30	0.24
Ethanol	Alcohol	0.30	0.24
1,2,4-Trimethlbenzene	Aromatic	0.29	0.23
CO	-	0.28	0.22
β-Ocimene	Monoterpene	0.26	0.21

4.3.5 O_3 production sensitivities to VOC / NO_x ratios

To better understand the complex non-linear chemistry at play, a box model was used to probe the chemical sensitivities of observed precursors to O_3 formation. The model was run 144 times, each with adjusted concentrations of VOCs and NO_x (scenario 1). The observed concentrations were multiplied by a factor to generate unique model runs from which $P(O_3)$ was calculated using Equations 4.9 - 4.11. The resultant $P(O_3)$ isopleth is presented in Figure 4.10.

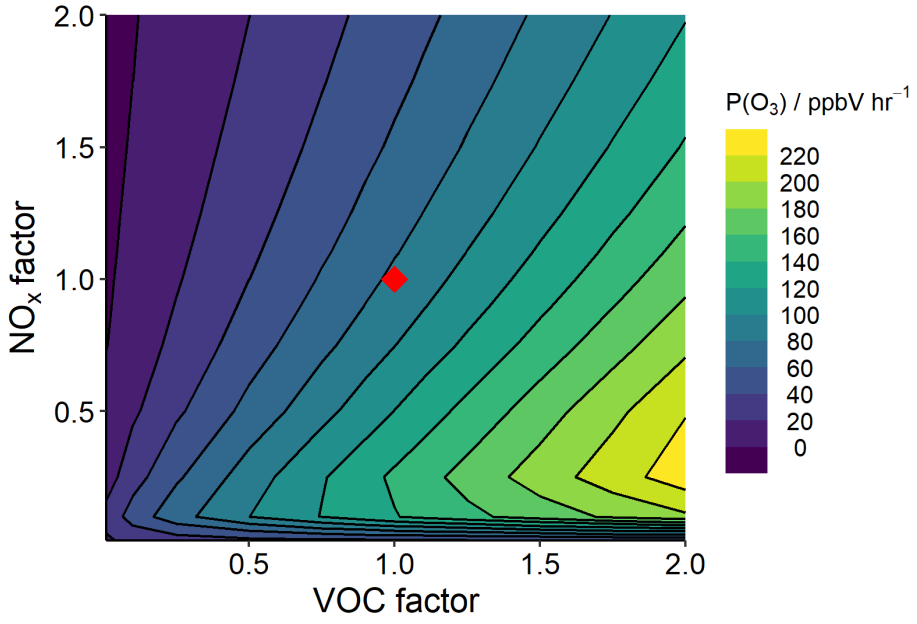

Figure 4.10: Mean modelled O_3 production, $P(O_3)$, isopleth between 08:00 and 12:00 based on varying VOC and NO_x concentrations in the model. The red diamond at point (1,1) represents modelled $P(O_3)$ at observed VOC and NO_x concentrations.

The modelled VOC–NO_x $P(O_3)$ isopleth supports the assignment of Delhi being, on average, in a VOC-limited photochemical regime (Sillman et al., 1990), with the diel profile of O_3 production peaking at 09:00. Reducing NO_x alone and maintaining VOC concentrations

would result in an increase in $P(O_3)$. Therefore reducing, or even maintaining, O_3 levels in the future will require a reduction in VOC emissions, if future emission control measures continue to target NO_x emissions in Delhi. This is consistent with a study of observational data in Delhi, whereby a SARS-CoV-2 lockdown led to a reduction in NO_x emissions and concentrations and an increase in the concentration of O_3 [158]. To implement an efficient and realistic VOC reduction plan, the key VOCs contributing to $P(O_3)$ need to be identified, along with their sources.

As has been previously discussed, O_3 concentrations limits of 50 ppbV were regularly exceeded during the campaign, with the maximum daily 8 h averages peaking at 88 ppbV (Figure 4.3). To successfully reduce O_3 to the limit of 50 ppbV, O_3 production must be reduced by 56%. This can be achieved by reducing NO_x by 25%, 50%, and 75% along with a concurrent reduction in VOCs of 48%, 61%, and 78%, respectively. Alternatively, if VOCs were halved, NO_x reductions could not exceed 29% to keep peak O_3 below 50 ppbV. To obtain a reduction in O_3 production without reducing VOCs would require a NO_x reduction of at least 92%. However, it is important to consider that reducing emissions of NO_x and VOCs by these values will only impact the in situ formation of O_3. Regional O_3 production leading to the transportation of O_3 from outside of Delhi is beyond the scope of this analysis and must also be taken into consideration by policy makers.

4.3.6 O_3 production sensitivity to VOCs by class

The impact of changing VOC concentrations (by class) on mean $P(O_3)$ was investigated using scenario 3 (section 4.2.4). For each model run, the constrained concentrations of all species in the class of interest were multiplied by a "VOC factor". Modelled $P(O_3)$ was calculated upon changing "VOC factor" for CO and six different VOC classes: alkanes, alkenes, aromatics, monoterpenes, isoprene, and alcohols. Changes in $P(O_3)$ were found to be most sensitive to changes in aromatics, followed by the monoterpenes and alkenes (Figure 4.11). Halving aromatic, monoterpene, and alkene concentrations independently (reducing a VOC factor of 1 to a VOC factor of 0.5, Figure 4.11) reduced modelled $P(O_3)$ by 15.6%, 13.1%, and 12.9%, respectively. However, future air quality control strategies are also likely to include a co-reduction in NO_x. As we observed in Figure 4.10, a reduction in NO_x coupled with an insufficient reduction in VOCs is likely to increase $P(O_3)$ in Delhi, under VOC-limited conditions. On concurrently reducing VOC class and NO_x by half (factor of 0.5, Figure 4.11), aromatics, alkenes, and monoterpenes lead to the smallest increase in $P(O_3)$ (24.9%, 29.8%, and 35.5% respectively). However, this still represents a significant increase in $P(O_3)$. This suggests targeting one VOC class alone in future pollutant reduction strategies is insufficient, and that reducing a source/sources emitting multiple VOC classes is important to avoid an increase in $P(O_3)$ on simultaneously reducing NO_x.

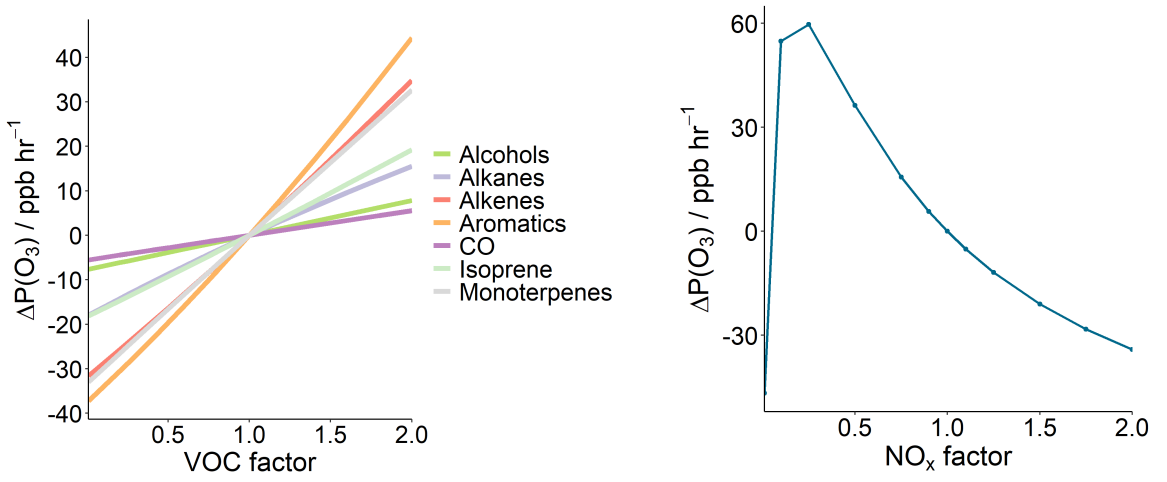

Figure 4.11: Modelled mean morning (08:00–12:00) change in $P(O_3)$ rate for CO and six VOC classes upon varying their concentrations by multiplying by the "VOC factor" (left) and by varying just NO_x (right).

4.3.7 The impact of aerosol surface area on $P(O_3)$

Aerosol particles in the troposphere can impact gas phase chemistry and photochemical activity, affecting $P(O_3)$, in a number of ways. Aerosols can interact with incoming solar radiation, either scattering or absorbing sunlight. The precise impact of aerosol is dependent on a range of factors including chemical composition, particle size distribution, and phase state. It has previously been shown that in highly polluted urban areas, attenuation of the actinic flux due to aerosol absorption can significantly reduce photolysis rates, and hence $P(O_3)$, by up to 30% [100, 185–187]. Conversely, aerosol scattering can potentially increase $P(O_3)$ by increasing the photolysis rates [101, 188].

Aerosol can also participate in heterogeneous chemistry; i.e. the uptake of radicals to aerosol, or reactions at the aerosol surface can affect gas phase radical budgets [189]. A recent regional modelling study linked increasing O_3 concentration trends between 2013 and 2017 in Beijing to decreasing $PM_{2.5}$ concentrations [190]. The study attributed this to the decreased uptake of HO_2 radicals to aerosol particles, leading to increased HO_2 available to participate in $P(O_3)$ (see equation 4.9). However, an experimental study in the North China Plain did not observe the effect [191]. The relationship between aerosol optical depth (AOD) and photolysis rates is strongly non-linear and has a larger impact at low solar zenith angles (i.e. in the morning/evening/high latitudes) [100].

To investigate the potential impact of aerosol related processes in Delhi, ASA and photolysis rates were varied independently in the model using a scaling factor ("Factor", Figure 4.12), and the resulting impact on $P(O_3)$ calculated. The first-order loss of HO_2 to aerosol surface area (k) was calculated using Equation 4.8 (scenario 5, section 4.2.4).

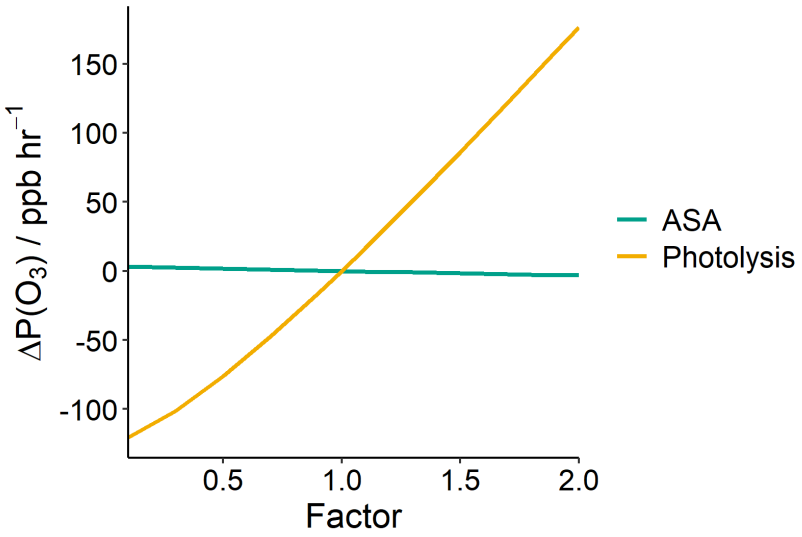

Figure 4.12: Impact of varying photolysis rates and ASA on the change in mean modelled morning O_3 production rates, $\Delta P(O_3)$ (08:00–12:00).

Changes in ASA, with respect to HO_2 uptake, were found to have minimal impact on the modelled mean morning $P(O_3)$ rate (08:00–12:00), as shown in Figure 4.12, in line with the observations of Tan et al., 2020 [191]. The lifetime of HO_2 is dominated by its reaction with NO, within the campaign-averaged NO concentrations observed. Changes to the photolysis rates have a large impact on $P(O_3)$ (Figure 4.12), with $P(O_3)$ increasing roughly linearly with increasing photolysis rates. The impact of changes to AOD on photolysis rates are non-linear and dependent on solar zenith angle (SZA) (i.e. time of day). This work shows that the majority of daily $P(O_3)$ occurs between 08:00 and 12:00, representing an SZA range of 35–80°. Aerosol loading is expected to reduce in Delhi going into the future if India implements air pollution controls in line with other countries. Based on the work of Wang et al., 2019 [100], reductions in PM, leading to reductions in AOD, could potentially increase $j(NO_2)$ by up to 30% at midday and up to 100% at 08:00. This will lead to increased photochemical activity and higher $P(O_3)$.

From an air quality perspective, it is important to consider reducing not only VOCs but also NO_x concentrations in Delhi. Along with this, reductions in PM should also be considered. As we have seen in Figure 4.12, reducing ASA does not significantly impact $P(O_3)$ through heterogenous chemistry. However, an ASA reduction will result in a decrease in AOD, which will in turn increase photolysis rates. A recent study by Chen et al., 2021 [192] modelled the impact of AOD on photolysis in Delhi during November 2018, and found that halving the AOD results in a 14% increase in $j(NO_2)$. In Delhi, total VOCs would need to be reduced by $\approx$ 50% to maintain current $P(O_3)$ rates if NO_x were halved and photolysis rates increased by 14%. However, the impact of reducing aerosol on photolysis rates is complex. Reductions in aerosol at ground level may lead to either increased or decreased photolysis rates near the surface, depending on the scattering properties of the aerosol. Changes in pho-

tolysis rates from increased or decreased aerosol loading may also vary throughout the depth of the boundary layer. The box model assumes photolysis rates are uniform throughout the boundary layer and that aerosols are well mixed. A more detailed study on the temporal and spatial patterns of aerosol in Delhi and its impact on photolysis rates is required to fully assess the aerosol impact on in situ O_3 production [185].

It is important to note that this study focuses on the sensitivity of $P(O_3)$ to ASA through HO_2 uptake only. Additional chemical consequences and feedbacks of decreasing aerosol, such as changes to HONO concentrations, have not been accounted for here. With the high levels of NO_2 observed in Delhi, the heterogenous conversion of NO_2 to HONO on particle surfaces may be an important mechanism [30, 193–195]. HONO reductions from decreased ASA may lead to reduced OH radical formation in Delhi; thus, the impact of ASA reduction on $P(O_3)$ may be underestimated in this work.

There are also additional uncertainties to consider when using a fixed HO_2 coefficient. The HO_2 uptake coefficient used in this study ($\gamma HO_2 = 0.2$) is a recommended value, derived from both historical laboratory data and model-observation comparisons [196–200]. The sensitivity of model generated HO_2 was explored by varying the HO_2 uptake coefficient between 0-1 (Figure 4.13).

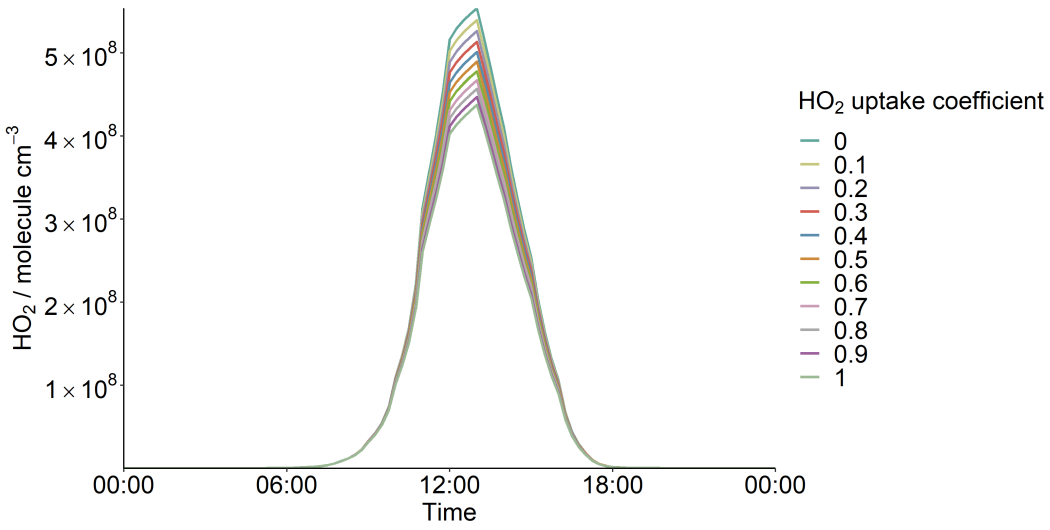

Figure 4.13: Diel profile of model generated concentrations of HO_2 at a range of different HO_2 uptake coefficients.

When the uptake coefficient is not accounted for ($\gamma HO_2 = 0$), there is a 5% increase in HO_2 concentration, compared to the base value of $\gamma HO_2 = 0.2$. Alternatively, if the base coefficient is an underestimation, an uptake coefficient of 1 yields a reduction in HO_2 of 17%. However, variations in the resulting O_3 production rate are much smaller. The difference in maximum $P(O_3)$ between the fixed value of $\gamma HO_2 = 0.2$, and the range of $\gamma HO_2 = 0$ - 1, is no more than 4%.

4.4 Discussion

If future air pollution controls in Delhi follow the air quality strategies prevalent or planned in many other countries, including the EU, there is a danger that urban O_3 concentrations could significantly increase, unless careful consideration is given to the specific atmospheric chemistry occurring in the city. Many other major cities across the globe have focused their air pollution abatement strategies on reducing NO_x and particulate emissions from traffic sources. Urban NO_x emissions (at tailpipe) are likely to decline over time, as a result of improved exhaust gas treatments, the turnover of the fleet to newer, less polluting vehicles, and the increasing prevalence of electric vehicles [118]. While this is also likely to reduce ambient VOC concentrations through reduction in tailpipe and evaporative emissions, this reduction may be smaller than for NO_x. The magnitude of resulting changes in $P(O_3)$ from reduced road transport emissions may depend on the proportion of VOCs emitted from road transport relative to other, non-vehicular sources. As demonstrated here, reductions in NO_x without sufficiently reducing VOC emissions may lead to large increases in $P(O_3)$ under a continued VOC-limited regime. Reducing traffic emissions will also likely lead to reduced aerosol loading in Delhi. Our study suggests a reduction in aerosol surface area will have very little direct effect on $P(O_3)$ via heterogenous chemistry, as HO_2 reactivity is dominated by its reaction with NO. However, an ASA reduction is likely to increase the amount of sunlight reaching the boundary layer and hence photolysis rates. This will lead to a subsequent increased $P(O_3)$, as discussed in more detail by Chen et al., 2021 [192].

$P(O_3)$ in Delhi was found to be most sensitive to reductions in aromatics and alkenes, and so monitoring the abundance and knowing the sources of these compounds in Delhi is essential for implementing effective pollutant reduction strategies to avoid a future rise in $P(O_3)$. As these classes are thought to come mainly from traffic sources, it is possible that reducing road transport emissions may reduce traffic-derived VOCs sufficiently, along with reducing NO_x, to perturb a large increase in $P(O_3)$. However, the proportion of VOCs in Delhi, and at IGDTUW, attributed to traffic sources is uncertain, and thus the extent to which road transport reductions will impact $P(O_3)$ is unknown.

More information of the effect of reductions in NO_x and VOCs by source can be obtained by varying sources described by emissions inventories. Anthropogenic emissions of NO_x, CO, and VOCs by source in Delhi are available from the EDGAR v5.0 Global Air Pollutant Emissions and EDGAR v4.3.2_VOC_spec inventories (https://edgar.jrc.ec. europa.eu/#). According to the inventory, all pollutants investigated in this analysis can be almost entirely described by five source sectors (Table 4.3): road transport (RT); railways, pipelines, and off-road transport (RPORT); energy for buildings (EB); combustion for manufacturing (CM); and process emissions (PE). However, it should be noted here that the EDGAR emissions inventory describes a coarse, low spatial-resolution, city-wide representation of emissions from Delhi. For this analysis, we assume the EDGAR sector split ratios for Delhi are representative of those

at the IGDTUW measurement site.

Model-constrained concentrations were varied by their contributions to sources in the EDGAR emissions inventory (scenario 7, section 4.2.4). Data from the inventory represent average annual emissions from source sectors, last updated for VOCs in 2012 and 2008 for monoterpenes, with 0.1° × 0.1° spatial resolution. VOCs were assumed to be described in full by all sources available from the inventory, with no biogenic influence. Isoprene was excluded from the analysis as it is assumed to have an entirely biogenic source. As a significant anthropogenic signature is seen from the monoterpenes, and because of their significance for $P(O_3)$ in this study, 50% are assumed to be from anthropogenic sources found in the EDGAR emission inventory for the purpose of this analysis. A full list and description of sources used from the EDGAR inventory can be found in Appendix B (Table B.2). Figure 4.14 shows the change in $P(O_3)$ rate when reducing VOCs and NO_x contributions from individual source sectors.

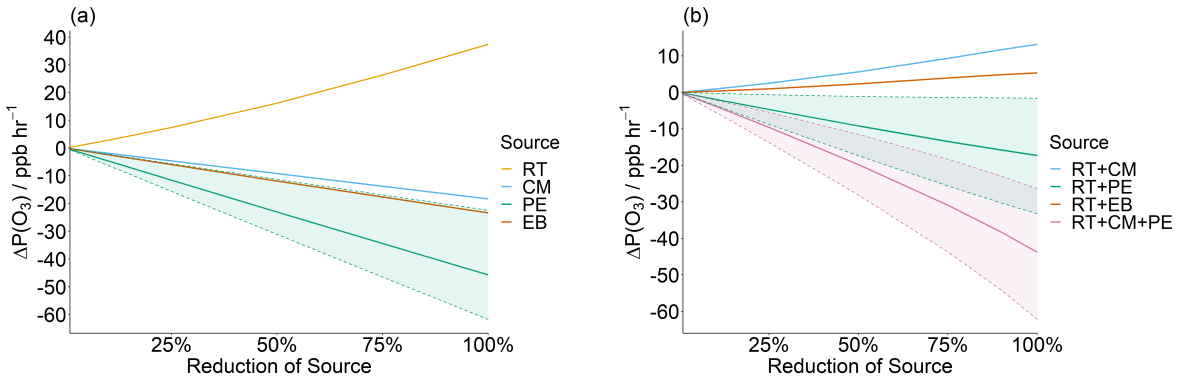

Figure 4.14: Change in $P(O_3)$ on reducing RT, CM, PE, and EB (a); and (b) reducing road transport simultaneously along with either (i) CM, (ii) PE, (iii) EB, (iii) CM, or PE. The shaded region, bounded by a dashed line, represents the variability in $\Delta P(O_3)$ when 0 – 100% of observed monoterpenes contribute to anthropogenic EDGAR source sectors that include PE. The solid lines represent the base case whereby 50% of monoterpenes are assumed to be from anthropogenic sources described in the EDGAR inventory (the other 50% are assumed to be from biogenic sources).

Based on this analysis, reducing the RT source in isolation results in increased $P(O_3)$, whilst reducing CM, PE, and EB independently leads to decreased $P(O_3)$. This is explained by CM, PE, and EB being major sources for VOCs, and RT also being a major source of NO_x. Although reducing RT also reduces some VOCs, particularly aromatic and higher alkane species, there is not sufficient VOC reduction to compensate for the large co-reduction in NO_x, leading to increased $P(O_3)$. Reducing RT by 100% would still lead to a modelled $P(O_3)$ increase of $\approx$ 40 ppb h^{-1} (Figure 4.14a). It is important to acknowledge the uncertainties in this analysis. The EDGAR emissions inventory attributes a low percentage split of VOCs to the RT source sector at the city level, perhaps underestimating the proportion of VOCs that

Table 4.3: Relative proportion of pollutants emitted from five EDGAR emission inventory source sectors: road transport (RT); railways, pipelines, and off-road transport (RPORT); energy for buildings (EB); combustion for manufacturing (CM); and process emissions (PE).

Species class	RT (%)	RPORT (%)	EB /%	CM (%)	PE (%)	Sum (%)
CO	85.0	2.5	8.1	4.1	0.1	99.9
NO_x	60.9	28.9	0.6	2.5	0.0	92.9
Acids	0.0	0.0	0.0	3.9	96.1	100.0
Alkanols	0.0	0.0	0.4	0.2	99.3	100.0
Alkanones	0.0	0.0	38.3	21.9	39.7	99.9
Benzene	10.9	0.0	47.4	34.3	0.3	92.9
Butanes	2.2	0.0	0.3	4.9	92.5	99.9
Chlorinated hydrocarbons	0.0	0.0	0.0	99.5	0.2	99.7
Dimethylbenzenes	12.3	0.0	10.5	18.8	57.8	99.5
Esters	0.0	0.0	18.1	44.7	37.1	99.9
Ethane	2.4	0.0	59.7	32.1	0.2	94.5
Ethene	5.2	0.0	57.5	31.8	1.0	95.5
Ethers	0.0	0.0	0.0	2.7	97.3	100.0
Ethyne	0.8	0.0	58.8	33.1	3.9	96.5
Hexanes and higher alkanes	30.2	0.0	8.4	8.6	52.2	99.3
Isoprenes	16.3	0.0	0.0	73.0	0.0	89.3
Methanal	0.0	2.1	38.0	7.6	8.8	56.6
Methylbenzene	10.2	0.0	29.0	31.4	25.8	96.4
Monoterpenes*	0.0	0.0	0.0	1.9	98.1	100.0
Other alkanals	0.0	0.1	60.2	35.8	0.8	96.8
Other alkenes alkynes	18.5	0.0	46.2	28.1	2.4	95.3
Other aromatics	49.1	0.1	19.0	16.6	10.8	95.6
Other NMVOC	0.0	0.0	13.1	7.5	78.9	99.5
Pentanes	42.6	0.0	0.1	50.0	6.6	99.3
Propane	1.3	0.0	18.0	29.5	49.7	98.4
Propene	15.7	0.0	48.6	30.2	1.0	95.5
Trimethylbenzenes	67.4	0.0	0.5	0.0	31.1	98.9

*The percentage of monoterpenes attributed to these sources in varied in the model and is assumed to be 50% in the base case.

would be reduced with RT reductions at the measurement site.

Air quality mitigation strategies should therefore focus on reducing RT, alongside one or more additional major VOC sources. For example, Figure 4.14b shows $P(O_3)$ begins to reduce when RT emissions are reduced along with PE. These reductions are even greater when RT is reduced with both PE and CM sources. When RT is reduced by 50% alongside PE and PE+CM, modelled $P(O_3)$ is reduced by $\approx$ 10 ppb h^{-1} and $\approx$ 20 ppb h^{-1}, respectively. The VOCs that contribute the most to PE and CM emissions are *n*-butane, propane, alcohols, toluene, and xylenes. Although alcohols and alkanes were not identified as the key VOC classes contributing to $P(O_3)$ (section 4.3.6), they are the two largest classes of VOCs observed in Delhi by mass, making up 42% and 18% of the total measured VOCs, respectively (Figure 4.4). Reducing the PE source thus leads to large reductions in VOCs by mass, helping to drive

down $P(O_3)$. However, it is worth noting that the effectiveness of reducing the RT+PE source on modelled $P(O_3)$ is dependent on the proportion of anthropogenic monoterpene emissions in Delhi. According to the EDGAR emission inventory, 98.1% of anthropogenic monoterpenes in Delhi are attributed to process emissions (PE) (Table 4.3). These emissions include sources such as emissions from chemical industry, and other industrial processes, and include solvent emissions and emissions from product use (see Table B.2 in Appendix B). As emissions from these sources are grouped together in the EDGAR inventory, the exact sources that monoterpenes are attributed to cannot be identified. The sensitivity of $\Delta P(O_3)$ from reducing process emission sources (PE, RT+PE, and RT+PE+CM) is shown by the shaded regions in Figure 4.14, where the dashed lines represent the sensitivity limits where the observed monoterpenes are between 0% and 100% anthropogenic (as opposed to biogenic). There is relatively little impact on $P(O_3)$ on reducing RT+PE when monoterpenes are assumed to have an entirely biogenic source. However, it is clear that although the degree to which reducing process emissions along with road transport in this study impacts $P(O_3)$ cannot be accurately determined, even if no monoterpenes are reduced within this source, reducing it does not negatively impact $P(O_3)$. It is also important to consider possible underestimations for the monoterpene contribution to RT. Monoterpene observations in Delhi were strongly correlated with CO emissions, suggesting anthropogenic sources [54]. The EDGAR emissions inventory assigns 0% of the anthropogenic monoterpenes in the inventory to the RT source sector (Table 4.3). An analysis of the PTR-QiTOF flux data, obtained at the IGDTUW measurement site directly after the concentration measurement period ended, suggests $\approx 60\%$ of the monoterpenes observed could be attributed to traffic factors [167]. A study by Wang et al., 2020 [165] suggested vehicular and burning sources may contribute to the anthropogenic emissions of biogenic molecules. Other possible sources of anthropogenic monoterpenes in Delhi are emissions from cooking herbs and spices, and from fragrances and personal care products [93, 148].

It should be noted that the EDGAR inventory data used in this study are cropped to the Delhi area, and thus some anthropogenic sources may be missing. One example of this is that of agricultural burning, which is frequent in areas surrounding Delhi and across the Indo-Gangetic Plain (IGP) [201, 202]. It is likely that regional sources of O_3 and its precursors will have a significant effect on Delhi's air quality, and vice versa. There are likely to be many missing sources from the EDGAR emissions inventory, along with discrepancies between the top-down and bottom-up data. In addition, we assume the ratios of VOCs and NO_x in each source sector for the Delhi region are representative of the ratios emitted near IGDTUW. Whilst the OH reactivity analysis provides an instantaneous assessment of a VOC's reactivity, based on local observations with a small spatial footprint, the EDGAR Delhi-wide sectoral split represents an aggregate of a wider region and may under-represent the RT VOC contribution observed at the measurement site. As a result, the magnitude of the modelled increased $P(O_3)$ when road transport is reduced may represent a worst-case scenario.

Chapter 5

Alkene ozonolysis chemistry

Alkene ozonolysis plays an important role in atmospheric chemistry, through the generation of radical species as highlighted in Chapter 3. The products of alkene ozonolysis reactions have different fates, dependant on alkene reactivity and structure [113, 137]. As different fates lead to different radical production efficiencies, it is important to understand the factors controlling the subsequent reactions of alkene ozonolysis. The Master Chemical Mechanism (MCM) is a *near explicit*, detailed atmospheric mechanism commonly utilized in box modelling studies to assess the chemical processing in both remote and urban environments. To reduce the computational cost of using a fully *explicit* mechanism, some key simplifications have been applied to the mechanism to limit its size without losing too much chemical detail. These simplifications include (i) neglecting low probability oxidation pathways; (ii) simplifying the degradation chemistry of minor reaction products; and (iii) grouping the reactions of peroxy radical (RO_2) through parameterisation. One key simplification in the MCM is in the mechanistic routes of Criegee intermediates (CI), formed alongside a carbonyl co-product in alkene ozonolysis reactions. In the MCM, many of the rates of CI stabilisation are identical, and not specific to individual CIs. In addition, the different fates of different conformers of asymmetrical CIs are not distinguished. This chapter aims to assess the fates of a range of different CIs, and to find trends in their product yields with respect to CI structure. The analysis presented here uses data collected during a campaign at the EUPHORE smog chamber in Valencia. During the campaign, instruments were operated by scientists at the facility. My role was to analyse and quality check preliminary data, and to monitor the success of the experiments. I was then responsible for prioritising experiments of interest, and re-scheduling experiments that required repeating within the allotted time-frame of the campaign.

5.1 The importance of alkene ozonolysis chemistry in urban environments

As discussed in Chapter 3, radical species play and important role in chemical processing in the atmosphere. These radicals are readily formed from the photolysis of VOCs, HONO and O^1D. As a result, radical formation is heavily dependant on photolysis rates, with radical concentrations tending to peak at mid-day. However, one possible non-photolytic source of radicals is via alkene ozonolysis. Alkene ozonolysis proceeds via the formation of a primary ozonoide (POZ), which rapidly decomposes to form at least one Criegee intermediate (CI) and carbonyl co-product. One key fate of CIs formed from this mechanism is unimolecular decomposition, ultimately leading to the formation of radical species (see section 5.2).

Although many studies have identified both alkene ozonolysis and photolysis processes as being the important sources of radicals in the summer months, the relative contribution of radicals from alkene ozonolysis may be of increased importance in the winter months, when photolysis rates are lower. One study investigating the key reaction pathways of radical initiation, propagation and termination in Birmingham found that alkene ozonolysis represented 46% of OH initiation sources in the summer months, which increased to 67% in the winter [116]. This was coupled with a reduction in the contribution to OH from O^1D from 24% in the summer to less than 1% in the winter.

In Delhi, HONO and O^1D photolysis, along with ozonolysis, all contributed significantly to OH initiation in the pre-monsoon (40%, 39% and 21% respectively) (see Chapter 3). However, the relative contribution from ozonolysis increased in the post-monsoon (30%), whilst the contribution from O^1D photolysis decreased (5%). Contributions of OH from photolysis routes are expected to fall further into the winter months, which would lead to an increase in the relative contribution from ozonolysis products. In the post-monsoon, j(HONO) is the largest contributor to OH formation (65%), due to very high concentrations of HONO, particularly in the night and early morning. However, future pollution abatement strategies may lead to reductions in NO_x in Delhi, and potentially lead to a reduction in HONO concentrations (see Chapter 4). If HONO concentrations are reduced, and ambient levels of unsaturated VOCs remain the same, this could further increase the percentage contribution of alkene ozonolysis to OH formation.

However, the propensity of a particular alkene to produce radicals is only partially understood. Although there have been many studies investigating the yield of CIs which undergo unimolecular decomposition to form radical species for smaller alkenes such as ethene, the fate of larger alkenes (C_{5+}) is yet to be investigated fully. In addition, some of the decomposition routes of asymmetric CIs are further complicated by the different mechanistic pathways of different CI conformers. These pathways may or may not lead to the formation of radicals, so knowing the relative proportions of CI conformers formed is important for understanding the

radical yields of a particular alkene ozonolysis mechanism. In addition, SCI themselves are atmospheric oxidants and can contribute to urban chemistry. This study aims to determine the proportion of CIs that are formed stabilised (SCI), as opposed to excited (CI*) for a variety of alkenes, thus giving some insight into the proportion of CIs that undergo unimolecular decomposition, leading to radical formation. A range of longer chain alkenes are investigated, from C_4 to C_6, and yields are compared to literature values where available.

5.2 Mechanisms of alkene ozonolysis

5.2.1 Formation of Criegee Intermediates

Atmospheric ozonolysis mechanisms are thought to progress via the Criegee mechanism [203]. This reaction proceeds via O_3 addition to the double bond of an alkene, to form a primary ozonide, POZ (Figure 5.1). The POZ then decomposes, forming a vibrationally excited CI (CI*), along with a stable carbonyl co-product. If the alkene is asymmetrical, then two combinations of CIs and carbonyls are possible. The resulting CIs may be formed unsubstituted, in the case of terminal alkene ozonolysis (CH_2OO), or substituted. The latter may be either di-substituted or mono-substituted. Calculations of the electronic structure of CIs suggest they have a strong zwitterionic character, as depicted in Figure 5.1 [112, 204]. However, calculations for smaller CI such as CH_2OO elude to a planar, biradical structure (Figure 5.2) [205]. These two resonance canonicals are depicted in Figure 5.2.

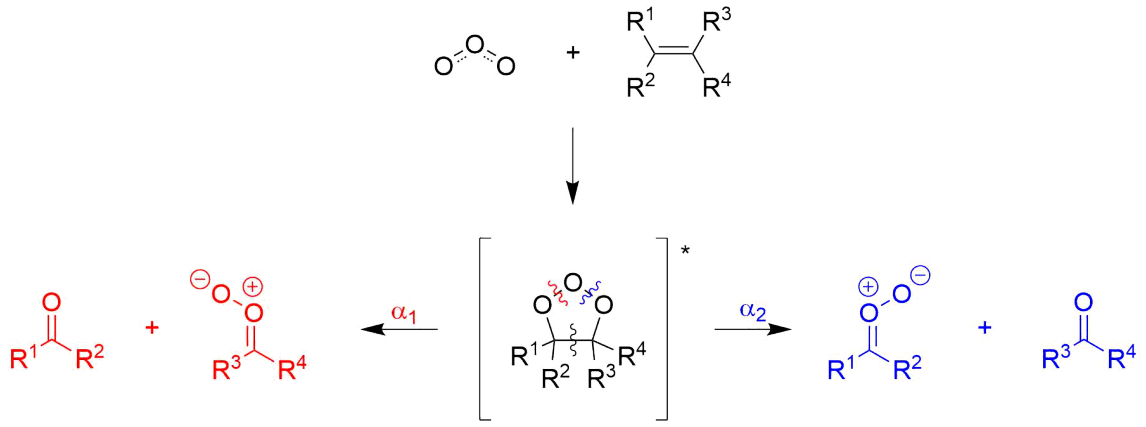

Figure 5.1: O_3 addition to alkenes, leading to the formation of a primary ozonide, and its resulting products. Adapted from Johnson and Marston, 2008 [112].

If the formed CI is asymmetrically di-substituted or mono-substituted, with a significant zwitterionic character, it can exist in both *syn* and *anti* conformations (Figure 5.3). The significant π character of the CI C=O bond creates an energy barrier for rotation, leading to two distinct conformers.

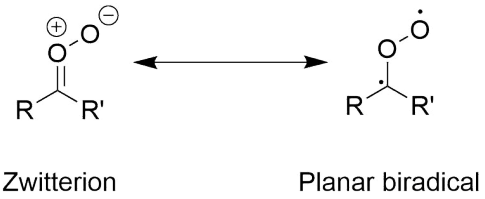

Figure 5.2: Resonance canonicals for Criegee intermediates, where R = alkyl, H. Adapted from Johnson and Marston, 2008 [112].

Figure 5.3: Asymmetrical criegee intermediates can be formed in both the *anti* and *syn* conformations.

CIs are initially formed energetically "excited" (CI*), before either undergoing unimolecular decomposition or collision stabilisation to form a stabilised CI (SCI). The proportion of SCIs formed within the CI population is dependant on the mean energy distribution of products formed upon decomposition of the POZ. Experimental studies have determined a relationship between the proportion of SCIs within a CI population, and the carbon chain length of the carbonyl co-product [113]. This can be explained by the distribution of energy across more non-hydrogen atoms. If we assume the same amount of energy is released in POZ decomposition, regardless of the parent alkene size, then increasing the number of atoms over which this energy can be distributed across the decomposition products, reduces the energy available to the CI, meaning they are more easily stabilised [113].

5.2.2 Unimolecular reactions

CI*s are thought to undergo unimolecular reactions, whereby the CI dissociates to form radical fragments, along with stable organic compounds and CO. These radical fragments are responsible for the atmospheric oxidation of VOCs, and play an important role in both remote and urban photochemistry. Understanding the fates of CIs and their different propensities to form radical species is of great importance to understanding the fundamental chemical processing occurring in the troposphere.

One key route for unimolecular CI decomposition is through CI ring closure to form an excited dioxirane. This excited species rapidly isomerises into an excited acid species, otherwise known as a "hot acid", before fragmenting to form OH along with some smaller, stable organic species, CO and CO_2. This mechanistic route is particularly important for *anti*-CI

and CH_2OO. The mechanism of this pathway is well understood for the simplest CI, unsubstituted CH_2OO, whereby "hot" formic acid fragments, forming OH, CO and CO_2 (pathway β_1, Figure 5.4). The OH radical may also be formed from CH_2OO via a concerted process involving the rearrangement and subsequent fragmentation of a four-membered transition state (pathway β_2, Figure 5.4). However, experimental studies of the deuterated CI suggest this pathway is only a minor source of the OH radical, and that the formation and fragmentation of the "hot acid" (β_1, Figure 5.4) is the dominant channel [206].

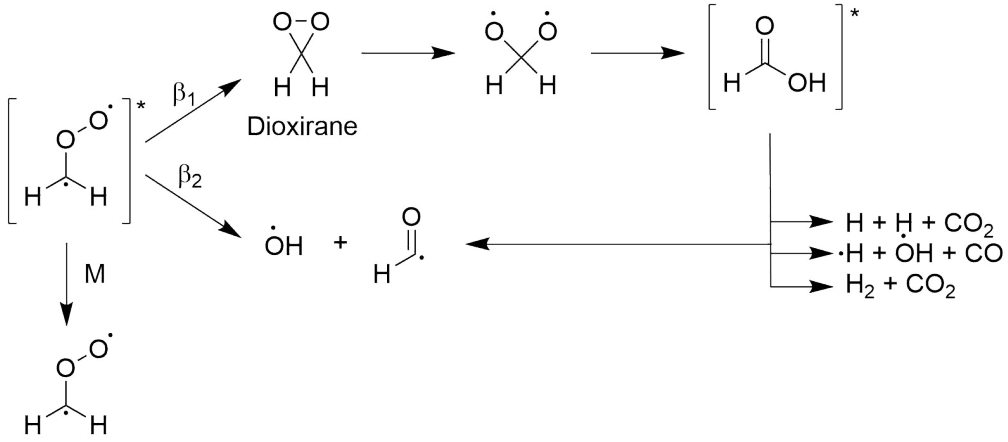

Figure 5.4: Unimolecular decomposition routes of the simplest CI, formaldehyde oxide (CH_2OO).

Additional mechanistic routes have been suggested for di-substituted and *syn*-mono-substituted CIs, due to hydrogen availability to the terminal oxygen. In disubstituted or *syn*-mono-substituted CIs, the presence of an alkyl group on the same side as the electron rich oxygen atom allows the CI to isomerise to an excited vinylhydroperoxide intermediate (VHP). This isomerisation occurs through a 1,4-sigmatropic shift. The VHP then rapidly decomposes to a vinoxy radical and OH. This mechanism is known as the "hydroperoxide channel", and was first proposed in gas-phase studies by Niki et al., 1987 [207]. For both disubstituted and *syn*-mono-substituted CIs, this channel is thought to be the dominant pathway, out-competing the "hot acid" formation route [112, 208]. The hydroperoxide mechanism is outlined in Figure 5.5.

The vinoxy radical formed via this pathway reacts with molecular oxygen, initially forming an excited β-oxo peroxy radical (Figure 5.6). This excited radical can be either collisionally stabilised, or decompose to stable carbonyl species, forming an additional OH radical in the process. The latter pathway is only efficient for mono-substituted CIs, since the mechanism requires an aldehydic hydrogen atom [209]. Stabilised β-oxo peroxy radicals readily react with HO_2 or RO_2 to form secondary aldehydes, CO and HO_2 (Figure 5.6). Alternatively, in the presence of NO they can form NO_2 and subsequently O_3, as observed in the radical propagated photochemical O_3 formation cycle described in Chapters 1 and 3.

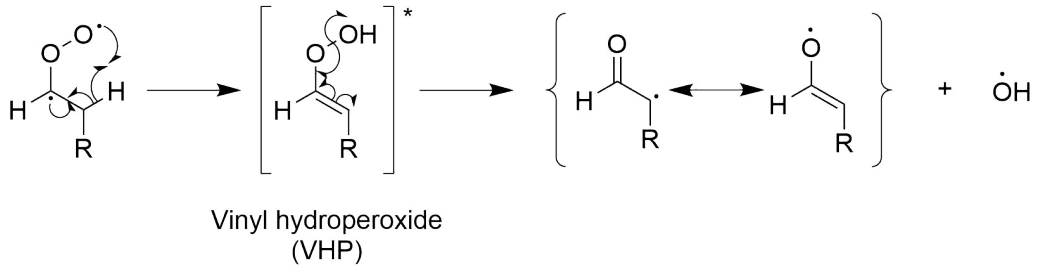

Figure 5.5: The "hydroperoxide" channel for di-substituted or *syn*-mono-substituted Criegee intermediates, where R = alkyl, H.

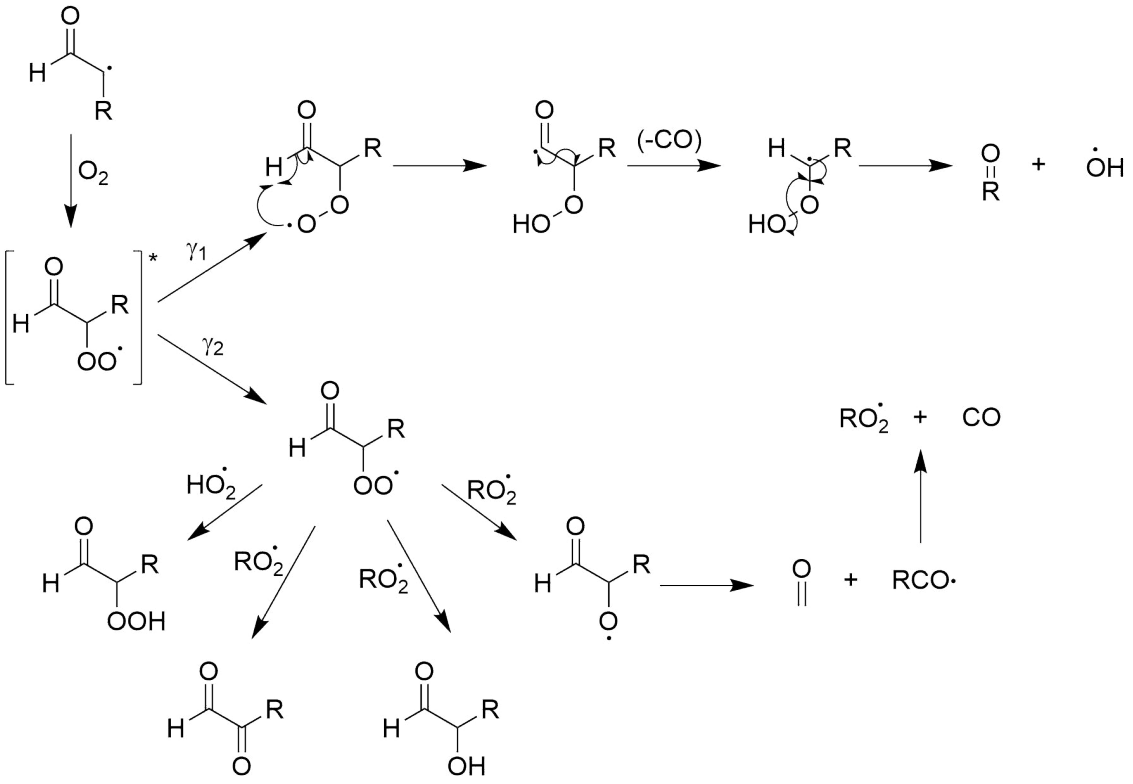

Figure 5.6: Mechanistic pathways of the β-oxo peroxy radical, where R = alkyl, H.

5.2.3 Bimolecular reactions

In the presence of reactive, stable species bimolecular reactions can happen rapidly, provided the lifetime of the CI is long enough. CI*s can be collisionally stabilised to form SCIs, increasing their atmospheric lifetime. SCIs may then react with H_2O, SO_2, NO, NO_2, CO, aldehydes, ketones, and small organic acids to form stable products. Due to the humidity of the atmosphere, reactions with H_2O dominate in the troposphere, leading to carbonyl and peroxide products. Bimolecular rate coefficients for CIs with a range of stable species are presented in Table 5.1. The rate at which these bimolecular reactions occur depends on the SCI conformation [210, 211].

Table 5.1: Bimolecular rate coefficients for CH_2OO, *syn*-CH_3CHOO, *anti*-CH_3CHOO, and $(CH_3)_2COO$ reactions with a range of stable species [137, 212].

Reaction	CI	Rate coefficient / cm^3 $molecule^{-1}$ s^{-1}	Reference
SO_2	CH_2OO	3.9 + 0.7 x 10^{-11}	Weltz et al., 2012 [213]
	syn-CH_3CHOO	(2.4 ± 0.3) x10^{-11}	Taatjes et al., 2013 [214]
	anti-CH_3CHOO	(6.7 ± 1.0) x 10^{-11}	Taatjes et al., 2013 [214]
	$(CH_3)_2COO$	(7.3 ± 0.5) x 10^{-11}	Chhantyal-Pun et al., 2017 [215]
NO_2	CH_2OO	7 +3/-2 x 10^{-12}	Weltz et al., 2012 [213]
	syn-CH_3CHOO	(2.0 ± 1.0) x 10^{-12}	Taatjes et al., 2013 [214]
	anti-CH_3CHOO	(2.0 ± 1.0) x 10^{-12}	Taatjes et al., 2013 [214]
	$(CH_3)_2COO$	5 x 10^{-12}	Chhantyal-Pun et al., 2017 [215]
H_2O	CH_2OO	4 x 10^{-15}	Weltz et al., 2012 [213]
	syn-CH_3CHOO	4 x 10^{-15}	Taatjes et al., 2013 [214]
	anti-CH_3CHOO	(1.0 ± 0.4) x 10^{-14}	Taatjes et al., 2013 [214]
	$(CH_3)_2COO$	(2.1 ± 0.6) x 10^{-15}	Newland et al., 2015 [216]
NO	CH_2OO	6 x 10^{-15}	Weltz et al., 2012 [213]
CH_3COCH_3	CH_2OO	2.3 + 0.3 x10^{-13}	Taatjes et al., 2012 [217]
CH_3CHO	CH_2OO	9.5 + 0.7 x10^{-13}	Taatjes et al., 2012 [217]
O_3	CH_2OO	1 x 10^{-13}	Weltz et al., 2012 [213]
	syn-CH_3CHOO	3.0 x 10^{-14}	Vereecken et al., 2015 [218]
	anti-CH_3CHOO	3.0 x 10^{-12}	Vereecken et al., 2015 [218]
	$(CH_3)_2COO$	8.0 x 10^{-14}	Vereecken et al., 2015 [218]
CO	CH_2OO	7 x 10^{-14}	Weltz et al., 2012 [213]
	syn-CH_3CHOO	7.0 x 10^{-21}	Vereecken et al., 2015 [218]
	anti-CH_3CHOO	8.0 x 10^{-20}	Vereecken et al., 2015 [218]
	$(CH_3)_2COO$	3.0 x 10^{-20}	Vereecken et al., 2015 [218]

Although the majority of SCIs formed in the atmosphere react with H_2O, the rate coefficient of this reaction is low relative to coefficients with other species (Table 5.1). For example, the rate coefficient of CH_2OO with SO_2 is ≈ 1000 greater than that of H_2O. SCIs react rapidly with SO_2 to form a carbonyl species and SO_3. For example, the CH_2OO CI (formaldehyde oxide) is scavenged by SO_2, forming formaldehyde as per equation 5.1.

$$CH_2OO + SO_2 \longrightarrow HCHO + SO_3 \tag{5.1}$$

.

The SO_3 formed in the process rapidly reacts with water to form sulfuric acid, which can lead to acid rain and sulfate aerosol (equation 5.2). H_2SO_4 may deposit onto existing particles to form new particles, which may impact climate forcing [219].

$$SO_3 + H_2O \longrightarrow H_2SO_4 \tag{5.2}$$

As the overwhelming majority of SCIs will decompose via bimolecular reactions when sufficient co-reactant is present, rather than unimolecular decomposition, chamber experiments can be designed to calculate the proportion of SCIs formed from a given alkene ozonolysis reaction. For example, in an excess of SO_2, reductions in SO_2 concentrations are directly proportional to the consumption of an SCI, under the right experimental conditions. On the reaction of the SCI with SO_2, an additional quantity of the carbonyl co-product is formed.

Calculating the increased yield of this carbonyl species under high SO_2 conditions compared to zero SO_2 conditions allows for a more indirect calculation of the yield of a specific SCI. The work presented here aims to use the propensity of SCIs to undergo bimolecular reactions under the right experimental conditions, to determine the total SCI yields of CI populations.

5.3 Experimental Summary

Alkene ozonolysis experiments were performed in an atmospheric simulation chamber under dark conditions to determine SCI yields for a range of alkenes, and to investigate the relative ratios of resultant alkene ozonolysis products. The alkene was introduced to the chamber containing O_3, and sometimes SO_2 in excess. SO_2, O_3, the alkene precursor, and a range of mechanistic products, were monitored throughout the experiment. Experiments under high SO_2 concentrations were conducted in the presence of $\approx$ 2000 ppbV of SO_2, under dry conditions, meaning the vast majority ($>$ 94%) of SCIs were scavenged by the SO_2. SF_6 was also added to the chamber before the addition of the alkene, and monitored throughout the experiment to determine rate of loss of compounds from the chamber, allowing for the calculation of chamber dilution rates (k_{dil}) for each experiment. To prevent additional chemical reactions occurring from OH radicals formed from the products of alkene ozonolysis, an OH scavenger (cyclohexane, *ca.* 75 ppbV) was added at the beginning of each experiment. Before adding the alkene to the chamber, five minutes of mixing time was required to allow for the complete mixing of species.

5.3.1 EUPHORE smog chamber

A series of alkene ozonolysis experiments were conducted at the EUropean PHOtoREactor (EUPHORE) facility in Valencia, Spain. The facility is equipped with two large atmospheric simulation chambers ($\approx$ 197 m^3 each), the dimensions of which are described in more detail in Becker, 1996 [220] and Becker, 1999 [221] (Figure 5.7). The chambers are fitted with a fluorine-ethene-propene (FEP) Teflon foil outer body, which is covered by an outer hood to create the dark conditions required for the experiments conducted in this study. An excess pressure of 0.75 - 1.5 Torr is applied to the chamber, to allow for the shape to be maintained. A consequence of this is the dilution of species out of the chamber, which can be accounted for in chamber dilution corrections described in section 5.3.3. The chamber is fitted with large vertical fans which ensure rapid mixing of the air within $\approx$ 2-3 minutes.

During this experimental work, the chambers were fitted with an extensive suite of instruments, including FTIR, PTR-MS, and O_3 and SO_2 analysers (see section 5.3.2). A summary the experimental conditions of each experiment is Table 5.2. An aliquot of SF_6, and cyclohexane ($\approx$ 75 ppmV) were added prior to each experiment, and monitored by FTIR. All experiments were performed in the dark, such that $j(NO_2) \leq 10^{-6}$ s^{-1}, and in dry conditions


Figure 5.7: The EUPHORE smog chambers, Valencia, Spain. Here, the hood of the left chamber is closed to prevent the transmittance of radiation, allowing for experimental work to be conducted in dark conditions.

to minimise bimolecular reactions of CIs with H_2O (RH $< 1\%$). The atmospheric pressure in the chamber was ≈ 1000 mbar, and temperatures varied between 297 - 305 K. The timescale of each experiment was generally 40 - 70 minutes, depending on the rate of ozonolysis for the alkene of interest. O_3 (≈ 500 ppbV), and SO_2 (when applicable), were added to the chamber. Before the addition of the alkene, the chamber was given 5 minutes to allow for complete mixing. The alkene was then added to the chamber (≈ 400 ppbV), and O_3, SO_2, and carbonyl products were monitored throughout the experiment.

Table 5.2: Initial concentrations of SO_2, O_3, and the alkene of interest (observed initial value), along with the approximate experimental time.

Alkene	Exp. I.D.	$[SO_2]_i$ / ppbV	$[O_3]_i$ / ppbV	$[\text{Alkene}]_i$ / ppbV	Exp. time / min
cis-but-2-ene	C2B1	0	516	318	40
	C2B2	2110	503	257	45
trans-but-2-ene	T2B1	0	505	273	46
	T2B2	539	536	336	41
	T2B3	1639	497	398	42
	T2B4	4901	520	412	42
	T2B5	9044	498	400*	45
2-methyl-but-2-ene	2M2B3	0	519	248	45
	2M2B4	1966	527	202	41
	2M2B5	4997	542	400*	45
cis-pent-2-ene	C2P1	0	551	400*	45
	C2P2	1925	509	400*	46
trans-pent-2-ene	T2P1	0	510	400*	40
	T2P2	2003	504	400*	46
cis-hex-2-ene	C2H1	0	504	400*	59
	C2H2	1981	527	400*	64

*Observational measurements of the initial concentrations are unavailable. The value shown here is the concentration of alkene prepared for introduction into the chamber.

5.3.2 Instrumentation

A range of alkene ozonolysis products, along with the alkene precursor, are monitored at the facility using Fourier Transform Infrared Spectroscopy (FTIR). Each chemical species has a specific IR fingerprint, relating to the vibrational frequencies of bonds within the molecule. The absorption of radiation at specific wavelengths is measured and concentrations of species in the chamber can be quantified using the Beer-Lambert law (see equation 2.5, Chapter 2).

The FTIR at EUPHORE operates at a time resolution of 5 minutes, at an infrared spectral range of 400 - 4000 cm^{-1} and spectral resolution of 0.5 cm^{-1}. The FTIR measurement accuracy is dependant on the uncertainty of the reference cross sections available, as well as the fitting process. The estimated uncertainties and detection limits for a range of species discussed in this work were provided by Dr. Mila Ròdenas García, and are presented in Table 5.3.

Table 5.3: Uncertainties and detection limits for species measured by FTIR, obtained from Instituto Universitario Centro de Estudios Ambientales del Mediterraneo, CEAM group. Detection limits are 3θ.

Species	Uncertainty /%	Detection Limit / ppb
Acetaldehyde	13.00	6.90
Acetone	13.80	1.74
Propanal	25.80	4.75
Cyclohexane	5.70	0.70

Selected compounds were also detected using PTR-MS instrumentation. The averaged uncertainties for these compounds during the campaign were determined by Dr. Teresa Vera at the EUPHORE facility, accounting for both instrument parameters and the response signal for each compound. The uncertainty and detection limits for acetaldehyde and acetone are provided in Table 5.4.

Table 5.4: Uncertainties and detection limits for species measured by PTR-MS, obtained from Instituto Universitario Centro de Estudios Ambientales del Mediterraneo, CEAM group. Detection limits are 3θ.

Species	Uncertainty /%	Detection Limit / ppb
Acetaldehyde	15	0.46
Acetone	2	0.27

O_3 is measured using a UV-vis O_3 analyser. This technique exploits the ability of O_3 to absorb UV light at 254 nm. As very few molecules in the atmosphere absorb light at this wavelength, O_3 can be selectively detected by exposing the sample to UV at 254 nm and determining the change in intensity between an O_3 scrubbed sample and the unscrubbed analyte. A more detailed description of this instrumentation is provided in Chapter 2.

SO_2 concentrations were monitored using a pulsed fluorescence analyser. SO_2 molecules absorb UV light at a specific wavelength to become excited. They then decay to a lower energy state, emitting UV light of a range of wavelengths. The emitted light is proportional to the SO_2 concentration (see Chapter 2 instrument description). Detection ranges for each instrument used are provided in Table 5.5.

Table 5.5: Approximate detection ranges and uncertainties of the instrumentation used during the experiments.

Instrument	Species	Detection range	Uncertainty
EcoTech (Serinus 10)	O_3	1 ppbV - 20 ppmV	0.5 ppbV or 0.2%
FTIR spectrometer with long path absorption	IR active species	pptV - ppmV	see Table 5.3
Thermo Scientific Model 43i	SO_2	1 - 1000 ppbV	1 ppbV or 1%

5.3.3 Chamber dilution corrections

The dilution of species from the chamber can be monitored by observing the first order decay of an inert species, SF_6. The rate of loss of SF_6 is calculated from the differential equation describing its first order kinetics as in equation 5.3.

$$Rate = -\frac{d[SF_6]}{dt} = k_{dil}[SF_6] \tag{5.3}$$

where k_{dil} is the chamber dilution rate coefficient, which can later be applied to all measured species in the chamber. Equation 5.3 can be rearranged and integrated on both sides, as in equation 5.4, giving equation 5.5.

$$\int_{[SF_6]_0}^{[SF_6]_t} \frac{d[SF_6]}{[SF_6]} = \int_{t_0}^{t} k_{dil}\ dt \tag{5.4}$$

$$ln[SF_6]_t - ln[SF_6]_0 = -k_{dil}\ t \tag{5.5}$$

Equation 5.5 can be rearranged to equation 5.6 and subsequently equation 5.7. By plotting $ln[SF_6]_0/ln[SF_6]_t$ against time, t, the chamber dilution rate, k_{dil}, can be determined for each experiment.

$$ln[SF_6]_t = -k_{dil}\ t + ln[SF_6]_0 \tag{5.6}$$

$$ln\left(\frac{[SF_6]_t}{[SF_6]_0}\right) = -k_{dil}\ t \tag{5.7}$$

This chamber dilution rate is the applied to all monitored species in the experiments. Figure 5.8 shows the calculated value of k_{dil} for a *trans*-pent-2-ene experiment (Experiment ID: T2P1) using the method described here.

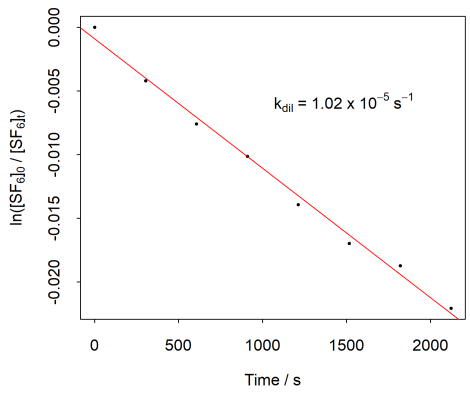

Figure 5.8: Change in $ln([SF_6]_0/[SF_6]_t)$ with time to determine the rate of decay of SF_6 (k_{dil}) during a *trans*-pent-2-ene experiment at zero SO_2 (T2P1).

5.4 Determining carbonyl yields

As discussed earlier, ozonolysis of asymmetrical alkenes leads to the formation of two different CIs and their respective carbonyl co-products. By simultaneously monitoring the change in carbonyl co-product formation with the loss of O_3, it is possible to determine the carbonyl co-product yields, which can hence be used to deduce the yield of each CI formed. This information allows us to apply a branching ratio to the primary ozonolysis products. The carbonyl co-product yields for two symmetrical alkenes: *cis*-but-2-ene and *trans*-but-2-ene; and four asymmetrical alkenes: 2-methyl-but-2-ene, *cis*-pent-2-ene, *trans*-pent-2-ene, and *cis*-hex-2-ene are discussed in this work. The carbonyl products were monitored using both FTIR and PTR-MS instrumentation, and the yields from the FTIR data are presented here. Chamber dilution rates have been applied to all data used in this analysis. As SCIs readily react with SO_2, leading to secondary formation of the primary carbonyl, primary carbonyl yields here are determined in zero SO_2 conditions (see section 5.2.3)

5.4.1 *cis*- and *trans*-but-2-ene

The symmetrical alkenes, *cis*-but-2-ene and *trans*-but-2-ene, form only one carbonyl co-product and one CI (acetaldehyde and methyl carbonyl oxide). Therefore, if the proposed Criegee mechanism (Figure 5.1) holds true, we expect O_3 to be lost, and acetaldehyde to be formed, in a 1:1 ratio. Figure 5.9 shows the change in acetaldehyde with O_3 during the zero SO_2 *cis*-but-2-ene and *trans*-but-2-ene experiments. The experimentally determined FTIR acetaldehyde yields for *cis*-but-2-ene and *trans*-but-2-ene were 1.00 ± 0.03 and 1.04 ± 0.07 respectively. For these two alkenes, a 100% yield of acetaldehyde has been achieved under the experimental conditions, within a 2θ error.

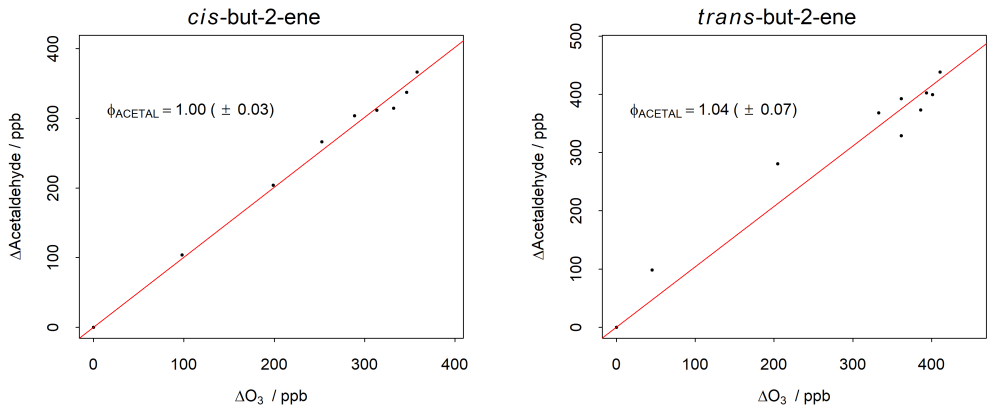

(a) Experiment ID: C2B1 (b) Experiment ID: T2B1

Figure 5.9: FTIR determined Δ Acetaldehyde vs.ΔO_3 during zero SO_2 experiments for *cis*-but-2-ene (C2B1) and *trans*-but-2-ene (T2B1).

5.4.2 2-methyl-but-2-ene

Due to its asymmetry, methyl-but-2-ene can form two CIs and their carbonyl co-products from its ozonolysis: acetaldehyde and acetone. The sum of the acetaldehyde and acetone yields under zero SO_2 is thus expected to equal 1.0. Figure 5.10 shows the change in acetaldehyde and acetone with O_3 during a zero SO_2 2-methyl-but-2-ene ozonolysis chamber experiment.

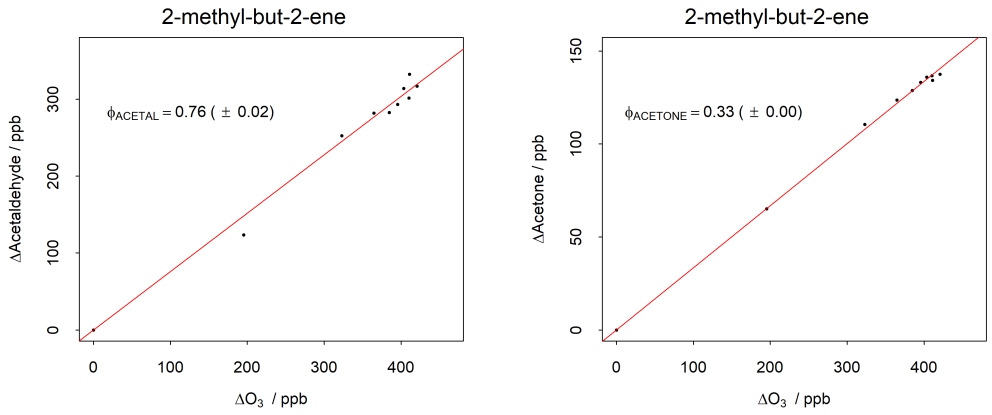

(a) Experiment ID: 2M2B3 (b) Experiment ID: 2M2B3

Figure 5.10: FTIR ΔAcetaldehyde (a) and ΔAcetone (b) vs. ΔO_3 during zero SO_2 experiments for 2-methyl-but-1-ene (2M2B3).

Experimentally determined yields of acetaldehyde and acetone from 2-methyl-but-2-ene ozonolysis were 0.76 ± 0.02 and 0.33 ± 0.00 respectively. The total primary carbonyl yield is approximately 1, as expected from the Criegee formation mechanism (Figure 5.1). This sug-

gests approximately two-thirds of the 2-methyl-but-2-ene primary ozonide decomposes into acetaldehyde and the acetone oxide CI, rather than acetone and the acetaldehyde oxide CI.

5.4.3 *cis*- and *trans*-pent-2-ene

The ozonolysis of *cis*-pent-2-ene and *trans*-pent-2-ene also leads to an asymmetrical POZ which can decompose into two different CIs and their carbonyl co-products. The resulting POZ decomposes into acetaldehyde or propanal, and their oxidised CI equivalents. Figure 5.11 shows the experimentally determined FTIR yields of acetaldehyde and propanal from *cis*-pent-2-ene and *trans*-pent-2-ene under zero SO_2 conditions.

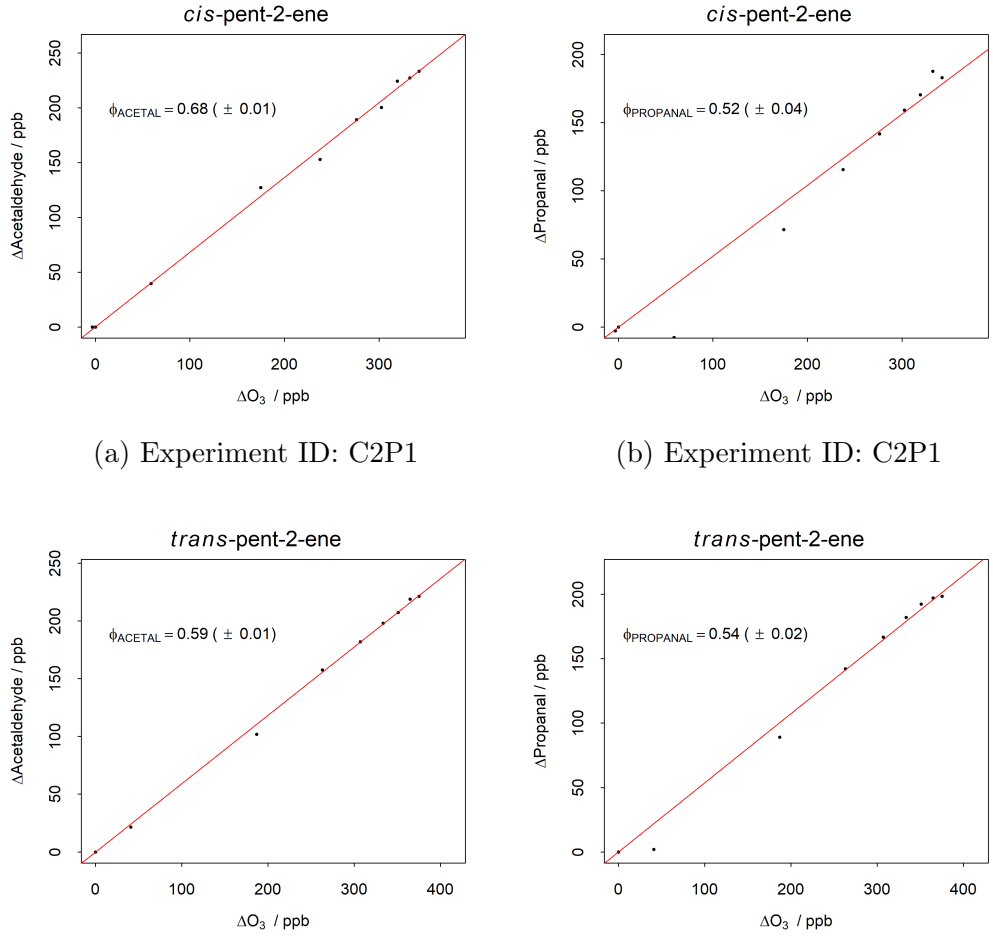

(a) Experiment ID: C2P1

(b) Experiment ID: C2P1

(c) Experiment ID: T2P1

(d) Experiment ID: T2P1

Figure 5.11: FTIR ΔAcetaldehyde and ΔAcetone vs. ΔO_3 during zero SO_2 experiments for *cis*-pent-2-ene (a) and (b) respectively, and *trans*-pent-2-ene (c) and (d) respectively.

The yields of acetaldehyde and propanal from *cis*-pent-2-ene ozonolysis were 0.68 ± 0.01 and 0.52 ± 0.04 respectively. The yields suggest that 31% more acetaldehyde is formed com-

pared to propanal. However, the total yield is greater than 1 (1.20 ± 0.5). This is due to a secondary formation route for acetaldehyde via the hydroperoxide POZ decomposition route (Figure 5.5). The mechanism for secondary acetaldehyde formation from the CH_3CH_2CHOO CI, formed from *cis*-pent-2-ene ozonolysis, is given in Figure 5.12.

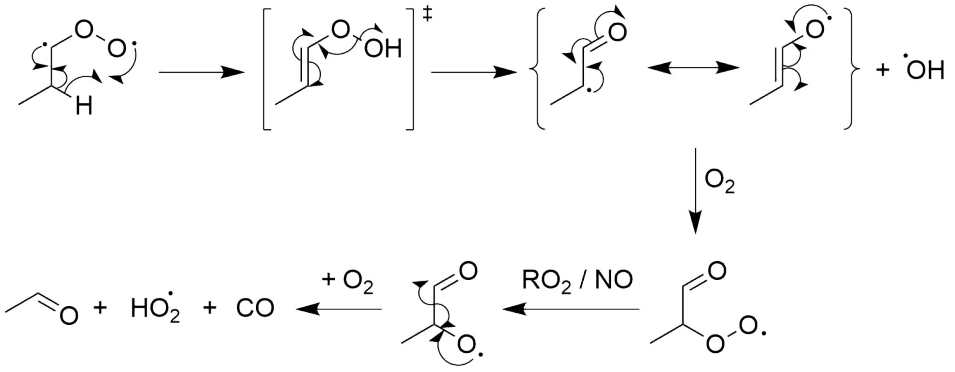

Figure 5.12: Unimolecular decomposition of *anti*-CH_3CH_2CHOO via the "hydroperoxide channel", forming secondary acetaldehyde.

The yields of acetaldehyde and propanal from *trans*-pent-2-ene were 0.59 ± 0.01 and 0.54 ± 0.02 respectively. As was observed from the *cis*-pent-2-ene carbonyl products, the total yield of the carbonyl co-products was greater than 1.0 (1.13 ± 0.03). Interestingly, propanal is formed in a similar yield from *trans*-pent-2-ene as from *cis*-pent-2-ene, but the acetaldehyde yield is smaller. This may suggest that there is less secondary acetaldehyde formation from POZ decomposition via the hydroperoxide channel. If this is true, there may be more *syn*-CH_3CH_2CHOO than *anti*-CH_3CH_2CHOO formed from *trans*-pent-2-ene compared to *cis*-pent2-ene ozonolysis. If the Criegee mechanism (Figure 5.1) holds true, the sum of the primary acetaldehyde and propanal yields should equal 1. If we assume there is no secondary propanal formed, we can deduce the primary formation yields of acetaldehyde to be 0.48 ± 0.01 and 0.46 ± 0.01 from *cis*- and *trans*-pent-2-ene respectively. This leaves a secondary acetaldehyde yield of 0.20 ± 0.01 and 0.13 ± 0.01 from *cis*-pent-2-ene and *trans*-pent-2-ene respectively. If we assume all *anti*-CH_3CH_2CHOO decomposes via the hydroperoxide channel, we can deduce that 42% and 28% of CH_3CH_2CHOO CIs are formed in the *anti* conformation from *cis*- and *trans*-pent-2-ene ozonolysis respectively.

5.4.4 *cis*-hex-2-ene

Finally, the primary carbonyl products of *cis*-hex-2-ene were investigated (Figure 5.13). Unfortunately, FTIR analysis of one of the carbonyl co-products, butanal, is difficult as the observed absorbance bands overlap with pentanal and hexanal. Since pentanal is a possible secondary carbonyl product from the hydroperoxide decomposition channel, and hexanal is a product formed from reactions of the scavenger species cyclohexane with OH, we cannot use this data to infer yields. As a result, only one possible carbonyl co-product, acetaldehyde,

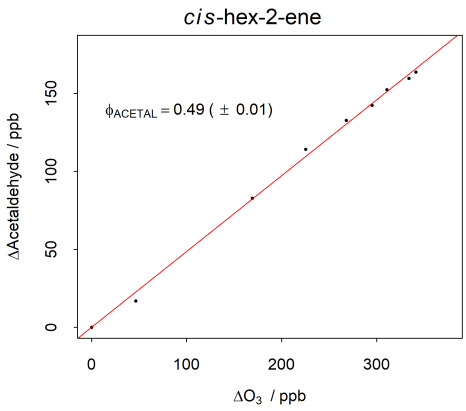

(a) Experiment ID: C2H1

Figure 5.13: FTIR ΔAcetaldehyde vs. ΔO_3 during zero SO_2 experiments for *cis*-hex-2-ene.

is presented here (Figure 5.13). The yield of acetaldehyde from *cis*-hex-2-ene ozonolysis was 0.49 ± 0.01. Assuming there is no secondary production of acetaldehyde in the CI decomposition process, this suggests the POZ formed from *cis*-hex-2-ene ozonolysis decomposes to form acetaldehyde and butanal oxides, and butanal and acetaldehyde oxide, in a 1:1 ratio.

5.4.5 Summary of carbonyl yields and comparison to literature values.

The primary carbonyl yields calculated from *cis*-but-2-ene, *trans*-but-2-ene, 2-methylbut-2-ene, *cis*-pent-2-ene, *trans*-pent-2-ene and *cis*-hex-2-ene are summarised in Table 5.6. The calculated yields are comparable to primary carbonyl yields reported in the literature.

Yields of acetaldehyde from *cis*-but-2-ene and *trans*-but-2-ene ozonolysis are marginally lower than values reported by Tuazon et al., 1997 [222] and Grosjean and Grosjean, 1997 [223], but are within the reported uncertainties. The yields of acetaldehyde and acetone from 2-methyl-but-2-ene ozonolysis are are within the uncertainties of reported yields in Tuazon et al., 1997 [222]. Yields reported here are marginally higher than those reported in Grosjean and Grosjean, 1997 [223].

Table 5.6: Primary carbonyl yields from ozone-alkene reactions, and comparisons to literature value [137].

Alkene	Primary carbonyl	Yield	Reference
cis-but-2-ene	acetaldehyde	1.00 ± 0.03	This work
		1.08 ± 0.08	Tuazon et al., 1997 [222]
		1.19 ± 0.14	Tuazon et al., 1997 [222]
trans-but-2-ene	acetaldehyde	1.04 ± 0.07	This work
		1.09 ± 0.09	Tuazon et al., 1997 [222]
		1.14 ± 0.14	Tuazon et al., 1997 [222]
2-methyl-but-2-ene	acetaldehyde	0.76 ± 0.02	This work
		0.69 ± 0.02	Grosjean and Grosjean, 1997 [223]
		0.75 ± 0.10	Tuazon et al., 1997 [222]
	acetone	0.33 ± 0.00	This work
		0.30 ± 0.01	Grosjean and Grosjean, 1997 [223]
		0.38 ± 0.01	Tuazon et al., 1997 [222]
		0.34 ± 0.03	Tuazon et al., 1997 [222]
cis-pent-2-ene	acetaldehyde	0.68 ± 0.01	This work
	propanal	0.52 ± 0.04	
trans-pent-2-ene	acetaldehyde	0.59 ± 0.01	This work
	propanal	0.54 ± 0.01	
cis-hex-2-ene	acetaldehyde	0.49 ± 0.01	This work

5.5 Total stabilised Criegee yields from SO_2 loss

Provided a CI exists with a long enough lifetime, bimolecular reactions are possible (see section 5.1). Excited CIs (CI*) can be collisionally stabilised, increasing their lifetime. SCIs react rapidly with SO_2 to form a carbonyl species and SO_3. For example, the CH_2OO CI (formaldehyde oxide) is scavenged by SO_2, forming formaldehyde as per equation 5.1. As a result, in excess SO_2, the loss of O_3 as a ratio of SO_2 loss is proportional to SCI formation, and can be used to infer SCI yields.

5.5.1 Calculating ϕ_{min}

The SCI yield can be determined by calculating the ratio of changes in SO_2 concentration with changes in O_3. Figure 5.14 shows the calculated minimum SCI yields (ϕ_{min}) for *cis*-but-2-ene, *trans*-but-2-ene, *cis*-pent-2-ene, *trans*-pent-2-ene, *cis*-hex-2-ene and 2-methyl-but-2-ene. The SCI yields were calculated using equation 5.8. If all CIs are formed stabilised and react with SO_2, then the ratio of SO_2:O_3 would be equal to 1. The calculated yield, ϕ_{min} represents the minimum SCI yield as, in reality, not all SCIs formed will react with SO_2. The gradient of a plot of ΔSO_2 against ΔO_3 is equal to the minimum SCI yield for that reaction, ϕ_{min} (Figure 5.14).

$$\frac{\Delta SO_2}{\Delta O_3} = \phi_{min} \tag{5.8}$$

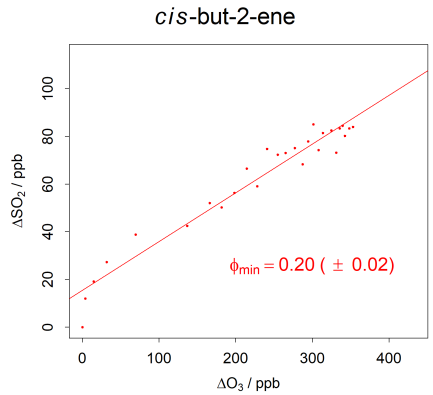

(a) Experiment ID: C2B2

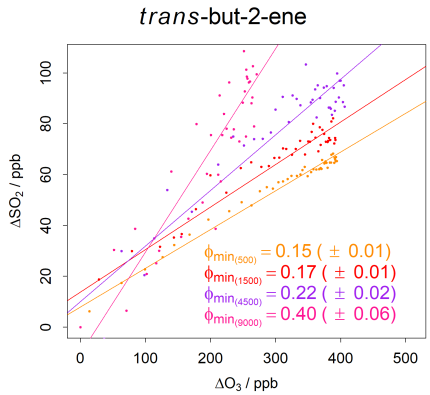

(b) Experiment ID: T2B(2,3,4,5)

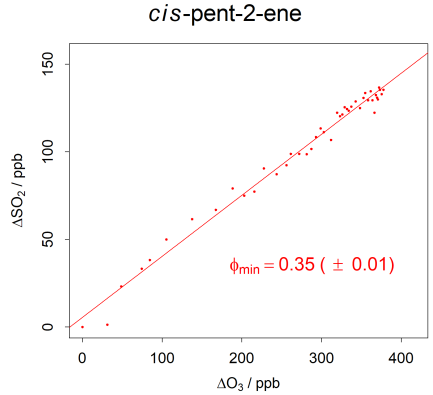

(c) Experiment ID: C2P2

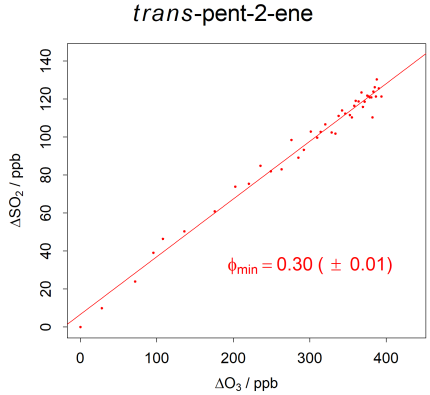

(d) Experiment ID: T2P2

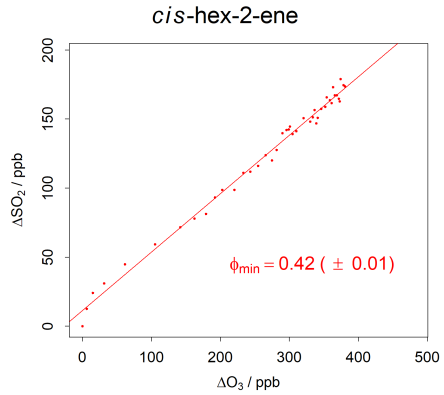

(e) Experiment ID: C2H2

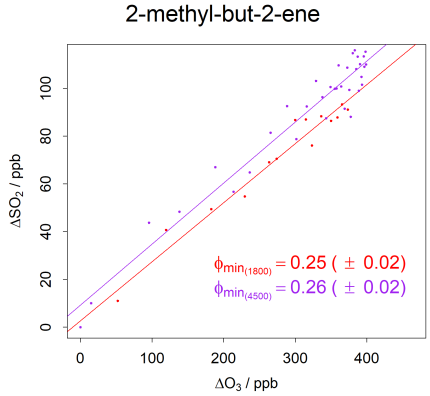

(f) Experiment ID: 2M2B(4,5)

Figure 5.14: ΔSO_2 vs. ΔO_3 during high SO_2 experiments for six alkenes, to determine ϕ_{min} $\pm 2\theta$.

5.5.2 Calculating ϕ_{total}

To calculate the total SCI yield, ϕ_{total}, SCI decomposition routes must be accounted for. The fraction of SCI that reacts with SO_2, f, can be calculated using equation 5.9, where k_{SCI+SO_2} and k_{decomp} are the loss rates for each SCI via reactions with SO_2 and unimolecular decomposition respectively. Literature values for k_{SCI+SO_2} and k_{decomp} are as reported in Vereecken et al., 2017 [224].

$$f = \frac{k_{SCI+SO_2}}{k_{SCI+SO_2} + k_{decomp}} \tag{5.9}$$

For species that produce multiple CIs, the total value of f is the sum of the calculated f values for each CI, after a branching ratio for each SCIs formation has been applied. The branching ratios used in this analysis were determined from the primary carbonyl yields from each ozonolysis reaction (see section 5.4). When *syn*:*anti* ratios could not be deduced from primary carbonyl yield data, a ratio of 1:1 was assumed. Calculated values of f are given in Table 5.7.

The total SCI yield, ϕ_{total}, can then be calculated using equation 5.10. The resulting values of ϕ_{total} are presented in Table 5.8.

$$\phi_{total} \cdot f = \phi_{min} \tag{5.10}$$

Table 5.7: Total f values for each high SO_2 experiment, and individually calculated f values multiplied by branching ratios (BR), calculated from the primary carbonyl yields calculated in section 5.4.

Experiment ID	$[SO_2]_i$ / ppbV	Branching Ratios (BR)	f(CI)*BR		f
C2B2	2111	0.5	*E*-CH_3CHOO:	0.496	0.953
		0.5	*Z*-CH_3CHOO:	0.456	
T2B2	539	0.5	*E*-CH_3CHOO:	0.486	0.850
		0.5	*Z*-CH_3CHOO:	0.364	
T2B3	1674	0.5	*E*-CH_3CHOO:	0.496	0.942
		0.5	*Z*-CH_3CHOO:	0.446	
T2B4	4901	0.5	*E*-CH_3CHOO:	0.498	0.979
		0.5	*Z*-CH_3CHOO:	0.480	
T2B5	9044	0.5	*E*-CH_3CHOO:	0.499	0.988
		0.5	*Z*-CH_3CHOO:	0.489	
2MB24	1965	0.335	*E*-CH_3CHOO:	0.332	0.947
		0.335	*Z*-CH_3CHOO:	0.304	
		0.33	$(CH_3)_2CHOO$	0.311	
2MB25	4866	0.335	*E*-CH_3CHOO:	0.334	0.978
		0.335	*Z*-CH_3CHOO:	0.322	
		0.33	$(CH_3)_2CHOO$	0.322	
C2P2	1914	0.24	*E*-CH_3CHOO:	0.238	0.932
		0.24	*Z*-CH_3CHOO:	0.217	
		0.22	*E*-C_2H_5CHOO:	0.216	
		0.30	*Z*-C_2H_5CHOO:	0.260	
T2P2	1973	0.23	*E*-CH_3CHOO:	0.228	0.923
		0.23	*Z*-CH_3CHOO:	0.209	
		0.15	*E*-C_2H_5CHOO:	0.150	
		0.39	*Z*-C_2H_5CHOO:	0.337	
C2H2	1918	0.245	*E*-CH_3CHOO:	0.243	0.937
		0.245	*Z*-CH_3CHOO:	0.222	
		0.255	*E*-C_3H_7CHOO	0.252	
		0.255	*Z*-C_3H_7CHOO	0.220	

Table 5.8: Total SCI yields (ϕ_{total}), for a range of alkenes, calculated by dividing ϕ_{min} by a reaction efficiency factor *f*.

Experiment	ϕ_{min}	ϕ_{total}
C2B2	0.20 ± 0.02	0.21 ± 0.02
T2B2	0.15 ± 0.01	0.18 ± 0.01
T2B3	0.17 ± 0.01	0.18 ± 0.01
T2B4	0.22 ± 0.02	0.22 ± 0.01
T2B5	0.40 ± 0.06	0.40 ± 0.06
2M2B4	0.25 ± 0.02	0.26 ± 0.02
2M2B5	0.26 ± 0.02	0.27 ± 0.02
C2P2	0.35 ± 0.01	0.38 ± 0.01
T2P2	0.30 ± 0.01	0.33 ± 0.01
C2H2	0.42 ± 0.01	0.45 ± 0.01

5.6 Calculating SCI yields from the change in primary carbonyl yields under zero and excess SO_2

It is possible to determine SCI yields by comparing the difference in primary carbonyl yields under zero SO_2 experimental conditions with excess SO_2 conditions. As described earlier, alkene ozonolysis leads to the formation of at least one CI and its carbonyl co-product. In the presence of a large excess of SO_2, the overwhelming majority SCIs are assumed to react with SO_2 to form an additional quantity of this carbonyl co-product and SO_3, as described by equation 5.1, section 5.1. Therefore, this difference in carbonyl co-product yields from experiments in both zero SO_2 ($Y_{carb_{(zero)}}$) and high SO_2 ($Y_{carb_{(excess)}}$) conditions can be used to determine the minimum yield of stabilised CI formed (ϕ_{min}). For the majority of carbonyl species formed, both FTIR and PTR-MS measurements were made during the experiments. For the calculation of yields using the PTR-MS data, the first five data points have been removed from all experiments due to extreme data curvature which was impacting the trendline. The justification for removing these points is discussed in more detail in section 5.6.6. The differences between yields calculated using both instruments will be discussed in this section.

5.6.1 *cis*- and *trans*-but-2-ene

Since only the acetaldehyde oxide and an acetaldehyde co-product are formed from the ozonolysis of *cis*-but-2-ene and *trans*-but-2-ene, the additional yield of acetaldehyde observed from high SO_2 experiments compared to zero SO_2 experiments is equal to ϕ_{min}. ϕ_{min} is thus calculated by subtracting $Y_{carb_{(zero)}}$ from $Y_{carb_{(excess)}}$. Figure 5.15 shows the change in acetaldehyde concentrations with changing O_3 concentrations during *cis*-but-2-ene experiments, under both zero and high SO_2 conditions.

The calculated values of ϕ_{min} using FTIR and PTR-MS data are -0.26 ± 0.10 and 0.21 ± 0.03 respectively. Interestingly, the higher acetaldehyde yields are observed during zero SO_2 conditions than high SO_2 conditions when the FTIR acetaldehyde data is used. This suggests there is a problem with this data, as negative yields cannot be explained by our current understanding of Criegee chemistry. One obvious explanation is an experimental mix-up of the zero and high SO_2 experiments, since the absolute value of the yield compares well with the ϕ_{min} value calculated using the change in SO_2 method ($\phi_{min} = 0.20 \pm 0.02$, section 5.5). However, this is unlikely as the data is timestamped, and the observed PTR-MS data does not agree with this data. Yields calculated using the acetaldehyde PTR-MS data are higher for high SO_2 conditions than zero SO_2 conditions, and the resultant value of ϕ_{min} is consistent with ϕ_{min} calculated using the ΔSO_2 method. A full analysis comparing the two instrumental techniques, and the reasons these discrepancies are observed, is discussed in more detail in section 5.6.6.

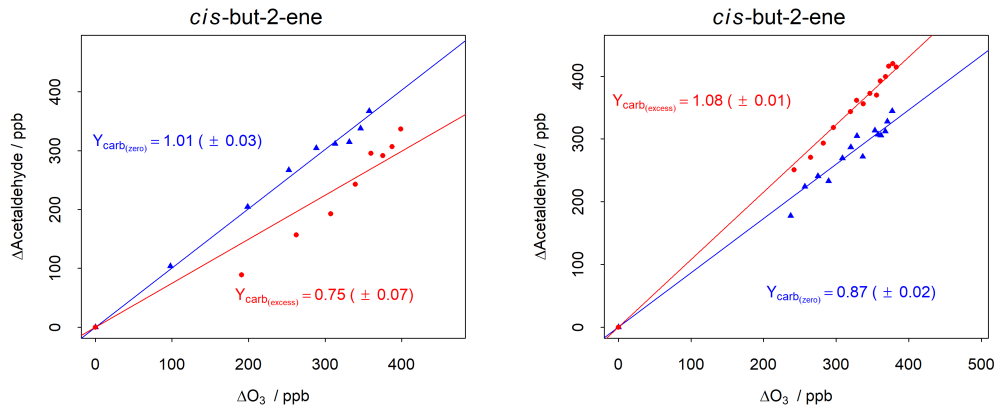

(a) FTIR (b) PTR-MS

Figure 5.15: ΔAcetaldehyde vs. ΔO_3 during zero SO_2 (blue, exp. ID: C2B1) and high SO_2 experiments (red, exp. ID: C2B2) for *cis*-but-2-ene using carbonyl data measured using FTIR (a) and PTR-MS (b).

The experimental yields of acetaldehyde from *trans*-but-2-ene ozonolysis are presented in Figure 5.16. For this alkene, there were multiple experiments performed at different concentra-

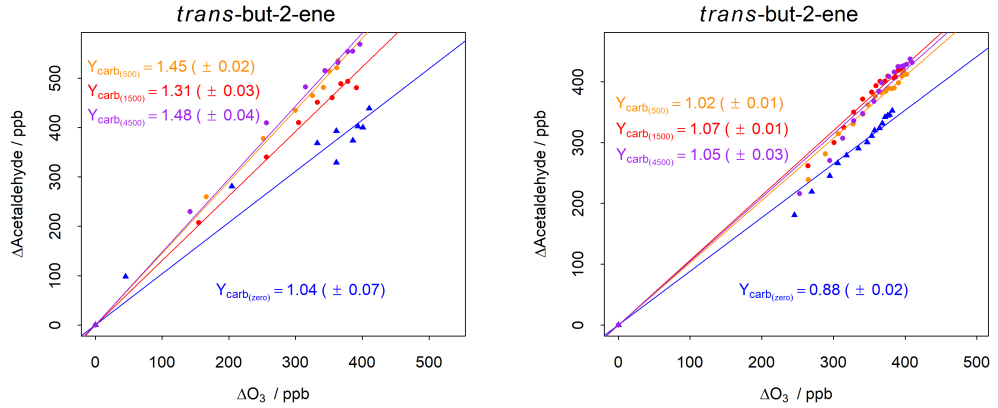

(a) FTIR (b) PTR-MS

Figure 5.16: ΔAcetaldehyde vs. ΔO_3 during zero SO_2 (blue, exp. ID: T2B1) and experiments at higher SO_2 concentrations of 500 ppbV (orange, exp. ID: T2B2); 1500 ppbV (red, exp. ID: T2B3) and 4500 ppbV (purple, exp. ID: T2B4) for *trans*-but-2-ene using carbonyl data measured using FTIR (a) and PTR-MS (b).

tions of SO_2 in the chamber. Using the FTIR data, calculated ϕ_{min} values for *trans*-but-2-ene were 0.41 ± 0.09, 0.27 ± 0.10 and 0.44 ± 0.11 from experiments conducted at 500 ppbV, 1500 ppbV and 4500 ppbV respectively. Yields calculated from experiments at 500 ppbV and 1500 ppbV agreed within uncertainties, whereas the yield calculated under 1500 ppbV of SO_2 was much lower. Yields taken from the PTR-MS data across the different concentrations of SO_2 are in greater agreement. Using this data, the calculated values of ϕ_{min} are 0.14 ± 0.03, 0.19

± 0.03 and 0.17 ± 0.05 under 500 ppbV, 1500 ppbV and 4500 ppbV of SO_2 respectively.

5.6.2 2-methyl-but-2-ene

The ozonolysis of 2-methyl-but-2-ene leads to the formation of two possible CI. The SCIs formed react with SO_2 to form an addition yield of the primary carbonyls acetaldehyde and acetone. Figure 5.17 shows the changes in acetaldehyde and acetone concentrations with changing O_3 concentrations during 2-methyl-but-2-ene experiments, under both zero and high SO_2 conditions. For 2-methyl-but-2-ene ozonolysis, there were two high SO_2 concentration

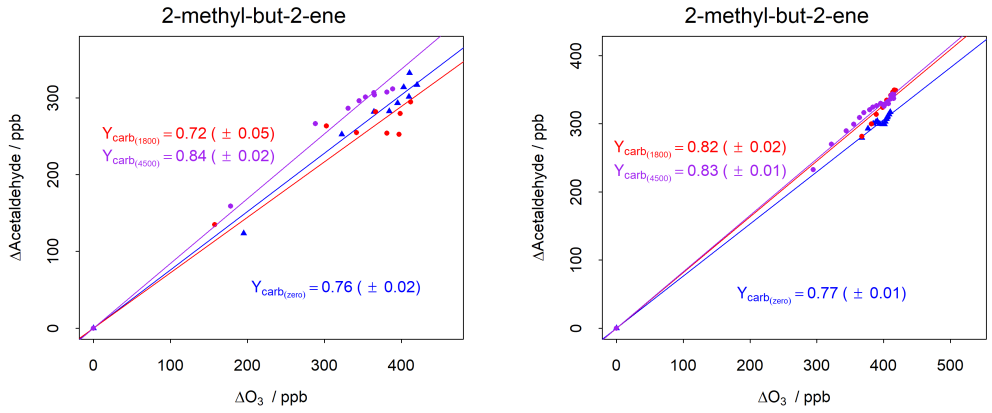

(a) FTIR (b) PTR-MS

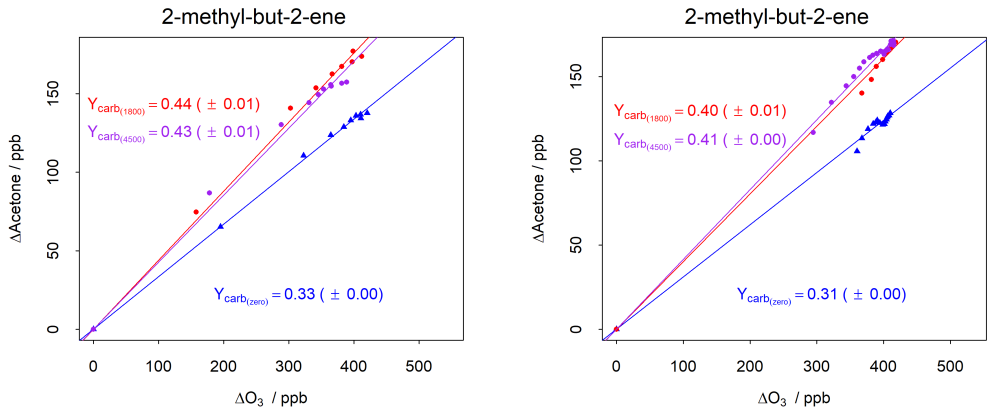

(c) FTIR (d) PTR-MS

Figure 5.17: ΔAcetaldehyde (a), (b) and ΔAcetone (c), (d), vs. ΔO_3 during zero SO_2 (blue, exp. ID: 2M2B3) and high SO_2 experiments: 1800 ppbV (red, exp. ID: 2M2B4) and 4500 ppbV (purple, exp. ID: 2M2B5) for 2-methyl-but-2-ene ozonolysis. Both FTIR (a), (c) and PTR-MS (b), (d), is used.

experiments, conducted at concentrations of SO_2 of 1800 ppbV and 4500 ppbV.

The yield of stabilised CH_3CHOO CI is calculated by subtracting the yields acetaldehyde

from the zero SO_2 experiment (exp. ID: 2M2B3), from the yield from higher SO_2 experiments. Using the FTIR data, the calculated yields of stabilised CH_3CHOO were -0.04 ± 0.07 and 0.08 ± 0.04 using data from the 1800 ppbV (exp. ID: 2M2B4) and 4500 ppbV (exp. ID: 2M2B5) SO_2 experiments respectively. The yield calculated from experiment 2M2B4 is negative, suggesting there is a problem with this data. In addition, the yield calculated from experiment 2M2B5 agrees well with the yields calculated from both values of SO_2 using the PTR-MS data. Yields of stabilised CH_3CHOO using this data are 0.05 ± 0.03 and 0.06 ± 0.02 from experiments 2M2B4 and 2M2B5 respectively.

The yields of stabilised $(CH_3)_2COO$ CI are calculated by subtracting the yields of acetone from experiment 2M2B3, from experiments 2M2B4 and 2M2B5. Using FTIR data, the yields of stabilised $(CH_3)_2COO$ were 0.11 ± 0.01 and 0.10 ± 0.01 for experiments 2M2B4 and 2M2B5 respectively. Yields from the PTR-MS data agree well with this, calculated as 0.09 ± 0.01 and 0.10 ± 0.00 from experiments 2M2B4 and 2M2B5 respectively.

The total value of ϕ_{min} can be calculated by summing the SCI yields from both POZ decomposition routes. Using the FTIR data, the values of ϕ_{min} are 0.07 ± 0.08 and 0.18 ± 0.05 using data from experiments 2M2B4 and 2M2B5 respectively. Using the PTR-MS observations, the summed values of ϕ_{min} are 0.14 ± 0.04 and 0.16 ± 0.02 respectively. These two yields, and the yield calculated using FTIR data from experiment 2M2B5, agree within their uncertainties.

5.6.3 *cis*- and *trans*-pent-2-ene

The ozonolysis of *cis*-pent-2-ene and *trans*-pent-2-ene produces two CIs and their carbonyl co-products: CH_3CHOO and propanal, and CH_3CH_2CHOO and acetaldehyde.

The yields of acetaldehyde from *cis*-pent-2-ene ozonolysis, CI-SO_2 bimolecular reactions using FTIR and PTR-MS data were 0.11 ± 0.02 and 0.14 ± 0.02 respectively. These values are in agreement within their uncertainties. The yield of propanal was 0.02 ± 0.05 using FTIR data. Only FTIR data is used to determine propanal yields as there is no available propanal data from the PTR-MS instrumentation. Therefore, the PTR-MS propanal data is excluded from the analysis. The summed ϕ_{min} from the FTIR data is 0.13 ± 0.07.

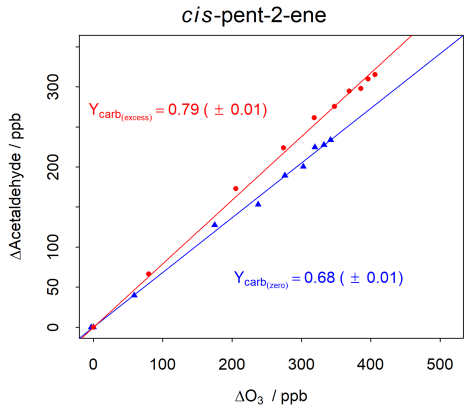

(a) FTIR

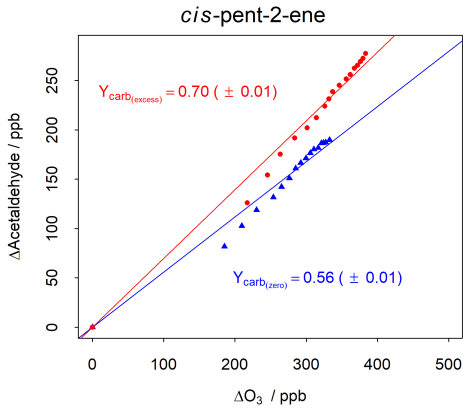

(b) PTR-MS

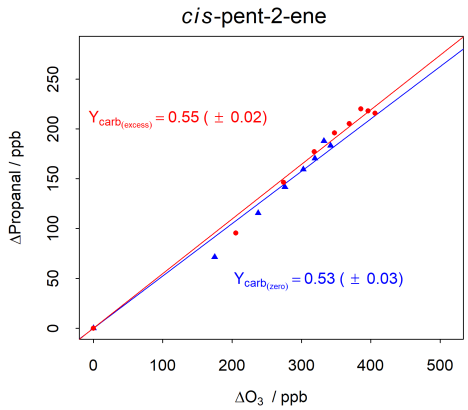

(c) FTIR

Figure 5.18: ΔAcetaldehyde (a), (b) and ΔPropanal (c), vs. ΔO_3 during zero SO_2 (blue, exp. ID: C2P1) and high SO_2 (red, exp. ID: C2P2) experiments for *cis*-pent-2-ene ozonolysis. Both FTIR (a), (c) and PTR-MS (b), is used. PTR-MS data for propanal is unavailable.

The yields of acetaldehyde and propanal from *trans*-pent-2-ene ozonolysis are presented in Figure 5.19. The yields of stabilised CH_3CHOO using FTIR and PTR-MS data were 0.18 ± 0.03 and 0.12 ± 0.02 respectively. The stabilised yield of CH_3CH_2CHOO using FTIR data was 0.17 ± 0.03. As with *cis*-pent-2-ene, there is no available PTR-MS propanal data. Therefore, using FTIR data only, the calculated value of ϕ_{min} for *trans*-pent-2-ene is 0.35 ± 0.06.

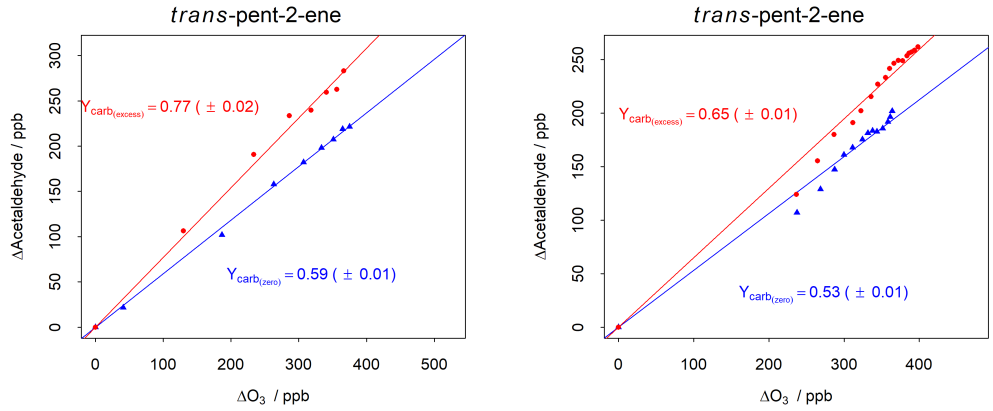

(a) FTIR (b) PTR-MS

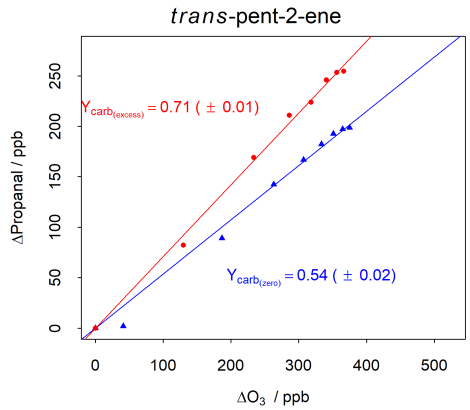

(c) FTIR

Figure 5.19: ΔAcetaldehyde (a), (b) and ΔPropanal (c), vs. ΔO_3 during zero SO_2 (blue, exp. ID: T2P1) and high SO_2 (red, exp. ID: T2P2) experiments for *trans*-pent-2-ene ozonolysis. Both FTIR (a), (c) and PTR-MS (b), is used where available.

5.6.4 *cis*-hex-2-ene

The ozonolysis of *cis*-hex-2-ene leads to the formation of the CH_3CHOO CI and C_3H_7CHOO CI. To determine the value of ϕ_{min}, the difference in yields in acetaldehyde and butanal under zero and high SO_2 conditions must be determined. Unfortunately, there is no butanal data available from either the FTIR or PTR-MS for the *cis*-hex-2-ene experiments, so only the acetaldehyde yields are presented here. The yields of acetaldehyde using FTIR and PTR-MS data are presented in Figure 5.20. There is a good agreement between the FTIR and PTR-MS derived yields of acetaldehyde. The yields of acetaldehyde from *cis*-hex-2-ene were 0.20 ± 0.03 and 0.16 ± 0.01, using FTIR and PTR-MS data respectively. The value of ϕ_{min} calculated earlier by observing the change in SO_2 concentrations with changing O_3 concentrations (see section 5.5), was 0.42 ± 0.01.

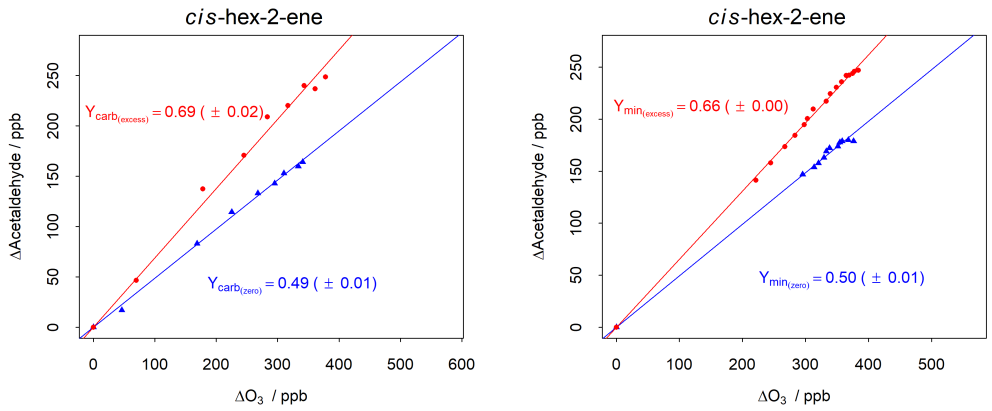

(a) FTIR (b) PTR-MS

Figure 5.20: ΔAcetaldehyde vs. ΔO_3 during zero SO_2 (blue, exp. ID: C2H1) and high SO_2 (red, exp. ID: C2H2) experiments for *cis*-hex-2-ene using carbonyl data measured using FTIR (a) and PTR-MS (b).

5.6.5 Calculation of $\phi_{total(partial)}$ using carbonyl yields

The calculated values of ϕ_{min} for each carbonyl species ($\phi_{min_{(partial)}}$), calculated by subtracting $Y_{carb_{(zero)}}$ from $Y_{carb_{(excess)}}$, are summarised in Table 5.9. Each calculated value of $\phi_{min_{(partial)}}$ has been divided by an efficiency factor, *f*, which accounts for the proportion of CIs that do not react with SO_2 in each experiment (see section 5.5).

The sum of all values of $\phi_{min_{(partial)}}$ for each alkene ozonolysis product gives the total minimum SCI yield, ϕ_{min}. The calculated values of ϕ_{total}, determined by dividing ϕ_{min} by an efficiency factor, *f*, for each CI are presented in Table 5.10. ϕ_{total} values derived from $\Delta SO_2/\Delta O_3$ calculations are also presented for comparison (see section 5.5.1). Values of ϕ_{total} derived from ΔCarbonyl/ΔO_3 (FTIR) are in good agreement with those derived from $\Delta SO_2/\Delta O_3$ regression plots for *trans*-but-2-ene (exp ID: T2B3), and *trans*-pent-2-ene, within the calculated uncertainties (2θ). For *cis*-but-2-ene and *trans*-but-2-ene, there is a greater agreement between the $\Delta SO_2/\Delta O_3$ derived ϕ_{total} and the ΔCarbonyl/ΔO_3 values using PTR-MS data, rather than FTIR data.

Table 5.9: Calculated values of $\phi_{min_{(partial)}}$ divided by an efficiency factor, f to give $\phi_{total_{(partial)}}$ (see section 5.5.1). Calculated SCI yields represent the proportion of total yield attributed to a give SCI. The sum of all $\phi_{total_{(partial)}}$ yields for a given alkene is equal to ϕ_{total}.

		$\phi_{min_{(partial)}}$		$\phi_{total_{(partial)}}$	
Experiment	Product	FTIR	PTR-MS	FTIR	PTR-MS
C2B2	Acetaldehyde	NA	0.21 ± 0.03	NA	0.22 ± 0.03
T2B2	Acetaldehyde	0.41 ± 0.09	0.14 ± 0.03	0.48 ± 0.09	0.16 ± 0.03
T2B3	Acetaldehyde	0.27 ± 0.10	0.19 ± 0.03	0.29 ± 0.10	0.20 ± 0.03
T2B4	Acetaldehyde	0.44 ± 0.11	0.17 ± 0.05	0.45 ± 0.11	0.17 ± 0.05
2M2B4	Acetaldehyde	NA	0.05 ± 0.03	NA	0.05 ± 0.03
2M2B5	Acetaldehyde	0.08 ± 0.04	0.06 ± 0.02	0.08 ± 0.04	0.06 ± 0.02
2M2B4	Acetone	0.11 ± 0.01	0.09 ± 0.01	0.12 ± 0.01	0.10 ± 0.01
2M2B5	Acetone	0.10 ± 0.01	0.10 ± 0.00	0.10 ± 0.01	0.10 ± 0.01
C2P2	Acetaldehyde	0.11 ± 0.02	0.14 ± 0.02	0.12 ± 0.02	0.15 ± 0.02
C2P2	Propanal	0.02 ± 0.05	NA	0.02 ± 0.05	NA
T2P2	Acetaldehyde	0.18 ± 0.03	0.12 ± 0.02	0.19 ± 0.03	0.13 ± 0.02
T2P2	Propanal	0.17 ± 0.03	NA	0.19 ± 0.03	NA
C2H2	Acetaldehyde	0.20 ± 0.03	0.16 ± 0.01	0.21 ± 0.03	0.17 ± 0.01

Table 5.10: Comparison of ϕ_{total} values, calculated by determining the total SCI yield from changes in SO_2 concentrations, and more indirectly by determining individual SCI yields from changes in carbonyl concentrations observed by both FTIR and PTR-MS.

Experiment	ϕ_{total}		
	$\Delta SO_2/\Delta O_3$	ΔCarbonyl/O_3 (FTIR)	ΔCarbonyl/O_3 (PTRMS)
C2B2	0.21 ± 0.02	NA	0.22 ± 0.03
T2B2	0.18 ± 0.01	0.48 ± 0.09	0.16 ± 0.03
T2B3	0.18 ± 0.01	0.29 ± 0.10	0.20 ± 0.03
T2B4	0.22 ± 0.01	0.45 ± 0.11	0.17 ± 0.05
T2B5	0.40 ± 0.06	NA	NA
2M2B4	0.26 ± 0.02	NA	0.15 ± 0.04
2M2B5	0.27 ± 0.02	0.18 ± 0.05	0.16 ± 0.03
C2P2	0.38 ± 0.01	0.14 ± 0.07	NA
T2P2	0.33 ± 0.01	0.38 ± 0.06	NA
C2H2	0.45 ± 0.01	NA	NA

5.6.6 Instrument Uncertainties

As we have observed in section 5.6.5, the observed yields of acetaldehyde, acetone and propanal from the chamber ozonolysis experiments may be different depending on whether the FTIR or PTR-MS carbonyl data was used. Higher yields of acetaldehyde in zero SO_2 conditions than high SO_2 conditions were observed using the FTIR data, which is unexpected. It is possible that the FTIR data analysis has been conducted using an automated software that auto picks peaks to identify each species. If this is the case, incorrect peaks may have been picked in the data analysis. Fundamental frequencies for both acetaldehyde and formaldehyde, a secondary carbonyl, appear across a similar range (2472 - 2835 cm^{-3}), and although these are normally distinguishable, it is possible the automated software has made an error. For example, it may

be possible that the CH_2 stretch observed in a formaldehyde FTIR spectrum (2874 cm^{-3}) has been confused with a CH stretch in an acetaldehyde spectrum (2822 cm^{-3}) [225]. However, as the software is likely to take into account peaks across the entire range, a discrepancy in one fundamental band is unlikely to lead to the incorrect compound being identified, and multiple discrepancies would be required for the software to incorrectly identify the species. Therefore, it is unlikely, but possible that the software has overestimated or underestimated the acetaldehyde absorption due to interferences with the formaldehyde spectrum, which has multiple peaks in the same range as acetaldehyde.

The first five data points from the PTR-MS analysis were removed, due to the data points curving away from the trendline. These data points are indicating that production of the carbonyl species is low relative to consumption of O_3. One likely cause of this is incomplete mixing when the species in introduced to the chamber. Due to the chamber design and instrument requirements, the PTR-MS samples the chamber from an inlet, whereas the FTIR scans the entire chamber. As a result, incomplete mixing may impact PTR-MS measurements more than the FTIR measurements. This curving is most visible during the 2-methyl-but-2-ene experiments (2MB23 and 2M2B4), where curving visibly reduces the gradient of the trendline. Figure 5.21 shows the trendline derived from using all data points from the PTR-MS acetaldehyde and acetone data.

In addition, the uncertainties quoted here represent two standard deviations of the data distribution, and do not account of additional instrumental uncertainties. The FTIR instrument uncertainties are often significant ($\approx$ 5 - 20%), and additional uncertainties may be added to the error, depending on the calculated instrument uncertainty for individual chemical species.

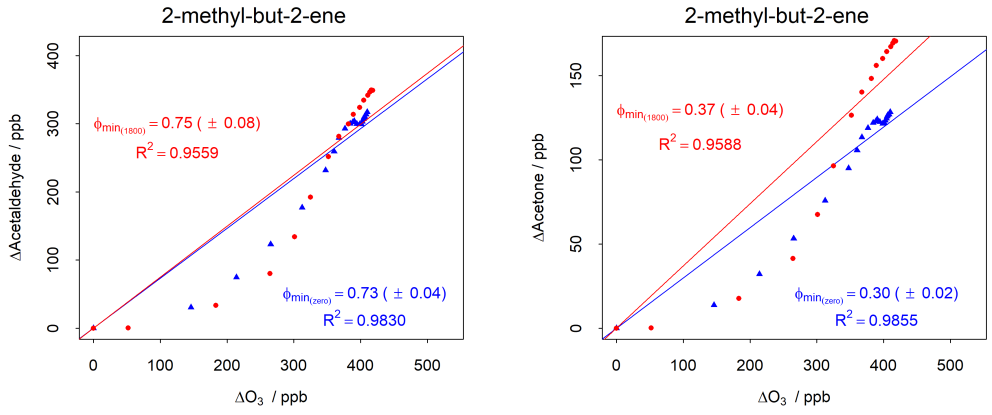

Figure 5.21: ΔAcetaldehyde and ΔAcetone (a), (b), vs. ΔO_3 during zero SO_2 (blue, exp. ID: 2M2B3) and high SO_2 (red, exp. ID: 2M2B4) experiments for 2-methyl-but-2-ene using carbonyl data measured by PTR-MS.

5.7 SCI yield trends, and comparison to literature values

5.7.1 SCI yields comparison to literature

A summary of the calculated SCI yields and available literature values is presented in Table 5.11. SCI yields for ethene, propene, 2,3-dimethylbut-2-ene, 2,4-dimethylbut-2-ene, 2,4-dimethylpent-2-ene and 2,3,4-trimethylpent-2-ene taken from Newland et al., 2020 are also presented here [113]. Although yields for these alkenes were not described in this thesis, they were determined from the same campaign work, under the same experimental conditions, and have been published in an article in which the author of this thesis is a co-author [113].

The SCI yield for *cis*-but-2-ene determined in this work is within the range previously reported in the literature (0.19 - 0.43). The calculated *trans*-but-2-ene SCI yields also fall within the range of values reported in the literature (0.13 - 0.53). Difference between yields can often be attributed to the different experimental conditions in each study. Large uncertainties were reported for the two largest yields, 0.53 ± 0.24 and 0.49 ± 0.22, determined in Berndt et al., 2012 [226] and Berndt et al., 2014 [227] respectively. These yields were determined using SO_2 as a scavenger, and monitoring the formed from SCI reacts with SO_2. H_2SO_4 was monitored and used to determine the proportion of SCI formed. As a result, the calculated SCI yields were linearly dependant on H_2SO_4 calibrations, which has a maximum error of ± 45%. The SCI yields determined from this work in very high SO_2 conditions (exp. ID. T2B5) also report similarly high SCI yields to Berndt et al., 2012 [226] and Berndt et al., 2014 [227]. In this experiment, initial SO_2 is ≈ 9000 ppbV. One of the possible complications of such as excess of SO_2 is the proportion of SO_2 lost via routes other than bimolecular reactions with the SCI. At very high concentrations of SO_2, a larger proportion of SO_2 may be attributed to wall losses. This introduces an additional error as, if the loss of SO_2 to the wall is not accounted for correctly, SO_2 is lost at a greater rate than is expected from just SCI bimolecular reactions, leading to larger calculated yields of SCI formation. There are many examples of studies for which the SCI yields for *trans*-but-2-ene, at lower SO_2 concentrations (exp. ID: T2B2, T2B3, T2B4), are in agreement [228–230].

Literature values of 2-methyl-but-2-ene stabilised CI yields are limited. SCI yields have previously been reported in Rickard et al., 1999 [239]. These values are much lower than those calculated in this work. One possible reason for this is linked to the method in which SCI yields were determined in this study. The study uses the indirect method of calculating the SCI yields, as described here in section 5.6.5. In this study, the change in carbonyl concentration during both high and zero SO_2 concentrations is determined, and the difference in carbonyl yields is used to determine the total SCI yield. For 2-methyl-2-butene experiments in this study, lower SCI yields were also observed using this approach compared to the yields calculated from $\Delta SO_2/\Delta O_3$. In addition, this more indirect approach uses data from two experiments rather than monitoring changing SO_2 in one experiment, leading to larger uncertainties.

Table 5.11: Calculated SCI yields for the ozonolysis of a range of alkenes, along with available literature values for comparison. Many literature yields are summarised in Calvert et al., 2015 [137].

Alkene	Exp. ID	SCI yield	Reference	SCI scavenger
Ethene	-	0.43 ± 0.02	Newland et al., 2020 [113]	SO_2
		0.38 ± 0.11	Hasson et al., 2001 [231]	H_2O
		0.39 ± 0.11	Hasson et al., 2001 [231]	HC(O)OH
		0.39	Hatakeyama et al., 1984 [228]	SO_2
		0.5	Neeb et al., 1996 [232]	HC(O)OH
		0.42	Neeb et al., 1997 [233]	H_2O
		0.52	Horie et al., 1999[229]	$CF_3C(O)CF_3$
		0.38	Su et al., 1980 [234]	HCHO, CH_3CHO, SO_2
		0.37	Kan et al., 1981 [235]	HCHO
		0.35	Niki et al., 1981 [236]	HCHO
		0.37 ± 0.04	Newland et al., 2015 [237]	SO_2
		0.54 ± 0.12	Alam et al., 2011 [238]	CO
Propene	-	0.34 ± 0.01	Newland et al., 2020 [113]	SO_2
		0.14	Neeb et al., 1997 [233]	H_2O
		0.25	Hatakeyama et al., 1984 [228]4	SO_2
cis-but-2-ene	C2B2	0.21 ± 0.02	This work	SO_2
		0.38 ± 0.05	Newland et al., 2015 [237]	SO_2
		0.19	Rickard et al., 1999 [239]	SO_2
		0.43	Cox and Penkett, 1972 [240]	SO_2
		0.18	Niki et al., 1997 [241]	HCHO
trans-but-2-ene	T2B2	0.18 ± 0.01	This work	SO_2
	T2B3	0.18 ± 0.01	This work	SO_2
	T2B4	0.22 ± 0.02	This work	SO_2
		0.28 ± 0.03	Newland et al., 2015 [237]	SO_2
		0.49 ± 0.22	Berndt et al., 2014 [227]	SO_2
		0.53 ± 0.24	Berndt et al., 2012 [226]	SO_2
		0.45	Cox and Penkett, 1972 [240]	SO_2
		0.19 ± 0.03	Hatakeyama et al., 1984 [228]	SO_2
		0.22	Horie et al., 1999 [229]	$CF_3C(O)CF_3$
		0.42	Horie et al., 1991[242]	HCHO
		0.24 ± 0.07	Hasson et al., 2001 [231]	H_2O
		0.13	Rickard et al., 1999 [239]	SO_2
2-methyl-but-2-ene	2M2B4	0.26 ± 0.02	This work	SO_2
	2M2B5	0.27 ± 0.02	This work	SO_2
		0.10	Rickard et al., 1999 [239]	SO_2
cis-pent-2-ene	C2P2	0.38 ± 0.01	This work	SO_2
trans-pent-2-ene	T2P2	0.32 ± 0.01	This work	SO_2
cis-hex-2-ene	C2H2	0.45 ± 0.01	This work	SO_2
2,3-dimethylbut-2-ene	-	0.31 ± 0.04	Newland et al., 2020 [113]	SO_2
		0.32 ± 0.02	Newland et al., 2020 [237]	SO_2
		0.45 ± 0.20	Berndt et al., 2014 [227]	SO_2
		0.62 ± 0.28	Berndt et al., 2012 [226]	SO_2
		0.10 ± 0.03	Hasson et al., 2001 [231]	H_2O
		0.30	Niki et al., 1987 [207]	HCHO
		0.11	Rickard et al., 1999 [239]	SO_2
2,4-dimethylpent-2-ene	-	0.41 ± 0.01	Newland et al., 2020 [113]	SO_2
2,3,4-trimethylpent-2-ene	-	0.49 ± 0.01	Newland et al., 2020 [113]	SO_2

No yields for *cis*-pent-2-ene, *trans*-pent-2-ene and *cis*-hex-2-ene could be found in the literature for comparison. However, SCI yields appear to increase with increasing carbon chain length. Further experimental work investigating the SCI yields of the pent-2-enes and

hex-2-enes would be useful to assess the SCI yields of these species, and to investigate a link between carbon chain length of the parent alkene and the resulting stabilised population of CIs. One interesting finding is that the *cis*- isomers of but-2-ene and pent-2-ene have greater SCI yields than their *trans*- counterparts. This is a consistent finding in the literature for *cis*- and *trans*-but-2-ene, with *trans*-but-2-ene SCI yields found to be 25 - 35% lower than *cis*-but-2-ene in Newland et al., 2015 [237] and Rickard et al., 1999 [239].

SCI yields from ethene, propene and 2,3-dimethylbut-2-ene were also determined as part of this campaign work, and literature is available for these species. As the simplest alkene, there are a wide number of studies were ethene ozonolysis SCI yields are reported. The SCI yield reported in this work is within the range of values previously reported in the literature (0.35 - 0.54). The current value for the ethene SCI yield used in the MCM (0.37), and the yield calculated here (0.43 ± 0.02), are both within the range of reported literature values. There are very few SCI yields reported from propene ozonolysis. The SCI yields determined in this campaign work were higher than those calculated in previous studies. In addition, the two literature values are not in good agreement. Further experimental work is required to fully assess the SCI yields of propene. SCI values of 2,3-dimethylbut-2-ene determined as part of this experimental work are within the range previously reported in the literature (0.10 - 0.62). These values are in very good agreement with those determined during an almost identically designed experiment, also conducted at the EUPHORE smog chamber [237]. SCI yields of 2,4-dimethylpent-2-ene and 2,3,4-trimethylpent-2-ene, were also determined as part of this campaign, and published in Newland et al., 2020 [113].

5.7.2 Trends in SCI yields

The yield of stabilised CIs, relative to excited CIs (1 - SCI yield) is important for understanding the chemical processes in the atmosphere, resulting from the ozonolysis of a particular alkene. As discussed earlier (see section 5.2), excited CIs (CI*s) readily undergo unimolecular decomposition processes, whereas SCIs are long-lived enough to undergo bimolecular reactions with stable species in the atmosphere. As a result of this, an increased yield of CI* (lower SCI yield) formed from ozonolysis reactions, leads to increased formation of radical species such as OH, HO_x and RO_x. Because of this, we expect the SCI yields determined in this study to be anti-correlated with OH yields, and thus correlated with 1-OH yields.

The SCI yields determined as part of this thesis were combined with the SCI yields determined in Newland et al., 2020 [113] to investigate trends. Figure 5.22(a) shows SCI yields (ϕ_{total}) are correlated with 1-OH yields defined in the literature [243], excluding a few exceptions with very high OH yields. This suggests that higher OH yields can be expected from alkenes with lower SCI yields, in line with reported SCI decomposition mechanisms (section 5.2.2, Figures 5.4, 5.5, and 5.6). The relationship between ϕ_{total} and 1-OH yields is not directly proportional. This is consistent with there being multiple unimolecular fates for CIs,

including dioxirane formation routes which do not form OH (Figure 5.4).

The trend in SCI yield with the carbon number of the parent alkene is presented in Figure 5.22(b). The SCI yield, ϕ_{total} decreases with carbon number until a low point at C_4. After this, stabilisation yields increase with increasing carbon number. As the C_4 alkenes have the lowest SCI yields, ozonolysis of these alkenes is likely to lead to the formation of a larger population of excited CIs (CI*), which readily undergo unimolecular decomposition via the VHP mechanism (section 5.2.2, Figure 5.5). As described earlier, depending on the the structure of the CI* formed, there will be different chemical fates. Some CI* decomposition routes will lead to the increased formation of radicals, important atmospheric oxidants and contributors to the NO_x catalysed photochemical cycles involved in O_3 and photochemical smog formation (see Chapter 1). As described in Chapter 3, and summarised earlier in this chapter (see section 5.1), alkene ozonolysis is an important source of OH radicals in Delhi, which are in turn important in situ O_3 production (see Chapter 4). The relationship between SCI yield and carbon number may thus be significant for places like Delhi, where large concentrations of C_4 alkenes are observed ($\approx$ 3.5 ppbV in the post-monsoon, see Chapter 3).

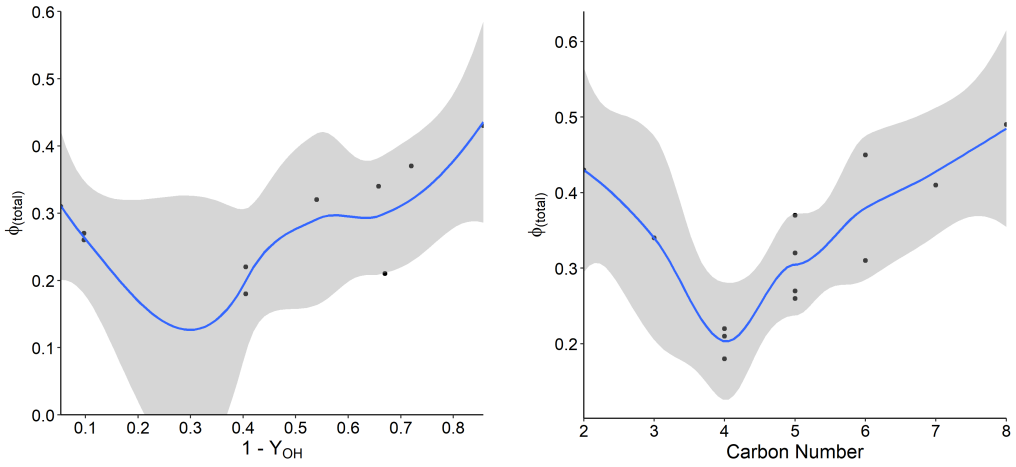

(a) 1-Y_{OH} (b) Carbon number

Figure 5.22: Change in $\phi_{(total)}$ with 1-Y_{OH} (a) and carbon number (b) for a range of alkene SCI yields determined in this study and in a sister publication, Newland et al., 2020 [113].

Currently, in the MCM, SCI yields from ethene, propene, and 2-methyl-but-2-ene are 0.37, 0.24 and 0.11 respectively. These values are lower than those calculated in this work (Table 5.11), possibly underestimating the proportion of CIs that are stabilised, and overestimating the proportion of CIs undergoing unimolecular decomposition to form OH radicals. The underestimation of SCI formation is significant, since SCIs are important atmospheric oxidants, and can lead to the formation of secondary organic aerosol which has both human health and climate impacts (see Chapter 1). MCM SCI yields for *cis*-but-2-ene, *trans*-but-2-ene, *cis*-pent-2-ene, *trans*-pent-2-ene and *cis*-hex-2-ene are 0.18. This is in good agreement with the SCI yields determined for *trans*-but-2-ene in this work, but is lower than SCI yields de-

termined for the other four alkenes. The MCM SCI yield for 2,3-dimethylbut-2-ene is zero, and assumes all of this alkene undergoes decomposition to form OH. This suggests direct OH formation from alkene ozonolysis in Delhi, as described in Chapter 3, may be overestimated from alkene ozonolysis reactions. This may have implications in both the Delhi pre-monsoon and post-monsoon campaigns, since ozonolysis represents 21% and 23% of day-time OH initiation during these campaigns respectively. If the contribution of ozonolysis to OH initiation is reduced, HONO and O^1D photolysis would be proportionally larger contributors to OH initiation. In addition, ozonolysis is an OH initiation route in the pre-monsoon campaign in the night, and so night-time OH initiation would be reduced. However, ozonolysis is also an important HO_2 and RO_2 initiation route. This may also be affected by changing SCI yields, and more work is required to investigate the impact of this. An additional box modelling study is required to fully assess the effect of changing SCI yields on the total radical budget.

Chapter 6

Summary and future work

The work presented in this thesis aimed to assess the chemical processes in Delhi's atmosphere, leading to in situ O_3 production. A comprehensive data set of 86 unique volatile organic compounds (VOCs) and oxygenated volatile organic compounds (o-VOCs) was collected during two intensive field campaigns at an urban site in Delhi, India. A broad range of supporting measurements was also collected, including NO, NO_2, CO, SO_2, O_3, HONO and aerosols (diameter and count). This work presents the concentration time series and diel profiles of key atmospheric species, before using them to constrain a tailored chemical box model, incorporating the detailed Master Chemical Mechanism (MCM). The study used campaign data available from both the pre-monsoon (May-June) and post-monsoon (October) seasons in Delhi, India in 2018.

For both the pre-monsoon and post-monsoon campaigns, two chemical models were produced, constrained to the diel of the observation data set. For each campaign, concentrations of OH, HO_2 and RO_2 were modelled, and a full radical budget analysis was derived to determine the key radical pathways driving the atmospheric chemistry. Though the radical budgets of the two models were similar in many ways, there were some distinct differences. One of the major differences was the sources of OH, which were mostly split between $O(^1D)$ and HONO photolysis in the pre-monsoon, but were predominantly from HONO photolysis in the post-monsoon. Ozonolysis was found to be a large contributor to radical initiation in both the pre-monsoon and post-monsoon campaigns, contributing to 23% and 27% of radical initiation respectively. The compounds with the largest contributions to radical initiation via ozonolysis were the but-2-enes and pent-2-enes. The rates of radical propagation were compared to other locations in the literature. Radical propagation was found to be higher than all UK locations for both campaigns, and was approximately x 10 greater in the post-monsoon, than had been determined in previous studies using campaign data from Birmingham, UK and Chelmsford, UK. The Delhi post-monsoon radical budget was compared to a published radical budget using data from a similar campaign in Beijing, China. Although the radical budget for the Delhi post-monsoon campaign showed higher rates of radical propagation compared to Beijing, O_3 concentrations were comparable. This was attributed to high rates of

radical termination in the Delhi post-monsoon radical budget.

The campaign tailored post-monsoon box model was used to investigate the sensitivity of in situ O_3 production to changes in VOCs, NO_x, aerosol and photolysis. The urban measurement site at the Indira Gandhi Delhi Technical University for Women was determined to be in a VOC-limited chemical regime. This analysis examined the sensitivity of VOC classes to mean morning $P(O_3)$, and the aromatic VOC class was identified as being the most important, with a 50 % reduction in ambient concentrations leading to a reduction in modelled morning $P(O_3)$ of 15.6%, followed by monoterpenes and alkenes (13.1% and 12.9%, respectively). The direct impact of the aerosol burden on $P(O_3)$ was found to be negligible with regards to heterogeneous radical uptake. However, $P(O_3)$ was sensitive to increasing photolysis, which may result from decreasing particulate matter that is likely to arise from future emission reduction strategies. Though it is important to reduce NO_x and particulate matter in all pollution abatement strategies, reducing NO_x without reducing VOCs was found to significantly increase $P(O_3)$. VOCs and NO_x were also evaluated by their respective contributions to different source sectors as defined in the EDGAR emissions inventory. Reducing emissions from road transport sources alone led to increased $P(O_3)$, even when the source was removed in its entirety. This suggests a balanced approach to pollution reduction strategies is required, and multiple sources should be targeted simultaneously for effective reduction, incorporating major monoaromatic, alkene, and anthropogenic monoterpene VOC sources. Reducing road transport emissions along with combustion from manufacturing and process emissions was found to be an effective way of reducing $P(O_3)$. Monoterpenes were found to have a significant impact on $P(O_3)$ and showed a diurnal profile consistent with other anthropogenic VOCs.

The products of alkene ozonolysis, an important source of radical species in Delhi, were further investigated through experimental work using an outdoor atmospheric simulation chamber. This work presents stabilised Criegee intermediate (SCI) yields and primary carbonyl yields for a range of alkenes. SCI and primary carbonyl yields for *cis*-but-2-ene, *trans*-but-2-ene, and 2-methyl-but-2-ene were comparable to values found in the literature. SCI and primary carbonyl yields for *cis*-pent-2-ene, *trans*-pent-2-ene and *cis*-hex-2-ene are presented here for the first time. When combined with the published SCI yields of other alkene species determined during the same experimental campaign at the smog chamber, SCI yields are determined to decrease from C_1 to C_4 alkenes, before increasing. This trend is also observed when SCI yields are plotted against 1 - Y_{OH} (where Y_{OH} is the OH yield of alkene ozonolysis, described in the literature). This is consistent with the current Criegee mechanism, whereby excited Criegee intermediates (CI*s) degrade entirely through unimolecular decomposition to yield radical species, unlike their stabilised counterparts which may additionally degrade through bimolecular reactions. The SCI yields determined in this work were larger than those described in the MCM. This means that the MCM may be overestimating the proportion of CIs undergoing unimolecular decomposition, and thus overestimating the concentrations of OH radicals. This may have important implications for both the radical budget analysis in

Chapter 3 and the ozone sensitivity study in Chapter 4. This is particularly significant for the radical budget analysis in Chapter 3, as the but-2-enes and pent-2-enes are identified as large contributors to radical initiation via ozonolysis. However, it is not possible to assess the scale of the implications, without undertaking an additional box model study whereby the mechanism is changed, and the analysis is repeated. This study may reveal differences in the ozonolysis contributions to radical initiation, possibly reducing the ozonolysis contribution to OH initiation. The box model study would also reveal the impact of higher SCI yields on HO_2 and RO_2 initiation from ozonolysis.

Future work should be carried out to determine the sources and fraction of anthropogenic emissions to the observed monoterpene concentrations measured in Delhi, with a recent study suggesting 60% of the monoterpenes observed at the site are coming from traffic related sources [167]. To further understand the complex urban atmospheric chemistry in Delhi, more model constraints are required, such as the measurement of radical species and k(OH). The potential effects of chlorine chemistry were also not investigated in this study and may have an important role in the local chemistry due to the prevalence of waste burning in the city [244]. Satellite observations and aircraft measurements may also help develop our understanding of the regional impacts of regional agricultural biomass burning on Delhi from neighbouring states. The next stage for this work is to incorporate the experimentally determined SCI yields of a broad range of alkenes into the MCM. Adapted mechanisms could be added to the campaign tailored box model. The impact of these SCI yields on Delhi's radical budget and the sensitivity of in situ O_3 production to these changes could be explored. This work highlights that a careful approach, considering the complexities of chemical processing in the urban atmosphere, is required for effective air quality improvement strategies.

Appendix A

Appendix: Publications

A.1 Publications related to this thesis

Throughout this PhD, I have contributed to a range of scientific publications by providing measurements, data analysis, scientific discussion, writing paper content, and the writing of code used in atmospheric box models. The publications, of which I am a first or co-author, most relevant to the work presented in this thesis are as follows:

B. Nelson et al. "In situ Ozone Production is highly sensitive to Volatile Organic Compounds in the Indian Megacity of Delhi". In: *Atmos. Chem. Phys.* 21 (2021), pp. 1–36

D. J. Bryant et al. "Biogenic and anthropogenic sources of isoprene and monoterpenes and their secondary organic aerosol in Delhi, India". In: *In preparation* (2021)

G. J. Stewart et al. "Sources of non-methane hydrocarbons in surface air in Delhi, India". In: *Faraday Discuss.* 226 (2021), pp. 409–431

G. J. Stewart et al. "Emissions of intermediate-volatility and semi-volatile organic compounds from domestic fuels used in Delhi , India". In: *Atmos. Chem. Phys.* 21 (2021), pp. 2407–2426

G. J. Stewart et al. "Emissions of non-methane volatile organic compounds from combustion of domestic fuels in Delhi , India". In: *Atmos. Chem. Phys* 21 (2021), pp. 2383–2406

G. J. Stewart et al. "Emission estimates and inventories of non-methane organic compounds from anthropogenic burning sources in India". In: *Atmos. Environ.: X* 11.100115 (2021)

G. J. Stewart et al. "Comprehensive organic emission profiles, secondary organic aerosol production potential, and OH reactivity of domestic fuel combustion in Delhi, India". In: *Environ. Sci.: Atmos.* 1 (2021), pp. 104–117

Y. Chen et al. “Avoiding high ozone pollution in Delhi, India”. In: *Faraday Discuss.* 226 (2021), pp. 502–514

A. C. Lewis et al. “An increasing role for solvent emissions and implications for future measurements of volatile organic compounds: Solvent emissions of VOCs”. In: *Phil. Trans. R. Soc. A* 378.20190328 (2020)

M. J. Newland et al. “Trends in stabilisation of Criegee intermediates from alkene ozonolysis”. In: *Phys. Chem. Chem. Phys.* 22 (2020), pp. 13698–13706

R. Sommariva et al. “AtChem (version 1), an open-source box model for the Master Chemical Mechanism”. In: *Geosci. Model Dev.* 13 (2020), pp. 169–183

A. Elzein et al. “A comparison of $PM_{2.5}$-bound polycyclic aromatic hydrocarbons in summer Beijing (China) and Delhi (India)”. In: *Atmos. Chem. Phys.* 20 (2020), pp. 14303–14319

A.2 Additional publications

The following are additional publications to which author contributions have been made. The following journal articles aren’t directly linked to the work presented in this thesis, but required the scientific knowledge and skills developed as part of this PhD.

S. T. Andersen et al. “Long-Term NO_x measurements in the remote marine tropical troposphere”. In: *Atmos. Meas. Tech.* 14 (2021), pp. 3071–3085

K. Ashworth et al. “Megacity and local contributions to regional air pollution: An aircraft case study over London”. In: *Atmos. Chem. Phys.* 20 (2020), pp. 7193–7216

J. R. Pitt et al. “Assessing London CO_2, CH_4 and CO emissions using aircraft measurements and dispersion modelling”. In: *Atmos. Chem. Phys.* 19 (2019), pp. 8931–8945

Appendix B

Appendix: Supporting information

B.1 Supporting information for Chapter 4

Table B.1: $\Delta P(O_3)_{increm}$ for 77 VOCs, averaged between 08:00 and 12:00 IST.

Species	$\Delta P(O_3)_{increm}$ / ppb h^{-1}
α-Phellandrene	0.30
α-Pinene	0.02
α-Terpinene	0.66
1,2-Butadiene	0.02
Benzene	0.02
β-Ocimene	0.26
β-Pinene	0.00
But-1-ene	0.12
Ethyne	0.00
Ethene	0.40
Ethanol	0.30
Ethane	0.01
Propyne	0.00
Propene	0.35
Propane	0.07
1,3-Butadiene	0.07
Isoprene	0.94
3-Carene	0.03
cis-But-2-ene	0.19
Methanol	0.08
Camphene	0.01
CO	0.28
1,2-Diethylbenzene	0.01
1,3-Diethylbenzene	0.02
1,4-Diethylbenzene	0.02
1,2-Dimethyl-4-ethylbenzene	0.06
1,3-Dimethyl-2-ethylbenzene	0.03
2,3-Dimethyl-1-ethylbenezne	0.02
2,4-Dimethyl-1-ethylbenzene	0.03
Ethylbenzene	0.06
γ-Terpinene	0.03
Hex-2-one	0.00
Hex-3-one	0.00
Isobutane	0.15
Isopentane	0.14
Isopropylbenzene	0.01

Limonene	0.09
m-Cymene	0.03
1-Methyl-3-propylbenzene	0.00
1-Methyl-4-propylbenzene	0.00
1-Methylpropylbenzene	0.00
2-Methylpropylbenzene	0.00
Methylpropene	0.23
m-Xylene	0.21
Myrcene	0.08
n-Butylbenzene	0.02
n-Decane	0.01
n-Undecane	0.00
n-Dodecane	0.01
n-Tridecane	0.05
n-Tetradecane	0.04
n-Butane	0.21
n-Pentane	0.07
n-Hexane	0.01
n-Heptane	0.01
n-Octane	0.00
n-Nonane	0.01
o-Cymene	0.00
o-Ethyltoluene	0.04
o-Xylene	0.14
Propylbenzene	0.01
p-Cymene	0.02
Pent-1-ene	0.03
p-Ethyltoluene	0.08
p-Xylene	0.13
Sabinene	0.01
Styrene	0.01
trans-But-2-ene	0.22
1,2,3,4-Tetramethylbenzene	0.04
1,2,3,5-Tetramethylbenzene	0.06
1,2,4,5-Tetramethylbenzene	0.04
1,2,3-Trimethylbenzene	0.09
1,2,4-Trimethylbenzene	0.29
1,3,5-Trimethylbenzene	0.12
Toluene	0.37
trans-Pent-2-ene	0.11
Terpinolene	0.03

Table B.2: Description of source sectors used in Chapter 4. IPCC 1996 codes and descriptions taken from the IPCC Common Reporting Framework [250].

Source	IPCC code (1996)		Description
Road transport (RT)	1A3b	1A3b	All combustion and evaporative emissions from fuel use in road vehicles, including agricultural vehicles on highways.
		i	Cars: automobiles designed primary for *trans*port of persons, with a capacity of 12 or fewer. Gross vehicle weight rating of 3900 kg or less. Includes passenger vehicles with and without 3-way catalysts.
		ii	Light duty trucks: Vehicles with a gross vehicle weight of 3900 kg or less, designed primarily for the *trans*portation of light-weight cargo or equipped with special features such as four-wheel drive for off-road operation. Includes light duty trucks with and without 3-way catalysts.
		iii	Heavy Duty trucks and buses: Any vehicle rated at more than 3900 kg gross vehicle weight or designed to carry more than 12 persons at a time.
		iv	Motorcycles: Any motor vehicle designed to travel with not more than three wheels in contact with the ground, and weighing less than 680 kg.
		v	Evaporative emissions from vehicles.
Railways, Pipelines and Off-Road transport (RPORT)	1A3c+1A3e	1A3c	Fuel combustion emissions from railways, including both freight and passenger traffic routes.
		1A3e	Combustion emissions from all remaining *trans*port activities including pipeline *trans*portation, ground activities in airports and harbours, and off-road activities not reported under agriculture or manufacturing industries and construction.
Energy for Buildings (EB)	1A4	1A4a	Emissions from fuel combustion in commercial and institutional buildings.
		1A4b	All emissions from residential fuel combustion in households.

		1A4c	Emissions from fuel combustion in agriculture, forestry or domestic inland coastal and deep-sea fishing. Includes traction vehicles, pump fuel use, grain drying, horticultural greenhouse and other agriculture, forestry or fishing related fuel use.
Combustion for Manufacturing (CM)	1A2	1A2	Emissions from combustion of fuels in industry including combustion for the generation of electricity and heat.
		1A2a	Iron and steel.
		1A2b	Non-ferrous metals.
		1A2c	Chemicals.
		1A2d	Pulp, paper and print.
		1A2e	Food processing, beverages and tobacco.
		1A2f	Other emissions from fuel combustion in industry, including from the construction branch.
Process emissions (PE)	2	2A	Emissions from industrial processes: mineral products.
		2A1	Cement production.
		2A2	Lime production.
		2A3	Limestone and dolomite use.
		2A4	Soda ash production and use.
		2A5	Asphalt roofing.
		2A6	Road paving with asphalt.
		2A7	Other.
		2B	Emissions from chemical industry.
		2B1	Ammonia production.
		2B2	Nitric acid production.
		2B3	Adipic acid production.
		2B4	Carbide production.
		2B5	Other.
		2C	Emissions from metal production industry.
		2C1	Iron and steel production.
		2C2	Ferroalloys production.
		2C3	Aluminium production.
		2C4	SF6 used in aluminium and magnesium foundries.
		2C5	Other.
		2D	Emissions from other production industries.

		2D1	Pulp and paper.
		2D2	Food and drink.
		2E	Production of halocarbons and sulfur hexafluoride.
		2E1	By-product emissions.
		2E2	Fugitive emissions.
		2E3	Other.
		2F	Consumption of halocarbons and sulfur hexafluoride.
		2F1	Refrigeration and air conditioning equipment.
		2F2	Foam blowing.
		2F3	Fire extinguishers.
		2F4	Aerosols.
		2F5	Solvents.
		2F5	Other.
		2G	Other emissions from industrial processes.
	3		Solvent and other product use. This category mainly covers volatile organic compound (VOC) emissions from solvents and other products containing VOCs.
		3A	Paint application.
		3B	Degreasing and dry cleaning.
		3C	Chemical products, manufacturing and processing.
		3D	Other, including the use of N_2O as a carrier gas, anaesthetic and propellant.

Bibliography

[1] B. Nelson, G. Stewart, W. Drysdale, M. Newland, A. Vaughan, R. Dunmore, P. Edwards, A. Lewis, J. Hamilton, W. J. F. Acton, C. N. Hewitt, L. Crilley, M. Alam, Ü. Şahin, D. Beddows, W. Bloss, E. Slater, L. Whalley, D. Heard, J. Cash, B. Langford, E. Nemitz, R. Sommariva, S. Cox, R. Gadi, B. Gurjar, J. Hopkins, A. Rickard, and J. Lee. "In situ Ozone Production is highly sensitive to Volatile Organic Compounds in the Indian Megacity of Delhi". In: *Atmos. Chem. Phys.* 21 (2021), pp. 1–36.

[2] E. Foote. "Circumstances affecting the heat of the sun's rays". In: *Am. J. Sci. Arts* 22 (1856), pp. 382–383.

[3] J. Tyndall. "The Bakerian Lecture - On the Absoprtion and Radiation of Heat by Gases and Vapours, and on the Physical Connexion of Radiation, Absorption, and Conduction". In: *Phil. Trans. R. Soc.* 151 (1861), pp. 1–36.

[4] J. D. Ortiz and R. Jackson. "Understanding Eunice Foote's 1856 experiments: heat absorption by atmospheric gases". In: *Notes Rec.* (2020), pp. 159–160.

[5] R. Revelle and H. E. Suess. "Carbon Dioxide Exchange Bewteen Atmosphere and Ocean and the Question of an Increase of Atmospheric CO_2 during the Past Decades". In: *Tellus* 9.1 (1957), pp. 18–27.

[6] C. D. Keeling. "The concentration and isotopic abundances of atmospheric carbon dioxide in rural areas". In: *Tellus* 12.2 (1960), pp. 200–203.

[7] M. Bell, D. L. Davis, and T. Fletcher. "A retrospective assessment of mortality from the London smog episode of 1952: The role of influenza and pollution". In: *J. Environ. Health. Perspect.* 112.1 (2004), pp. 6–8.

[8] A. J. Haagen-Smit. "Chemistry and Physiology of Los Angeles Smog". In: *J. Ind. Eng. Chem.* 44.6 (1952), pp. 1342–1346.

[9] P. Barlow. *Annex A Regulation 28: Report To Prevent Future Deaths (1)*. 2021, p. 3. URL: https://www.judiciary.uk/publications/ella-kissi-debrah/%0Ahttps://www.judiciary.uk/about-the-judiciary/the-justice-system/jurisdictions/civil-jurisdiction/%0Ahttps://www.judiciary.uk/wp-content/uploads/2021/04/Ella-Kissi-Debrah-2021-0113-1.pdf.

[10] E. Von Schneidemesser, P. S. Monks, J. D. Allan, L. Bruhwiler, P. Forster, D. Fowler, A. Lauer, W. T. Morgan, P. Paasonen, M. Righi, K. Sindelarova, and M. A. Sutton. "Chemistry and the Linkages between Air Quality and Climate Change". In: *Chem. Rev.* 115 (2015), pp. 3856–3897.

[11] DEFRA UK. *Air Quality and Climate Change : A UK Perspective*. 2007. URL: `https://uk-air.defra.gov.uk/assets/documents/reports/aqeg/fullreport.pdf`.

[12] P. Brimblecombe. "The Clean Air Act after 50 years". In: *Weather* 61.11 (2007), pp. 311–314.

[13] World Health Organization. *Burden of disease from ambient air pollution for 2016*. Tech. rep. 2018, pp. 1–4.

[14] J. Lelieveld, J. S. Evans, M. Fnais, D. Giannadaki, and A. Pozzer. "The contribution of outdoor air pollution sources to premature mortality on a global scale". In: *Nature* 525.7569 (2015), pp. 367–371.

[15] I. Manisalidis, E. Stavropoulou, A. Stavropoulos, and E. Bezirtzoglou. "Environmental and Health Impacts of Air Pollution: A Review". In: *Front. Public Health* 8:14 (2020), pp. 1–13.

[16] I. C. Eze, E. Schaffner, E. Fischer, T. Schikowski, M. Adam, M. Imboden, M. Tsai, D. Carballo, A. von Eckardstein, N. Künzli, C. Schindler, and N. Probst-Hensch. "Long-term air pollution exposure and diabetes in a population-based Swiss cohort". In: *Environ. Int.* 70 (2014), pp. 95–105.

[17] World Health Organisation. *Review of evidence on health aspects of air pollution – REVIHAAP Project: Technical Report*. Tech. rep. 2013, pp. 35–42.

[18] J. C. Chen and J. Schwartz. "Neurobehavioral effects of ambient air pollution on cognitive performance in US adults". In: *Neurotoxicology* 30 (2009), pp. 231–239.

[19] T. Sharkhuu, D. L. Doerfler, C. Copeland, R. W. Luebke, and M. I. Gilmour. "Effect of maternal exposure to ozone on reproductive outcome and immune, inflammatory, and allergic responses in the offspring". In: *J. Immunotoxicol.* 8.2 (2011), pp. 183–194.

[20] IPCC Core Writing Team, R. K. Pachauri, and L. A. Meyer. *Climate Change 2014 Synthesis Report*. Tech. rep. 2015, p. 151.

[21] E. A. Ainsworth. "Understanding and improving global crop response to ozone pollution". In: *Plant Journal* 90 (2017), pp. 886–897.

[22] G. Mills, K. Sharps, D. Simpson, H. Pleijel, M. Broberg, J. Uddling, F. Jaramillo, W. J. Davies, F. Dentener, M. Van den Berg, M. Agrawal, S. B. Agrawal, E. A. Ainsworth, P. Büker, L. Emberson, Z. Feng, H. Harmens, F. Hayes, K. Kobayashi, E. Paoletti, and R. Van Dingenen. "Ozone pollution will compromise efforts to increase global wheat production". In: *Glob. Change Biol.* 24.8 (2018), pp. 3560–3574.

[23] R. W. Atkinson, G. W. Fuller, H. R. Anderson, R. M. Harrison, and B. Armstrong. "Urban ambient particle metrics and health: A time-series analysis". In: *Epidemiology* 21.4 (2010), pp. 501–511.

[24] R. Chen, Y. Li, Y. Ma, G. Pan, G. Zeng, X. Xu, B. Chen, and H. Kan. "Coarse particles and mortality in three Chinese cities: The China Air Pollution and Health Effects Study (CAPES)". In: *Sci. Total Environ.* 409 (2011), pp. 4934–4938.

[25] S. Mallone, M. Stafoggia, A. Faustini, G. Paolo Gobbi, A. Marconi, and F. Forastiere. "Saharan dust and associations between particulate matter and daily mortality in Rome, Italy". In: *J. Environ. Health. Perspect.* 119.10 (2011), pp. 1409–1414.

[26] W. G. Kreyling, S. Hirn, and C. Schleh. "Nanoparticles in the lung". In: *Comprehensive Toxicology: Third Edition* 28.12 (2010), pp. 1275–1276.

[27] J. W. Cook, C. L. Hewett, and I. Hieger. "The Isolation of a Cancer-producing Hydrocarbon from Coal Tar. Parts I, II, and III". In: *J. Chem. Soc.* 106 (1933), pp. 395–405.

[28] D. H. Phillips. "Fifty years of benzo(a)pyrene". In: *Nature* 303 (1983), pp. 468–472.

[29] European Environment Agency. *Air quality in Europe - 2013 Report: EEA report No. 9/2013*. 9. 2013, p. 112. URL: `http://www.eea.europa.eu/publications/air-quality-in-europe-2013`.

[30] J. D. Lee, L. K. Whalley, D. E. Heard, D. Stone, R. E. Dunmore, J. F. Hamilton, D. E. Young, J. D. Allan, S. Laufs, and J. Kleffmann. "Detailed budget analysis of HONO in central London reveals a missing daytime source". In: *Atmos. Chem. Phys.* 16 (2016), pp. 2747–2764.

[31] X. Zhou, K. Civerolo, H. Dai, G. Huang, J. Schwab, and K. Demerjian. "Summertime nitrous acid chemistry in the atmospheric boundary layer at a rural site in New York State". In: *J. Geophys. Res.* 107.D21.4590 (2002), p. 11.

[32] J. Kleffmann, T. Gavriloaiei, A. Hofzumahaus, F. Holland, R. Koppmann, L. Rupp, E. Schlosser, M. Siese, and A. Wahner. "Daytime formation of nitrous acid: A major source of OH radicals in a forest". In: *Geophys. Res. Lett.* 32.L05818 (2005), p. 4.

[33] K. Acker, D. Möller, W. Wieprecht, F. X. Meixner, B. Bohn, S. Gilge, C. Plass-Dülmer, and H. Berresheim. "Strong daytime production of OH from HNO_2 at a rural mountain site". In: *Geophys. Res. Lett.* 33.L02809 (2006), p. 4.

[34] H. Su, Y. Cheng, R. Oswald, T. Behrendt, I. Trebs, F. X. Meixner, M. O. Andreae, P. Cheng, Y. Zhang, and U. Pöschl. "Soil nitrite as a source of atmospheric HONO and OH radicals". In: *Science* 333 (2011), pp. 1616–1618.

[35] R. Oswald, T. Behrendt, M. Ermel, D. Wu, H. Su, Y. Cheng, C. Breuninger, A. Moravek, E. Mougin, C. Delon, B. Loubet, A. Pommerening-Röser, M. Sörgel, U. Pöschl, T. Hoffmann, M. O. Andreae, F. X. Meixner, and I. Trebs. "HONO emissions from soil bacteria as a major source of atmospheric reactive nitrogen". In: *Science* 341 (2013), pp. 1233–1235.

[36] X. Zhou, H. Gao, Y. He, G. Huang, S. B. Bertman, K. Civerolo, and J. Schwab. "Nitric acid photolysis on surfaces in low-NOx environments: Significant atmospheric implications". In: *Geophys. Res. Lett.* 30.23.2217 (2003), p. 4.

[37] C. George, R. S. Strekowski, J. Kleffmann, K. Stemmler, and M. Ammann. "Photoenhanced uptake of gaseous NO_2 on solid organic compounds: A photochemical source of HONO?" In: *Faraday Discuss.* 130 (2005), pp. 195–210.

[38] R. Kurtenbach, K. H. Becker, J. A. Gomes, J. Kleffmann, J. C. Lörzer, M. Spittler, P. Wiesen, R. Ackermann, A. Geyer, and U. Platt. "Investigations of emissions and heterogeneous formation of HONO in a road traffic tunnel". In: *Atmos. Environ.* 35 (2001), pp. 3385–3394.

[39] S. Li, J. Matthews, and A. Sinha. "Atmospheric hydroxyl radical production from electronically excited NO_2 and H_2O". In: *Science* 319 (2008), pp. 1657–1660.

[40] R. Atkinson, D. L. Baulch, R. A. Cox, J. N. Crowley, R. F. Hampson, R. G. Hynes, M. E. Jenkin, M. J. Rossi, and J. Troe. "IUPAC Task Group on Atmospheric Chemical Kinetic Data Evaluation". In: *Atmos. Chem. Phys.* 4 (2004), pp. 1461–1738. URL: `http://iupac.pole-ether.fr`.

[41] M. J. Newland, M. E. Jenkin, and A. R. Rickard. "Elucidating the fate of the OH-adduct in toluene oxidation under tropospheric boundary layer conditions". In: *Proc. Natl. Acad. Sci. U.S.A* 114.38 (2017), E7856–E7857.

[42] J. C. Ditto, E. B. Barnes, P. Khare, M. Takeuchi, T. Joo, A. A. T. Bui, J. Lee-Taylor, G. Eris, Y. Chen, B. Aumont, J. L. Jimenez, N. L. Ng, R. J. Griffin, and D. R. Gentner. "An omnipresent diversity and variability in the chemical composition of atmospheric functionalized organic aerosol". In: *Commun. Chem.* 75.1 (2018).

[43] P. Leighton. *Photochemistry of Air Pollution*. Academic Press Inc., 1961.

[44] L. J. Carpenter, K. C. Clemitshaw, R. A. Burgess, S. A. Penkett, J. N. Cape, and G. G. McFadyen. "Investigation and evaluation of the NO_x/O_3 photochemical steady state". In: *Atmos. Environ.* 32.19 (1998), pp. 3353–3365.

[45] T. Wang, L. Xue, P. Brimblecombe, Y. F. Lam, L. Li, and L. Zhang. "Ozone pollution in China: A review of concentrations, meteorological influences, chemical precursors, and effects". In: *Sci. Total Environ.* 575 (2017), pp. 1582–1596.

[46] B. J. Finlayson-Pitts and J. N. Pitts. "Atmospheric chemistry of tropospheric ozone formation: Scientific and regulatory implications". In: *J. Air and Waste* 43 (1993), pp. 1091–1100.

[47] IQAir. "World Air Quality Report". In: *2020 World Air Quality Report* August (2020), pp. 1–41. URL: `https://www.iqair.com/world-most-polluted-cities/world-air-quality-report-2020-en.pdf`.

[48] Health Effects Institute and Institute for Health Metrics and Evaluation's Global Burden of Desease project. *State of Global Air*. 2020. URL: `https://www.stateofglobalair.org/resources`.

[49] A. Roychowdhury and A. Somvanshi. *Ground-level ozone in Delhi-NCR : Unmasking the hidden and growing health risk*. Tech. rep. Centre for Science and Environment Analysis, 2021, pp. 1–16.

[50] R. Dube. *Revised national air quality standards*. The Gazette of India, Controller of Publications, Delhi-110054, 2009, pp. 1–4.

[51] S. M. Saunders, M. E. Jenkin, R. G. Derwent, and M. J. Pilling. "Protocol for the development of the Master Chemical Mechanism, MCM v3 (Part A): Tropospheric degradation of non-aromatic volatile organic compounds". In: *Atmos. Chem. Phys.* 3 (2003), pp. 161–180.

[52] M. E. Jenkin, S. M. Saunders, and M. J. Pilling. "The tropospheric degradation of volatile organic compounds: A protocol for mechanism development". In: *Atmos. Environ.* 31.1 (1997), pp. 81–104.

[53] S. L. Jain, B. C. Arya, A. Kumar, S. D. Ghude, and P. S. Kulkarni. "Observational study of surface ozone at New Delhi, India". In: *Int. J. Remote Sens.* 26.16 (2005), pp. 3515–3524.

[54] G. J. Stewart, B. S. Nelson, W. S. Drysdale, W. J. F. Acton, A. R. Vaughan, J. R. Hopkins, R. E. Dunmore, C. N. Hewitt, E. Nemitz, N. Mullinger, B. Langford, Shivani, E. Reyes-Villegas, R. Gadi, A. R. Rickard, J. D. Lee, and J. F. Hamilton. "Sources of non-methane hydrocarbons in surface air in Delhi, India". In: *Faraday Discuss.* 226 (2021), pp. 409–431.

[55] J. R. Hopkins, A. C. Lewis, and K. A. Read. "A two-column method for long-term monitoring of non-methane hydrocarbons (NMHCs) and oxygenated volatile organic compounds (o-VOCs)". In: *J. Environ. Monit.* 5 (2003), pp. 8–13.

[56] R. E. Dunmore, J. R. Hopkins, R. T. Lidster, J. D. Lee, M. J. Evans, A. R. Rickard, A. C. Lewis, and J. F. Hamilton. "Diesel-related hydrocarbons can dominate gas phase reactive carbon in megacities". In: *Atmos. Chem. Phys.* 15 (2015), pp. 9983–9996.

[57] L. K. Whalley, D. Stone, B. Bandy, R. Dunmore, J. F. Hamilton, J. Hopkins, J. D. Lee, A. C. Lewis, and D. E. Heard. "Atmospheric OH reactivity in central London: Observations, model predictions and estimates of in situ ozone production". In: *Atmos. Chem. Phys.* 16 (2016), pp. 2109–2122.

[58] L. K. Whalley, D. Stone, R. Dunmore, J. Hamilton, J. R. Hopkins, J. D. Lee, A. C. Lewis, P. Williams, J. Kleffmann, S. Laufs, R. Woodward-Massey, and D. E. Heard. "Understanding in situ ozone production in the summertime through radical observations and modelling studies during the Clean air for London project (ClearfLo)". In: *Atmos. Chem. Phys.* 18 (2018), pp. 2547–2571.

[59] L. Whalley, E. Slater, R. Woodward-Massey, C. Ye, J. Lee, F. Squires, J. Hopkins, R. Dunmore, M. Shaw, J. Hamilton, A. Lewis, A. Mehra, S. Worrall, A. Bacak, T. Bannan, H. Coe, B. Ouyang, R. Jones, L. Crilley, L. Kramer, W. Bloss, T. Vu, S. Kotthaus, S. Grimmond, Y. Sun, W. Xu, S. Yue, L. Ren, W. J. F. Acton, C. N. Hewitt, X.

Wang, P. Fu, and D. Heard. "Evaluating the sensitivity of radical chemistry and ozone formation to ambient VOCs and NO_x in Beijing". In: *Atmos. Chem. Phys.* 21 (2021), pp. 2125–2147.

[60] S. Garraway. "Measurement and modelling of volatile organic compounds in a tropical rainforest environment". PhD thesis. 2018, p. 260.

[61] R. J. Grenfell, M. J. Milton, A. M. Harling, G. M. Vargha, C. Brookes, P. G. Quincey, and P. T. Woods. "Standard mixtures of ambient volatile organic compounds in synthetic and whole air with stable reference values". In: *J. Geophys. Res. Atmos.* 115.D14302 (2010), pp. 1–16.

[62] World Meteorological Organisation Global Atmosphere Watch. *GAW Report No . 171 A WMO / GAW Expert Workshop on Global Long-Term Measurements of Volatile Organic Compounds (VOCs)*. Tech. rep. WMO/TD No. 1373. 2006, pp. 1–31.

[63] ACTRIS. *ACTRIS measurement guidelines on VOCs*. Tech. rep. 2014. URL: `http://www.actris.net`.

[64] R. W. LaClair, P. A. Bueno, and J. V. Seeley. "A systematic analysis of a flow-switching modulator for comprehensive two-dimensional gas chromatography". In: *J. Sep. Sci.* 27 (2004), pp. 389–396.

[65] R. E. Dunmore. "Characterisation of urban and remote atmospheres using comprehensive two dimensional gas chromatography". PhD thesis. 2015, p. 277.

[66] R. T. Lidster, J. F. Hamilton, J. D. Lee, A. C. Lewis, J. R. Hopkins, S. Punjabi, A. R. Rickard, and J. C. Young. "The impact of monoaromatic hydrocarbons on OH reactivity in the coastal UK boundary layer and free troposphere". In: *Atmos. Chem. Phys.* 14 (2014), pp. 6677–6693.

[67] E. Nemitz, M. S. Alam, W. S. Drysdale, R. E. Dunmore, J. Hamilton, J. R. Hopkins, B. Langford, B. S. Nelson, G. J. Stewart, W. J. F. Acton, A. R. Vaughan, and L. K. Whalley. *(APHH India) Megacity Delhi atmospheric emission quantification, assessment and impacts (DelhiFlux)*. 2020. URL: `https://catalogue.ceda.ac.uk/uuid/ba27c1c6a03b450e9269f668566658ec`.

[68] F. A. Squires. "Gas Phase Air Pollution in Remote and Urban Atmospheres: From the Azores to Beijing". PhD thesis. 2020, p. 273.

[69] Z. Huang, Y. Zhang, Q. Yan, Z. Zhang, and X. Wang. "Real-time monitoring of respiratory adsorption factors of volatile organic compounds in ambient air by proton transfer reaction time-of-flight mass spectrometry." In: *J. Hazard. Mater.* 320 (2016), pp. 547–555.

[70] J. Kleffmann, J. Heland, R. Kurtenbach, J. Lorzer, and P. Wiesen. "A new instrument (LOPAP) for the detection of nitrous acid (HONO)". In: *Environ. Sci. Pollut. R.* 4 (2002), pp. 48–54.

[71] S. T. Andersen, L. J. Carpenter, B. S. Nelson, L. Neves, K. A. Read, C. Reed, M. Ward, M. J. Rowlinson, and J. D. Lee. "Long-Term NO_x measurements in the remote marine tropical troposphere". In: *Atmos. Meas. Tech.* 14 (2021), pp. 3071–3085.

[72] I. B. Pollack, B. M. Lerner, and T. B. Ryerson. "Evaluation of ultraviolet light-emitting diodes for detection of atmospheric NO_2 by photolysis - Chemiluminescence". In: *J. Atmos. Chem.* 65.2-3 (2010), pp. 111–125.

[73] C. Reed, M. J. Evans, P. Di Carlo, J. D. Lee, and L. J. Carpenter. "Interferences in photolytic NO_2 measurements: Explanation for an apparent missing oxidant?" In: *Atmos. Chem. Phys.* 16 (2016), pp. 4707–4724.

[74] F. Squires, E. Nemitz, B. Langford, O. Wild, W. Drysdale, W. J. F. Acton, P. Fu, C. S. B. Grimmond, J. Hamilton, C. N. Hewitt, M. Hollaway, S. Kotthaus, J. Lee, S. Metzger, N. Pingintha-Durden, M. Shaw, A. Vaughan, X. Wang, R. Wu, Q. Zhang, and Y. Zhang. "Measurements of traffic dominated pollutant emissions in a Chinese megacity". In: *Atmos. Chem. Phys.* 20 (2020), pp. 8737–8761.

[75] J. Heland, J. Kleffmann, R. Kurtenbach, and P. Wiesen. "A new instrument to measure gaseous nitrous acid (HONO) in the atmosphere". In: *J. Environ. Sci. Technol.* 35 (2001), pp. 3207–3212.

[76] J. Kleffmann and P. Wiesen. "Technical Note: Quantification of interferences of wet chemical HONO LOPAP measurements under simulated polar conditions". In: *Atmos. Chem. Phys.* 8 (2008), pp. 6813–6822.

[77] A. R. Koss, K. Sekimoto, J. B. Gilman, V. Selimovic, M. M. Coggon, K. J. Zarzana, B. Yuan, B. M. Lerner, S. S. Brown, J. L. Jimenez, J. Krechmer, J. M. Roberts, C. Warneke, R. J. Yokelson, and J. De Gouw. "Non-methane organic gas emissions from biomass burning: Identification, quantification, and emission factors from PTR-ToF during the FIREX 2016 laboratory experiment". In: *Atmos. Chem. Phys.* 18 (2018), pp. 3299–3319.

[78] L. R. Crilley, W. J. Acton, M. S. Alam, R. Sommariva, L. J. Kramer, W. S. Drysdale, J. D. Lee, E. Nemitz, B. Langford, C. N. Hewitt, and W. J. Bloss. "Measurements of nitrous acid in Delhi: insights into sources". In: *TBC* (2021).

[79] A. Jordan, S. Haidacher, G. Hanel, E. Hartungen, L. Märk, H. Seehauser, R. Schottkowsky, P. Sulzer, and T. D. Märk. "A high resolution and high sensitivity proton-transfer-reaction time-of-flight mass spectrometer (PTR-TOF-MS)". In: *Int. J. Mass Spectrom.* 286 (2009), pp. 122–128.

[80] D. C. Beddows, M. Dall'Osto, and R. M. Harrison. "An enhanced procedure for the merging of atmospheric particle size distribution data measured using electrical mobility and time-of-flight analysers". In: *Aerosol Sci. Tech.* 44 (2010), pp. 930–938.

[81] TSI Incorporated. *TSI Application note PR-001 - Aerosol statistics, lognormal distributions and dN/dlogDp.* Tech. rep. 2012, p. 6.

[82] C. W. Spicer, D. W. Joseph, and W. M. Ollison. "A Re-Examination of Ambient Air Ozone Monitor Interferences". In: *J. Air & Waste Manage. Assoc.* 60 (2010), pp. 1353–1364.

[83] J. Liu, Z. Liu, Z. Ma, S. Yang, D. Yao, S. Zhao, B. Hu, G. Tang, J. Sun, M. Cheng, Z. Xu, and Y. Wang. "Detailed budget analysis of HONO in Beijing, China: Implication on atmosphere oxidation capacity in polluted megacity". In: *Atmos. Environ.* 244 (2021).

[84] A. C. Lewis, N. Carslaw, P. J. Marriott, R. M. Kinghorn, P. Morrison, A. L. Lee, K. D. Bartie, and M. J. Pilling. "A larger pool of ozone-forming carbon compounds in urban atmospheres". In: *Nature* 405 (2000), pp. 778–781.

[85] J. F. Hamilton and A. C. Lewis. "Monoaromatic complexity in urban air and gasoline assessed using comprehensive GC and fast GC-TOF/MS". In: *Atmos. Environ.* 37 (2003), pp. 589–602.

[86] C. Geron, R. Rasmussen, R. R. Arnts, and A. Guenther. "A review and synthesis of monoterpene speciation from forests in the United States". In: *Atmos. Environ.* 34 (2000), pp. 1761–1781.

[87] World Health Organisation. *Exposure to Benzene: A Major Public Health Concern.* Tech. rep. 2010, p. 5.

[88] R. Goel and S. K. Guttikunda. "Evolution of on-road vehicle exhaust emissions in Delhi". In: *Atmos. Environ.* 105 (2015), pp. 78–90.

[89] R. Goel, D. Mohan, S. K. Guttikunda, and G. Tiwari. "Assessment of motor vehicle use characteristics in three Indian cities". In: *Transportation Research Part D* 44 (2015), pp. 254–265.

[90] N. Labhsetwar, P. Rao, S. Kumar, R. Vijay, and T. Banerji. *Short Term and Localised Air Pollution Control System for Crematoria, Dump site and others in Delhi.* 2019, pp. 1–153.

[91] N. Kumar, P. Vrat, and Sushil. "A simulation study of unit exchange spares management of diesel locomotives in the Indian Railways". In: *Int. J. Prod. Econ.* 33 (1993).

[92] A. J. Kean, R. F. Sawyer, and R. A. Harley. "A Fuel-Based Assessment of Off-Road Diesel Engine Emissions". In: *J. Air Waste Manage. Assoc.* 50 (2000).

[93] F. Klein, N. J. Farren, C. Bozzetti, K. R. Daellenbach, D. Kilic, N. K. Kumar, S. M. Pieber, J. G. Slowik, R. N. Tuthill, J. F. Hamilton, U. Baltensperger, A. S. Prévôt, and I. El Haddad. "Indoor terpene emissions from cooking with herbs and pepper and their secondary organic aerosol production potential". In: *Sci. Rep.* 6 (2016), pp. 1–7.

[94] J. Zhang, W. Chen, J. Li, S. Yu, and W. Zhao. "VOCs and Particulate Pollution due to Incense Burning in Temples, China". In: *Procedia Engineering* 121 (2015).

[95] P. S. Monks, A. R. Rickard, S. L. Hall, and N. A. Richards. "Attenuation of spectral actinic flux and photolysis frequencies at the surface through homogenous cloud fields". In: *J. Geophys. Res.* 109.D17206 (2004), pp. 1–12.

[96] W. Stockwell and J. Calvert. "The near ultraviolet absorption spectrum of gaseous HONO and N_2O_3". In: *J. Chem. Inf. Model.* 8 (1978), pp. 193–203.

[97] J. Stutz, E. S. Kim, U. Platt, P. Bruno, C. Perrino, and A. Febo. "UV-visible absorption cross sections of nitrous acid and agrees well with literature Quartz". In: *J. Geophys. Res.* 105.D11 (2000), pp. 14585–14592.

[98] U.S.Embassy and Consulates' Air Quality Monitor in India. *$PM_{2.5}$ Air Quality Index data*. 2018. URL: `https://in.usembassy.gov/embassy-consulates/new-delhi/air-quality-data/`.

[99] World Air Quality Index Project. *$PM_{2.5}$ Air Quality Index data*. 2018. URL: `https://waqi.info/`.

[100] W. Wang, X. Li, M. Shao, M. Hu, L. Zeng, Y. Wu, and T. Tan. "The impact of aerosols on photolysis frequencies and ozone production in Beijing during the 4-year period 2012-2015". In: *Atmos. Chem. Phys.* 19 (2019), pp. 9413–9429.

[101] S. He and G. R. Carmichael. "Sensitivity of photolysis rates and ozone production in the troposphere to aerosol properties". In: *J. Geophys. Res. Atmos.* 104.D21 (1999), pp. 26307–26324.

[102] S. Mani, S. Agrawal, A. Jain, and K. Ganesan. *State of Clean Cooking Energy Access in India: Insights from the India Residential Energy Survey (IRES) 2020*. 2021, p. 62.

[103] P. Gomes. *The recent movement towards a four-day working week*. 2022, p. 5. URL: `https://iceanet.org/wp-content/uploads/2022/01/Gones.pdf`.

[104] G. J. Dollard, C. J. Dore, and M. E. Jenkin. "Ambient concentrations of 1,3-butadiene in the UK." In: *Chemico-Biological Interactions* 135-136 (2001), pp. 177–206.

[105] M. Li, Q. Zhang, B. Zheng, D. Tong, Y. Lei, F. Liu, C. Hong, S. Kang, L. Yan, Y. Zhang, Y. Bo, H. Su, Y. Cheng, and K. He. "Persistent growth of anthropogenic non-methane volatile organic compound (NMVOC) emissions in China during 1990-2017: Drivers, speciation and ozone formation potential". In: *Atmos. Chem. Phys.* 19 (2019), pp. 8897–8913.

[106] X. Lu, J. Hong, L. Zhang, O. R. Cooper, M. G. Schultz, X. Xu, T. Wang, M. Gao, Y. Zhao, and Y. Zhang. "Severe Surface Ozone Pollution in China: A Global Perspective". In: *J. Environ. Sci. Technol. Lett.* 5 (2018), pp. 487–494.

[107] M. J. Newland, D. J. Bryant, R. E. Dunmore, T. J. Bannan, W. Joe, B. Langford, J. R. Hopkins, F. A. Squires, W. Dixon, W. S. Drysdale, P. D. Ivatt, M. J. Evans, P. M. Edwards, L. K. Whalley, D. E. Heard, E. J. Slater, R. Woodward-Massey, C. Ye, A. Mehra, S. D. Worrall, A. Bacak, H. Coe, C. J. Percival, C. Nicholas Hewitt, J. D. Lee, T. Cui, J. D. Surratt, X. Wang, A. C. Lewis, A. R. Rickard, and J. F. Hamilton. "Low-NO atmospheric oxidation pathways in a polluted megacity". In: *Atmos. Chem. Phys.* 21 (2021), pp. 1613–1625.

[108] R. Atkinson, D. L. Baulch, R. A. Cox, J. N. Crowley, R. F. Hampson, R. G. Hynes, M. E. Jenkin, M. J. Rossi, and J. Troe. "Evaluated kinetic and photochemical data for atmospheric chemistry: Volume I - gas phase reactions of O_x, HO_x, NO_x and SO_x species". In: *Atmos. Chem. Phys.* 4 (2004), pp. 1461–1738.

[109] D. M. Chate, S. D. Ghude, G. Beig, A. S. Mahajan, C. Jena, R. Srinivas, A. Dahiya, and N. Kumar. "Deviations from the O_3-NO-NO_2 photo-stationary state in Delhi, India". In: *Atmos. Environ.* 96 (2014), pp. 353–358.

[110] E. G. Nisbet, M. R. Manning, E. J. Dlugokencky, R. E. Fisher, E. Lowry, S. E. Michel, C. Lund Myhre, S. M. Platt, G. Allen, P. Bousquet, R. Brownlow, M. Cain, J. L. France, O. Hermansen, R. Hossaini, A. E. Jones, I. Levin, A. C. Manning, G. Mhyre, J. A. Pyle, B. H. Vaughn, N. J. Warwick, and J. W. C. White. "Very Strong Atmospheric Methane Growth in the 4 Years 2014-2017: Implications for the Paris Agreement". In: *Global Biogeochemical Cycles* 33 (2019), pp. 318–342.

[111] D. J. Jacob. "Heterogeneous chemistry and tropospheric ozone". In: *Atmos. Environ.* (2000).

[112] D. Johnson and G. Marston. "The gas-phase ozonolysis of unsaturated volatile organic compounds in the troposphere". In: *Chem. Soc. Rev.* 37 (2008), pp. 699–716.

[113] M. J. Newland, B. S. Nelson, A. Muñoz, M. Ródenas, T. Vera, J. Tárrega, and A. R. Rickard. "Trends in stabilisation of Criegee intermediates from alkene ozonolysis". In: *Phys. Chem. Chem. Phys.* 22 (2020), pp. 13698–13706.

[114] A. Novelli, L. Vereecken, J. Lelieveld, and H. Harder. "Direct observation of OH formation from stabilised Criegee intermediates". In: *Phys. Chem. Chem. Phys.* 16 (2014), pp. 19941–19951.

[115] D. Grosjean, E. Grosjean, and E. L. I. William. "Thermal decomposition of PAN, PPN and Vinyl–PAN". In: *J. Air Waste Manag. Assoc.* 44 (1994), pp. 391–396.

[116] K. M. Emmerson, N. Carslaw, L. J. Carpenter, D. E. Heard, J. D. Lee, and M. J. Pilling. "Urban atmospheric chemistry during the PUMA campaign 1: Comparison of modelled OH and HO_2 concentrations with measurements". In: *J. Atmos. Chem.* 52 (2005), pp. 143–164.

[117] K. M. Emmerson, N. Carslaw, D. C. Carslaw, J. D. Lee, G. McFiggans, W. Bloss, T. Gravestock, D. E. Heard, J. Hopkins, T. Ingham, M. J. Pilling, S. C. Smith, M. J. Jacob, and P. S. Monks. "Free radical modelling studies during the UK TORCH Campaign in summer 2003". In: *Atmos. Chem. Phys.* 7 (2007), pp. 167–181.

[118] L. T. Molina. "Introductory Lecture: Air Quality in Megacities". In: *Faraday Discuss.* 226 (2021), pp. 9–52.

[119] United Nations Department of Economic and Social Affairs. "The World's Cities in 2018: Data booklet". In: *Populatation Division* ST/ESA/ SE (2018), p. 34.

[120] United Nations Department of Economic and Social Affairs. *World Urbanization Prospects: The 2018 Revision*. Tech. rep. 2019.

[121] R. B. Skeie, G. Myhre, Ø. Hodnebrog, P. J. Cameron-Smith, M. Deushi, M. I. Hegglin, L. W. Horowitz, R. J. Kramer, M. Michou, M. J. Mills, D. J. Olivié, F. M. Connor, D. Paynter, B. H. Samset, A. Sellar, D. Shindell, T. Takemura, S. Tilmes, and T. Wu. "Historical total ozone radiative forcing derived from CMIP6 simulations". In: *NPJ Clim. Atmos. Sci.* 32 (2020).

[122] S. Avnery, D. L. Mauzerall, J. Liu, and L. W. Horowitz. "Global crop yield reductions due to surface ozone exposure: 2. Year 2030 potential crop production losses and economic damage under two scenarios of O_3 pollution". In: *Atmos. Environ.* 45 (2011), pp. 2297–2309. URL: http://dx.doi.org/10.1016/j.atmosenv.2011.01.002.

[123] M. Jerrett, R. T. Burnett, C. A. Pope, K. Ito, G. Thurston, D. Krewski, Y. Shi, E. Calle, and M. Thun. "Long-Term Ozone Exposure and Mortality". In: *N. Engl. J. Med.* 360 (2009), pp. 1085–1095. URL: https://doi.org/10.1056/NEJMoa0803894.

[124] G. D. Thurston, M. Lippmann, M. B. Scott, and J. M. Fine. "Summertime haze air pollution and children with asthma". In: *Am. J. Respir. Crit. Care Med.* 155 (1997), pp. 654–660.

[125] World Health Organization. *Air quality guidelines Global update 2005: Particulate matter, ozone, nitrogen dioxide and sulfur dioxide.* Tech. rep. 2005.

[126] E. S. Schelegle, C. A. Morales, W. F. Walby, S. Marion, and R. P. Allen. "6.6-Hour inhalation of ozone concentrations from 60 to 87 parts per billion in healthy humans". In: *Am. J. Respir. Crit. Care Med.* 180 (2009), pp. 265–272.

[127] Z. L. Fleming, R. M. Doherty, E. Von Schneidemesser, C. S. Malley, O. R. Cooper, J. P. Pinto, A. Colette, X. Xu, D. Simpson, M. G. Schultz, A. S. Lefohn, S. Hamad, R. Moolla, S. Solberg, and Z. Feng. "Tropospheric Ozone Assessment Report: Present-day ozone distribution and trends relevant to human health". In: *Elementa* 6.12 (2018), p. 43.

[128] Royal Society. *Ground-level ozone in the 21st century: future trends, impacts and policy implications.* October. 2008, p. 134. URL: http://www.royalsociety.org/Ground-level-ozone-in-the-21st-century-future-trends-impacts-and-policy-implications-/.

[129] X. Lu, L. Zhang, X. Wang, M. Gao, K. Li, Y. Zhang, X. Yue, and Y. Zhang. "Rapid Increases in Warm-Season Surface Ozone and Resulting Health Impact in China since 2013". In: *J. Environ. Sci. Technol. Lett.* 7 (2020), pp. 240–247.

[130] D. D. Parrish, J. F. Lamarque, V. Naik, L. Horowitz, D. T. Shindell, J. Staehelin, R. Derwent, O. R. Cooper, H. Tanimoto, A. Volz-Thomas, S. Gilge, H. E. Scheel, M. Steinbacher, and M. Fröhlich. "Long-term changes in lower tropospheric baseline ozone concentrations: Comparing chemistry-climate models and observations at northern midlatitudes". In: *J. Geophys. Res.* 119 (2014), pp. 5719–5736.

[131] D. Tarasick, I. E. Galbally, O. R. Cooper, M. G. Schultz, G. Ancellet, T. Leblanc, T. J. Wallington, J. Ziemke, X. Liu, M. Steinbacher, J. Staehelin, C. Vigouroux, J. W. Hannigan, O. García, G. Foret, P. Zanis, E. Weatherhead, I. Petropavlovskikh, H. Worden, M. Osman, J. Liu, K. L. Chang, A. Gaudel, M. Lin, M. Granados-Muñoz, A. M. Thompson, S. J. Oltmans, J. Cuesta, G. Dufour, V. Thouret, B. Hassler, T. Trickl, and J. L. Neu. "Tropospheric ozone assessment report: Tropospheric ozone from 1877 to 2016, observed levels, trends and uncertainties". In: *Elementa* 7 (2019).

[132] A. Gaudel et al. "Tropospheric Ozone Assessment Report: Present-day distribution and trends of tropospheric ozone relevant to climate and global atmospheric chemistry model evaluation". In: *Elementa* 6 (2018).

[133] O. R. Cooper, M. G. Schultz, S. Schröder, K. L. Chang, A. Gaudel, G. C. Benítez, E. Cuevas, M. Fröhlich, I. E. Galbally, S. Molloy, D. Kubistin, X. Lu, A. McClure-Begley, P. Nédélec, J. O'Brien, S. J. Oltmans, I. Petropavlovskikh, L. Ries, I. Senik, K. Sjöberg, S. Solberg, G. T. Spain, W. Spangl, M. Steinbacher, D. Tarasick, V. Thouret, and X. Xu. "Multi-decadal surface ozone trends at globally distributed remote locations". In: *Elementa* 8.23 (2020).

[134] A. Gaudel, O. R. Cooper, K. L. Chang, I. Bourgeois, J. R. Ziemke, S. A. Strode, L. D. Oman, P. Sellitto, P. Nédélec, R. Blot, V. Thouret, and C. Granier. "Aircraft observations since the 1990s reveal increases of tropospheric ozone at multiple locations across the Northern Hemisphere". In: *Sci. Adv.* 6.eaba8272 (2020), pp. 1–12.

[135] Z. Liao, Z. Ling, M. Gao, J. Sun, W. Zhao, P. Ma, J. Quan, and S. Fan. "Tropospheric Ozone Variability Over Hong Kong Based on Recent 20 years (2000–2019) Ozonesonde Observation". In: *J. Geophys. Res. Atmos.* 126.e2020JD033054 (2021), pp. 1–22.

[136] J. R. Ziemke, L. D. Oman, S. A. Strode, A. R. Douglass, M. A. Olsen, R. D. McPeters, P. K. Bhartia, L. Froidevaux, G. J. Labow, J. C. Witte, A. M. Thompson, D. P. Haffner, N. A. Kramarova, S. M. Frith, L. K. Huang, G. R. Jaross, C. J. Seftor, M. T. Deland, and S. L. Taylor. "Trends in global tropospheric ozone inferred from a composite record of TOMS/OMI/MLS/OMPS satellite measurements and the MERRA-2 GMI simulation". In: *Atmos. Chem. Phys.* 19 (2019), pp. 3257–3269.

[137] J. Calvert, J. Orlando, W. Stockwell, and T. Wallington. *The Mechanisms of Reactions Influencing Atmospheric Ozone*. Oxford University Press, New York, 2015.

[138] K. Li, D. J. Jacob, H. Liao, Y. Qiu, L. Shen, S. Zhai, K. H. Bates, M. P. Sulprizio, S. Song, X. Lu, Q. Zhang, B. Zheng, Y. Zhang, J. Zhang, H. C. Lee, and S. K. Kuk. "Ozone pollution in the North China Plain spreading into the late-winter haze season." In: *Proc. Natl. Acad. Sci. U.S.A* 118.10 (2021), pp. 1–7.

[139] S. Sillman. "The relation between ozone, NO_x and hydrocarbons in urban and polluted rural environments". In: *Atmos. Environ.* 33 (1999), pp. 1821–1845.

[140] S. Sillman, A. Logan, and C. Wofsy. "The Sensitivity of Ozone to Nitrogen Oxides and Hydrocarbons in Regional Ozone Episodes". In: *J. Geophys. Res.* 95 (1990), pp. 1837–1851.

[141] M. E. Jenkin, R. G. Derwent, and T. J. Wallington. "Photochemical ozone creation potentials for volatile organic compounds: Rationalization and estimation". In: *Atmos. Environ.* 163 (2017), pp. 128–137. URL: http://dx.doi.org/10.1016/j.atmosenv.2017.05.024.

[142] F. Geng, X. Tie, J. Xu, G. Zhou, L. Peng, W. Gao, X. Tang, and C. Zhao. "Characterizations of ozone, NO_x, and VOCs measured in Shanghai, China". In: *Atmos. Environ.* 42 (2008), pp. 6873–6883.

[143] L. Ran, C. S. Zhao, W. Y. Xu, X. Q. Lu, M. Han, W. L. Lin, P. Yan, X. B. Xu, Z. Z. Deng, N. Ma, P. F. Liu, J. Yu, W. D. Liang, and L. L. Chen. "VOC reactivity and its effect on ozone production during the HaChi summer campaign". In: *Atmos. Chem. Phys.* 11 (2011), pp. 4657–4667.

[144] S. Kim, D. Sanchez, M. Wang, R. Seco, D. Jeong, S. Hughes, B. Barletta, D. R. Blake, J. Jung, D. Kim, G. Lee, M. Lee, J. Ahn, S. D. Lee, G. Cho, M. Y. Sung, Y. H. Lee, D. B. Kim, Y. Kim, J. H. Woo, D. Jo, R. Park, J. H. Park, Y. D. Hong, and J. H. Hong. "OH reactivity in urban and suburban regions in Seoul, South Korea-an East Asian megacity in a rapid transition". In: *Faraday Discuss.* 189 (2016), pp. 231–251.

[145] S. Lou, F. Holland, F. Rohrer, K. Lu, B. Bohn, T. Brauers, C. C. Chang, H. Fuchs, R. Häseler, K. Kita, Y. Kondo, X. Li, M. Shao, L. Zeng, A. Wahner, Y. Zhang, W. Wang, and A. Hofzumahaus. "Atmospheric OH reactivities in the Pearl River Delta - China in summer 2006: Measurement and model results". In: *Atmos. Chem. Phys.* 10 (2010), pp. 11243–11260.

[146] I. J. Simpson, D. R. Blake, N. J. Blake, S. Meinardi, B. Barletta, S. C. Hughes, L. T. Fleming, J. H. Crawford, G. S. Diskin, L. K. Emmons, A. Fried, H. Guo, D. A. Peterson, A. Wisthaler, J.-H. Woo, J. Barré, B. Gaubert, J. Kim, M. J. Kim, Y. Kim, C. Knote, T. Mikoviny, S. E. Pusede, J. R. Schroeder, Y. Wang, P. O. Wennberg, and L. Zeng. "Characterization, sources and reactivity of volatile organic compounds (VOCs) in Seoul and surrounding regions during KORUS-AQ". In: *Elementa: Sci. Anth.* 8 (2020).

[147] M. Zavala, W. H. Brune, E. Velasco, A. Retama, L. A. Cruz-Alavez, and L. T. Molina. "Changes in ozone production and VOC reactivity in the atmosphere of the Mexico City Metropolitan Area". In: *Atmos. Environ.* 238 (2020), p. 117747.

[148] B. C. McDonald, J. A. De Gouw, J. B. Gilman, S. H. Jathar, A. Akherati, C. D. Cappa, J. L. Jimenez, J. Lee-Taylor, P. L. Hayes, S. A. McKeen, Y. Y. Cui, S. W. Kim, D. R. Gentner, G. Isaacman-VanWertz, A. H. Goldstein, R. A. Harley, G. J. Frost, J. M. Roberts, T. B. Ryerson, and M. Trainer. "Volatile chemical products emerging as largest petrochemical source of urban organic emissions". In: *Science* 359 (2018), pp. 760–764.

[149] A. K. Georgoulias, R. A. Van Der, P. Stammes, K. Folkert Boersma, and H. J. Eskes. "Trends and trend reversal detection in 2 decades of tropospheric NO_2 satellite observations". In: *Atmos. Chem. Phys.* 19 (2019), pp. 6269–6294.

[150] A. Font, L. Guiseppin, M. Blangiardo, V. Ghersi, and G. W. Ghersi Fuller. "A tale of two cities : is air pollution improving in Paris and London?" In: *Environ. Pollut.* 249 (2019), pp. 1–12.

[151] Q. Zhang, Y. Zheng, D. Tong, M. Shao, S. Wang, Y. Zhang, X. Xu, J. Wang, H. He, W. Liu, Y. Ding, Y. Lei, J. Li, Z. Wang, X. Zhang, Y. Wang, J. Cheng, Y. Liu, Q. Shi, L. Yan, G. Geng, C. Hong, M. Li, F. Liu, B. Zheng, J. Cao, A. Ding, J. Gao, Q. Fu, J. Huo, B. Liu, Z. Liu, F. Yang, K. He, and J. Hao. "Drivers of improved $PM_{2.5}$ air quality in China from 2013 to 2017". In: *Proc. Natl. Acad. Sci. U.S.A* 116.49 (2019), pp. 24463–24469.

[152] N. A. Krotkov, C. A. McLinden, C. Li, L. N. Lamsal, E. A. Celarier, S. V. Marchenko, W. H. Swartz, E. J. Bucsela, J. Joiner, B. N. Duncan, K. Folkert Boersma, J. Pepijn Veefkind, P. F. Levelt, V. E. Fioletov, R. R. Dickerson, H. He, Z. Lu, and D. G. Streets. "Aura OMI observations of regional SO_2 and NO_2 pollution changes from 2005 to 2015". In: *Atmos. Chem. Phys.* 16 (2016), pp. 4605–4629.

[153] F. Liu, Q. Zhang, R. J. Van Der A, B. Zheng, D. Tong, L. Yan, Y. Zheng, and K. He. "Recent reduction in NO_x emissions over China: Synthesis of satellite observations and emission inventories". In: *Environ. Res. Lett.* 11.114002 (2016), p. 9.

[154] K. Miyazaki, H. Eskes, K. Sudo, K. Folkert Boersma, K. Bowman, and Y. Kanaya. "Decadal changes in global surface NO_x emissions from multi-constituent satellite data assimilation". In: *Atmos. Chem. Phys.* 17 (2017), pp. 807–837.

[155] World Health Organization. *Global Urban Ambient Air Pollution Database*. 2014. URL: `http://www.who.int/phe/health_topics/outdoorair/databases/cities/en/`.

[156] G. Bansal and A. Bandivadekar. *Overview of India's Vehicle Emissions Control Program Past Successes and Future Prospects*. 2013, pp. 1–180.

[157] P. Kumar, S. Gulia, R. M. Harrison, and M. Khare. "The influence of odd–even car trial on fine and coarse particles in Delhi". In: *Environ. Pollut.* 225 (2017), pp. 20–30.

[158] S. Jain and T. Sharma. "Social and travel lockdown impact considering coronavirus disease (Covid-19) on air quality in megacities of india: Present benefits, future challenges and way forward". In: *Aerosol Air Qual. Res.* 20 (2020), pp. 1222–1236.

[159] S. Mahato, S. Pal, and K. G. Ghosh. "Effect of lockdown amid COVID-19 pandemic on air quality of the megacity Delhi, India". In: *Sci. Total Environ.* 730 (2020), p. 139086. URL: `https://doi.org/10.1016/j.scitotenv.2020.139086`.

[160] S. Sharma, M. Zhang, Anshika, J. Gao, H. Zhang, and S. H. Kota. "Effect of restricted emissions during COVID-19 on air quality in India". In: *Sci. Total Environ.* 728 (2020), p. 138878.

[161] Z. Shi, C. Song, B. Liu, G. Lu, J. Xu, T. Van Vu, R. J. Elliott, W. Li, W. J. Bloss, and R. M. Harrison. "Abrupt but smaller than expected changes in surface air quality attributable to COVID-19 lockdowns". In: *Sci. Adv.* 7.3 (2021).

[162] A. Sharma, S. K. Sharma, Rohtash, and T. K. Mandal. "Influence of ozone precursors and particulate matter on the variation of surface ozone at an urban site of Delhi, India". In: *Sustain. Environ. Res.* 26 (2016), pp. 76–83.

[163] N. Jain, A. Bhatia, and H. Pathak. "Emission of air pollutants from crop residue burning in India". In: *Aerosol Air Qual. Res.* 14 (2014), pp. 422–430.

[164] R. Sawlani, R. Agnihotri, C. Sharma, P. K. Patra, A. P. Dimri, K. Ram, and R. L. Verma. "The severe Delhi SMOG of 2016: A case of delayed crop residue burning, coincident firecracker emissions, and atypical meteorology". In: *Atmos. Pollut. Res.* 10 (2019), pp. 868–879.

[165] L. Wang, J. G. Slowik, N. Tripathi, D. Bhattu, P. Rai, V. Kumar, P. Vats, R. Satish, U. Baltensperger, D. Ganguly, N. Rastogi, L. K. Sahu, S. N. Tripathi, and A. S. Prévôt. "Source characterization of volatile organic compounds measured by proton-transfer-reaction time-of-flight mass spectrometers in Delhi, India". In: *Atmos. Chem. Phys.* 20 (2020), pp. 9753–9770.

[166] S. K. Guttikunda and G. Calori. "A GIS based emissions inventory at 1 km × 1 km spatial resolution for air pollution analysis in Delhi, India". In: *Atmos. Environ.* 67 (2013), pp. 101–111.

[167] J. M. Cash, E. Nemitz, C. Di Marco, N. J. Mullinger, M. R. Heal, W. J. F. Acton, C. N. Hewitt, P. K. Misztal, T. K. Mandal, Shivani, R. Gadi, B. R. Gurjar, and B. Langford. "Source apportionment of VOC fluxes in Old Delhi using high resolution proton transfer reaction mass spectrometry". In: *in preparation* (2021).

[168] G. J. Stewart, B. S. Nelson, W. J. F. Acton, A. R. Vaughan, N. J. Farren, J. R. Hopkins, M. W. Ward, S. J. Swift, R. Arya, A. Mondal, R. Jangirh, S. Ahlawat, L. Yadav, S. K. Sharma, S. S. M. Yunus, C. N. Hewitt, E. Nemitz, N. Mullinger, R. Gadi, L. K. Sahu, N. Tripathi, A. R. Rickard, J. D. Lee, T. K. Mandal, and J. F. Hamilton. "Emissions of intermediate-volatility and semi-volatile organic compounds from domestic fuels used in Delhi , India". In: *Atmos. Chem. Phys.* 21 (2021), pp. 2407–2426.

[169] G. J. Stewart, W. J. F. Acton, B. S. Nelson, A. R. Vaughan, J. R. Hopkins, R. Arya, A. Mondal, R. Jangirh, S. Ahlawat, L. Yadav, S. K. Sharma, R. E. Dunmore, S. S. M. Yunus, C. N. Hewitt, E. Nemitz, N. Mullinger, R. Gadi, L. K. Sahu, N. Tripathi, A. R. Rickard, J. D. Lee, T. K. Mandal, and J. F. Hamilton. "Emissions of non-methane volatile organic compounds from combustion of domestic fuels in Delhi , India". In: *Atmos. Chem. Phys* 21 (2021), pp. 2383–2406.

[170] G. J. Stewart, B. S. Nelson, W. J. F. Acton, A. R. Vaughan, J. R. Hopkins, S. S. M. Yunus, C. N. Hewitt, E. G. Nemitz, N. Mullinger, R. Gadi, A. R. Rickard, J. D. Lee, T. K. Mandal, and J. F. Hamilton. "Emission estimates and inventories of non-methane organic compounds from anthropogenic burning sources in India". In: *Atmos. Environ.: X* 11.100115 (2021).

[171] G. J. Stewart, B. S. Nelson, W. J. F. Acton, A. R. Vaughan, J. R. Hopkins, S. S. M. Yunus, C. N. Hewitt, E. Nemitz, T. K. Mandal, R. Gadi, L. K. Sahu, A. R. Rickard, J. D. Lee, and J. F. Hamilton. "Comprehensive organic emission profiles, secondary organic aerosol production potential, and OH reactivity of domestic fuel combustion in Delhi, India". In: *Environ. Sci.: Atmos.* 1 (2021), pp. 104–117.

[172] R. Atkinson, D. L. Baulch, R. A. Cox, J. N. Crowley, R. F. Hampson, R. G. Hynes, M. E. Jenkin, M. J. Rossi, J. Troe, and IUPAC Subcommittee. "Evaluated kinetic and photochemical data for atmospheric chemistry: Volume II - gas phase reactions of organic species". In: *Atmos. Chem. Phys.* 6 (2006), pp. 3625–4055.

[173] R. Atkinson and J. Arey. "Atmospheric Degradation of Volatile Organic Compounds Atmospheric Degradation of Volatile Organic Compounds". In: *Chem. Rev.* 103 (2003), pp. 4605–4638.

[174] M. E. Jenkin, J. C. Young, and A. R. Rickard. "The MCM v3.3.1 degradation scheme for isoprene". In: *Atmos. Chem. Phys.* 15 (2015), pp. 11433–11459.

[175] R. Sommariva, S. Cox, C. Martin, K. Borońska, J. Young, P. K. Jimack, M. J. Pilling, V. N. Matthaios, B. S. Nelson, M. J. Newland, M. Panagi, W. J. Bloss, P. S. Monks, and A. R. Rickard. "AtChem (version 1), an open-source box model for the Master Chemical Mechanism". In: *Geosci. Model Dev.* 13 (2020), pp. 169–183.

[176] F. Meng, M. Qin, K. Tang, J. Duan, W. Fang, S. Liang, K. Ye, P. Xie, Y. Sun, C. Xie, C. Ye, P. Fu, J. Liu, and W. Liu. "High-resolution vertical distribution and sources of HONO and NO_2 in the nocturnal boundary layer in urban Beijing, China". In: *Atmos. Chem. Phys.* 20 (8 2019), pp. 5071–5092.

[177] Y. F. Elshorbany, J. Kleffmann, R. Kurtenbach, M. Rubio, E. Lissi, G. Villena, E. Gramsch, A. R. Rickard, M. J. Pilling, and P. Wiesen. "Summertime photochemical ozone formation in Santiago, Chile". In: *Atmos. Environ.* 43 (2009), pp. 6398–6407.

[178] I. B. Pollack, T. B. Ryerson, M. Trainer, J. A. Neuman, J. M. Roberts, and D. D. Parrish. "Trends in ozone, its precursors, and related secondary oxidation products in Los Angeles, California: A synthesis of measurements from 1960 to 2010". In: *J. Geophys. Res. Atmos.* 118 (2013), pp. 5893–5911.

[179] Z. Tan, K. Lu, M. Jiang, R. Su, H. Wang, S. Lou, Q. Fu, C. Zhai, Q. Tan, D. Yue, D. Chen, Z. Wang, S. Xie, L. Zeng, and Y. Zhang. "Daytime atmospheric oxidation capacity in four Chinese megacities during the photochemically polluted season: a case study based on box model simulation". In: *Atmos. Chem. Phys.* 19 (2019), pp. 3493–3513.

[180] Shivani, R. Gadi, S. K. Sharma, T. K. Mandal, R. Kumar, S. Mona, S. Kumar, and S. Kumar. "Levels and sources of organic compounds in fine ambient aerosols over National Capital Region of India". In: *Environ. Sci. Pollut. Res.* 25 (2018), pp. 31071–31090.

[181] G. I. Gkatzelis, M. M. Coggon, B. C. Mcdonald, J. Peischl, J. B. Gilman, K. C. Aikin, M. A. Robinson, F. Canonaco, A. S. H. Prevot, and M. Trainer. "Observations Confirm that Volatile Chemical Products Are a Major Source of Petrochemical Emissions in U.S. Cities". In: *Environ. Sci. Technol.* 55.8 (2021), pp. 4332–4343.

[182] X. Ren, W. H. Brune, J. Mao, M. J. Mitchell, R. L. Lesher, J. B. Simpas, A. R. Metcalf, J. J. Schwab, C. Cai, Y. Li, K. L. Demerjian, H. D. Felton, G. Boynton, A. Adams, J. Perry, Y. He, X. Zhou, and J. Hou. "Behavior of OH and HO_2 in the winter atmosphere in New York City". In: *Atmos. Environ.* 40 (2006), pp. 252–263.

[183] T. R. Shirley, W. H. Brune, X. Ren, J. Mao, R. Lesher, B. Cardenas, R. Volkamer, L. T. Molina, M. J. Molina, B. Lamb, E. Velasco, T. Jobson, and M. Alexander. "Atmospheric oxidation in the Mexico City Metropolitan Area (MCMA) during April 2003". In: *Atmos. Chem. Phys.* 6 (2006), pp. 6041–6076.

[184] A. Yoshino, Y. Sadanaga, K. Watanabe, S. Kato, Y. Miyakawa, J. Matsumoto, and Y. Kajii. "Measurement of total OH reactivity by laser-induced pump and probe technique-comprehensive observations in the urban atmosphere of Tokyo". In: *Atmos. Environ.* 40 (2006), pp. 7869–7881.

[185] T. Castro, S. Madronich, S. Rivale, A. Muhlia, and B. Mar. "The influence of aerosols on photochemical smog in Mexico City". In: *Atmos. Environ.* 35 (2001), pp. 1765–1772.

[186] M. Hollaway, O. Wild, T. Yang, Y. Sun, W. Xu, C. Xie, L. Whalley, E. Slater, D. Heard, and D. Liu. "Photochemical impacts of haze pollution in an urban environment". In: *Atmos. Chem. Phys.* 19 (2019), pp. 9699–9714.

[187] E. Real and K. Sartelet. "Modeling of photolysis rates over Europe: Impact on chemical gaseous species and aerosols". In: *Atmos. Chem. Phys.* 11 (2011), pp. 1711–1727.

[188] R. R. Dickerson, S. Kondragunta, G. Stenchikov, K. L. Civerolo, B. G. Doddridge, and B. N. Holben. "The impact of aerosols on solar ultraviolet radiation and photochemical smog". In: *Science* 278 (1997), pp. 827–830.

[189] C. George, M. Ammann, B. D'Anna, D. J. Donaldson, and S. A. Nizkorodov. "Heterogeneous Photochemistry in the Atmosphere". In: *Chem. Rev.* 115 (2015), pp. 4218–4258.

[190] K. Li, D. J. Jacob, H. Liao, L. Shen, Q. Zhang, and K. H. Bates. "Anthropogenic drivers of 2013–2017 trends in summer surface ozone in China". In: *Proc. Natl. Acad. Sci. U.S.A* 116.2 (2019), pp. 422–427.

[191] Z. Tan, A. Hofzumahaus, K. Lu, S. S. Brown, F. Holland, L. G. Huey, A. Kiendler-Scharr, X. Li, X. Liu, N. Ma, K. E. Min, F. Rohrer, M. Shao, A. Wahner, Y. Wang, A. Wiedensohler, Y. Wu, Z. Wu, L. Zeng, Y. Zhang, and H. Fuchs. "No Evidence for a Significant Impact of Heterogeneous Chemistry on Radical Concentrations in the North China Plain in Summer 2014". In: *J. Environ. Sci. Technol.* 54 (2020), pp. 5973–5979.

[192] Y. Chen, G. Beig, S. Archer-Nicholls, W. Drysdale, J. Acton, D. Lowe, B. S. Nelson, J. D. Lee, L. Ran, Y. Wang, Z. Wu, S. K. Sahu, R. S. Sokhi, V. Singh, R. Gadi, C. N. Hewitt, E. Nemitz, A. Archibald, G. McFiggins, and O. Wild. "Avoiding high ozone pollution in Delhi, India". In: *Faraday Discuss.* 226 (2021), pp. 502–514.

[193] Z. Liu, Y. Wang, F. Costabile, A. Amoroso, C. Zhao, G. L. Huey, R. Stickel, J. Liao, and T. Zhu. "Evidence of Aerosols as a Media for Rapid Daytime HONO Production over China". In: *Environ. Sci. Technol.* 48 (2014), pp. 14386–14391.

[194] S. Tong, S. Hou, Y. Zhang, B. Chu, Y. Liu, H. He, P. Zhao, and M. Ge. "Exploring the nitrous acid (HONO) formation mechanism in winter Beijing: Direct emissions and heterogeneous production in urban and suburban areas". In: *Faraday Discuss.* 189 (2016), pp. 213–230.

[195] X. Lu, Y. Wang, J. Li, L. Shen, and J. C. H. Fung. "Evidence of heterogeneous HONO formation from aerosols and the regional photochemical impact of this HONO source". In: *Environ. Res. Lett.* 13 (2018).

[196] D. R. Hanson, J. B. Burkholder, C. J. Howard, and A. R. Ravishankara. "Measurement of OH and HO_2 radical uptake coefficients on water and sulfuric acid surfaces". In: *J. Phys. Chem.* 96 (1992), pp. 4979–4985.

[197] Y. M. Gershenzon, V. M. Grigorieva, A. V. Ivanov, and R. G. Remorov. "O_3 and OH Sensitivity to heterogeneous sinks of HO_x and CH_3O_2 on aerosol particles". In: *Faraday Discuss.* 100 (1995), pp. 83–100.

[198] P. L. Cooper and J. P. Abbatt. "Heterogeneous Interactions of OH and HO_2 Radicals with Surfaces Characteristic of Atmospheric Participate Matter". In: *J. Phys. Chem.* 100 (1996), pp. 2249–2254.

[199] D. A. Plummer, J. C. McConnell, P. B. Shepson, D. R. Hastie, and H. Niki. "Modeling of ozone formation at a rural site in Southern Ontario". In: *Atmos. Environ.* 30.12 (1996), pp. 2195–2217.

[200] L. Jaegle, D. J. Jacob, W. H. Brune, I. Faloona, D. T. B. G. Heikes, G. W. Sachse, G. L. Gregory, G. Ferry, D. R. Blake, and R. E. Shetter. "Photochemistry of HO_x in the upper troposphere at northern midlatitudes". In: *J. Geophys. Res.* 105.D3 (2000), pp. 3877–3892.

[201] R. Jat and B. R. Gurjar. "Contribution of different source sectors and source regions of Indo-Gangetic Plain in India to $PM_{2.5}$ pollution and its short-term health impacts during peak polluted winter". In: *Atmos. Pollut. Res.* 12 (2021), pp. 89–100.

[202] S. H. Kulkarni, S. D. Ghude, C. Jena, R. K. Karumuri, B. Sinha, V. Sinha, R. Kumar, V. K. Soni, and M. Khare. "How Much Does Large-Scale Crop Residue Burning Affect the Air Quality in Delhi?" In: *Environ. Sci. Technol.* 54 (2020), pp. 4790–4799.

[203] R. Criegee. "Mechanism of Ozonolysis". In: *Angewandte Chemie International Edition in English* 14.11 (1975), pp. 745–752.

[204] D. Cremer. "Theoretical Determination of Molecular Structure and Conformation. 6. The Criegee Intermediate. Evidence for a Stabilization of Its Syn Form by Alkyl Substituents". In: *J. Am. Chem. Soc.* 101.24 (1979), pp. 7199–7205.

[205] D. Cremer, J. Gauss, E. Kraka, J. F. Stanton, and R. J. Bartlett. "A CCSD (T) investigation of carbonyl oxide and dioxirane. Equilibrium geometries, dipole moments, infrared spectra, heats of formation and isomerization energies". In: *Chem. Phys. Letts* 209.5-6 (1993), pp. 547–556.

[206] J. H. Kroll, N. M. Donahue, V. J. Cee, K. L. Demerjian, and J. G. Anderson. "Gas-phase ozonolysis of alkenes: Formation of OH from anti carbonyl oxides". In: *J. Am. Chem. Soc.* 124.29 (2002), pp. 8518–8519.

[207] H. Niki, P. D. Maker, C. M. Savage, L. P. Breitenbach, and M. D. Hurley. "FTIR spectroscopic study of the mechanism for the gas-phase reaction between ozone and tetramethylethylene". In: *J. Phys. Chem.* 91 (1987), pp. 941–946.

[208] M. Olzmann, E. Kraka, D. Cremer, R. Gutbrod, and S. Andersson. "Energetics, kinetics, and product distributions of the reactions of ozone with ethene and 2,3-dimethyl-2-butene". In: *J. Phys. Chem. A* 101 (1997), pp. 9421–9429.

[209] K. T. Kuwata, L. K. Valin, and A. D. Converse. "Quantum chemical and master equation simulations of isoprene ozonolysis". In: *J. Phys. Chem. A* 109 (2005), pp. 2514–2524.

[210] A. B. Ryzhkov and P. A. Ariya. "A theoretical study of the reactions of parent and substituted Criegee intermediates with water and the water dimer". In: *Phys. Chem. Chem. Phys.* 6 (2004), pp. 5042–5050.

[211] J. Jr-Min Lin and W. Chao. "Structure-dependent reactivity of Criegee intermediates studied with spectroscopic methods". In: *Chem. Soc. Rev.* 46 (2017), pp. 7483–7497.

[212] M. A. Khan, C. J. Percival, R. L. Caravan, C. A. Taatjes, and D. E. Shallcross. "Criegee intermediates and their impacts on the troposphere". In: *Environ. Sci.: Process. Impacts* 20 (2018), pp. 437–453.

[213] O. Weltz, J. D. Savee, D. L. Osborn, S. S. Vasu, C. J. Percival, D. E. Shallcross, and C. A. Taatjes. "Direct Kinetic Measurements of Criegee Intermediate (CH_2OO) Formed by Reaction of CH_2I with O_2". In: *Science* 335 (2012), pp. 204–207.

[214] C. A. Taatjes, O. Welz, A. J. Eskola, J. D. Savee, A. M. Scheer, D. E. Shallcross, B. Rotavera, E. P. F. Lee, J. M. Dyke, D. K. W. Mok, D. L. Osborn, and C. J. Percival. "Direct Measurements of Conformer-Dependant Reactivity of the Criegee Intermediate CH_3CHOO". In: *Science* 340 (2013), pp. 177–181.

[215] R. Chhantyal-Pun, O. Welz, J. D. Savee, A. J. Eskola, E. P. Lee, L. Blacker, H. R. Hill, M. Ashcroft, M. A. H. Khan, G. C. Lloyd-Jones, L. Evans, B. Rotavera, H. Huang, D. L. Osborn, D. K. Mok, J. M. Dyke, D. E. Shallcross, C. J. Percival, A. J. Orr-Ewing, and C. A. Taatjes. "Direct Measurements of Unimolecular and Bimolecular Reaction Kinetics of the Criegee Intermediate $(CH_3)_2COO$". In: *J. Phys. Chem. A* 121 (2017), pp. 4–15.

[216] M. J. Newland, A. R. Rickard, L. Vereecken, A. Muñoz, M. Ródenas, and W. J. Bloss. "Atmospheric isoprene ozonolysis: Impacts of stabilised Criegee intermediate reactions with SO_2, H_2O and dimethyl sulfide". In: *Atmos. Chem. Phys.* 15 (2015), pp. 9521–9536.

[217] C. A. Taatjes, O. Welz, A. J. Eskola, J. D. Savee, D. L. Osborn, E. P. Lee, J. M. Dyke, D. W. Mok, D. E. Shallcross, and C. J. Percival. "Direct measurement of Criegee intermediate (CH_2OO) reactions with acetone, acetaldehyde, and hexafluoroacetone". In: *Phys. Chem. Chem. Phys.* 14 (2012), pp. 10391–10400.

[218] L. Vereecken, A. R. Rickard, M. J. Newland, and W. J. Bloss. "Theoretical study of the reactions of Criegee intermediates with ozone, alkylhydroperoxides, and carbon monoxide". In: *Phys. Chem. Chem. Phys.* 17 (2015), pp. 23847–23858.

[219] T. Takemura. "Return to different climate states by reducing sulphate aerosols under future CO_2 concentrations". In: *Sci. Rep.* 10.1 (2020), pp. 1–7.

[220] K. H. Becker. *EUPHORE: Final Report to the European Commission, Contract EV5V-CT92-0059*. Tech. rep. Germany: Bergische Universitat Wuppertal, 1996.

[221] K. H. Becker. *In situ EUPHORE Radical Measurement (EUROPHAM) final Report to the European Commission, Contract ENV4-CT95-0011*. Tech. rep. Germany: Bergische Universitat Wuppertal, 1999.

[222] E. C. Tuazon, S. M. Aschmann, J. Arey, and R. Atkinson. "Products of the gas-phase reactions of O_3 with a series of methyl-substituted ethenes". In: *J. Environ. Sci. Technol.* 31.10 (1997), pp. 3004–3009.

[223] E. Grosjean and D. Grosjean. "Gas Phase Reaction of Alkenes with Ozone: Formation Yields of Primary Carbonyls and Biradicals". In: *J. Environ. Sci. Technol.* 31.10 (1997), pp. 2421–2427.

[224] L. Vereecken and A. Novelli. "Unimolecular decay strongly limits the atmospheric impact of Criegee intermediates". In: *Phys. Chem. Chem. Phys.* 19 (2017), pp. 31599–31612.

[225] P. Cossee and J. H. Schachtschneider. "Vibrational analysis of acetone, acetaldehyde, and formaldehyde". In: *J. Chem. Phys.* 44.1 (1966), pp. 97–111.

[226] T. Berndt, T. Jokinen, R. L. Mauldin, T. Petää, H. Herrmann, H. Junninen, P. Paasonen, D. R. Worsnop, and M. Sipilä. "Gas-phase ozonolysis of selected olefins: The yield of stabilized criegee intermediate and the reactivity toward SO_2". In: *J. Phys. Chem. Lett.* 3 (2012), pp. 2892–2896.

[227] T. Berndt, T. Jokinen, M. Sipilä, R. L. Mauldin, H. Herrmann, F. Stratmann, H. Junninen, and M. Kulmala. "H_2SO_4 formation from the gas-phase reaction of stabilized Criegee Intermediates with SO_2: Influence of water vapour content and temperature". In: *Atmos. Environ.* 89 (2014), pp. 603–612.

[228] S. Hatakeyama, H. Kobayashi, and H. Akimoto. "Gas-Phase Oxidation of SO_2 in the Ozone-Olefin Reactions". In: *J. Phys. Chem.* 88 (1984), pp. 4736–4739.

[229] O. Horie, C. Schäfer, and G. K. Moortgat. "High reactivity of hexafluoro acetone toward Criegee intermediates in the gas-phase ozonolysis of simple alkenes". In: *Int. J. Chem. Kinet.* 31.4 (1999), pp. 261–269.

[230] A. S. Hasson, G. Orzechowska, and S. E. Paulson. "Production of stabilized Criegee intermediates and peroxides in the gas phase ozonolysis of alkenes 1. Ethene, trans-2-butene, and 2,3-dimethyl-2-butene". In: *J. Geophys. Res. Atmos.* 106.D24 (2001), pp. 34131–34142.

[231] A. S. Hasson, T. Kuwata, and S. E. Paulson. "Production of stabilized Criegee intermediates and peroxides in the gas phase ozonolysis of alkenes 2. Asymmetric and biogenic alkenes". In: *J. Geophys. Res.* 106.D24 (2001), pp. 34143–34153.

[232] P. Neeb, O. Horie, and G. K. Moortgat. "Gas-phase ozonolysis of ethene in the presence of hydroxylic compounds". In: *Int. J. Chem. Kinet.* 28.10 (1996), pp. 721–730.

[233] P. Neeb, F. Sauer, O. Horie, and G. K. Moortgat. "Erratum: Formation of hydroxymethyl hydroperoxide and formic acid in alkene ozonolysis in the presence of water vapour". In: *Atmos. Environ.* 31.10 (1997), pp. 1417–1423.

[234] F. Su, J. G. Calvert, and J. H. Shaw. "A FT IR Spectroscopic Study of the Ozone-Ethene Reaction Mechanism in O_2-Rich Mixtures". In: *J. Phys. Chem.* 84 (1980), pp. 239–246.

[235] C. S. Kan, F. Su, J. G. Calvert, and S. J. H. "Mechanism of the Ozone-Ethene Reaction in Dilute N_2/O_2 Mixtures Near 1-atm Pressure". In: *J. Phys. Chem.* 85.16 (1981), pp. 2359–2363.

[236] H. Niki, P. D. Maker, C. M. Savage, and L. P. Breltenbach. "A FT IR Study of a Transitory Product in the Gas-Phase Ozone-Ethylene Reaction". In: *J. Phys. Chem.* 85 (1981), pp. 1024–1027.

[237] M. J. Newland, A. R. Rickard, M. S. Alam, L. Vereecken, A. Muñoz, M. Ródenas, and W. J. Bloss. "Kinetics of stabilised Criegee intermediates derived from alkene ozonolysis: reactions with SO_2 , H_2O and decomposition under boundary layer conditions". In: *Phys. Chem. Chem. Phys.* 17 (2015), pp. 4076–4088.

[238] M. S. Alam. "Total radical production and degradation products from alkene ozonolysis". PhD thesis. 2011, p. 274.

[239] A. R. Rickard, D. Johnson, C. D. McGill, and G. Marslon. "OH yields in the gas-phase reactions of ozone with alkenes". In: *J. Phys. Chem. A* 103 (1999), pp. 7656–7664.

[240] R. A. Cox and S. A. Penkett. "Aerosol formation from sulphur dioxide in the presence of ozone and olefinic hydrocarbons". In: *J. Chem. Soc., Faraday Trans. 1: Physical Chemistry in Condensed Phases* 68 (1972), pp. 1735–1753.

[241] H. Niki, P. Maker, C. M. Savage, and L. P. Breitenbach. "Fourier Transform IR Spectroscopic Observation of Propylene Ozonide in the Gas Phase Reaction of Ozone-Cis-2-Butene-Formaldehyde". In: *Chem. Phys. Letts* 46.2 (1977), pp. 327–330.

[242] O. Horie and G. K. Moortgat. "Decomposition pathways of the excited Criegee intermediates in the ozonolysis of simple alkenes". In: *Atmos. Environ. Part A, General Topics* 25A.9 (1991), pp. 1881–1896.

[243] M. J. Newland, C. Mouchel-Vallon, R. Valorso, B. Aumont, L. Vereecken, M. E. Jenkin, and A. R. Rickard. "Estimation of mechanistic parameters in the gas-phase reactions of ozone with alkenes for use in automated mechanism construction". In: *In preparation* (2021).

[244] S. S. Gunthe, P. Liu, U. Panda, S. S. Raj, A. Sharma, E. Darbyshire, E. Reyes-Villegas, J. Allan, Y. Chen, X. Wang, S. Song, M. L. Pöhlker, L. Shi, Y. Wang, S. M. Kommula, T. Liu, R. Ravikrishna, G. McFiggans, L. J. Mickley, S. T. Martin, U. Pöschl, M. O. Andreae, and H. Coe. "Enhanced aerosol particle growth sustained by high continental chlorine emission in India". In: *Nat. Geosci.* 14 (2021), pp. 77–84. URL: http://dx.doi.org/10.1038/s41561-020-00677-x.

[245] D. J. Bryant, G. S. Stewart, B. S. Nelson, S. J. Swift, S. Hapsari Budisulistiorini, W. S. Drysdale, A. R. Vaughan, F. Squires, M. J. Newland, J. R. Hopkins, J. M. Cash, B. Langford, E. Nemitz, W. J. F. Acton, C. N. Hewitt, Shivani, R. Gadi, J. D. Lee, A. R. Rickard, and J. F. Hamilton. "Biogenic and anthropogenic sources of isoprene and monoterpenes and their secondary organic aerosol in Delhi, India". In: *In preparation* (2021).

[246] A. C. Lewis, J. R. Hopkins, D. C. Carslaw, J. F. Hamilton, B. S. Nelson, G. Stewart, J. Dernie, N. Passant, and T. Murrells. "An increasing role for solvent emissions and implications for future measurements of volatile organic compounds: Solvent emissions of VOCs". In: *Phil. Trans. R. Soc. A* 378.20190328 (2020).

[247] A. Elzein, G. J. Stewart, S. J. Swift, B. S. Nelson, L. R. Crilley, M. S. Alam, E. Reyes-Villegas, R. Gadi, R. M. Harrison, J. F. Hamilton, and A. C. Lewis. "A comparison of $PM_{2.5}$-bound polycyclic aromatic hydrocarbons in summer Beijing (China) and Delhi (India)". In: *Atmos. Chem. Phys.* 20 (2020), pp. 14303–14319.

[248] K. Ashworth, S. Bucci, P. J. Gallimore, J. Lee, B. S. Nelson, A. Sanchez-Marroquín, M. B. Schimpf, P. D. Smith, W. S. Drysdale, J. R. Hopkins, J. D. Lee, J. R. Pitt, P. DI Carlo, R. Krejci, and J. B. McQuaid. "Megacity and local contributions to regional air pollution: An aircraft case study over London". In: *Atmos. Chem. Phys.* 20 (2020), pp. 7193–7216.

[249] J. R. Pitt, G. Allen, S. J. Bauguitte, M. W. Gallagher, J. D. Lee, W. Drysdale, B. Nelson, A. J. Manning, and P. I. Palmer. "Assessing London CO_2, CH_4 and CO emissions using aircraft measurements and dispersion modelling". In: *Atmos. Chem. Phys.* 19 (2019), pp. 8931–8945.

[250] I. P. on Climate Change Common Reporting Framework. *Revised 1996 IPCC Guidelines for National Greenhouse Gas Inventories: Reporting Instructions*. Tech. rep. 1996, p. 5.